UNIVERSITÄT
DUISBURG
ESSEN

Open-Minded

Calcium Phosphate Nanoparticles for Medical Application: Drug and Vaccine Delivery

M.Sc. Olga Rotan
from Kharkiv, Ukraine

- zur Erlangung des akademischen Grades Doktorin der Naturwissenschaften (Dr. rer. nat.) -

Faculty of Chemistry
University of Duisburg-Essen, Germany

2015

Die vorliegende Arbeit wurde im Zeitraum von August 2010 bis September 2015 im Arbeitskreis von Prof. Dr. Matthias Epple am Institut für Anorganische Chemie der Universität Duisburg-Essen durchgeführt.

1. Gutachter: Prof. Dr. Matthias Epple
2. Gutachterin: Prof. Dr. Astrid M. Westendorf
Vorsitzender: Prof. Dr. Oliver J. Schmitz

Tag der Disputation: 14. März 2016

Eidesstattliche Erklärung

Hiermit versichere ich, die vorliegende Arbeit mit dem Titel

"Calcium Phosphate Nanoparticles for Medical Application: Drug and Vaccine Delivery"

selbst verfasst und keine außer den angegebenen Hilfsmitteln und Quellen verwendet zu haben. Zudem erkläre ich, dass ich die Arbeit in dieser oder einer ähnlichen Form bei keiner anderen Fakultät eingereicht und bisher an keinem Promotionsverfahren teilgenommen habe.

Ort, Datum	Unterschrift (Olga Rotan)

To my Family

Contents

Abbreviations

AAS	Atomic absorption spectroscopy
Ab	Antibody
Ag	Antigen
APCs	Antigen-presenting cells
ATP	Adenosine triphosphate
BMP	Bone morphologenic protein
BSA	Bovine serum albumin
BSE	Back-scattered electrons
CaP	Calcium phosphate
CD	Cluster of differentiation
CIE	Clathrin-independent endocytosis
CLSM	Confocal laser scanning microscopy
CMC	Carboxymethylcellulose
CME	Clathrin-mediated endocytosis
CpG	Cytosine-phosphodiester bond-Guanine
DAPI	4',6-diamidin-2-phenylindol
DC	Dendritic cell
DLS	Dynamic light scattering
DMEM	Dulbecco's Modified Eagle's Medium
DMSO	Dimethyl sulfoxide
DNA	Deoxyribonucleic acid

dsRNA	Double-stranded RNA
DT	Diphtheria toxin
DLVO theory	Derjaguin, Landau, Verwey and Overbeek theory
EBSD	Diffracted back-scattered electrons
EDTA	Ethylenediaminetetraacetate
EGFP	Enhanced green fluorescent protein
ELISA	Enzyme-Linked Immunosorbent Assay
ELISpot	Enzyme-Linked ImmunoSpot Assay
EPR effect	Enhanced permeability and retention effect
FACS	Fluorescence-activated cell sorting
FCS	Fetal calf serum
FDA	Food and drugs administration
FFU	Focus-forming units
FITC	Fluorescein isothiocyanate
FPM	Fluid phase markers
FV	Friend virus
GPI	Glycosylphosphatidylinisitol
GPSR	G protein-coupled receptors
GTPase	Guanosine triphosphatase
GzmB	Granzyme B
HA	Hemagglutinin
HAP	Hydroxyapatite
HAV	Hepatitis A virus
HBL	Human blood lymphocytes
HBV	Hepatitis B virus
HCV	Hepatitis C virus

HIV	Human immunodeficiency virus
hMSC	Human mesenchymal stem cells
HPV	Hepatitis papillomavirus
HTRA	High temperature requirement protein
i.m.	Intramuscular
i.p.	Intraperitoneal
IC	Infectious centers
IC_{50}	Half maximal inhibitory concentration
IFN	Interferone
Ig	Immunoglobuline
IL	Interleukin
KO mice	Knockout mice
LN	Lymph node
LPS	Lipopolysaccarides
MΦ	Macrophages
MALT	Mucosa-associated lymphoid tissue
MFI	Mean fluorescence intensity
MHC	Major histocompatibilty complex
MP	Microparticles
MRI	Magnetic resonance imaging
MSCGM	Mesenchymal Stem Cell Growth Medium
MTT	3-(4,5-dimethylthiazol-2-yl)-2,5-diphenyltetrazolium bromide
M_w	Molecular weight
NFAT	Nuclear factor of activated T cells
NK cells	Natural killer cells
NLS	Nuclear localization signals

NPC	Nuclear pore complex
NPs	Nanoparticles
NTA	Nanoparticle tracking analysis
ODN	Oligodeoxynucleotides
p.a.	Pro Analysis
P/S	Penicillin and streptomycin
PAMAM	Poly(amidoamine)
PAMPs	Pathogen-associated molecular patterns
PBS	Phosphate buffered saline
PDI	Polydispersity index
pDNA	Plasmide DNA
PEG	Poly-(ethylene)-glycol
PEG-co-PLA	Poly-(ethylene glycol-co-lactide)
PEI	Polyethylenimine
PFU	Plaque-forming units
PLA	D,L-polylactide
PMA	Phorbol-12-myristate-13-acetate
Poly(I:C)	Polyinosinic-polycytidylic acid
PRR	Pattern recognition receptor
PSS	Polystyrene sulfonate
pTHPP	5,10,15,20-tetrakis(4-hydroxyphenyl)-21H,23H-porphine
QD	Quantum dots
qPCR	Quantitative polymerase chain reaction
Rho	Ras homologue
RNA	Ribonucleic acid
ROS	Reactive oxygen species

RPMI-1640	Roswell Park Memorial Institute 1640 medium
RT	Room temperature
RTK	Receptor tyrosine kinase
SD	Standard deviation
SEM	Scanning electron microscopy
SEM	Standard error of the mean (in statistics)
SFFU	Spleen focus-forming units
siRNA	Small interfering RNA
ST	Shiga toxin
SV40	Simian virus 40
T_H cells	T helper cells
T_C cells	Cytotoxic T cells
Tf	Transferrin
TLR	Toll-like receptor
TNF	Tumor necrosis factor
Tregs	Regulatory T cells
TRITC	Tetramethylrhodamine isothiocyanate
U mL^{-1}	Units per mL
USF	Ultrasound finger
UV-Vis spectroscopy	Ultraviolet-visible spectroscopy
VEGF-A	Vascular endothelial growth factor A
VLP	Virus-like particles
WBC	White blood cells
wt	Wild type

1 Introduction

Each piece, or part, of the whole of nature is always merely an approximation to the complete truth, or the complete truth so far as we know it. In fact, everything we know is only some kind of approximation, because we know that we do not know all the laws as yet. Therefore, things must be learned only to be unlearned again or, more likely, to be corrected. ... The test of all knowledge is experiment. Experiment is the sole judge of scientific "truth".

Richard Feynman, Lectures on Physics (1964)

Nano- (from Ancient Greek $\nu\alpha\nu o\varsigma$ – dwarf) technology enables designing and assembling matter on atomic, molecular, and supramolecular scale, i.e. on the dimensions ranging from 1 to 100 nanometers (10^{-9} meters, nm). Nowadays it embraces a broad area of scientific research and industrial application in many fields, starting from material development for space research [1] to cosmetics and sunscreens [2].

The fundamental concepts of nanotechnology were first discussed in 1959 by Nobel laureate physicist Richard Feynman in his talk "Plenty of Room at the Bottom" [3], where he described the possibility of direct manipulation of atoms for synthesis of matter. Fifteen years later, the term "nano-technology" was first used by Norio Taniguchi of the Tokyo University of Science in 1974 in his paper "On the Basic Concept of 'Nano-Technology'" [4].

The use of nanotechnology-based techniques for medical purposes, i.e. nanomedicine, has great potential in terms of curing some world-threatening diseases such as Alzheimer's, Parkinson's disease, atherosclerosis, etc., fighting multiple types of cancer, and preventing infectious disease through developing novel nanoparticles-based vaccines. In addition, the emerging field in nanomedicine,

called "theranostics", can help to simplify many medical treatment procedures by combining diagnostics and therapeutics in a single nanoparticulate agent. Moreover, nanomedicine is now being developed towards cell medicine, i.e. treating and manipulating at the level of cells, subcellular compartments, and even single molecules, thereby helping to drastically decrease the side effects of drugs, reduce their dosage, and make medical procedures more individual-oriented.

Many diverse nanoscale structures for biomedical applications like liposomes, dendrimers, polyplexes, conjugates, organic, inorganic, and metallic nanoparticles [5] have been designed. By tailoring their physical and chemical features such as size, shape, composition, surface charge, and functionalization, these structures can have different biological functions and can be used for various purposes such as *in vitro* and *in vivo* diagnostics, targeting and eliminating cancer cells, delivery of therapeutic molecules inside the cells, activation of the immune system, etc.

This work deals with the synthesis, characterization, and biomedical application of functionalized calcium phosphate nanoparticles. After being loaded with various molecules of biological and synthetic origin, these synthesized nanoparticles were tested as transport system for crossing the cell membrane barrier. The primary focus of research was to study the cellular uptake of cargo-loaded nanoparticles for drug delivery as well as for application as a potential vaccination tool.

2 Theoretical background

2.1 Nanotechnology and nanomedicine

Nanotechnology-based techniques offer immense development opportunities for various fields, of medicine such as pharmaceutics [6], treatment of cancer [7], *in vivo* imaging and diagnostics [8,9], material for implants [10], tissue regeneration [11], cell medicine [12], and gene therapy [13, 14].

Nanomedicine can be described as the application of nanoscaled or nanostructured materials that are in size at least one dimension below 300 nm [15] for medical or biomedical purposes. However, many earlier definitions used 100 nm as the upper limit [16], based on the fact that quantum effects were often restricted to this dimension limit [17, 18]. Special physicochemical properties were shown for nanoparticles larger than 100 nm, e.g. the plasmon-resonance in gold nanoshells with a diameter of 150 nm, which are currently under clinical trials for anticancer thermal therapy [19]. In the pharmaceutical and biomedical areas, the term "nano" is not restricted to 100 nm and a number of biological effects were obtained with particles having a size of 100-400 nm. For example, at the tissue level, liposomes up to 200 nm in diameter remain longer in bloodstream than those with a diameter of 70 nm [20]. Besides, the passive tumor targeting through the enhanced permeability and retention (EPR) effect was shown for the particles within 100-200 nm range, and even for 400 nm particles, the accumulation in tumor tissue was demonstrated [21]. As to the cellular uptake, many particle properties play an important role [22], but size is a key factor. For example, cells with no phagocytic activity are able to internalize nanoparticles up to 200 nm in diameter [23–25]. Hardy *et al.* reported that a size of 50 nm is

optimal for a high uptake efficiency [25], whereas macrophages can phagocytose particles up to 500 nm in diameter [26].

Nanomedicine uses benefits of two general phenomena that occur at the nanoscale: transition in physicochemical properties and transition in physiological properties [15]. To these transition phenomena belong the high ratio of surface area to volume as well as tunable optical, electrical, magnetic, mechanical, chemical [27–29], and biological properties. Many (if not all) biochemical processes in living cells naturally occur at the nanoscale. For example, the oxygen-carrier protein hemoglobin is 5.5 nm in diameter and a strand of DNA is only about 2 nm in width [27].

Table 2.1 Some examples of application of nanoparticles in medicine.

Nanoparticles	**Examples**	**Application in medicine**
Metallic	Gold, silver, titan, iron, platinum	Thermal anticancer treatment, MRI contrast, *in vitro* diagnostics
Quantum dots	CdSe, CdS, CdS/ZnS	Fluorescent contrast, *in vitro* diagnostics
Inorganic	Silica, calcium phosphate, barium sulfate	Drug and gene delivery, *in vivo* imaging, vaccination, X-ray contrast agent, bone cement additives
Carbon nanostructures	Fullerenes, graphene, single- and multi-wall nanotubes, nanodiamonds	Increasing imaging facility of magnetic resonance (MR), improving imaging-based diagnosis
Polymer-based	Hydrogels, dendrimers, nanofibers, polymersomes	Drug and gene delivery, anticancer treatment, antiviral treatment
Lipid-based vehicles	Liposmes, micelles, solid lipid nanoparticles	Drug and gene delivery, anticancer treatment

Nanoparticles for medical application come in a great variety [5]. They include metallic nanoparticles [30–33], quantum dots, inorganic nanoparticles [34–37],

carbon nanostructures [38–47], polymer-based nanoparticles [48–60], and lipid-based vehicles [6, 61, 62]. Some prominent examples of their application in medicine are summarized in Table 2.1.

2.1.1 Gene therapy and drug delivery with nanoparticles

One of the most promising areas of application of nanoparticles is drug delivery and gene therapy. These techniques are generally associated with the elimination of malignant tissues and fighting widespread neurodegenerative diseases. Nanoparticles of different kinds can help medical science to overcome these disorders in human body [63], for example, by delivering some vital genes into the cells, where these genes are inactive or absent, in the form of plasmid DNA (pDNA). Since unprotected DNA is not able to penetrate the cell membrane and is degraded either inside or outside the cell by nucleases, a delivery agent in the form of nanoparticles (calcium phosphate, gold) [64–68], viral agents (retrovirus- or adenovirus-based) [69, 70], liposomes/micells [71], or cationic polyelectrolyte (polyethylenimine) [72–75] is needed [76].

In contrast, when some genes are overexpressed in a particular cell type or tissue, this can also lead to serious disorders in the human body (acquired or inherited diseases), including the development of cancer. As a result, the so-called "gene silencing" technique is used to "silence" particular genes in terms of protein production [77–83]. This method is similar to gene delivery, whereas the delivered cargo is small RNA molecules, either small interfering RNA (siRNA) or microRNA. These RNAs interfere with double-stranded RNA (dsRNA) that carries information about the synthesis of specific protein, thus blocking the transcription process in cytoplasm [76].

Functionalized nanoparticles are key players in the field of drug and vaccine delivery [84–86], because they can significantly enhance the delivery efficacy, thus dramatically decreasing overall drug toxicity [87, 88]. This can permit the application of potentially comparable toxic drugs or compounds that are not

able to penetrate some biological barriers. A combinational approach of using nanomedicine with traditional clinical therapies can bring us a step forward regarding, e.g. the treatment of cancer. Recent studies of timed combination therapy on animals where siRNA and an anticancer drug were released sequentially from liposomal nanoparticles may help to reveal the mechanisms to overcome chemoresistance [89].

2.1.2 Potential risks

Over the last two decades, nanotoxicologists have been studying the influence of nanomaterials on single cell up to the whole organism. It has been found that interactions between nanomaterials, cells, animals, humans, and the environment are remarkably complex. The toxicity of nanoparticles can be defined as the ability of the nanoscaled structures to adversely affect the normal physiology and structure of tissues and organs in humans and animals [90]. It is thought that toxicity depends on such physicochemical parameters of the nanoparticles as particle size, shape, surface charge, chemical composition, biodegradability, as well as clinical parameters like application routes, nanoparticle concentration or duration of exposure [90, 91]. Recent studies suggest that cytotoxic effect is related to the development of oxidative stress and pro-inflammatory gene activation in exposed cells and tissues, as well as the subsequent damage to proteins, membranes and DNA [91–95]. For instance, the pro-inflammatory effect was observed after the exposure of human endothelial cells to cobalt, silicon dioxide, and titanium dioxide nanoparticles through enhanced production of the IL-8 cytokine [91]. However, the exact mechanisms are yet unknown.

The adverse effects of exposure to nanoparticles are likely associated with a range of acute and chronic effects, including inflammation, exacerbation of asthma, metal fume fever, fibrosis, chronic inflammatory lung diseases, or carcinogenesis. [96–98].

Extensive research and ongoing debates on the regulation of nanomaterials are

happening across the world [88, 99, 100]. The Joint Research Centre of European Commission considers this issue at the European level [101]:

"*Nanotechnology is a key enabling technology and has great potential for addressing societal challenges including energy supply and health care. Nonetheless, the use of nanomaterials also raises safety concerns, which need to be addressed in a Europe-wide regulatory context. ...In the past years, many new nanomaterial-related applications have been developed. Those include a number of consumer products such as UV-filters in sun creams and anti-odor textiles. However, many medical and technical applications such as tumor therapies, lithium-ion batteries for driving electric cars, or solar panels also exist. Those applications have the potential to create major technological breakthroughs, and therefore nanomaterials have been identified as a key enabling technology. Products underpinned by nanotechnology are forecast to grow from a global volume of 200€ billion in 2009 to 2€ trillion by 2015.*" [102]

Thus, as government and business communities continue to invest heavily in nanotechnology, the potential toxicological effect of the developed nanomaterials need also to be explored. Besides, nanotechnology has a lot to offer to the field of human healthcare and medicine, improving diagnostics and paving the way to regenerative medicine. It can provide qualitative and personalized healthcare and yet make it more affordable.

2.2 Calcium phosphate nanoparticles

2.2.1 Hydroxyapatite

Hydroxyapatite (HAP) is the main mineral component of biological hard tissues, like bone (65-70%) [103], dentin (70%) and enamel (97%) [103–106]. HAP is a mineral belonging to the family of apatites, whose general formula is $M_5(ZO_4)_3X$, where M represents an ion of rare-earth metal (Ca^{2+}, Cd^{2+}, Sr^{2+},

Ba^{2+}, Mg^{2+}, Pb^{2+} or Zn^{2+}); ZO_4 is PO_4^{3-}, CO_3^{2-} or SO_4^{2-}; and X is OH^-, F^-, Cl^- or CO_3^{2-} [107]. HAP is, thus, described by the formula $Ca_{10}(PO_4)_6(OH)_2$ or in a reduced form as $Ca_5(PO_4)_3OH$ [107, 108]. HAP is the most stable calcium phosphate (CaP) compound in the pH range from 4.2-12.4 [107, 108]. However, in biological tissues such as human bone, HAP can undergo an extensive substitution of ions, for example (Ca, X)$_5$(PO_4 Y)$_3$(OH, Z), where X: Na^{2+}, Mg^{2+}, K^+, Sr^{2+} and others; Y: CO_3^{2-} or HPO_3^{2-}; and Z: Cl^- or F^- [107, 108]. As a ceramic material HAP represents a chemical compound with a mixture of ionic and covalent bonds. Depending on the stoichiometry, pH value, temperature, and other conditions, CaP can form different phases with specific configurations and properties [107, 108], ranging from the most water soluble monocalcium phosphate monohydrate ($Ca(H_2PO_4)_2{\cdot}H_2O$) with a Ca/P ratio of 0.5, through HAP with a Ca/P ratio of 1.67 and with the lowest water solubility, to tetracalcium phosphate ($Ca_4(PO_4)_2O$) with a Ca/P ratio of 2.0 [103].

2.2.2 Synthesis of calcium phosphate nanoparticles

There are numerous methods of synthesis of CaP particles, including reactions in solid state [109–112], continuous precipitation from solution [113–116], hydrothermal processing [117, 118], electrospraying [119], electrospining [120], ultrasound [121], plasma deposition [122], and many others [107]. The method of wet chemical precipitation, described previously by Sokolova *et al.* [123], was used in this work to obtain the CaP core of the nanoparticles. It is a widely used method due to its simplicity and inexpensiveness [124, 125], and it involves a rather simple reaction of precipitation of CaP nanoparticles from solutions containing the Ca^{2+} and PO_4^{3-} salts $Ca(NO_3)_2$ and $(NH_4)_2HPO_4$, respectively. The cargo molecules (e.g. oligonucleotides and proteins), which are dissolved in water are added subsequently to the nanoparticles' dispersion and are adsorbed onto the particles' surface non-covalently due to hydrophobic or van der Waals forces [107], as well as electrostatic interaction (Figure 2.1). Afterwards, the

solution of Ca^{2+} and PO_4^{3-} containing precursors are added to form another shell of CaP and finally the nanoparticles are stabilized with polyelectrolyte molecules such as oligonucleotides.

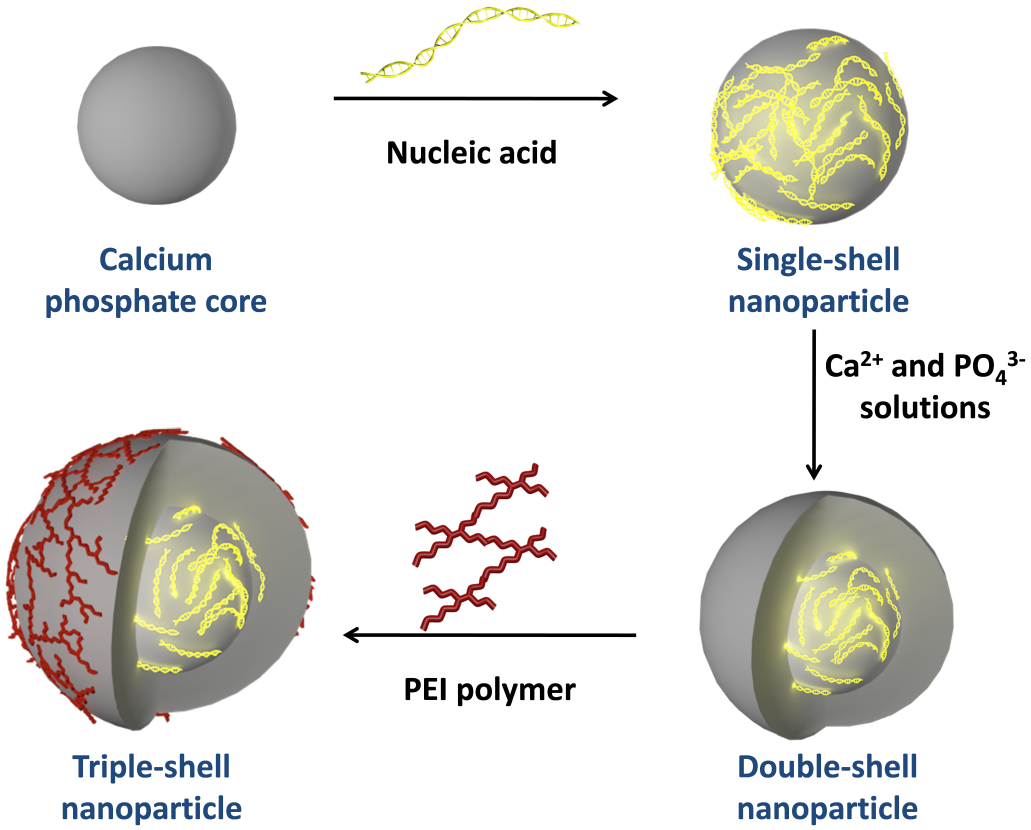

Figure 2.1 The scheme of synthesis of multi-shell calcium phosphate nanoparticles.

HAP forms sparingly soluble salt crystals in neutral and alkaline aqueous solutions and is well soluble in acidic environment. The precipitation of these crystals can occur in different morphologies (spherical, rod-like, filaments, plate- or needle-shape particles) [126–131]. Therefore, the modulation of interaction between growing inorganic particles, as well as their morphology by electrostatic and steric interactions is strongly desired. For this purpose, the zeta potential of colloidal nanoparticles can be modified by functionalizing the nanoparticles with different cationic and anionic polyelectrolytes (Figure 2.2).

A hydrated layer comprising relatively mobile ions is assumed to be present

on the surface of the nanoparticles in the dispersion. The composition of this layer depends on the pH value of the solution as well as the ionic content of the medium. The ratio of Ca^{2+} to PO_4^{3-} ions in the solution is also important as it triggers the precipitation of a specific phase combination [107].

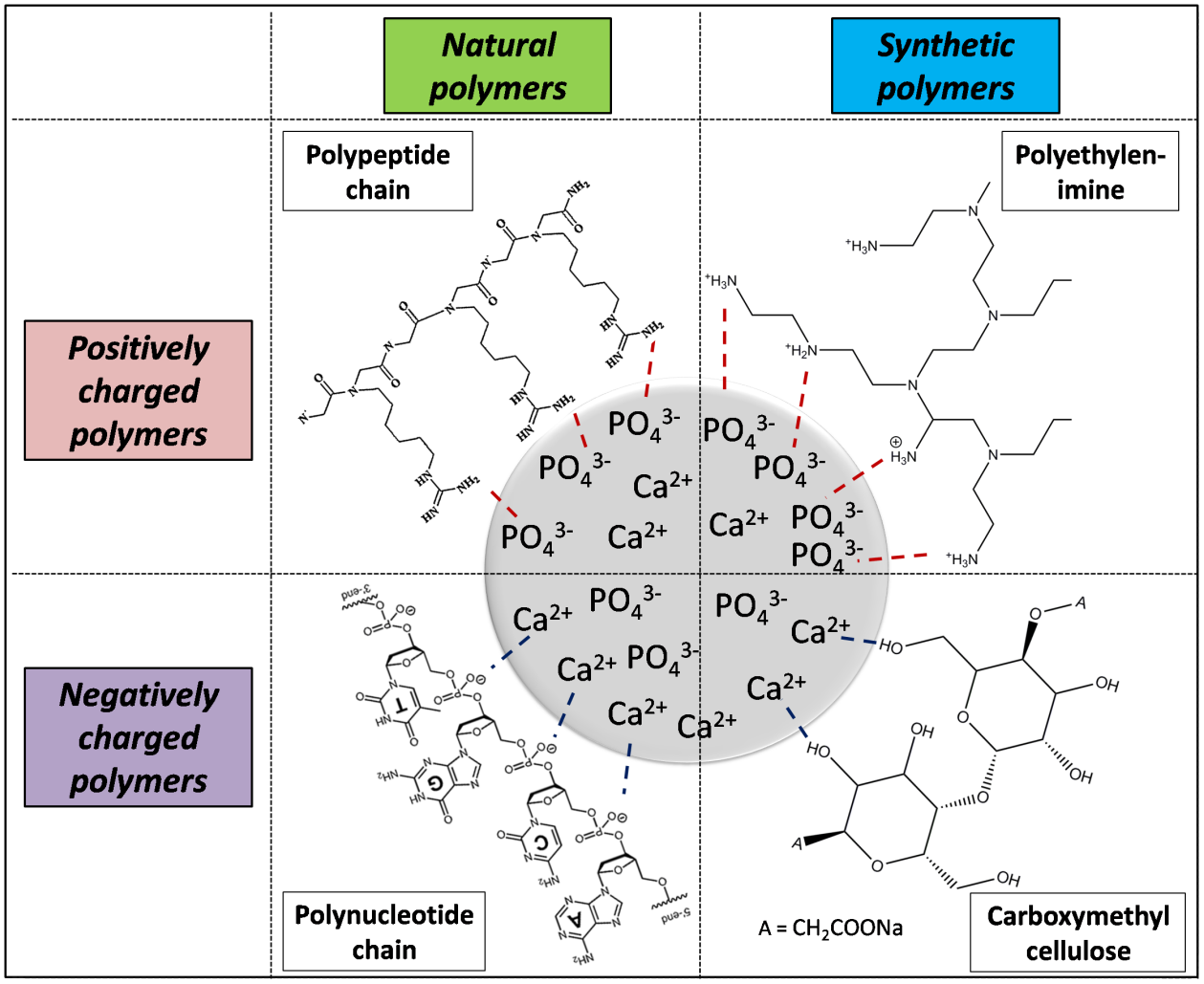

Figure 2.2 Different polyelectrolytes to functionalize and stabilize calcium phosphate nanoparticles in dispersion.

2.2.3 Calcium phosphate nanoparticles as a colloid system

The synthesized CaP nanoparticles are present in aqueous dispersion, thereby forming a colloid dispersion. In colloids, particles continuously experience the in-

fluence of Brownian motion, gravity, convection, and other forces. If two particles are brought together too closely, they attract to each other due to the van der Waals forces. In the absence of repulsion counterforce, the particles will collide and form the agglomerates, which results in destabilization of the colloidal system and the eventual sedimentation of the particles from the solution. Hence, to achieve stable colloid dispersions, the forces of repulsion and attraction should be balanced.

There are two mechanisms that counteract the van der Waals forces of attraction in colloids: electrostatic and polymeric stabilization. Owing to the first mechanism, the attraction of the particles is balanced by the Coulomb force of electrostatic repulsion of the electrical double-layer of the particles with the same charge [132, 133].

The electrical double layer is a layer of oppositely charged ions from the dispersion medium surrounding the particle (Figure 2.3). The electrical double layer has no charge (electrically neutral). This layer comprises the following parts: the surface charge is presented by the charged ions of the particles on its surface; the stern layer is the layer of the counter ions from the dispersion medium that are closely attached to the surface of the nanoparticles by the electrostatic force; the diffuse layer is a film of the solvent molecules that immediately surrounds the particle and contains free ions, mostly of the opposite charge (these ions are also affected by the electrostatic force of the charged particle but to a much lower extent); the slipping plane (or shear plane) is the outer boundary of the layer that remains along with the moving in the medium particle.

The electric potential (zeta potential) of the double layer has its maximum on the surface plane and then drops exponentially with the increase in the distance from the particle surface (Figure 2.3) reaching zero in the bulk solution. The zeta potential of the particles in the dispersion is measured on the stern plane.

The mechanism of electrostatic balance between the electrical double-layer of the particles and the van der Waals attraction force is described by the DLVO

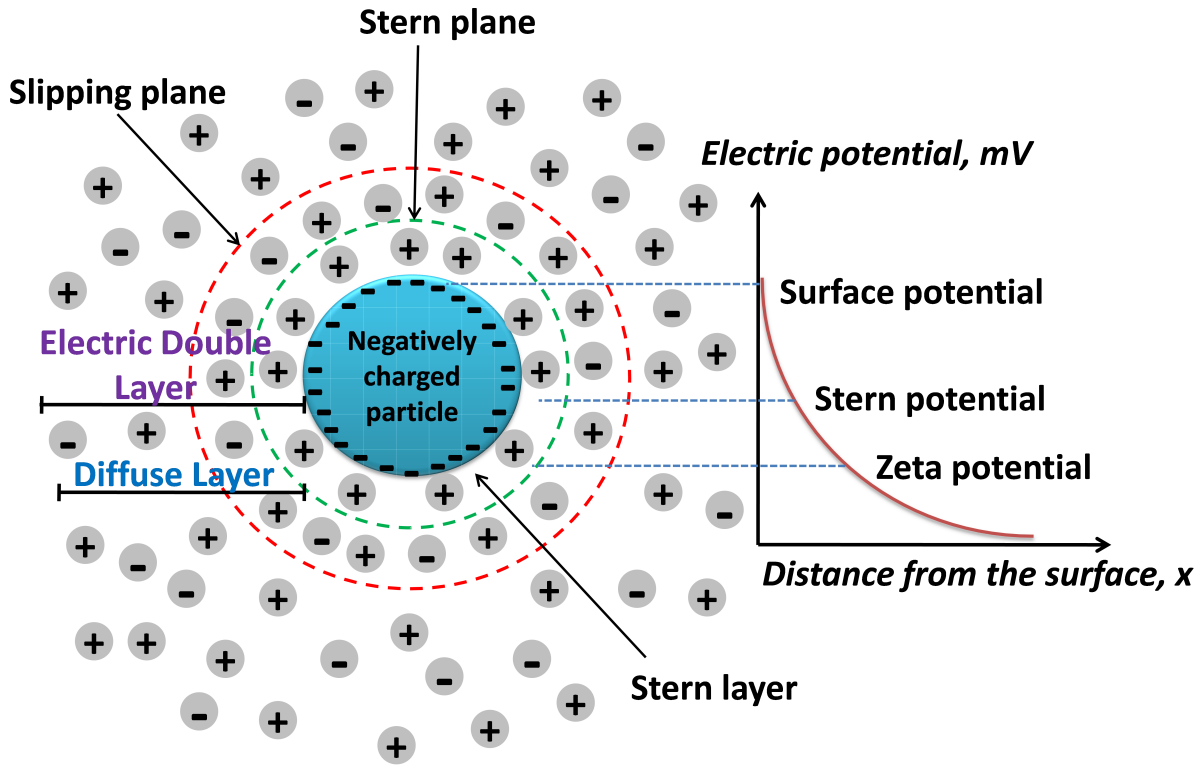

Figure 2.3 The structure of electrical double-layer of a particle in the colloid.

theory which was developed in the 1940s by Derjaguin, Landau, Verwey, and Overbeek. There are, however, some assumptions that need to be considered while applying this theory: 1) the dispersion is dilute; 2) the electrical charge and other properties are uniformly distributed over the surface of the particles; 3) only van der Waals and electrostatic forces act on the dispersed particles; 4) the distribution on the ions in the dispersion is determined by Brownian motion, electrostatic force, and entropic dispersion [132].

The DLVO theory states that the colloidal stability of the particles is determined by the total energy (G_T) of interaction between two particles, represented by the sum of the energy of attractive interaction because of van der Waals forces (G_A) and repulsive electrostatic energy (G_R):

$$G_T = G_A + G_R$$

For the spherical particles, van der Waals potential energy (G_A) and repulsive

electrostatic potential energy (G_R) values are calculated as follows:

$$G_A = \frac{-Ar}{12x}$$

with A: Hamaker constant; r: radius of the particles; x: distance between the surfaces of two particles.

$$G_R = 2\pi\varepsilon\varepsilon_0 r\zeta 2e^{-kx}$$

with ε: dielectric constant of the solvent; ε_0: vacuum permittivity; ζ: zeta potential; k: a function of the ionic concentration (k^{-1} is the characteristic thickness of the electric double layer, Debye length).

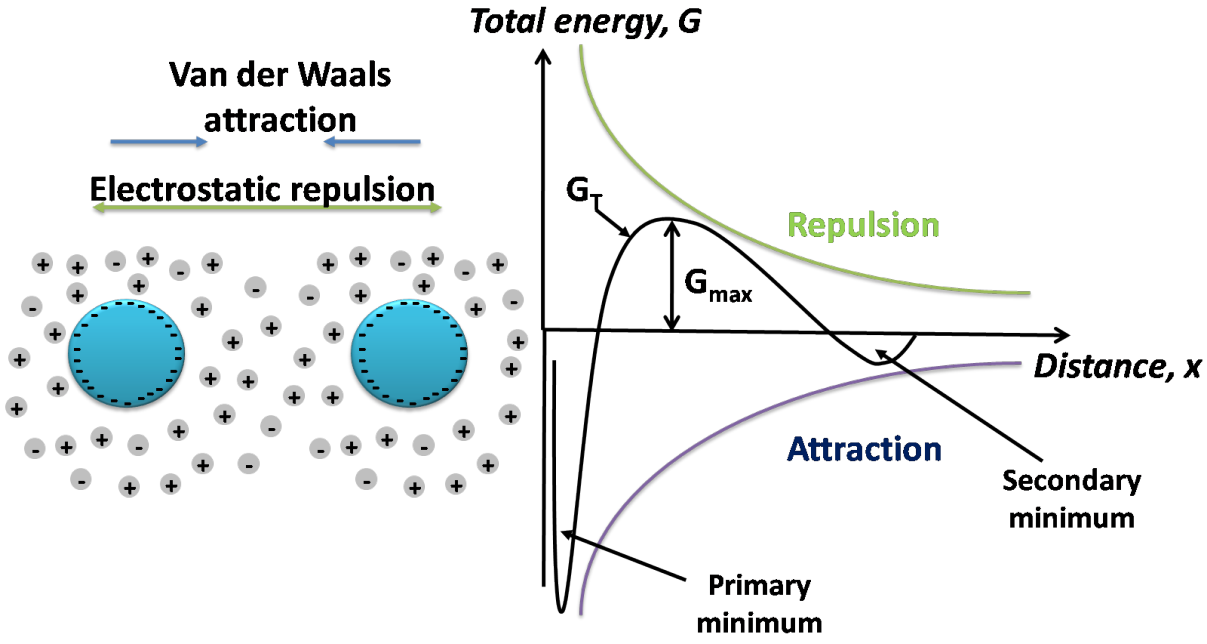

Figure 2.4 The mechanism of the DLVO theory.

The potential energy of interaction between two spherical particles is depicted and described in Figure 2.4. G_R decays exponentially with increasing distance, approaching zero at large x, whereas G_A shows inverse power law and tends to zero. The G_T curve shows two minima and one maximum peaks. The maximum peak (G_{max}) refers to the energy maximum barrier and is dependent on the

zeta potential, the electrolyte concentration, and the ion charge [133]. This maximum barrier has to be much larger than the thermal energy of the particles in order to obtain a stable colloid. This is achieved by a high zeta potential (>40 mV) and a low electrolyte concentration ($<10^{-2}$ mol L^{-1}). The primary minimum corresponds to the distance by which the particles undergo coagulation when they are able to overcome the energy barrier (G_{max}) [133]. The secondary minimum corresponds to the distance between two particles where they are in a stable equilibrium and may undergo a loose aggregation but can be easily redispersed [132].

Polymeric stabilization of colloids involves the addition of the polymer molecules to the dispersion in order to prevent the particle's agglomeration. This occurs due to the repulsive force created by polymeric molecules that counteract the attractive van der Waals forces between two particles. The polymeric stabilization can be performed in two ways: by steric stabilization, where the polymer molecules are directly attached to the particle surface and form a coating that creates a repulsive force and separates the particles from one another, and by depletion stabilization, which involves dissolved (free) polymeric molecules in the dispersion medium, creating repulsive forces between nearing particles (Figure 2.5) [132].

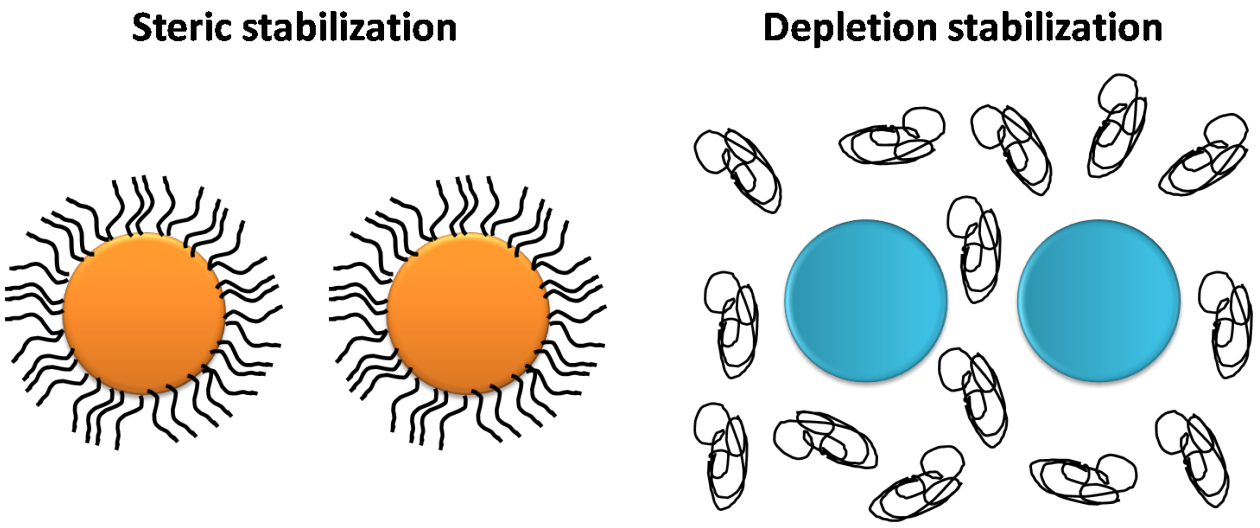

Figure 2.5 Polymeric stabilization of colloids.

2.2.4 Application in bio- and nanomedicine

Materials from CaP are widely used in medicine for substituting damaged or impaired hard tissues. However, the application of CaP is not limited to this. For example, it is used in chromatography for separating of proteins and DNA [134, 135]. Colloidal CaP was shown to stabilize casein micelles in milk [136]. It has also been used as a nutrition supplement, a growth and fertilization agent in the food and agricultural industry [137]. But with the developments in the field of nanomedicine, CaP as a form of colloidally stabilized nanoparticles has drawn big attention as a potential agent for drug delivery, *in vivo* imaging, gene therapy, vaccination, etc. Additionally, there are several other reasons why CaP nanoparticles (NPs) have such potential:

- The synthesis is scalable, easy, time-saving, and inexpensive. The encapsulation of various components of synthetic and biological nature is possible. The binding affinity to DNA molecules was shown [138].
- The synthesis is performed under ambient conditions. Various morphologies and sizes of the NPs can be obtained [139–142].
- The active compounds are protected inside the multi-shell structure of the NPs [64].
- The NPs can penetrate the cell membrane and, are thus able to deliver molecules across the membrane barrier [12, 143].
- The material is non-toxic. The degradation of CaP NPs occurs in lysosomes under low pH and does not produce any toxic components. The over-concentrated Ca^{2+} ions are pumped out of the cell through ion channels [144].
- Good biocompatibility. Compounds of CaP NPs are naturally found in biological hard tissues (bone, dentin, and enamel) in amorphous and crystal phases. It is not a foreign compound in living cells and the human body in general. The human blood contains Ca^{2+} and PO_4^{3-} ions in concentrations

1-5 mM [103, 107].

- NPs are stable in blood and other biological solutions where pH>6. They are not prone to enzymatic degradation [103].
- Good storage abilities (in colloidal form for two weeks under 4 °C, in lyophilized form for many months).

The main drawback of using CaP nanoparticles *in vivo* is, however, the risk of possible atherosclerotic complications associated with undesirable sediments along the arterial walls [145, 146].

Nonetheless, examples of CaP nanoparticles application for bio- and nano-medicine include the following: encapsulation of antibiotics gatifloxacine [147], ciprofloxacin [148], as well as gentamicin and vancomycin [149]; loading with DNA, encoded vascular endothelial growth factor (VEGF-A) and protein BMP-7 for induction of the new bone and vascular tissues formation [150]; encapsulating immunostimulatory molecules and viral peptides to stimulate specific antiviral immune responses [151–154].

2.3 The mechanism of nanoparticle uptake by cells

2.3.1 Plasma membrane

The cell membrane is a crucial structure of a living cell. The plasma membrane in eukaryotic cells is a thin interface that encloses the cell and maintains the essential differences between the cytosol and the extracellular environment. The plasma membrane consists of a lipid bilayer (about 5 nm thick [155]), mostly of phospholipids (phosphoglycerides and sphingomyelin), cholesterol, and membrane proteins. The organization of this film is mostly due to a non-covalent interaction between the lipid molecules. The lipid bilayer provides the membrane with its fluid

structure and relatively impermeable barrier function for water-soluble molecules while proteins provide the rigidness to the structure. The fluidity of the membrane is directly dependent on its composition and the temperature (the higher the temperature, the more fluid the membrane becomes). Cholesterol and proteins, on the contrary, can modulate the stability and permeability in the specific place of the membrane. When a molecule of cholesterol is inserted near the backbone of a phospholipid, it decreases the permeability of this region of the membrane through the decreasing mobility of the first CH_2-groups of the phospholipid. Thus, the lipid bilayer becomes more rigid and less permeable for small water-soluble molecules.

Membrane proteins play more than a structural role. They are responsible for transporting specific molecules across the membrane (ion channels and receptor-mediated endocytosis), membrane-associated enzymatic processes (e.g. synthesis of ATP), and interconnection of membrane body with the cytoskeleton inside the cell (lipoproteins, G proteins). They also function as transmembrane receptors for different regulative molecules, hormones, and cytokines, through which the cellular metabolism and gene machinery are orchestrated.

Another important property of the plasma membrane is asymmetry. First of all, this refers to the lipid composition. The outer monolayer comprises mostly choline-bearing phospholipids that carry overall neutral charge. In the inner monolayer, the phospholipids containing terminal primary amino groups, the phosphate moieties, and the carboxy groups with overall negative charge are located. As a result, there is significant difference in the charge between two monolayers in the membrane. In the live cells, this asymmetry is constantly maintained and serves as an indicator for live cells in the animal or human body [155]. A more extreme asymmetry is observed in the glycosylation of lipids and membrane proteins. These glycosylated molecules are almost exclusively presented in the outer monolayer, thus forming the negatively charged network of proteoglycans, glycoproteins, and glycolipids [156]. Denoted as glycocalyx, this network covers the whole surface of the living cell and functions in cell-cell recognition, communica-

tion, and interaction [157].

2.3.2 Mechanisms of endocytosis

Being a dynamic structure, the plasma membrane not only segregates the inner milieu of the cell from the extracellular environment, but also provides the selective transport of small and large molecules between the cytosol and extracellular compartments. Ions and small molecules such as amino acids, sugars, small signal molecules and water can traverse the membrane through channels or by means of special membrane transport proteins. Macromolecules can be internalized only inside the membrane-bound vesicles derived by invagination and pinching off the pieces of plasma membrane. This process is called "endocytosis" [158].

Endocytosis can be accomplished by various mechanisms, depending on the cell type and the internalized cargo [153, 159]. Typically, the mechanisms of endocytosis are categorized in the following manner (Table 2.2).

Phagocytosis is generally restricted to specialized mammalian cells, while pinocytosis occurs in all cell types in four major classes: macropinocytosis, clathrin-mediated endocytosis (CME), caveolin-mediated endocytosis, and clathrin- and caveolin-independent endocytosis. The endocytosis, performed in these five major forms, plays a key role in such complex physiological and biochemical processes, as antigen-presentation, hormone-mediated signal transduction, immune surveillance, cellular metabolism, and homeostasis [158].

Phagocytosis is mainly conducted by specialized mammalian cells such as monocytes, macrophages (MΦ), dendritic cells (DCs), and neutrophils. It is involved in the clearance of pathogens, e.g. bacteria or fungi, as well as of necrotic cell debris, apoptotic cells, [160] and foreign objects of comparable size (latex beads, nanoparticles, etc.). This highly regulated process is activated through specific cell-surface receptors such as the complement or phosphatidiylserine receptor that recognizes damaged or dead cells, and through signaling cascades mediated by Rho-family GTPases [161].

Table 2.2 Morphological and molecular characteristics of endocytotic mechanisms. FPM: Fluid phase markers, GPI: Glycosylphosphatidylinisitol, GPSR: G protein-coupled receptors, MHC: major histocompatibilty complex, RTK: receptor tyrosine kinase, SV40: simian virus 40.

Mechanism	**Phagocytosis**	**Pinocytosis**			
		Macropinocytosis	**Clathrin-mediated endocytosis**	**Caveolin-mediated endocytosis**	**Clathrin- and caveolin-indipendent**
Size of cargo	1-5 μm	>1 μm	120 nm	60 nm	90 nm
Implicated cargoes	Pathogens, apoptotic remnants	FPM, RTK	RTK, GPSR, transferrin receptor	GPI-linked proteins, SV40,	FPM, GPI-linked proteins, cytokine receptors, MHC I proteins, proteoglycans, CD59
Morphology	Cargo shaped	Highly ruffled	Vesicular	Vesicular / tubulo-vesicular	Tubular, ring-like, vesicular

Similarly to the phagocytosis, macropinocytosis is induced by Rho-family GTPases, which trigger the formation of membrane protrusions by actin filaments. These protrusions collapse onto and fuse with the cell membrane, unlike in phagocytosis. This type of endocytosis is involved in the following events: cell migration [162], immune surveillance [163], and uptake of some bacteria [164].

Caveolin-mediated endocytosis is performed through flask-shaped invaginations of the membrane, called caveolae. These are usually formed in the cholesterol- and sphingolipid-rich regions of the plasma membrane, where various membrane transporters and signaling molecules are concentrated [165]. Caveolin is a dimeric

protein that conducts the formation of the caveolae in the following way. It binds to the cholesterol, inserts a loop into the inner leaflet of the membrane and builds a caveolin coating by self-association on the surface of the membrane invagination [158]. The most important processes that are regulated by this type of endocytosis are lipid homeostasis (through intracellular cholesterol trafficking), vasodilatation (through regulation of endothelial nitric oxide synthase) [165,166], and transcellular transport (e.g. of serum albumin) [166].

Clathrin-mediated endocytosis is not cell type-specific and occurs in all mammalian cells, providing continuous uptake of nutrients such as iron-laden transferrin and cholesterol-laden low-density lipoproteins [167, 168]. This type of endocytosis is mediated through clathrin protein "triskelions", comprising three heavy and three light chains. These clathrin triskelions assemble into a polygonal lattice on the inner layer of the membrane. This deforms the overlying plasma membrane into a vesicle-like form and finally pitches off the clathrin-coated vesicle [158]. Clathrin-mediated endocytosis was shown to be involved in numerous cellular processes, namely intracellular communication during tissue and organ development [169, 170], maintaining cell and serum homeostasis [158], controlling the strength of synaptic transmission in neurons, which might have a role in learning and memory [171], and efficient recycling of synaptic vesicle membrane proteins after neurotransmission [172].

Clathrin- and caveolin-independent endocytosis refers to the internalization of the macromolecules that are promoted by mechanisms other than those described above. This was, for example, shown for lipid rafts (small structures of 40-50 nm in diameter on the cell surface [158]). The internalization of IL-2 receptors on lymphocytes associated with lipid rafts or rapid endocytosis in neurons was detected to perform in clathrin- and caveolin-independent manner [173,174]. Other mechanisms of clathrin- and caveolin-independent endocytosis include Arf6-dependent, Flotilin-dependent, Cdc42-dependent, and RhoA-dependent mechanisms [175]. In general it must be stated that the mechanisms of endocytosis are still poorly understood and described.

2.3.3 Internalization on the nanoparticles

With rising interest in nanomedicine in recent years, a lot of research has been done to understand the internalization of nanoparticles for purposes like drug delivery and imaging *in vitro* as well as *in vivo* [176–181]. It has been, however, stated that such a complex process as endocytosis of nanoparticles cannot be generalized: the efficiency and results of cellular uptake are clearly dependent on the properties of both nanoparticles and cells [182]. Such physicochemical parameters of nanoparticles like size, shape, geometry, surface charge, chemical composition influence the uptake efficiency [175]. Some examples are summarized in Table 2.3.

One should also notice that initially colloidally stable "small" nanoparticles will often agglomerate in biological fluids such as cell culture media, supplemented with calf serum, into "bigger" nano- or even submicroparticles, surrounded by absorbed proteins ("protein corona") [183]. Hence, the cells *in vitro* and *in vivo* are almost never exposed to the nanoparticles in the way they were initially manufactured.

Nonetheless, some generalizing remarks can be made in terms of nanoparticle size and charge. It was shown [184–186] that nanoparticles of 20-50 nm in diameter are taken up faster and better by the cells than bigger particles. It is also generally believed that positively charged nanoparticles are better internalized by cells due to the electrostatic interaction between the positive charge of nanoparticles and the negative charge of the plasma membrane of the cells [153, 159, 187, 188], namely through interaction with heparan sulfate proteoglycans on the cell surface [183, 189]. Nazarenus *et al.* describe in their work [183] main issues on the nanoparticles internalization and the colloid-chemical parameters that strongly influence the cellular uptake of the nanoparticulate matter. The following summary statement can be made based on this publication: small, charged, and elongated nanoparticles are taken up better than big, neutral, and flat ones.

In contrast, the uptake efficiency is strongly influenced by cell-type, origin of

cells, cell density, concentration of the nanoparticles, exposure scenarios, and the presence of serum supplement in the cell medium [182, 183]. For the influence of cell type, one can look at the two independent studies by Harush-Frenkel *et al.* [190] and Zhang *et al.* [191] who tested positively and negatively charged nanoparticles of equal size. In fact, the studies on HeLa cells showed a two times more efficient uptake of positively charged nanoparticles [190].

Table 2.3 Dependence of internalization results *in vitro* from physicochemical parameters of applied nanomaterials.

Physico-chemical parameter	Description of the particles	Results of the uptake	Cell type
Geometry	Polystyrene, elliptic, size 1-10 μm	MΦ internalized particles fast when they were attached to its sharper side, whereas attachment from the dull side of the particle resulted in no uptake at all	Alveolar macrophages (MΦ) [192, 193]
Charge	PEG-co-PLA, anionic vs. PEG-co-PLA + stearylamine, cationic; 100 nm	Uptake of cationic NPs was better than anionic in both cell types. MDCK cells used CME for both NPs types: cationic NPs were routed to transcytosis, anionic NPs to lysosomes. HeLa used CME + caveolin-mediated endocytosis for anionic NPs and CME + micropinositosys for cationic NPs	Fibroblasts and epithelial cells (polarized MDCK and non-polarized HeLa) [194–197]
Surface modifications	Quantum dots (QD), functionalized with Transferrin (Tf) (50 nm), or Shiga toxin (ST) (30 nm)	QD + Tf were internalized by CME, but they resided in perinuclear endosomes. Tf alone was taken up by CME but ended up in the lysosome. QD + ST were internalized by and ended up in endosomes. ST alone accumulated in the Golgi apparatus	HeLa [198]

Shape	Cross-linked PEG-based hydrogels, cationic; cubic (2-5 μm), cylindrical microparticles (MPs)(0.5-1 x 1 μm) and cylindrical NPs (100-200 x 200-450 nm)	All particles were taken up by CME, caveoline-mediated and macropinocytosis. NPs were internalized faster than MPs. Cylinders of 150 x 450 nm were internalized faster than cylinders 200 x 200 nm and 100 x 300 nm	HeLa [199, 200]
Size	Polysiloxane NPs, anionic 43 nm vs. 24 nm	43 nm NPs entered with CME and ended up in endolysosomal compartment. 24 nm NPs entered with clathrin- and caveolin-independent pathway bypassed the lysosomes and ended up in perinuclear space	HeLa [201]
Dendrimer generation	PAMAM dendrimers, amine-modified G2 vs. G4 generations	G2 dendrimers entered primarily by CME, G4 utilized multiple routes	Caco-2 B16f10 [202, 203]
Structure	Branched PEI (bPEI) vs. linear PEI (lPEI) in polyplexes with DNA	bPEI polyplexes predominantly used CME in COS-7 and both CME and caveoline-mediated pathways in HeLa; lPEI utilized CME independently from cell types. lPEI polyplexes utilized both CME and caveolin-dependent pathways	COS-7, HeLa [203–205]

In contrast, the results of experiments reported by Zhang *et al.* revealed an opposite effect on the HEK cell line. Whereas, non-adherent (suspension) cell lines were reported to show no significant uptake of the nanoparticles at all [183, 206].

Thus, in light of the controversial information, research should pay more attention to the mechanisms of the endocytosis in different cell types. So far, most of the uptake studies have focused on non-polarized cells (cells with a homogeneous morphology). However, it has been reported that polarized and non-polarized cells utilize different uptake mechanisms [207] (see also Table 2.3).

Based on our research [14, 151, 153, 208] and the knowledge gained from the literature [209, 210], we propose the following scheme of cellular uptake and intracellular fate of multi-shell calcium phosphate nanoparticles on the example of nanoparticles, functionalized with DNA and PEI for transfection of cells (Figure 2.6). Positively charged functionalized calcium phosphate nanoparticles interact with the negatively charged cell membrane via electrostatic interaction and enter the cell by macropinocytosis [12, 153, 211, 212]. The protonated amine groups in the PEI molecules increase the osmotic pressure in the endosome, thus leading to the disruption of the endosomal membrane and releasing the PEI/DNA complexes into the cytoplasm.

It has been also reported recently about the role of Ca^{2+} ions in promoting gene vector transportation into the nucleus. First, calcium ions, along with other ions, play an important role in endosomal escape by triggering an osmotic imbalance and preventing the vector's degradation in lysosome. Secondly, after release in the cytosol, Ca^{2+} ions stabilize the gene vector (this is important, especially when no PEI or other cationic polyelectrolyte is used) and protect it from degradation in the cytoplasm [150, 213]. This happens due to the high affinity of the negatively charged nucleic acid backbone, containing phosphate groups, towards positively charged calcium ions in CaP nanoparticles, resulting in gene vector condensation and packing [214–216]. Thirdly, calcium ions were shown to facilitate the nuclear internalization of the gene vector through nuclear pore complexes (NPCs) [159].

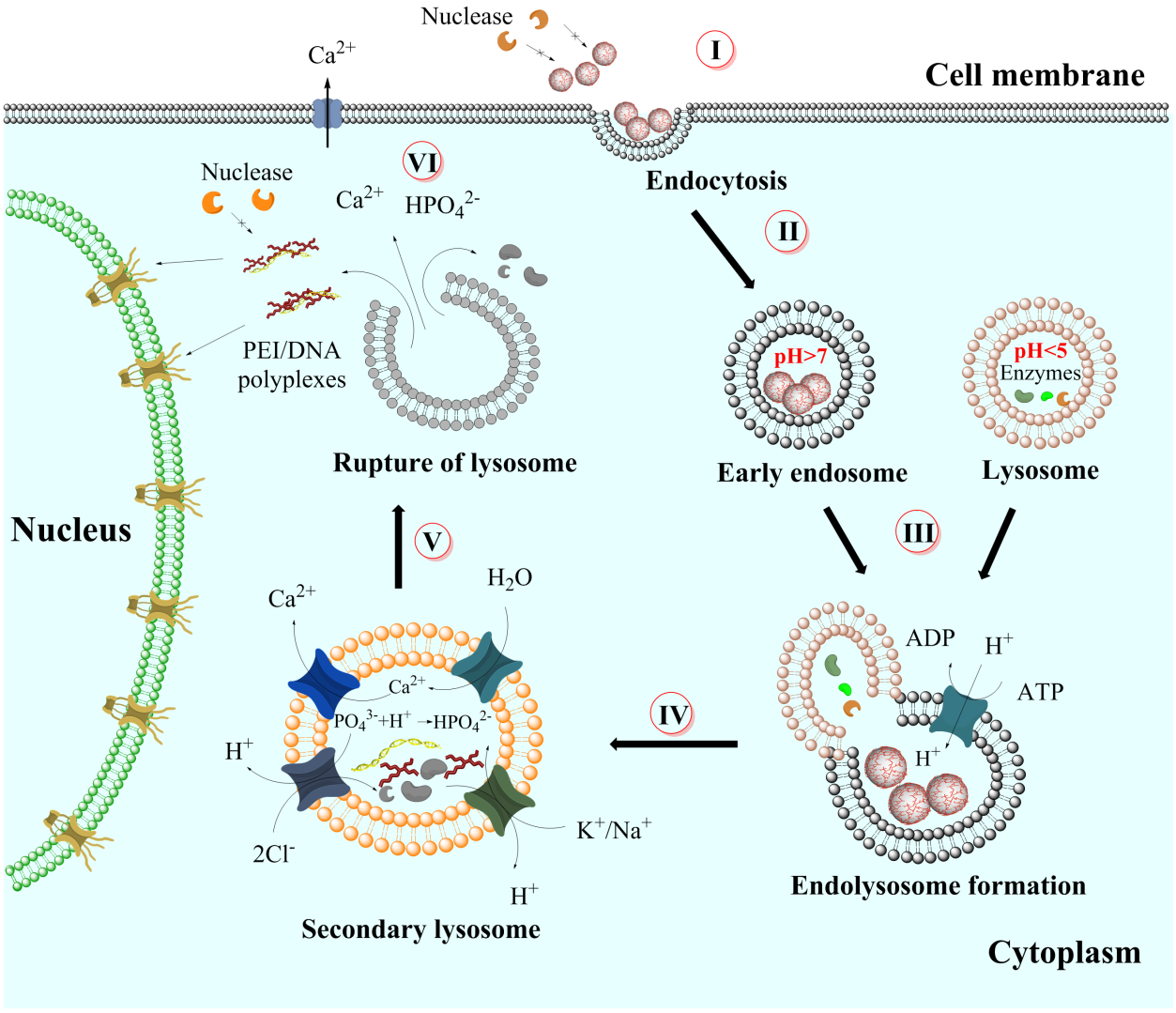

Figure 2.6 The internalization pathway of multi-shell calcium phosphate nanoparticles, functionalized with DNA for transfection. **I**: Nanoparticles interact with the cell membrane; nucleases cannot degrade DNA molecules as they are protected with the second shell of calcium phosphate. **II**: Nanoparticles are internalized by endocytosis. **III**: Fusion of the lysosome with enzymes and endosome containing nanoparticles; formation of the endolysosome. **IV**: Formation of secondary lysosome, activation of v-ATPase, lowering pH, phosphate groups are neutralizing free protons through formation of hydrogen phosphate ions; increase in osmotic pressure by pumping Cl^{-}, Na^{+}/K^{+} ions and water molecules inside the lysosome. **V**: Rupture of lysosome, the DNA-PEI complexes are released into the cytoplasm and moving toward nucleus where the DNA will be processed; lysosomal enzymes are inactivated due to neutral pH value in the cytosol. **VI**: Excessive Ca^{2+} ions are pumped out of the cell via ion channels.

2.3.4 Inhibition of endocytosis

To study which specific mechanism is responsible for the uptake of particular nanoparticles or other cargoes, the inhibitors in endocytosis are used. As of now, a certain number of pharmacological inhibitors are available on the market and proved to inhibit one or another endocytotic pathway. The summarized data with the description of the inhibitors that are now widely used in uptake studies are presented in Table 2.4.

As can be seen from the table, the approach "one inhibitor, one pathway" is often far away from reality. It especially concerns the depletion of cholesterol, as many mechanisms of endocytosis are cholesterol-dependent [159, 221–224]. Moreover, Nystatin was shown to be cytotoxic and methyl-β-cyclodextrin could destroy the plasma membrane and induce ion leakage [221]. Recently, it was also reported that the efficacy of such inhibitors as genestein and methyl-β-cyclodextrin on the uptake of transferrin and lactosylceramide was highly cell line-dependend [226].

The complexity of interaction of nanoparticles with plasma membrane and the endocytotic pathways is still far beyond our full understanding. There are many studies on specific cell lines or on particular endocytotic pathway, or only with a few nanoparticles having different parameters. Thus, a general picture still needs to be created. A close collaboration between the experts with different scientific backgrounds may help to resolve this puzzle in the future.

Table 2.4 Description of endocytotic pathways inhibitors [182]. CME: clathrin-mediated endocytosis, CIE: clathrin-independent endocytosis.

Inhibitor	Inhibited mechanism	Effect	Comments
Amiloride and its derivatives (EIPA and HOE-694)	Macropinocytosis	Blocks Rac1 and Cdc42 signaling pathways [217, 218] by lowering submembraneous pH	
Chlorpromazine	CME [219]	Inhibits Rho GTPase	Not efficient in some cell lines
Cytochalasin D, Latrunculin A	Mainly macropinocytosis	Inhibits actin polymerization and may lead to actin disassembly [220]	Not always efficient in adherent cells [220]
Jasplakinolide	Macropinocytosis	Stabilize actin filaments and promotes actin assembly [220]	
Dynasore	Caveolin/lipid raft-dependent, RhoA-dependent, phagocytosis	Inhibits function of dynamin protein	
Methyl-β-cyclodextrin	Macropinocytosis, CME [221, 222] and CIE [159, 223, 224]	Cholesterol depletion/extraction	The possible leakage of K^+ ions should be taken into consideration
Filipin	Caveolin-mediated, macropinocytosis [159,223,224], CME [221, 222]	Interacts with cholesterol	
Nystatin	Caveolin-mediated, macropinocytosis [159,223,224], CME [221, 222]	Interacts with cholesterol	Toxic
Lovastatin	Influence on all cholesterol-dependent mechanisms	Inhibits synthesis of cholesterol, thus lowering its content in membrane	Uncertain action
Genistein	Inhibits several tyrosine kinases	Inhibits caveolae formation [225]	Affects several processes at a time. Not specific
Wortmannin and LY94002	Macropinocytosis and RhoA-mediated endocytosis	Inhibit phosphatidylinositol 3-kinase	

2.4 Vaccination and immune response

2.4.1 Organization of the immune system

The immune system is a complex network consisting of organs, cells (Table 2.5), and molecules with specialized roles that defend the living organism from infections. It is also responsible for destroying malignant cells within the body.

The organs of immune system are divided into primary or central lymphoid organs (bone marrow and thymus) and peripheral lymphoid organs (spleen, lymph nodes, and mucosa-associated lymphoid tissues (MALT)). Anatomical and physiological barriers such as epithelia, mucosa, tears, respiratory tract, oral cavity, stomach, and small and large intestines also play an important role in the defense from pathogenic infection [227].

All cells of the immune system are derived from bone marrow stem cells as a result of a process called hematopoiesis. During this multi-stage process, stem cells undergo differentiation either into mature cells (B cells, natural killer cells, granulocytes) under the stimulation of specific cytokines, called colony-stimulating factors, or into precursors of cells (immature thymocytes) that leave bone marrow for thymus to continue their maturation. Red blood cells and platelets are also formed during the hematopoiesis.

In the thymus, the maturation and final selection of T cells take place. About 95-98% of all lymphocytes do not pass this selection and are sequestered in thymus [228]. Mature lymphocytes then migrate through the peripheral blood circulation into secondary lymphoid organs such as spleen, lymph nodes, Peyer's patches, and others.

Lymph nodes in the form of clusters are widely distributed throughout the body, mainly in places of major blood vessel pathways, and along with the lymphatic liquid form the lymphatic system in the body. Lymph is drained from blood stream through the lymph node and filtered for possible foreign bodies,

microorganisms, cancer cells, inflammatory cytokines, or antigens. Lymph nodes themselves represent highly structured organs, containing, among others, B cells, follicular dendritic cells, macrophages, plasma cells, and T cells (mainly T helper cells) [229].

The spleen is the largest single lymphoid organ in the human body. It comprises two tissue types: red pulp and white pulp. Red pulp contains large number of erythrocytes, resident macrophages, dendritic cells, granulocytes, plasma cells, and lymphocytes. This is the place where aged red blood cells and platelets are destroyed. The white pulp contains lymphoid tissue, consisting of mainly T lymphocytes, 75% of which are $CD4^+$ T cells (T helper cells). The spleen filters the blood and is the main organ where the antibodies are being synthesized and released into the blood stream. In addition, dendritic cells and macrophages catch the foreign antigens from the blood stream passing through the spleen. People who lack this organ (e.g. through splenectomy) are highly susceptible to bacterial infections such as *pneumococci* and *memingococci*.

Mucosa-associated lymphoid tissue (MALT) makes up more than 50% of lymphoid tissue in the body. It incorporates lymphoid tissue associated with gut, bronchus, and genitourinary tracts. The major function of these organs is to provide local immunity through the production of IgE and IgA. These structures contain a number of different immune cells: $CD4^+$ and $CD8^+$ T cells, B cells, plasma cells, dendritic cells, macrophages, eosinophils, and mast cells.

Table 2.5 Description of the cells of the immune system.

Origin	Morphology	Function	Cell Type	Description
Lymphoid	Mononuclear	Cytotoxicity	*NK cells*	Make up 15% of human blood lymphocytes (HBL); express no Ag-specific receptors; kill cells with low expression of MHC Class I (indicator for abnormality); are effective during early stages of viral infection; are activated by IFNα and IL-2; produce IFNγ [230]
			$CD8^+$ T cells	Express MHC Class II molecules; are cytotoxic T cells (T_C cells); produce perforins and granzymes to eliminate malignant or infected cells [230]
		Regulation	*$CD4^+$ T cells*	Along with $CD8^+$ T cells make up 70% of all HBL; express MHC Class I molecules; secret cytokines to promote cell-mediated immunity (T_{H1}) and Ab-mediated immunity (T_{H2}) [230]

			$\gamma\beta$-*T cells*	Represent 10-15% of human blood T cells; abundant in epithelia of gut, lung, and skin; secrete cytokines to promote Ab-mediated immunity [230]
		Ab production, Ag presentation	*B cells*	Make up 5-15% of human blood lymphocytes (HBL); require help from T_H cells for activation; produce Igs [230]
Myeloid		Ag presentation	*Dendritic cells*	Are bone marrow-derived and located throughout the body; are the most efficient APCs; induce primary activation of $CD4^+$ and $CD8^+$ T cells; provide "self-tolerance" against body's own cells [230]
		Ag presentation, phagocytosis	*Monocytes / macrophages*	Make up 5-10% of blood mononuclear leucocytes; differentiate into MΦ when migrate into tissues; contain granules with lysozyme, acid hydrolases, and mieloperoxidases; destroy particulate material, pathogens, and dead cells; are activated through IFNγ, prostaglandins, and leucotrienes [230]

	Polymorphonuclear leucocytes / Granulocytes		*Neutrophils*	Make up 60-70% of white blood cells (WBC); short-living (2-3 days); migrate into tissues and involved in acute response to bacterial infection; contain granules like in MΦ + antimicrobial proteins (defensins and serprocidins) [230]
		Extracellular digestion	*Eosinophils*	Represent 2-5% of WBC; secrete their granules (include among others, ROS) for extracellular digestion of big infectious pathogens (e.g. parasitic worms); produce cytokines, prostaglandins, and leucotrienes [230]
		Inflammation	*Basophils*	Make up <1% of WBC; are activated by anaphylatoxins (C3a and C5a peptides) or by Ag binding to IgE antibody on the cell surface; release inflammatory mediators (heparin, histamine, etc.) to attract lymphocytes, monocytes, and granulocytes to the site of inflammation [230]
			Mast cells	

2.4.2 Mechanisms of immune response

Immunity is provided by two parts of the immune system that closely cooperate with each other and can be distinguished by a number of specifications (see Table 2.6), two of these being the time of reaction and its specificity.

The cells of the innate immunity are represented by neutrophils, macrophages, eosinophils, basophils, and mast cells. Their short description and functions are given in Table 2.5. The innate immune response is developed mainly by recruiting neutrophils at the site of infection to eradicate pathogens [231]. During early stages of infection, the activated macrophages release cytokines (among them are various colony-stimulating factors) that drive the division of myeloid precursor cells in bone marrow, resulting in a dramatic increase of lymphocytes in the blood circulation (neutrophils leucocytosis). Transported to the site of infection, the recruited neutrophils eliminate the pathogen by phagocytosis, involving the production of reactive oxygen species (ROS) [228].

The complement system, consisting of about 20 serum glycoproteins, also plays an important role in the innate immunity. This system is activated by three major pathways: antigen-antibody reaction (classical way), polysaccharides from yeast and gram negative bacteria (alternative way), and presence of foreign substance. This activation happens in a cascade sequence with amplification stages, which means that activation of a single molecule leads to the generation of thousands of other molecules. All three pathways have a common point where they act in a similar manner, i.e. the activation of C3 component on the surface of the cell with further activation of C5-C9 components, resulting in a formation of transmembrane pores and death of the cell by osmotic lysis [228]. Normal cells of the body carry inhibitory proteins on the surface that stop this cascade process, thus avoiding lysis. Microorganisms or unhealthy cells, however, lack this inhibitory system and are highly susceptible to the complement system.

The main feature of the adaptive immunity is the use of antigen-specific receptors on the surface of T and B cells to promote a targeted response against

the pathogen. This process takes place in two stages. The first stage happens in the following manner. The antigen is taken up either in the lymphoid tissue or on the site of the infection by the dendritic cell (or another antigen-presenting cell), which then migrates to the nearest lymph node and presents the processed antigen in a complex with MHC molecules to the $CD4^+$ (MHC Class II) and $CD8^+$ (MHC Class I) T cells, leading to the priming, activation, and proliferation of the cells. This process is called activation of primary naive T cells. The functions of these cell types are described in Table 2.5. After the activation, some T cells remain in the lymph node as central memory cells and are responsible for accelerated activation of the immune response after the subsequent exposure to the same pathogen. This type of cells stays active in the body up to 10 years or more [228]. The second stage, the response itself, is mediated through activated T cells leaving the lymphoid tissue, and activated B cells (plasma cells) releasing the antibodies into the blood stream and tissue fluids. In particular, $CD4^+$ T cells (T helper cells) are responsible for orchestrating the cell-mediated part of immune response by activating other immune cells, e.g. B cells. $CD8^+$ T cells (cytotoxic cells) are involved in the elimination of virus-infected and malignant cells of the body.

B cells, while performing an antigen-presenting activity, are mostly responsible for producing antibodies. These proteins (immunoglobulins or Ig), among other things, neutralize toxins in the blood stream; opsonize bacteria, protozoa, and other pathogens; prevent adherence of microorganisms onto the mucosa surfaces; and activate the complement system [228]. There are five classes of antibody molecules known: IgA, IgD, IgE, IgG, and IgM. Igs of G Class are the main antibodies found in the blood and tissue, and are responsible for a majority of antibody-mediated clearance of pathogens [232]. IgM plays an important role in providing the humoral immune response in earlier stages of B cell-mediated immunity [232, 233]. Immunoglobulins of E Class trigger the release of histamine from mast cells and basophils during the development of allergic reaction, and are also involved in protection against parasitic worms [232]. IgD has been shown to

activate the production of antimicrobial factors in mast cells and basophils [234].

Table 2.6 Comparison of innate and adaptive immune responses.

Immune System	
Innate (nonspecific) immune response	**Adaptive (specific) immune response**
Responses occur to the same extent, regardless of the frequency of infection by the same pathogen.	Responses improve on repeated exposure to a given infection agent.
Function through phagocytic cells (neutrophils, monocytes, and macrophages), cells that induce inflammation (basophils, mast cells, and eosinophils), and natural killer cells (NK cells).	Involve APCs (dendritic cells, monocytes, and macrophages) to display the Ag to lymphocytes and collaborate with them to induce the response. Involve the proliferation of antigen-specific B and T cells, through binding their surface receptors to antigen.
Molecular components include peptides of complement system, acute-phase proteins, and cytokines such as interferons.	B cells secrete immunoglobulins, the Ag-specific Ab responsible for eliminating extracellular pathogen. T cells help B cells to produce Ab and can eliminate intracellular pathogens by activating MΦ and by killing infected cells.
Physical, chemical, and microbiological barriers [228], including skin, gut, stomach juice, etc.	Responses are generated in the lymph nodes, spleen, and mucosa-associated lymphoid tissue (MALT).
The innate immune response takes place within minutes but lacks specificity [228]. Is determined for life by the genetic information.	Adaptive response is precise but takes several days or weeks to develop. It has memory, provided by specific antibodies, and memory cells that remain life-long in the body after infection [228].
The cooperation between innate and acquired responses is essential for eliminating pathogens	

B cells function in mucosal areas, associated with gut, respiratory and urogenital tract, where they prevent the reproduction of the pathogen microflora through producing IgA [235]. Interestingly, the immune response generated at one site of mucosa-associated tissue will activate the response to the same pathogen at other sites. This fact can be used for achieving the therapeutic effect by vaccination at one mucosal site to induce generalized mucosal immunity [236].

2.4.3 Nanotechnology for vaccination

The immune system represents a major target for the development of treatment strategies for fighting against tumors, infectious and autoimmune diseases [228]. Among other things, these approaches include prophylactic and therapeutic vaccination with immunogenic adjuvants and pathogen proteins (or part of these proteins) to drive a pathogen-specific immune response [237].

A vaccination's main goal is to induce a specific immune response and an immunological memory in the recipient towards a pathogen, ideally with minimal or no side effects and long-lasting protection [154]. Modern vaccination technology dates back to the 18^{th} century when Edward Jenner discovered immunization with non-pathogenic smallpox virus from animals (cows) against highly fatal human smallpox virus. In the 20^{th} century, with the help of recombinant DNA technologies, vaccines against influenza, hepatitis A virus (HAV), hepatitis B virus (HBV), and the human papillomavirus (HPV) were developed and produced world-wide [154].

Today, there are various vaccine types, used in both prophylactic and therapeutic vaccinations. They can be categorized as follows: attenuated virus, inactivated (killed) virus, virus subunits, virus-like particles (VLPs), and DNA vaccines. Although these vaccines possess high immunogenicity, they are also sometimes associated with serious risks of virulence reversion, immunotoxicity, immunocompromising of patients, and complex and expensive production [238–241].

In this regard, application of nanometric materials (1-1000 nm) [242] offers

tremendous opportunities for the development of new immunization strategies, immunomodulatory agents, and vaccination tools. Over the decades, numerous nanoparticulate systems of different sizes and origins have been tested as potential tools for immunization against various infections [154, 242]. For example, one can name dendrimers (<5 nm) [243, 244], polymers (10-20 nm) [245, 246], virus-like particles (15-30 nm) [247, 248], DNA-polyplexes (50-100 nm) [249–251], liposomes (>150 nm) [246, 252], nanoparticles (150-250 nm) [30, 154, 253], and nanoemulsions (400 nm) [254, 255], all of which have been tested as novel immunostimulatory vaccines.

These nanomedical approaches posses some potential advantages over conventional antiviral therapies. They include high stability, well-defined composition, and the possibility of large-scale production [154, 256]. Moreover, it is possible to tailor the nanoparticulate system by incorporating, encapsulating, or conjugating various immunomodulating molecules, targeting antibodies, drugs, or vaccines to address specific cell populations and tuning drug or vaccine release [257–259]. This multiplicity of molecules can be incorporated into one set on the produced nanoparticles, thus providing multifunctional tool to achieve better immunization results. Biodegradable multi-shell functionalized calcium phosphate nanoparticles developed by Sokolova *et al.* [123] and further studied and described in this work can serve as a prominent example of such systems. These nanoparticles can encapsulate antigens and adjuvants in their core that APCs can process and then present to $CD4^+$ and $CD8^+$ T cells (Figure 2.7). The application of such functionalized nanoparticles showed a significant improvement in antigen delivery efficiency and enhancement of the immune response compared to soluble immunoactive ligands and proteins [152].

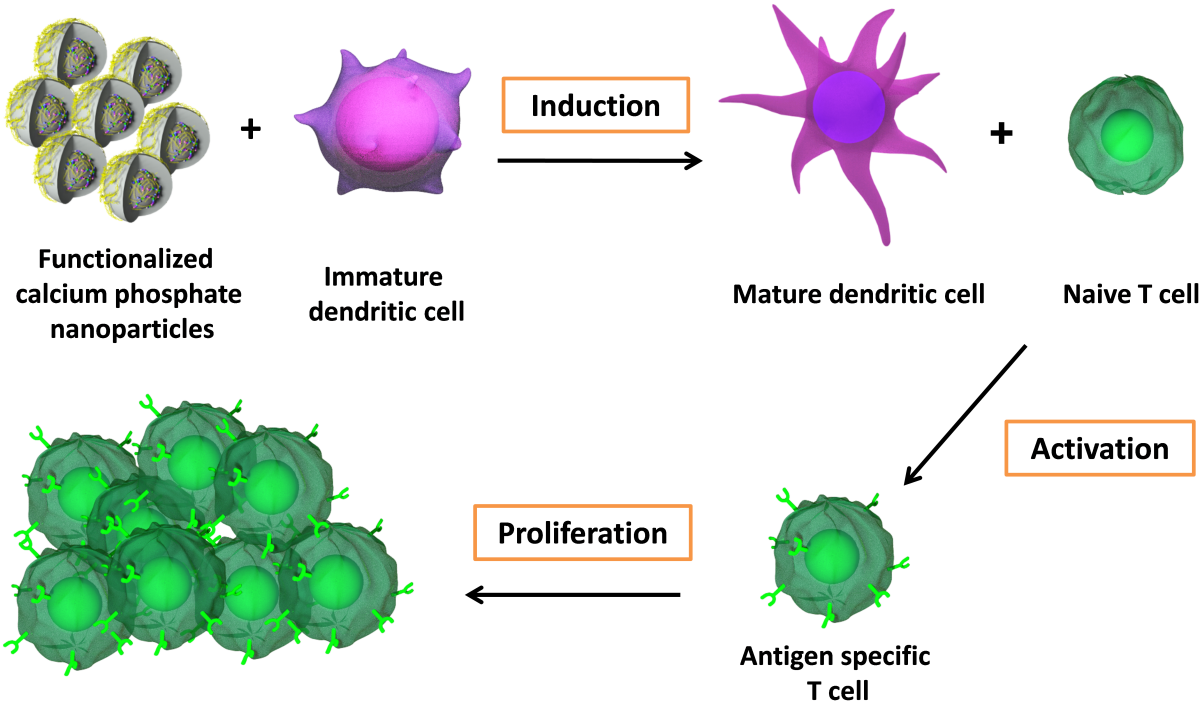

Figure 2.7 The scheme of induction of antigen-specific immune response via immunization with functionalized calcium phosphate nanoparticles.

Additionally, we have demonstrated that the treatment of chronic viral infection on the Friend virus model with such calcium phosphate nanoparticles, loaded with virus-derived proteins and CpG adjuvant could significantly improve the antiviral immune response and effectively suppress the viral replication. As currently available treatments of chronic viral infections like HCV, HBV, or HIV are still far from satisfactory level, new therapeutic strategies are highly desirable. Thus, biodegradable, non-toxic, and effective nanoparticles, based on calcium phosphate, can serve as an excellent example of a novel vaccination tool.

3 Materials and Methods

3.1 Synthesis of calcium phosphate nanoparticles

3.1.1 Preparation of single- and multi-shell calcium phosphate nanoparticles

All calcium phosphate nanoparticles used for the experiments were prepared using a method of continuous rapid precipitation in water at room temperature (RT), developed by Sokolova *et al.* [123, 151] in the following manner (Figure 3.1). An aqueous solution of diammonium hydrogen phosphate (3.74 mM, pH=9, Merck, p.a.) and an aqueous solution of calcium nitrate (6.25 mM, pH=9, Merck, p.a.) were mixed rapidly by pumping into a glass vessel with a constant maximum speed and constant stirring with a magnetic bar. The pH value of the diammonium hydrogen phosphate and the calcium nitrate solutions were adjusted beforehand with 0.1 M NaOH (Merck, p.a.). The required amount of the calcium phosphate nanoparticle dispersion was transferred by a pipette into an Eppendorf tube, followed by functionalization with polyelectrolyte molecules to prevent aggregation and to stabilize the nanoparticles in solution. Due to the selected concentrations and the equal amount of pumped Ca^{2+} and PO_4^{3-}-ions containing solutions in the reaction vessel, the core of calcium phosphate nanoparticles was presumably formed in stoichiometric Ca/P-proportion, referred as hydroxyapatite ($Ca_{10}(PO_4)_6(OH)_2$). By the functionalization with polyelectrolyte, which can be at the same time the molecule of interest if it possesses a strongly negative or

positive charge, the first shell is constructed.

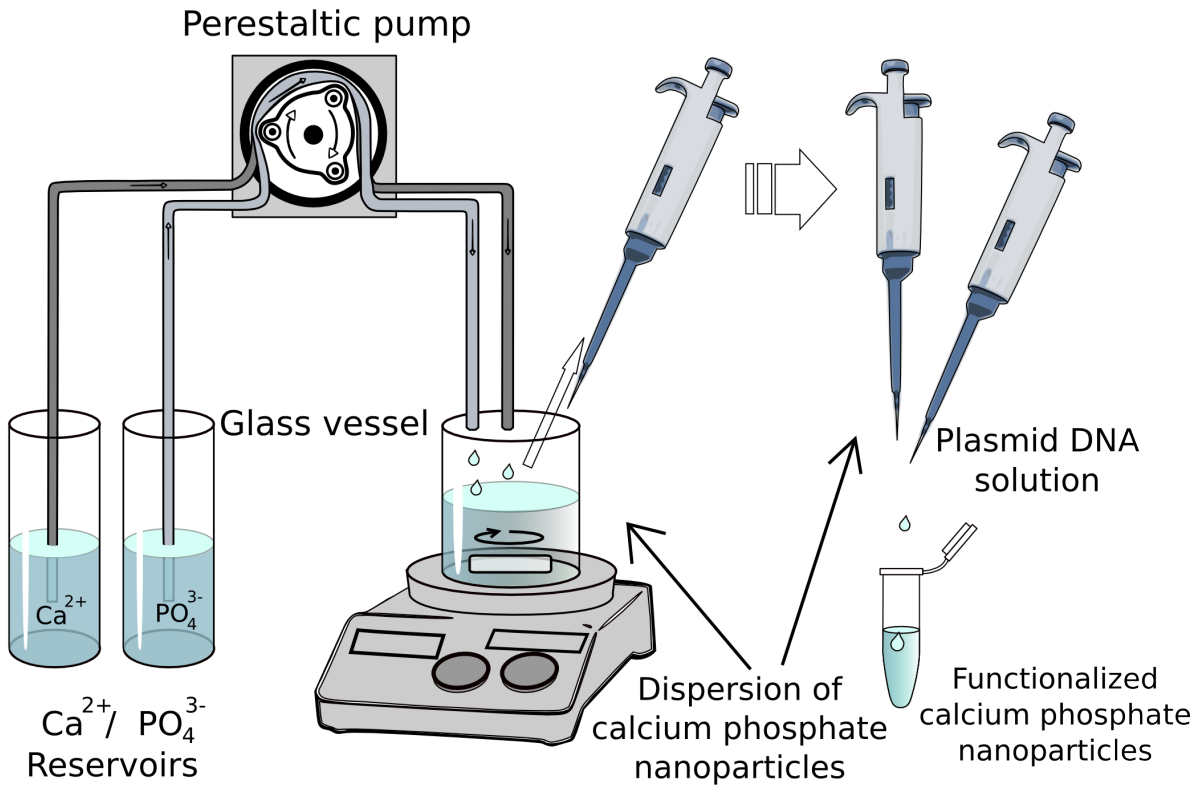

Figure 3.1 Schematic representation of synthesis of functionalized single-shell calcium phosphate nanoparticles.

Triple-shell nanoparticles were prepared by adding the same amount of diammonium hydrogen phosphate and the calcium nitrate solutions directly into the Eppendorf tube, in such a way that the total volume of added solutions was equal to the volume of dispersion of calcium phosphate nanoparticles taken directly after the preparation from the reaction vessel. Thus, a layer of calcium phosphate was formed. This layer protects the inner molecules from degradation. Finally, the nanoparticles were functionalized with the polyelectrolyte solution for a steric stabilization, forming a third shell. After each step of addition, the nanoparticle colloid was mixed thoroughly by a Vortex shaker (Vortex-Genie 2, Scientific Industries Inc., USA).

3.1.2 Preparation of single-shell calcium phosphate nanoparticles for the transport of various molecules

PEI-carrying nanoparticles were prepared in the following way: aqueous solutions of calcium lactate (18 mM) and diammonium hydrogen phosphate (10.8 mM) were rapidly pumped into a glass vessel. Within one minute 200 µL of the calcium phosphate nanoparticle dispersion were taken with a syringe and rapidly mixed with 720 µL of rhodamine-labeled PEI (1.08 g L^{-1}; pH 10, adjusted with ammonia solution). This dispersion was stored for two days at room temperature and afterwards purified by centrifugation and redispersion by ultrasonication (UP50H, Hielscher, Ultrasound Technology; sonotrode 3, cycle 0.8, amplitude 50%, 45 s) in 360 µL water.

Because *p*THPP porphyrin molecules are not water-soluble and hence unable to stabilize the calcium phosphate nanoparticles, they were firstly functionalized either with polycationalic PEI or polyanionic polymer PSS (polystyrene sulfonate). The PEI-stabilized porphyrin-carrying nanoparticles were prepared in the following manner: aqueous solutions of calcium lactate (18 mM), diammonium hydrogen phosphate (10.8 mM), and PEI (2 g L^{-1}) were simultaneously pumped into a stirred glass vessel in a volume ratio of 5:5:7 mL containing 20 mL of ultrapure water for 1 min at room temperature. After 1 min of stirring, 1 mL of *p*THPP (1 g L^{-1} in ethanol) was added to the dispersion. This obtained nanoparticle dispersion was stored at room temperature for 2 days. Then 25 mL of this dispersion was centrifuged and redispersed by ultrasonication (UP50H, Hielscher, Ultrasound Technology; sonotrode 7, cycle 0.8, amplitude 50%, 90 s) in 20 mL water.

PSS-stabilized anionic porphyrin-carrying calcium phosphate nanoparticles were synthesized by simultaneously pumping aqueous solutions of calcium lactate (18 mM, pH 10), diammonium hydrogen phosphate (10.8 mM, pH 10), and PSS (2 g L^{-1}, pH 10) in a volume ratio of 5:5:10 mL into a stirred glass vessel containing 20 mL of ultrapure water for 1 min at room temperature. After stirring for 1 min, 1 mL

of *p*THPP (1 g L^{-1} in ethanol) was added to the nanoparticle dispersion. For 4 days this dispersion was stored at room temperature. After that 25 mL of this dispersion was centrifuged and redispersed by ultrasonication (UP50H, Hielscher, Ultrasound Technology; sonotrode 7, cycle 0.8, amplitude 30%, 90 s) in 20 mL of pure water.

Peptide-carrying nanoparticles were synthesized in the following manner: PEI-stabilized CaP nanoparticles were prepared as described before for the *p*THPP-carrying nanoparticles synthesis. After ultrasonic redispersion in pure water 100 µL of a fluorescing peptide solution (FITC-Pep, 1 g L^{-1}) was added to 1 mL of this dispersion and left for 30 min. The dispersion was centrifuged and redispersed by ultrasonication (UP50H, Hielscher, Ultrasound Technology; sonotrode 3, cycle 0.8, amplitude 50%, 45 s) in 1 mL of pure water.

The nanoparticles carrying rhodamine-labeled PEI, *p*THPP, and synthetic peptide were synthesized by Dr Jan Klesing.

3.1.3 Purification of functionalized calcium phosphate nanoparticles

Freshly synthesized dispersions of nanoparticles were purified by centrifugation (Heraeus Fresco 21 centrifuge, Thermo Scientific) at 21,000 g for 30 min, and subsequent redispersion of the nanoparticles' pellet in pure water by ultrasound finger (USF) (UP50H, Hielscher, Ultrasound technology; Sonotrode 2) with the following settings: amplitude 60%; cycle 0.8; time 10 s (for all nucleic acid-carrying nanoparticles) or 30 s (for nanoparticles carrying not ultrasound-sensitive molecules).

3.1.4 Calculation of the number of fluorescently-labeled molecules and calcium phosphate nanoparticles in the dispersion

After the synthesis, CaP nanoparticles, functionalized with various fluorescent molecules, were sedimented by centrifugation. The supernatant was collected to quantify the number of non-adsorbed fluorescent molecules by quantitative UV-Vis spectroscopy using the calibration curve of the particular fluorescent molecule.

The precipitate containing nanoparticles was redispersed in the original volume of ultrapure water and analyzed using atomic absorption spectroscopy (AAS). The obtained concentration of calcium in the sample was converted into the mass of calcium phosphate in the whole sample with regard to the hydroxyapatite phase of the obtained nanoparticles ($Ca_{10}(PO_4)_6(OH)_2$):

$$m(\mathrm{CaP}) = \frac{c(\mathrm{Ca}) \cdot M(\mathrm{Ca_{10}(PO_4)_6(OH)_2})}{10 M(\mathrm{Ca})}$$

The nanoparticle concentration was calculated by taking the mass of calcium phosphate in the dispersion and assuming spherical nanoparticles with a diameter obtained by SEM. Thus, the number of nanoparticles per m^3 can be calculated in the following manner:

$$N(\mathrm{NP}) = \frac{m(\mathrm{CaP})}{m(\mathrm{NP})} = \frac{3m(\mathrm{CaP})}{4\pi r(\mathrm{NP})^3 \rho(\mathrm{CaP})}$$

where $N(\mathrm{NP})$: the number of nanoparticles per m^3; $m(\mathrm{CaP})$: the mass of synthesized calcium phosphate nanoparticles per m^3; $r(\mathrm{NP})$: the average radius of one nanoparticle; $\rho(\mathrm{CaP})$: the density of hydroxyapatite phase of calcium phosphate (3140 kg m^{-3}).

The concentration of adsorbed molecules was calculated by the subtraction of the value, measured in the supernatant, from the theoretical concentration of

the molecule in the nanoparticle dispersion. The number of fluorescent molecules can thus be, determined in the following manner:

$$N(\text{molecule}) = c(\text{molecule}) \cdot N_A$$

where N(molecule): the number of fluorescent molecules per m^3; c(molecule): the concentration of the fluorescent molecules in the nanoparticle dispersion; N_A: Avogadro constant ($6.022 \cdot 10^{23}$ mol^{-1}).

The number of molecules per nanoparticle was obtained by dividing of the total number of molecules by the total number of nanoparticles per m^3. The number of functionalized nanoparticles per cell in the cell culture experiments was calculated accordingly.

3.2 Physicochemical methods

3.2.1 Dynamic light scattering (DLS)

Dynamic light scattering is a physical method that allows to determine the hydrodynamic radius of particles in colloids. This technique is based on the principle that the particles move randomly in the liquid phase, i.e. undergo Brownian motion, and on the assumption that the measured particles have a spherical shape. Thus, the movement of these particles can be described by the Stokes-Einstein equation:

$$D = \frac{k_B T}{6\pi\eta R_h}$$

where D: the diffusion coefficient, k_B: the Boltzmann's constant, T: the temperature in Kelvin degrees, η: the solvent viscosity, R_h: the hydrodynamic radius of the particle.

The larger the particles, the slower their velocity. Hence, they will have smaller

coefficient of diffusion compared to smaller particles. In most DLS systems, a laser of known wavelength shines onto a cuvette with a sample solution, and the intensity of the scattered light (with a changed wavelength due to a Doppler shift when the light hits the moving particle) is collected by a detector, and the particle size distribution of the sample is determined by software algorithms. The amount of collected scattered light depends on such particle properties as molecular weight, size, and shape, as well as the refractive index of the solvent and the particle itself. Before reaching the detector, the scattered light from individual particles interfere with each other, thus leading to a fluctuation in the scattering intensity. With the help of an autocorrelation function, the diffusion velocity is calculated with regard to the correlation between time and scattering intensity.

The zeta potential can be described as an electrical potential of a particle, that exists in some small distance from its surface. Through measurement of this characteristic, the prediction of the long-term stability of the nanoparticle dispersion is possible. The zeta potential is derived from measuring the electrophoretic mobility of charged particles in dispersion when they are subjected to an electric field. By applying the Smoluchowski approximation to the measured mobilities of the particles, the zeta potential can be determined.

$$\zeta = \frac{3\eta\mu}{2\epsilon f(k_H r)}$$

where ζ: zeta potential, η: viscosity, μ: electrophoretic mobility, ϵ: dielectric constant, r: radius of the particle, k_H: Debye-Hückel parameter, $f(k_H r)$: Henry function.

The Henry function depends on the radius of the spherical particle (r), the Debye-Hückel parameter (k_H), and according to the Hückel-Smoluchowski approximation, has either the value 1.0 or 1.5.

The measurements for the computation of the zeta potential as well as the determination of the hydrodynamic diameter were accomplished with a Malvern

Zetasizer NanoZS instrument (λ=532 nm).

3.2.2 Nanoparticles tracking analysis (NTA)

Nanoparticle Tracking Analysis (NTA) uses two properties, i.e. light scattering and Brownian motion, in order to determine the particle size distribution of samples in suspension. A laser beam is passed through the sample chamber, and the particles in suspension that are located in the path of this beam scatter the light so that they can be easily visualized through a microscope with 20x magnification. A video camera, mounted on the microscope, generates a video file of the particles that move due to the Brownian motion in the suspension. The software keeps track of many particles simultaneously and, using the Stokes-Einstein equation, calculates their hydrodynamic diameter.

The measurements of the nanoparticles' hydrodynamic diameter were performed with a Nanosight LM10 HS (Malvern Instruments Ltd).

3.2.3 Scanning electron microscopy (SEM)

The scanning electron microscope (SEM) is a type of electron microscope that uses a focused beam of high-energy electrons to generate high-resolution images of a solid sample surface. With the help of the signals derived from electron-sample interactions, information about the sample, including external morphology (texture) of the sample, its chemical composition, as well as crystalline structure and orientation of materials can be revealed.

The principle of the SEM imaging is as follows. Accelerated electrons carrying significant amounts of kinetic energy are focused by magnetic field lenses into a narrow beam that scans the surface area of a sample. The image resolution is determined by the diameter of this electron beam. When the electrons reach the surface of the solid sample, their kinetic energy is transformed into a variety of signals. These signals include secondary electrons, back-scattered electrons

(BSE), diffracted back-scattered electrons (EBSD that are used to determine crystal structures and orientations of minerals), photons (characteristic X-rays that are used for elemental analysis), visible light (cathodoluminescence), and heat. Secondary electrons are responsible for the formation of the actual contrast of the 3D image, showing the morphology and topography of the scattered sample [260].

SEM imaging was performed with ESEM Quanta 400 instrument (FEI) after gold-palladium sputtering of the samples.

3.2.4 Ultraviolet-visible (UV-Vis) spectroscopy

UV-Vis spectroscopy is a physical method for the quantitative determination of a species concentration in solution through the absorbance of this substance in visible and near-UV as well as near-infrared ranges, i.e. in the wavelength range of 200-800 nm. The correlation between concentration of the species of interest and the intensity of light before and after passing the cuvette with the solution (absorption) is described by the Lambert-Beer law:

$$A = \log_{10}\left(\frac{I_0}{I}\right) = \epsilon c L,$$

where A: measured absorbance in Absorbance Units (AU), I_0: the intensity of the irradiated light at a given wavelength, I: transmitted intensity, L: path length through the sample, c: concentration of the absorbing species. ϵ: constant extinction coefficient (depends on the species and wavelength).

UV-Vis spectroscopic studies were performed on a Varian Cary Bio 300 spectrometer. The samples were measured in a quartz micro cuvette. To exclude the influence of the dispersant or solvent on the absorbance of the samples, reference measurements of pure dispersant or solvent were carried out. For a qualitative conversion of the absorbance of the measured samples into the mg mL^{-1} units, the calibration curve, obtained under the same measurement conditions with the

known concentration of the molecule of interest, was used.

3.2.5 Atomic absorption spectroscopy (AAS)

Atomic absorption spectroscopy (AAS) is an analytical method used to identify the presence and concentration of chemical elements by analyzing the absorption of light by free atoms when they are vaporized and absorb certain frequencies of light. The atoms are brought to the excitation state by absorbing ultraviolet or visible light in a defined quantity for a short period of time (nanoseconds). This amount of energy and wavelength corresponds specifically to a particular element. Besides, the characteristic absorption lines are very narrow, which gives AAS its elemental selectivity. The amount of the analyte is directly correlated with the absorption value. Therefore, the concentration can be determined from a working curve after calibrating the instrument with standards of known concentration.

The measurement of samples was performed with an M series atom absorption spectrometer (Thermo electron corporation, Schwerte).

3.2.6 Lyophilization (freeze-drying)

Often biological materials must be dehydrated to keep them stable for a long term. Drying always causes some loss of activity or other damage of biomolecules. Lyophilization is a method of dehydratation that significantly reduces such damage [261].

Lyophilization is the process where water (or another solvent) is removed from a frozen material by sublimation at low temperature and reduced pressure (vacuum). It occurs when a liquid sample is frozen and the pressure in lyophilization chamber is lowered below the triple point of the substance, so the frozen water from the sample undergoes sublimation. This means a direct transition of water molecules from the solid state to the gaseous state.

Immediately after the synthesis, the dispersions of nanoparticles were frozen in

liquid nitrogen (-196 °C) in the presence of trehalose (20 mg mL^{-1}, Fluka), to build a sugar matrix for the nanoparticles. The lyophilization was carried out in Alpha 2-4 LSC (Martin Christ, Osterode, Germany) at -7 °C, 31 Pa, 48-72 h, and stored at -20 °C until they were redispersed in pure water directly before the application.

3.3 Applied molecules

3.3.1 Antigenic viral peptides

The influenza protein hemagglutinin (HA) is a major viral surface antigen. This strain-specific glycoprotein consists of two polypeptide chains (H1 and H2). In the form of a trimer, HA is responsible for the attachment of the virus to the host cell [262].

It is well known that $CD4^+$ T helper (T_H) lymphocytes recognize peptides along with Class II MHC-encoded molecules, whereas $CD8^+$ T cytotoxic cells react to the peptides in association with Class I MHC-encoded molecules expressed on the surface of antigen-presenting cells (APCs). These peptides with a length of 10-15 residues are generated during the processing of the native protein by APCs [263]. Studies with a T cell clone from BALB/c and CBA mice immunized with the whole influenza virus with a single substitution on the amino acid sequence in HA have revealed the importance of certain residues in the sequence, wherein the changes dramatically affect reactivity. Thus, these conservative residues were shown to play a major role in antigen-presenting process [263].

For our studies on the influenza virus, the following residues of immunogenic peptides of the influenza virus A/PR/8/34 were used: $HA_{512-520}$ (MHC Class I-restricted, sequence YQILAIYSTVASSLVLL, 1 mg mL^{-1}, Intavis AG, Cologne, Germany) and $HA_{110-120}$ (for MHC Class II-restricted, sequence SVSSFERFER-FEIFPKESS, 1 mg mL^{-1}, Intavis AG, Cologne, Germany).

For our studies on the Friend virus, the following residues of immunogenic peptides of the Friend virus were used: $GagL_{85-93}$ (MHC Class I-restricted, sequence CCLCLTVFL, 1 mg mL^{-1}, JPT Peptide Technologies GmbH, Berlin Germany) and the surface protein $gp70_{123-141}$ (MHC Class II-restricted, sequence EPLTSLTPRCNTAWNRLKL, 1 mg mL^{-1}, JPT Peptide Technologies GmbH, Berlin Germany).

3.3.2 Bioactive peptides (LxVPc1)

LxVPc1 peptide is a synthetic molecule that can block the phosphorylation activity of calcineurin towards the NFAT signal molecule, thus inhibiting the activation of the proinflammatory pathway in macrophages. This is an interesting approach to fight inflammation-related transplantation failures.

The LxVPc1 peptide was synthesized along with its mutant type LxVPc1mut by the company Pepscan® in the following sequences:
LxVPc1 (FITC-Ahx-DQYLAVPQHPYQWAK-OH, M_w=1844.04 g mol^{-1}, 1 mg mL^{-1});
LxVPc1mut (FITC-Ahx-DQYAAAAQHPYQWAK-OH, M_w=1747.87 g mol^{-1}, 1 mg mL^{-1}).

3.3.3 Bovine serum albumin (BSA)

BSA is a ubiquitous globular protein derived from bovine serum. It is often used as a standard protein in many biological applications and methods. It consists of 583 amino acidic residues and has a molecular weight of 66.5 kDa.

For our experiments we used BSA, labeled with fluorescein isothiocyanate (FITC) or tetramethylrhodamine isothiocyanate (TRITC) (Sigma-Aldrich, Germany, 1 mg mL^{-1}).

3.3.4 Calixarene dimer

This new calixarene dimer with 4-6 positive charges (see Figure 3.2) is able to specifically bind to the major groove of the DNA duplex due to its chemical and topological characteristics. It is currently examined with respect to its potential to prevent cell proliferation and to induce apoptosis in cancer cells [264].

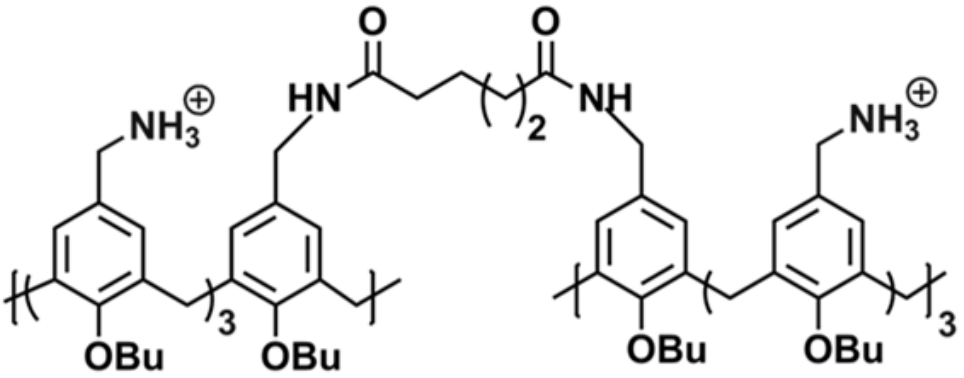

Figure 3.2 The chemical structure of calixarene dimer.

The calixarene dimer compound was synthesized in the group of Prof. Thomas Schrader (Institute for Organic Chemistry, University of Duisburg-Essen, Germany, M_w=1859.03 g mol^{-1}, 1 mg mL^{-1}).

3.3.5 Carboxymethyl cellulose (CMC)

Carboxymethyl cellulose (CMC) is a water-soluble polyanionic polymeric derivative of cellulose with carboxymethyl groups (-CH_2-COOH) bound to some of the hydroxyl groups of the glucopyranose monomers in the cellulose backbone. Due to its nontoxic and hypoallergenic properties, CMC is widely used in the food industry under the label E466 as a viscosity modifier or thickener and stabilizer. It is also a constituent of many non-food products such as toothpaste, diet pills, water-based paints, detergents, and various paper products.

For our experiments, we used a solution of sodium carboxymethyl cellulose

(M_w=262 g mol^{-1}, Sigma-Aldrich, 2 mg mL^{-1}).

3.3.6 CpG: Toll-like receptor 9 (TLR9) ligand

CpG oligodeoxynucleotides (CpG ODN) are short (6-30 nucleotides [265]), single-stranded DNA molecules containing a CpG dinucleotide motif (Cytosine-phosphodiester bond-Guanine), which in unmethylated state can act as an immunostimulant [266]. Owing to their high abundance in microbial genomes and rareness in genomes of vertebrates, CpG motifs are considered to be pathogen-associated molecular patterns (PAMPs) [267]. The unmethylated CpG PAMP is recognized by the intracellular pattern recognition receptor (PRR) Toll-like receptor 9 (TLR9), which is constitutively expressed in cells of the innate and adaptive immune system, including plasmacytoid dendritic cells, monocytes, natural killer (NK) cells, and B cells in humans and higher primates [268, 269]. This mechanism is used to detect viral, fungal, and bacterial infection through recognition of pathogen DNA motifs.

The reported effect of immunostimulation with CpG ODN include cytokine secretion and upregulation of costimulatory molecules of macrophages and dendritic cells (DC) [270–272]; activation, polyclonal proliferation, and immunoglobulin secretion of B cells [273]; direct and indirect costimulatory effects for T cells [274]; as well as enhancing effects on haemopoiesis [275]. These mentioned effects make CpG a powerful adjuvant in activation of adaptive immune response [276, 277]. Moreover, it has been shown that CpG strongly supports the induction of cytotoxic T cell responses that are crucial for eliminating the infected cells, carrying intracellular pathogens [278]. Furthermore, CpG has the capacity to induce T helper type 1 (T_{H1})-dominated immune responses [277, 279] and can redirect ongoing T_{H1} responses [279]. Thus, CpG ODN have been recognized as a new and effective class of adjuvants that can be used for vaccination against allergies, infectious diseases, and tumors [276, 280].

For our studies, we used B-type CpG 1826 with the following sequence

5'-TCCATGACGTTCCTGACGTT-3' (Eurofins MWG Operon, Ebersberg, Germany, 0.4 mg mL^{-1}).

3.3.7 High temperature requirement A1 (HTRA1) protein

The high temperature requirement A (HtrA) family of serine proteases belongs to a highly conserved set of proteases found in single and multicellular organisms. HtrAs differ from other serine proteases in sequence homology in the presence of a catalytic domain and one or two C-terminal PDZ domains that mediate specific protein-protein interactions. The key functions of HtrA family members are related to protein quality control.

HTRA1 is one of the most studied members of HtrA family in human, which is known to be involved in various biological processes from tumor suppression and control of proliferation to cell migration and neurodegeneration [281]. It was shown that overexpression of HTRA1 inhibited tumor growth *in vitro* and *in vivo* [282]. This data suggests that HTRA1 might function as a tumor suppressor. In the extracellular matrix, HTRA1 cleaves numerous secreted proteins such as fibronectin, fibromodulin, aggrecan, Type II collagen, biglycan, clusterin, and others. It is suggested that HTRA1 has cellular (20% of protein) as well as extracellular (80% of protein) localization [283]. The regulation of the cellular distribution of HTRA1 is, however, unknown.

For our experiments, we used HTRA1 that was produced according to the literature [282], labeled with Alexa488 (Invitrogen, USA) according to the manufacturer's manual, and purified by gel electrophoresis in the group of Prof. Michael Ehrmann (Centre for Medical Biotechnology (ZMB), University of Duisburg-Essen). The final concentration of Alexa488-labeled HTRA1 and HTRA1ΔPDZ (HTRA1 without PDZ domains) was 1 mg mL^{-1}; M_w(HTRA1)=37 kDa, M_w(HTRA1ΔPDZ)=25 kDa.

3.3.8 High temperature requirement A2 (HTRA2) protein

HTRA2 is a human serine protease located in the intermembrane compartment [284] of mitochondria. It is known to be involved in mitochondrial quality control, namely through interactions with antiapoptotic protein HAX-1 [285]. The degradation of this protein by HTRA2 induces autophagy, resulting in the clearance of damaged mitochondria. The functional unit of HTRA2 structurally appears as a trimer molecule with central protease domains and a PDZ domain, located on the C-terminus, which is characteristic for the HtrA family. The PDZ domain preferentially binds to the C-terminus of the target-protein and modulates the proteolytic activity of the trypsin-like protease domain [286]. A normal protease activity of HTRA2 is required for mitochondrial homeostasis in mice and humans. It was shown that mice with the inactivated (muted) form of HTRA2 display phenotypes similar to Parkinson's disease [287], which is associated with amyloid precursor protein metabolism [288]. Neurodegenerative disorders are strongly associated with the aggregation of proteins or protein fragments as well as the accumulation of unfolded proteins in mitochondria. This implies that HTRA2 protease plays a significant role in maintaining cellular homeostasis by means of protein quality control.

For our experiments, we used HTRA2 that was produced according to the literature [282], labeled with Alexa488 (Invitrogen, USA) according to the manufacturer's manual, and purified by gel electrophoresis in the group of Prof. Michael Ehrmann (Centre for Medical Biotechnology (ZMB), University of Duisburg-Essen). The final concentration of Alexa488-labeled HTRA2 was 1 mg mL^{-1} (M_w=49 kDa).

3.3.9 Lysozyme-inhibiting polymer

A polyfunctional anionic copolymer was developed for the selective inhibition of lysozyme as a supramolecular enzyme inhibition model. The activity of this polymer is provided by cooperative interaction of selected binding co-monomers

with critical amino acid residues on the protein surface, specifically exploiting electrostatic interactions, hydrophobic forces, and substrate mimicry [289–292]. Its functional parts are as follows: bisphosphonates as molecular tweezers for arginine and lysine residues; unipolar dodecyl tails for aliphatic and aromatic amino acids; glucosamine moieties, which imitate the lysozyme's natural substrate (bacterial cell walls); dansyl molecule as fluorescent label (see Figure 3.3).

The polymer was synthesized in the group of Prof. Thomas Schrader (Institute for Organic Chemistry, University of Duisburg-Essen, Germany, 1 mg mL^{-1}, M_w=181.5 kg mol^{-1}).

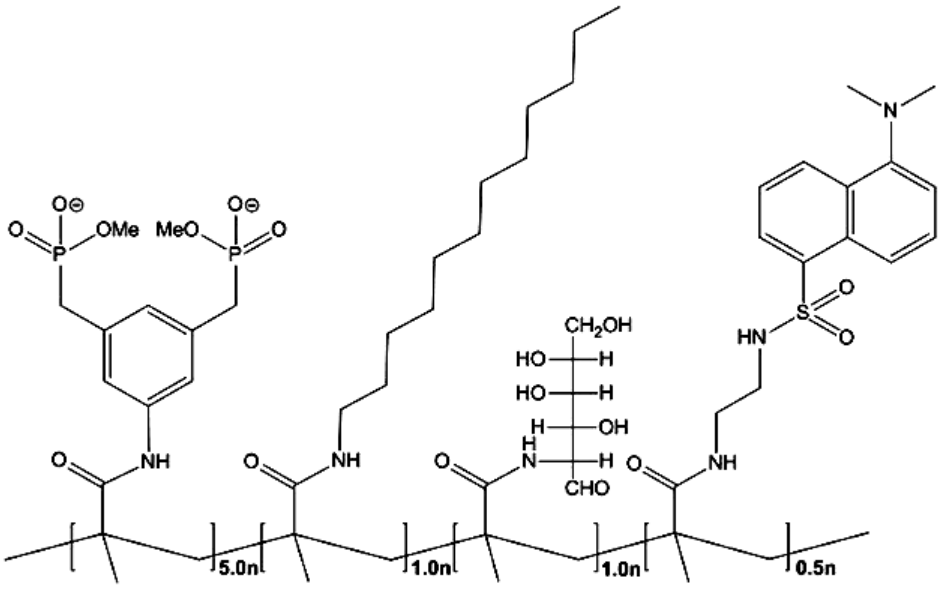

Figure 3.3 The chemical structure of the lysozyme-inhibiting polymer.

3.3.10 Molecular tweezers

The pathological misfolding and self-assembly of key proteins inside and outside the nerve cells are the hallmarks of severe neurological disorders, the so-called amyloidosis. Prominent examples of such disorders are Alzheimer's disease, Parkinson's disease, Creutzfeldt-Jakob and related prion diseases, senile systemic amyloidosis, dialysis-related amyloidosis, and Type-II diabetes. Any prevention strategy that has the potential to treat amyloidosis by inhibition or modulation

of these processes is thus of great significance.

Of late, molecular tweezers have been discovered and demonstrated to inhibit specific protein-protein interactions that lead to the formation of amyloidogenic aggregates inside cells. These amphiphilic compounds carrying 2-4 negative charges (Figure 3.4) hold great promise for the development of disease-modifying therapies if they can be transported across cell membranes and inhibit aberrant protein misfolding [293].

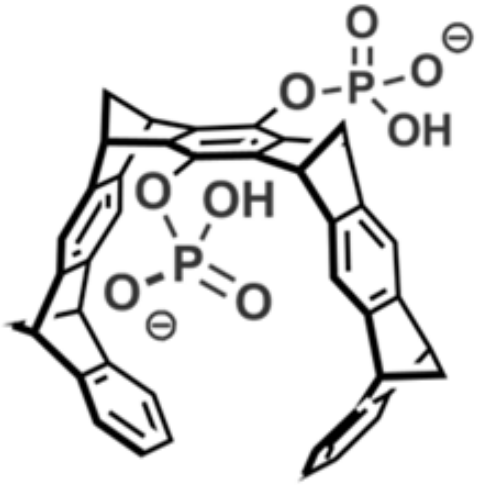

Figure 3.4 The chemical structure of molecular tweezers.

The molecular tweezers were synthesized in the group of Prof. Thomas Schrader (Institute for Organic Chemistry, University of Duisburg-Essen, Germany, M_w=814.57 g mol^{-1}, 1 mg mL^{-1}).

3.3.11 Plasmid DNA

Plasmid is an extrachromosomal circular double-stranded single DNA molecule found in bacteria, which encodes a sequence of a specific protein (or proteins) and may autonomously replicate. Vectors are small, engineered plasmids that are widely used for transfection of eukaryotic cells to delivery non-hosting gene for production of a specific protein. They are usually derived by replication in

transformed prokaryotic cells such as *Escherichia Coli* (*E.Coli*) and then purifying with the help of plasmid DNA purification kits.

For our transfection experiments, the plasmid DNA that encoded the synthesis of enhanced green fluorescence protein (EGFP) was obtained by transforming *E.Coli* (Dh5α subtype) with a pcDNA3EGFP plasmid according to standard protocol and purified with NucleoBond® PC 10000 EF endotoxin-free plasmid DNA purification kit (Macherey-Nagel® , Dueren, Germany), according to the manufacturer's manual (M_w=4.0·10^6 g mol^{-1}, 6160 base pairs).

3.3.12 Polyethylenimine (PEI)

Polyethylenimine (PEI) is a polycationic polymer comprising of repeating units of amine groups and two carbon aliphatic CH_2-CH_2 spacers. In its linear form, PEI contains only secondary amines, whereas branched PEI contains primary, secondary, and tertiary amino groups. It is a commercially available compound, produced on industrial scale for many applications [294]. It is widely known as polymeric transfection agent. PEI is able to condense negatively charged DNA molecules into positively charged polyplexes, which have high affinity towards negatively charged cell membrane and is internalized by cells via endocytosis. PEI is reported to be highly effective and also cytotoxic to some degree [295]. It implies two different mechanisms [296] causing the cell death either by necrosis, damaging the cell membrane followed by cytosol leakage, or by apoptosis, disrupting the mitochondrial membrane after internalization.

For our experiments, we used branched PEI (M_w=25 kg mol^{-1}, Sigma-Aldrich, 2 mg mL^{-1}).

3.3.13 Protamine

Protamine is the member of a small arginine-rich proteins family. It is a naturally occurring polypeptide with membrane-translocating and nuclear-localizing activity

[297–300]. It is generally recognized as being safe by the Food and Drug Administration (FDA) [301]. Protamine is found to be a prominent compound as it can facilitate the entrance of DNA into the nucleus by efficient binding to negatively charged DNA molecules and providing its highly compact configuration [300, 302, 303]. Protamine carries four nuclear localization sequences (NLSs), which facilitate the translocation of the protamine-DNA complex into the nucleus [297, 304–306].

For our studies, we used protamine sulfate (Merck, Darmstadt, Germany; M_w=4-10 kDa, 10 mg mL^{-1}).

3.4 Applied materials and methods for cell culture experiments

3.4.1 Cell lines and applied chemicals

In Table 3.1, the cell lines and primary cell cultures used along with the corresponding cell media are listed. The cells were used in a particular cell line range of cell passages (number of cell divisions), freshly defrosted and cultivated 10-14 days prior to being taken into the experiment. The adherent cell lines, which get attached to the bottom of the cell culture flask, were passaged every 3-4 days when their confluency (cell density) reached 80-90%. The non-adherent cells, which live and proliferate in the cell medium as suspension, were passaged once a week when their concentration reached 1-2·10^6 cells per mL of cell medium.

Cell culture medium is a basal liquid nutrient essential for cultivating the cells outside the living organisms (*in vitro*) for different purposes. Basal cell culture medium contains a mixture of defined nutrients (amino acids, inorganic salts, glucose, vitamins and other organic nutrients) dissolved in a buffered physiological saline solution (see Table 4.12). Most culture media also contain pH-indicators like Phenol Red, which signals on the pH changes in the cell culture medium

during the cultivation process. Basal media can be modified by the addition of various supplements to generate a complete growth medium for a specific cell line.

For cultivation of the above mentioned cell lines and primary cells, the following cell culture media and chemicals, purchased from Gibco® , Life Technologies, USA (if not stated otherwise), were used: DMEM-Dulbecco's Modified Eagle's Medium; RPMI-1640 medium-Roswell Park Memorial Institute medium; MSCGM-Mesenchymal Stem Cell Growth Medium (MSCGM® , Lonza); HEPES buffer (5mM); L-glutamine (5mM); penicillin/streptomycin (P/S) (antibiotics for prevention of bacterial contamination) and fetal calf serum (FCS) containing growth factors, as serum supplement.

Table 3.1 List of all cell lines used in the biological experiments. FCS: fetal calf serum.

Cell type	Description	Cell morphology and properties	Range of passage number	Cell medium
HeLa	Human epithelial cervical cancer cell line	Epithelial, adherent	P8-50	DMEM + 100 U mL^{-1} penicillin/streptomycin + 10% FCS
MG-63	Human osteosarcoma cell line	Fibroblasts, adherent	P37-50	DMEM + 100 U mL^{-1} penicillin/streptomycin + 10% FCS
THP-1	Human acute monocytic leukemia cell line	Monocytes/ Macrophages, suspension	P45-50	RPMI-1640 + 100 U mL^{-1} penicillin/ streptomycin + 10% FCS + 5mM HEPES + 5mM L-glutamine
hMSC	Normal human bone marrow derived mesenchymal stem cells	Multipotent stromal cells, adherent	P5-7	MSCGM + 100 U mL^{-1} penicillin/ streptomycin + 10% FCS

3.4.2 Light and fluorescence microscopy

Fluorescence is a form of luminescence by which a substance emits light with longer wavelength (less energy) per photon after absorption of light with shorter wavelength (more energy). This phenomenon lies in the basis of fluorescence microscopy. A typical fluorescence microscope consist of (but is not limited to) a light source (usually a mercury-vapor lamp or a xenon arc lamp), the excitation filter, the dichroic mirror, collector lens, the emission filter and objective. The light source emits white light, which while passing through the excitation filter selects the specific wavelength for the excitation of a fluorophore. The specimen

previously stained with a fluorescent dye (DAPI, Cell mask® , Alexa488, Cy5, etc.) is illuminated with this light which the fluorescent molecules absorb. This causes them to emits light with longer wavelength (less energy per photon) and, thus, another color. The emitted light then goes through spectral emission filters separating it from other residual unspecific fluorescence and giving one bright color of lower wavelength, which can be observed by naked eye. The filters and the dichroic mirror are chosen to match the spectral excitation and emission characteristics of the fluorophore used to label the specimen [307].

The light and fluorescence microscopy was performed with a Zeiss Axiovert 40 CFL (Carl Zeiss, Goettingen, Germany) and a Keyence Biorevo BZ-9000 (Osaka, Japan) equipped with filters for TRITC (excitation: 540 nm, emission: 605 nm), GFP BP (excitation: 470 nm, emission: 535 nm) and DAPI (excitation: 360 nm, emission: 460 nm) channels under 40x and 100x magnification.

3.4.3 Confocal laser scanning microscopy (CLSM)

Confocal laser scanning microscopy (CLSM) is one of the light microscopic techniques that allows to obtain high-resolution optical images of micrometer or submicrometer range objects, including fixed and living cells or cell compartments, tissues, as well as colloidal dispersions [308].

This technique has become an essential tool in biomedical sciences and related fields, owing to the possibilities offered compared to traditional optical fluorescence microscopy. In a conventional microscope, the entire fluorescently labeled specimen is irradiated with the emitted light, often resulting in a blurred image, because the fluorophores on all levels of the sample are exited simultaneously and overlay one another. Besides, it could lead to photo bleaching of fluorophores, causing a loss of image quality. In contrast, in confocal microscopy only one selected depth level of the specimen is irradiated at a time. The images of the specimen, labeled with multiply fluorophores, are acquired via point-by-point scanning of selected plane, while scattered fluorescent light outside of the focal

plane is shielded through a pinhole. This process can be repeated within selected sample depth and then the obtained serial of images could be reconstructed in a three-dimensional object. This process is called optical sectioning or Z-stack.

Investigations of cells were performed on a Leica SP5 confocal inverse CLSM in the group of Prof. Perihan Nalbant at the University of Duisburg-Essen, as well as on a Zeiss LSM 510, Axiovert 200 in the group of Prof. Eric Metzen at Essen University Hospital.

3.4.4 Fluorescence-activated cell sorting (FACS) analysis

Fluorescence-activated cell sorting (FACS) is a specialized form of flow cytometry that enables sorting a heterogeneous mixture of cells into two or more fractions, one cell at a time, according to the specific light scattering and fluorescent characteristics of each cell. Using this method, the fluorescent signals from individual cells in cell mixture can be quickly and easily quantified and the cells of particular interest can be collected into separate vessel.

The mechanism of FACS is described as follows. The cell suspension is centered in a narrow, rapidly flowing stream of liquid in a narrow needle. The flow undergoes vibration to achieve large separation distances between cells. This flow passes between the laser (or lasers) with a specific wavelength to excite the cell, and the detectors, which detect the cell fluorescence intensity, its size and granularity, depending on the obtained scattered light. Depending on the chosen characteristics, the flow receives a corresponding charge, flowing through an electrical charging ring and breaks into droplets. Under the influence of electrostatic deflectors, the charged droplets, containing one cell each are divided into test tubes corresponding to their charge.

The FACS analysis was performed with a FACSCalibur instrument (BD Biosciences, USA) in the group of Prof. Michael Ehrmann (Centre for Medical Biotechnology, University of Duisburg-Essen).

3.4.5 Viability test (MTT assay)

The MTT assay is a colorimetric assay for measuring the metabolic activity of cells. This method is based on the ability of NAD(P)H-dependent cellular oxidoreductase to reduce MTT (3-(4,5-dimethylthiazol-2-yl)-2,5-diphenyltetrazolium bromide) to insoluble formazan compound of purple color in the mitochondria of living cells (Figure 3.5). Using this method, one can assess the viability and the proliferation rate of cells *in vitro*. It can also be used to determine the cytotoxicity of potential medicinal agents and toxic materials because these agents would stimulate or inhibit cell viability and proliferation. The absorbance of the colored solution can be quantified by measuring it at a certain wavelength (λ=570 nm) by a spectrophotometer.

The protocol used for determining the cell viability in our experiments was as follows. MTT (Sigma, Taufkirchen, Germany) was dissolved in PBS (5 mg mL^{-1}) and then diluted to 1 mg mL^{-1} in the cell culture medium. The cell culture medium of the cells treated with nanoparticles or control was replaced by 300 μL of the MTT solution and incubated for 1 h at 37 °C under 5% CO_2 in humidified atmosphere. Then 300 μL of DMSO was added to the cells. After 30 min, three aliquots (100 μL) per sample were taken for spectrophotometric analysis with a Multiscan FC instrument (Thermo Fisher scientific, Vantaa, Finland) at λ=570 nm. The absorption of treated cells was normalized to the untreated cells (Mock), thereby indicating the relative level of cell death.

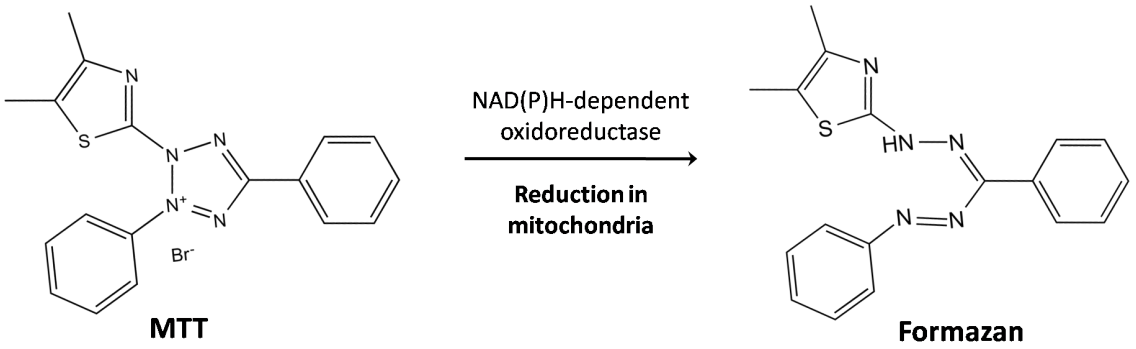

Figure 3.5 The reduction reaction of MTT in mitochondria.

3.4.6 Lysozyme activity assay

Lysozyme (muramidase) is a ubiquitous and well-characterized enzyme that naturally occurs in different animal and plant tissues as well as secretions (e.g. saliva, tears, serum, urine, seminal fluid, and milk). Lysozyme hydrolyzes β-(1-4)-glucosidic bonds between N-acetylmuramic acid and N-acetyl-D-glucosamine residues presented in the mucopolysaccharide cell wall of a variety of microorganisms, thus possesses an explicit antibacterial effect.

The EnzChek® Lysozyme Assay Kit (Molecular Probes® , Life Technologies, USA) is a sensitive assay to measure levels of lysozyme activity in solution. This fluorescence-based assay can detect lysozyme activity down to 20 U mL^{-1}. The assay measures lysozyme activity on *Micrococcus lysodeikticus* cell walls that are labeled to such a degree that the fluorescence is quenched. Lysozyme action can prevent this quenching, thereby yielding a dramatic increase in fluorescence that is proportional to lysozyme activity. The fluorescence increase can be measured by using a spectrofluorometer, mini-fluorometer, or fluorescence microplate reader that can detect fluorescence.

The determination of lysozyme activity in THP-1 cells using this assay was carried out in the following manner. THP-1 cells ($1{\cdot}10^6$ cells per well) were seeded in 12-well plates in 1 mL of RPMI-1640 medium. The cells were differentiated by additions of PMA as described in Subsection 3.5.2. Afterwards, the cell cul-

ture medium was removed and new medium containing lipopolysaccharides (LPS, 10 μg mL^{-1}) and aprotinin (pancreatic trypsin inhibitor, ApplChem, 2 μg mL^{-1}) was added to the cells, so that the total volume of added cell medium was 1 mL. The sample was left for incubation for 48 h. Then 100 μL of nanoparticles suspension or soluble polymer were added to the cells and incubated for 24 h. Afterwards, the cell medium was collected into Eppendorf tubes and centrifuged for 10 min at 2,000 g under 4 °C. The cells were washed with PBS and subsequently lysed with the addition of 450 μL of CelLytic® M Cell Lysis Reagent (Sigma-Aldrich, Steinheim, Germany) and incubation on the Shaker (Oehmen, Labortechnik) for 5 min. This followed by collection the cell lysate into the Eppendorf tube and subsequent centrifugation for 10 min by 14,000 g at 4 °C to remove cellular debris. The obtained samples were then used for the EnzChek® assay, according to the manufacturer's manual.

In brief, 50 μL aliquots of each sample (cell lysate and cell medium, 4 aliquots each) were transferred into a black 96-well plate for measuring fluorescent samples (Sarstedt, USA). Along with this the lysozyme standard curve was prepared by filling 8 wells with 50 μL of phosphate reaction buffer and adding 50 μL of the 1,000 U mL^{-1} stock solution of lysozyme to the first well, mixing by pipetting and transferring 50 μL to the second well. This procedure was repeated subsequently for the next wells, except for discarding 50 μL from the mixture in the seventh well and adding nothing to the eighth. Thus, the lysozyme concentration ranged from 500 U mL^{-1} to 0 U mL^{-1} in the 50 μL volumes. After the addition of 50 μL of DQ lysozyme substrate working suspension (50 μg mL^{-1} stock suspension diluted in phosphate buffer) to each well, the concentration of the substrate in each well was 25 μg mL^{-1} and final concentrations of lysozyme in standard curve samples ranged from 250 U mL^{-1} to 0 U mL^{-1} in the 100 μL volume. The mixtures were incubated for 1 h at 37 °C, protected from light. The fluorescence measurements were carried out on a fluorescence microplate reader (SpectraMax M5e, Molecular Devices, in the group of Prof. Michael Ehrmann, Centre for Medical Biotechnology, University of Duisburg-Essen) by using filters

for absorption (λ=485 nm) and emission (λ=538 nm). The obtained values were then converted into lysozyme activity in U mL^{-1} using a calibration curve. All samples were measured in quadruplicates. At least 3 independent experiments were carried out. The statistical analysis of the obtained data was performed using Student's t-test, where p-value$<$0.5 was accepted as statistically significant difference.

For determining of lysozyme-inhibiting polymer efficiency in the samples without cells in different milieus, the standard lysozyme solution in concentration of 1.4 nM was added to the wells containing either phosphate buffer, RPMI-1640 without FCS or RPMI-1640 + 10% FCS. The polymer was added in different concentrations (0.11, 1.1, 2.2, and 3.3 nM) to the lysozyme-containing solutions and incubated for 5 min at 37 °C. The solution with no addition of inhibitor polymer was used as positive control (100% lysozyme activity). Then the samples were transferred into black 96-well plate for measuring fluorescent samples in 50 µL aliquots and treated according to the above mentioned protocol. All samples were measured in quadruplicates in two independent experiments.

3.5 Cell culture methods

3.5.1 Cultivation of secondary cell lines and primary cells

All cell lines and primary cells (hMSC) were cultured in the corresponding media (see Table 3.1) at 37 °C under humidified atmosphere, containing 5% CO_2 in 25 cm^2 or 50 cm^2 cell culture flasks (Sarstedt, USA) in incubator. After achieving 80-90% confluence, adherent cell lines were washed twice with PBS and then treated with a trypsin/EDTA solution (Gibco® , Life Technologies, USA) for 3 min at 37 °C to detach cells from the cell culture flask surface. After this, the corresponding cell medium was added to the cell suspension and transferred to the falcon tube for centrifugation (Heraeus Multifuge X1R, 900 rpm, 3 min,

RT). Then the trypsin-containing supernatant was removed and the cells were subsequently resuspended in fresh medium and transferred to a cell culture flask or seeded for the experiments into corresponding well plates or slides.

The suspension cell line THP-1 was cultivated in corresponding medium (see Table 3.1) and at the same conditions as adherent cell lines at concentration between $1{\cdot}10^5$-$1{\cdot}10^6$ cells mL^{-1}. After reaching the concentration of $1{\cdot}10^6$ cells mL^{-1}, the cells were transferred into the falcon tube and collected by centrifugation (Heraeus Multifuge X1R, 900 rpm, 3 min, RT). After the removal of the supernatant, the cells were resuspended in fresh medium and transferred into a cell culture flask, or seeded for the experiments into corresponding well plates or slides.

The number of cells, added for further cultivation to the cell culture flask, was adjusted so the passage of each cell line was repeated 1-2 times a week. The cell number was determined with the help of a hemacytometer, adding 10 µL of cell suspension (obtained after centrifugation) to the chamber of hemocytometer, covered by cover glass, and by manually counting the cells in 4 big squares using light microscope at 10x magnification. The cell number was calculated as follows: the mean value from 4 squares multiplied by 10^4 to estimate the number of cells per mL of cell suspension.

To estimate the number of healthy suspension cells they were treated in the same way as the adherent, except that before adding the aliquote to the hemacytometer chamber, they were previously diluted in the Trypan Blue® reagent (Gibco® , Life Technologies, USA) in a 1:10 ratio (10 µL of cell suspension to 90 µL of Trypan Blue® solution). Afterwards, a 10 µL aliquote of Trypan Blue® -treated suspension cells were placed into the hemacytometer chamber and counted as mentioned above. In this case, the cells that took up the blue dye (appear blue in light microscope) were considered non-viable and were not counted.

3.5.2 Differentiation of suspension cells

Before imaging the suspension cells of the THP-1 cell line with light and fluorescence microscopy and CLSM as well as carrying out EnzCheck® assays, the cells must become adherent. This can be done by stimulating the cells to differentiate from suspension-proliferating monocytes into adherent multinuclear, non-dividing macrophages. For this purpose, the seeded THP-1 cells were treated with PMA (phorbol-12-myristate-13-acetate, Sigma-Aldrich, USA, 0.1 mg mL^{-1}) solution with the final concentration 100 nM per well (1 µL stock solution of PMA to 2 mL of cell medium) and then left to differentiate for 3 days. Then the medium for differentiation was substituted by the same amount of fresh one and the differentiated cells were used further in the experiments.

3.5.3 Cryoconservation and thawing of cells

In order to be able to use fresh and adequate cells for experiments, they must be aliquoted and stored properly with minimal damage and loss of cell viability, as well as excluding the risk of contamination and mutation of the cells. For this reason, all cell lines and primary cells used were exposed to the process of cryoconservation as follows. Cultured cells were washed twice with PBS, trypsinized, and centrifuged as described previously in Subsection 3.5.1. Then they were redispersed in the corresponding cell medium containing 10% DMSO (100 µL in 1 mL of total cell medium for cryoconservation) with the concentration $1{\cdot}10^6$ cell mL^{-1} per one cryogenic vial. These vials were exposed to a slow cooling over 24 h at -80 °C and then transferred into a Dewar container with liquid nitrogen (-196 °C) for prolonged storage.

For thawing, the cells were rapidly taken out from the liquid nitrogen and heated to 37 °C within 1 min. To avoid an osmotic shock, the cells were immediately transferred into 10 mL preheated (37 °C) cell culture medium. The thawed cells were then centrifuged (Heraeus Multifuge X1R, 900 rpm, 3 min, RT), resuspended

in fresh medium, and transferred to the cell culture flask. In order to remove the residues of DMSO, the medium was changed again after 18 h (overnight).

3.5.4 Cell transfection and determination of the transfection efficiency

HeLa cells and MG-63 cells were cultivated in the corresponding medium (see Table 3.1) at 37 °C under 5% CO_2 atmosphere. On the day before the transfection experiment, the cells were trypsinized and seeded in 96-well plates with a density of $5{\cdot}10^3$ cells per well in 100 µL of cell culture medium. Approximately 24 h later, the cell medium in all samples was removed and a fresh medium containing functionalized nanoparticles or corresponding controls in 1:10 ratio, i.e. 10 µL of each nanoparticle dispersion and 90 µL of cell culture medium, was added to the cells and incubated for 7 h. Nanoparticles without protamine or PEI and polyplexes (DNA/Protamine/PEI) were set as control groups. After 7 h incubation, the cell culture medium containing the transfection agents was changed and the cells were left for another 72 h incubation.

The transfection efficiency was determined by transmission light microscopy and fluorescence microscopy (Carl Zeiss MicroImaging, Göttingen, Germany, magnification 100x) 72 h after transfection. The transfection efficiency of the nanoparticles and corresponding controls was determined by fluorescence and light microscopy as follows:

$$\frac{\text{Number of EGFP-expressing cells (green fluorescence)}}{\text{Total number of cells}} \cdot 100\%$$

Dead cells (as recognized by their shape) were not included in the computation. Each sample was performed in duplicates and imaged at three different places within one well, giving a total of six images per sample. The statistical analysis of obtained data was performed using Student's t-test, where a p-value$<$0.5 was

accepted as a statistically significant difference. The values are written as mean value ± standard deviation (SD) in %.

3.5.5 Studies of uptake of nanoparticles

All cell types were cultured in corresponding cell culture media (see Subsection 3.4.1) at 37 °C and 5% CO_2. About 18 h prior to uptake experiments, the cells were trypsinized and seeded in cell culture well plates with the overall density of $1{\cdot}10^5$ cells per well in 1 mL cell medium. The suspension cells were first treated with PMA (see Subsection 3.5.2) so that they became differentiated and adherent. For the uptake studies, the cells were treated with corresponding nanoparticles' colloids in ratio of 1:11 (50 µL of the particle dispersion was added to cell culture well, containing 500 µL cell medium). The cells were incubated for 3 h or longer (depending on the experiment), after which the whole cell culture medium was removed and cells were washed three times with PBS to remove the cell medium and the nanoparticles that were not taken up by the cells. Afterwards, the cell samples were immediately imaged using light and fluorescence microscopy (Zeiss Axiovert 40 CFL or Keyence BZ-9000 fluorescent microscope).

3.5.6 Fixation of cells for CLSM

For performing CLSM on fixated cells, they were treated as follows. Cells were seeded into special 4- or 8-wells cell culture coverslips (Falcon® Culture Slides, DB Biosciences) in density $0.5{\cdot}10^5$-$1{\cdot}10^5$ in 500 µL cell medium, depending on the well size, and cultivated overnight. For fixation of suspension cells, they were differentiated beforehand, as previously described.

After treating the cells with different samples and during various cultivation periods they were fixated and stained in the following manner. The cell medium was removed and the cells were washed 3 times with PBS. Then they were treated with formaldehyde solution (2.5% dissolved in PBS) for 20 min at room

temperature (RT). The used solution of formaldehyde was collected into a separate waste container and the cells were washed twice with PBS. Afterwards, the cells were stained subsequently with different fluorescent dyes, labeling either cell membrane (Cell Mask® , Molecular Probes™, Life Technologies, USA), chromatin (DAPI, 4',6-diamidin-2-phenylindol, Molecular Probes™, Life Technologies, USA) or actin filaments (Actin phalloidine488, Molecular Probes™, Life Technologies, USA) and incubated for 5, 7 or 15 min at 37 °C, respectively. After each staining, all samples were washed twice with PBS to remove the unbounded dye. Finally, the slides were treated with mountain medium (Dako, Agilent Technologies) and carefully covered with cover glass so that no air bubbles emerged. The cover slips were stored in aluminum foil at 4 °C for long-term storage.

3.5.7 Inhibition of endocytosis

To study the role of different endocytotic pathways in the uptake of the functionalized calcium phosphate nanoparticles and the HTRA1 protein a selective inhibition of various pathways was applied. The list of the inhibitors used and the corresponding inhibited pathways, as well as the concentrations used, are given in Table 3.2.

The selection of the concentrations used and protocol was adjusted from the literature [153]. Briefly, the day before the start of the experiment, MG-63 cells were seeded in 6-well plates with a density of $5 \cdot 10^5$ cells per well. On the following day, the cell culture medium was removed by fresh cell medium containing inhibitors, in total volume of 2 mL and cultivated for 30 min. As a control group, the cells treated with normal cell medium with no inhibitors and left either at 37 °C (positive control) or 4 °C (negative control) for 30 min were used. Afterwards, the nanoparticles or the protein were added to the corresponding cell samples and incubated for another 3 h. Then all samples were washed 3 times with PBS, detached with trypsin/EDTA complex (3 min by 37 °C) and

transferred into 15 mL falcon tubes by adding to each cell sample 3 mL of cell medium. The cells were then washed 3 times by centrifugation (1,700 g, 5 min, 4 °C) and subsequent resuspension in 4 mL PBS. After final centrifugation, all samples were resuspended in 2% formaldehyde solution and incubated for 20 min at RT. Then 0.6 mL of PBS were added to each sample and the cells were washed 3 times by centrifugation (1,700 g, 5 min, 4 °C) and subsequently resuspended in 3 mL PBS. As the last washing step, each sample was resuspended in 1 mL PBS and stored in dark at 4 °C. The prepared cell samples were then transferred to FACS tubes for measurements (see Subsection 3.4.4).

Table 3.2 The list of endocytosis inhibitors used in biological experiments.

Inhibitor	**Inhibited pathway / structure**	**C (inhibitor) in stock solution / µg mL^{-1}**	**V (inhibitor) added / µL**	**C (inhibitor) per well / µg mL^{-1}**
Wortmannin	Macropino-cytosis	10	20	0.1
LY294002	Macropino-cytosis	1000	40	20
Nystatin	Caveolin-mediated endocytosis / Lipid Rafts	2000	10	10
Nocodazole	Microtubules of cytoskeleton	1000	20	10
Chlorpromazine	Clathrin-mediated endocytosis	100	20	1

4 Results and Discussion

4.1 Transport of molecules into the cell with calcium phosphate nanoparticles

4.1.1 DNA-, protamine- and PEI-functionalized calcium phosphate nanoparticles for transfection

4.1.1.1 Characterization of functionalized calcium phosphate nanoparticles

Nanoparticles for transfection experiments were prepared as described above in Subsection 3.1.1 and were not purified. For characterization purposes the nanoparticles were functionalized with model DNA from herring sperm (Sigma-Aldrich, M_w=10-30 kg mol^{-1}, 1 mg mL^{-1}). The volume ratio of calcium phosphate colloid to nucleic acids solution, used for the synthesis, was 5:1. The triple-shell structure of nanoparticles was used to protect the sensitive biomolecules from nucleases and other risks of degradation in and outside the living cell. As a final shell for steric and electrostatic stabilization, polyethylenimine, which is a positively charged polyelectrolyte, was used in different amounts (see Table 4.1). For transfection experiments, calcium phosphate nanoparticles were loaded with functional pcDNA-EGFP. In order to increase the transfection efficacy of the nanoparticles, they were additionally functionalized with protamine in different configurations. Additional control samples carried either no CaP, protamine or PEI were prepared. In Table 4.1, the final concentrations of calcium phosphate, DNA, protamine, and PEI in the nanoparticle dispersion are shown.

Table 4.1 The final concentrations of calcium phosphate, DNA, protamine, and PEI in the nanoparticles dispersion.

	Sample	Concentration / μg mL^{-1}			
		CaP	**DNA**	**Protamine**	**PEI**
A	CaP/DNA/Protamine/CaP/PEI0.05	1447	107	533	80
B	CaP/DNA/Protamine/CaP/PEI0.1	1391	103	513	153
C	CaP/DNA/Protamine/CaP/PEI0.2	1292	95	476	286
D	DNA/Protamine/PEI0.05	0	107	533	80
E	DNA/Protamine/PEI0.1	0	103	513	153
F	DNA/Protamine/PEI0.2	0	95	476	286
G	CaP/DNA/CaP/PEI0.05	1528	113	0	108
H	CaP/DNA/CaP/PEI0.1	1466	108	0	162
I	CaP/DNA/CaP/PEI0.2	1356	100	0	300
J	CaP/DNA/CaP/Protamine	1507	111	555	0

In Table 4.2 the colloid-chemical characterization data of the synthesized nanoparticles are shown. All samples had relatively good polydispersity index ($<$0.5) and a size between 200 and 300 nm. The addition of PEI lends a strong positive surface charge to the nanoparticles, preventing the nanoparticles from agglomeration, and also facilitating the uptake process and preventing the DNA from subsequent degradation in lysosomes due to the "proton sponge effect" (see Figure 2.6).

Table 4.2 Colloid-chemical characterization data of the synthesized nanoparticles. PDI: polydispersity index from dynamic light scattering.

	Sample	PDI	Particle size / nm	Zeta potential / mV
A	CaP/DNA/Protamine/CaP/PEI0.05	0.470	207	+30
B	CaP/DNA/Protamine/CaP/PEI0.1	0.407	238	+28
C	CaP/DNA/Protamine/CaP/PEI0.2	0.390	247	+33
D	CaP/DNA/CaP/PEI0.05	0.420	239	+20
E	CaP/DNA/CaP/PEI0.1	0.306	285	+36
F	CaP/DNA/CaP/PEI0.2	0.390	271	+37
G	CaP/DNA/CaP/Protamine	0.496	464	+5

The scanning electron micrographs (Figure 4.1) showed spherical nanoparticles with an actual size up to 100 nm. This value is slightly different from the measurements obtained with DLS, indicating some agglomeration in dispersion.

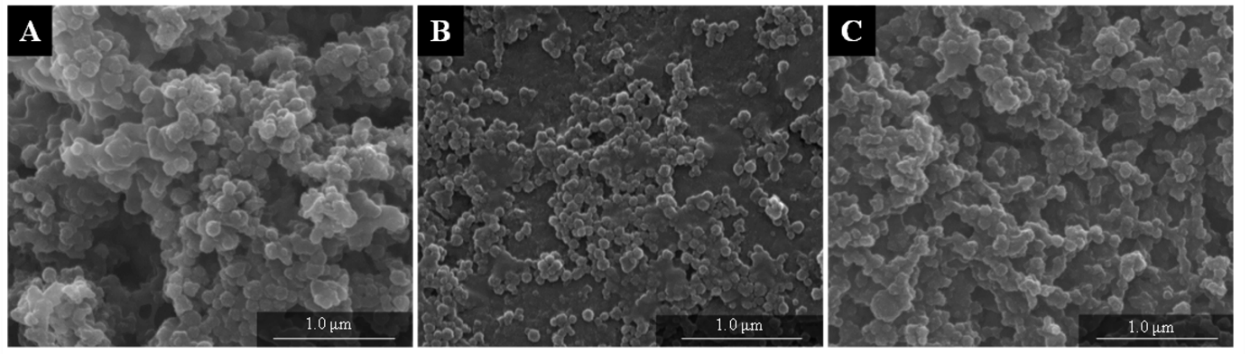

Figure 4.1 Scanning electron micrographs of DNA-, protamine- and PEI-loaded calcium phosphate nanoparticles: (A) CaP/DNA/Protamine/CaP/PEI0.05; (B) CaP/DNA/Protamine/CaP/PEI0.1; (C) CaP/DNA/Protamine/CaP/PEI0.2.

4.1.1.2 Results of transfection experiments

For the transfection experiments, two different cell lines of human origin were used, namely HeLa (epithelial cell line) and MG-63 (osteoblast-like cell line). For the transfection protocol and cell cultivation procedures, refer to Subsection 3.5.1.

The evaluated results of the transfection with multi-shell CaP/DNA/Protamine/-CaP/PEI nanoparticles and controls, as well as the cell viability of both cell lines, are summarized in Table 4.3. The transfection efficiency was shown to be between 39% and 54% for both cell lines, and did not have strict dependency on the concentration of PEI (Figure 4.2 A). However, the viability of cells showed a direct dependency on the PEI concentration in the nanoparticles' samples: it decreased from 94% to 73% for HeLa and, in the case of the more sensitive MG-63 cell line, the viability decreased dramatically from 67% to 8% with an increased concentration of PEI (Figure 4.2 B; Table 4.3, samples A, D, G). In the control groups (Table 4.3, samples without calcium phosphate B, E, H and without protamine C, F, I), the transfection efficiency and the cell viability were significantly reduced. This indicated the toxic influence of PEI and the necessity of nanoparticles and protamine for a high transfection efficiency. On the contrary, the control sample K without PEI showed very poor transfection efficiency on the level of 5%, which demonstrated that the presence of PEI is still needed for effective transfection despite its harmful effect on the cells.

In contrast, the addition of protamine into CaP/DNA/CaP/PEI nanoparticles enhanced the transfection efficiency of both cell lines by improving the nuclear import of the plasmid DNA. Protamine-DNA complexes are able to bind to importins that attach to cytoplasmic filaments of the nuclear pore complex, resulting in nuclear entry and subsequent transcription and translation processes through the host cell gene expression machinery.

Table 4.3 Results of transfection efficiency and cell viability of HeLa and MG-63 cells. Mean value ± standard deviation (SD). * $p<0.05$ compared to CaP/DNA-Protamine/CaP/PEI0.05, 0.1 and 0.2 respectively. TE: Transfection efficiency, CV: Cell viability.

Sample		HeLa cells		MG-63 cells	
		TE / %	CV / %	TE / %	CV / %
A	CaP/DNA/Protamine/CaP/PEI0.05	45 ± 8	94 ± 5	49 ± 5	67 ± 1
B	DNA/Protamine/PEI0.05	26 ± 6*	35 ± 9*	17 ± 6*	13 ± 7*
C	CaP/DNA/CaP/PEI0.05	20 ± 7*	23 ± 8*	22 ± 7	42 ± 7*
D	CaP/DNA/Protamine/CaP/PEI0.1	39 ± 10	84 ± 6	52 ± 6	56 ± 7
E	DNA/Protamine/PEI0.1	1 ± 1*	5 ± 4*	3 ± 1*	4 ± 3*
F	CaP/DNA/CaP/PEI0.01	33 ± 5	21 ± 6*	39 ± 6*	14 ± 6*
G	CaP/DNA/Protamine/CaP/PEI0.2	47 ± 7	73 ± 7	54 ± 8	8 ± 3
H	DNA/Protamine/PEI0.2	29 ± 9*	5 ± 3*	8 ± 6*	4 ± 2*
I	CaP/DNA/CaP/PEI0.2	29 ± 12*	5 ± 3*	39 ± 9	5 ± 3
J	CaP/DNA/CaP/Protamine	5 ± 3*	119 ± 8	4 ± 2*	77 ± 9

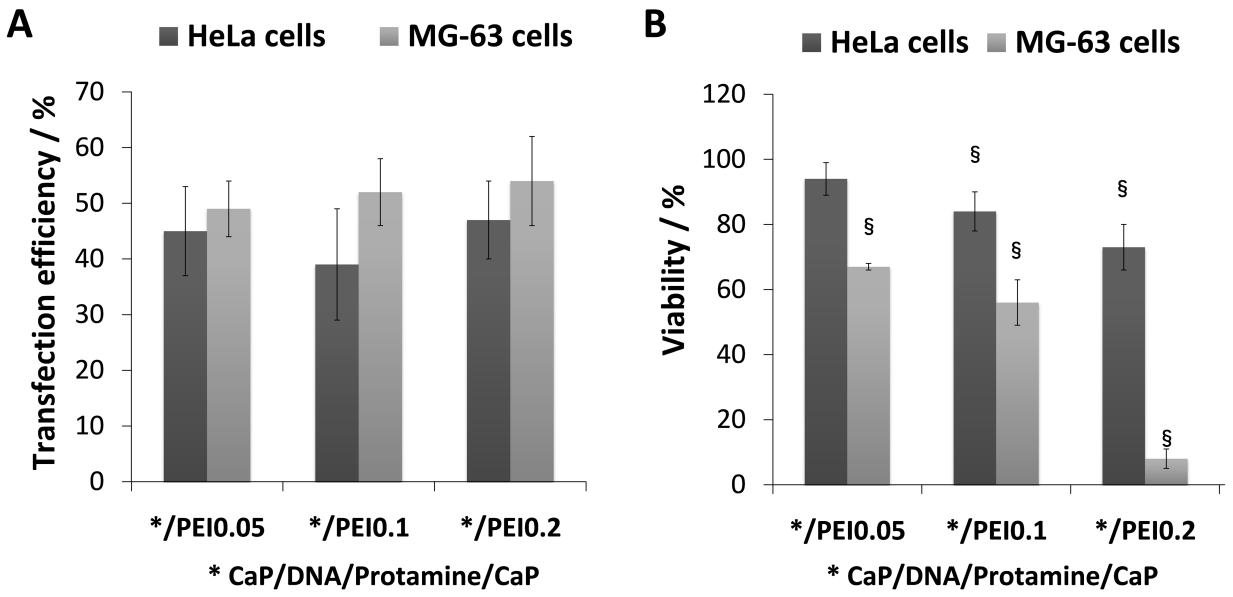

Figure 4.2 Comparison of transfection efficiency (**A**) and cell viability (**B**) of HeLa and MG-63 cells. § $p<0.05$ compared to the untreated control.

As can be seen from the summarized Table 4.3, CaP/DNA/Protamine/CaP-/PEI0.05 nanoparticles (sample A) have a high transfection efficiency, combined with good viability for both cell lines (Figure 4.2), which made them good candidates for further experiments. Figure 4.3 illustrates the representative light and fluorescent microscopy micrographs of HeLa and MG-63 cell, transfected with CaP/DNA/Protamine/CaP/PEI0.05 nanoparticles.

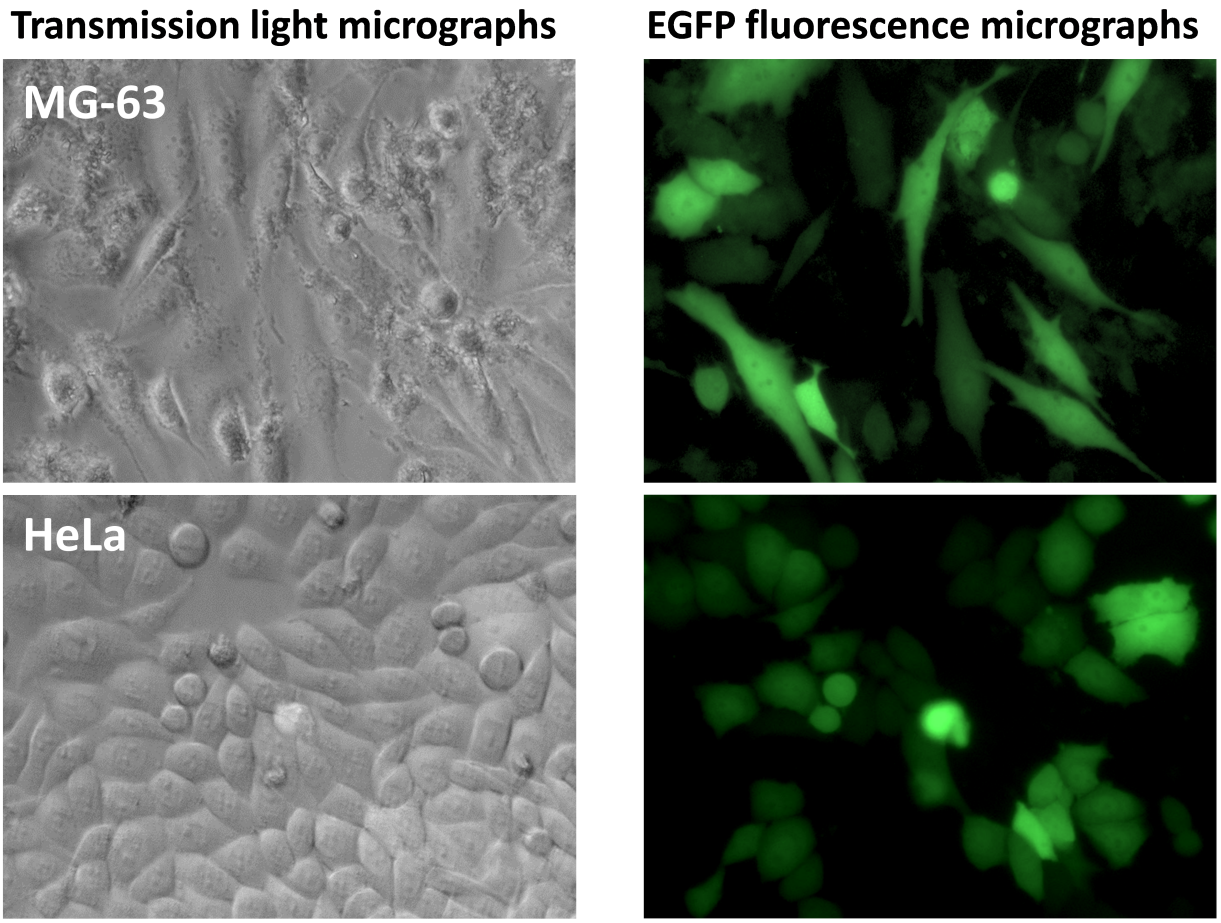

Figure 4.3 Transmission light and fluorescence microscopy of HeLa and MG-63 cells, transfected with CaP/DNA/Protamine/CaP/PEI0.05 nanoparticles. Transfected cells appear green on fluorescence microscopy; 100x magnification.

The next step was to check whether the amount of the nanoparticle dispersion could influence the parameters of the transfection, i.e. efficiency and viability. We used the same control groups for our experiments and this time varied the

amount of the nanoparticle dispersion, which was given to the cells from 1.25 up to 10 µL per 100 µL of cell medium. In Table 4.4, the corresponding amounts of calcium phosphate, DNA, protamine, and PEI per well are given. The results from the transfection experiments on both cell lines are summarized in Table 4.5. The transfection efficiency increased significantly with the increase in the nanoparticle concentration in cell medium for both cell lines: for HeLa from 4% to 38% and for MG-63 from 5% to 39%. However, the viability rate of MG-63 cells decreased almost to half from 110% to 59% with increasing concentration of the nanoparticles. Interestingly, however, it remained unchanged for HeLa cells. It is also of note that the optimal amount of CaP/DNA/Protamine/CaP/PEI0.05 nanoparticle dispersion was different for each cell line. The best results of transfection, i.e. optimal efficacy and viability for HeLa cells, were achieved with amount nanoparticle dispersion of 10 µL to 100 µL of cell medium, whereas for MG-63 the amount was four times smaller (2.5 µL) (see Figure 4.4).

Table 4.4 Final concentrations of CaP, DNA-EGFP, protamine, and PEI in nanoparticle dispersions per 100 µL of cell medium.

V (sample) / µL	Sample	Concentration / µg per 100 µL of cell medium			
		CaP	DNA	Pro-tamine	PEI
10	CaP/DNA/Protamine/CaP/PEI0.05	14.46	1.07	5.3	0.8
	DNA/Protamine/PEI0.05	0	1.07	5.3	0.8
	CaP/DNA/CaP/PEI0.05	15.28	1.12	0	0.85
	CaP/DNA/CaP/Protamine	15.07	1	5.6	0
5	CaP/DNA/Protamine/CaP/PEI0.05	7.23	0.54	2.6	0.4
	DNA/Protamine/PEI0.05	0	0.54	2.6	0.4
	CaP/DNA/CaP/PEI0.05	7.14	0.56	0	0.42
	CaP/DNA/CaP/Protamine	7.53	0.5	2.8	0
2.5	CaP/DNA/Protamine/CaP/PEI0.05	3.16	0.27	1.3	0.2
	DNA/Protamine/PEI0.05	0	0.27	1.3	0.2
	CaP/DNA/CaP/PEI0.05	3.57	0.28	0	0.21
	CaP/DNA/CaP/Protamine	3.76	0.25	1.4	0
1.25	CaP/DNA/Protamine/CaP/PEI0.05	1.86	0.13	0.65	0.1
	DNA/Protamine/PEI0.05	0	0.13	0.65	0.1
	CaP/DNA/CaP/PEI0.05	1.78	0.14	0	0.11
	CaP/DNA/CaP/Protamine	1.88	0.13	0.7	0

In Figure 4.4, representative light and fluorescence micrographs of HeLa and MG-63 cells after transfection with different amounts of CaP/DNA/Protamine/-CaP/PEI0.05 nanoparticles are shown.

Table 4.5 Transfection efficiency and cell viability of HeLa and MG-63 cells at different concentrations of nanoparticles (per 100 µL of cell medium). Mean value ± standard deviation (SD). * $p<0.05$ compared to CaP/DNA/Protamine/-CaP/PEI0.05 nanoparticles. TE: Transfection efficiency, CV: Cell viability.

V (sample) / µL	Sample	HeLa cells		MG-63 cells	
		TE / %	CV / %	TE / %	CV / %
10	CaP/DNA/Protamine/CaP/PEI0.05	38 ± 6	91 ± 3	39 ± 4	59 ± 7
	DNA/Protamine/PEI0.05	30 ± 7	12 ± 7*	21 ± 8*	11 ± 6*
	CaP/DNA/CaP/PEI0.05	28 ± 7*	12 ± 1*	30 ± 5	31 ± 7*
	CaP/DNA/CaP/Protamine	4 ± 2*	118 ± 9	5 ± 3*	78 ± 9
5	CaP/DNA/Protamine/CaP/PEI0.05	19 ± 7	121 ± 6	38 ± 6	72 ± 10
	DNA/Protamine/PEI0.05	13 ± 5	91 ± 4	23 ± 7*	36 ± 8*
	CaP/DNA/CaP/PEI0.05	13 ± 7	34 ± 6*	27 ± 8*	42 ± 6*
	CaP/DNA/CaP/Protamine	3 ± 1*	116 ± 8	3 ± 1*	83 ± 12
2.5	CaP/DNA/Protamine/CaP/PEI0.05	12 ± 3	117 ± 8	32 ± 5	109 ± 5
	DNA/Protamine/PEI0.05	13 ± 4	113 ± 9	16 ± 7*	97 ± 9
	CaP/DNA/CaP/PEI0.05	9 ± 5	99 ± 6	7 ± 5*	80 ± 5*
	CaP/DNA/CaP/Protamine	2 ± 1*	106 ± 9	1 ± 2*	105 ± 11
1.25	CaP/DNA/Protamine/CaP/PEI0.05	4 ± 2	114 ± 9	5 ± 2	110 ± 8
	DNA/Protamine/PEI0.05	6 ± 2	119 ± 8	4 ± 1	91 ± 8
	CaP/DNA/CaP/PEI0.05	2 ± 2	111 ± 8	6 ± 4	82 ± 8
	CaP/DNA/CaP/Protamine	1 ± 1*	115 ± 9	2 ± 1*	95 ± 10

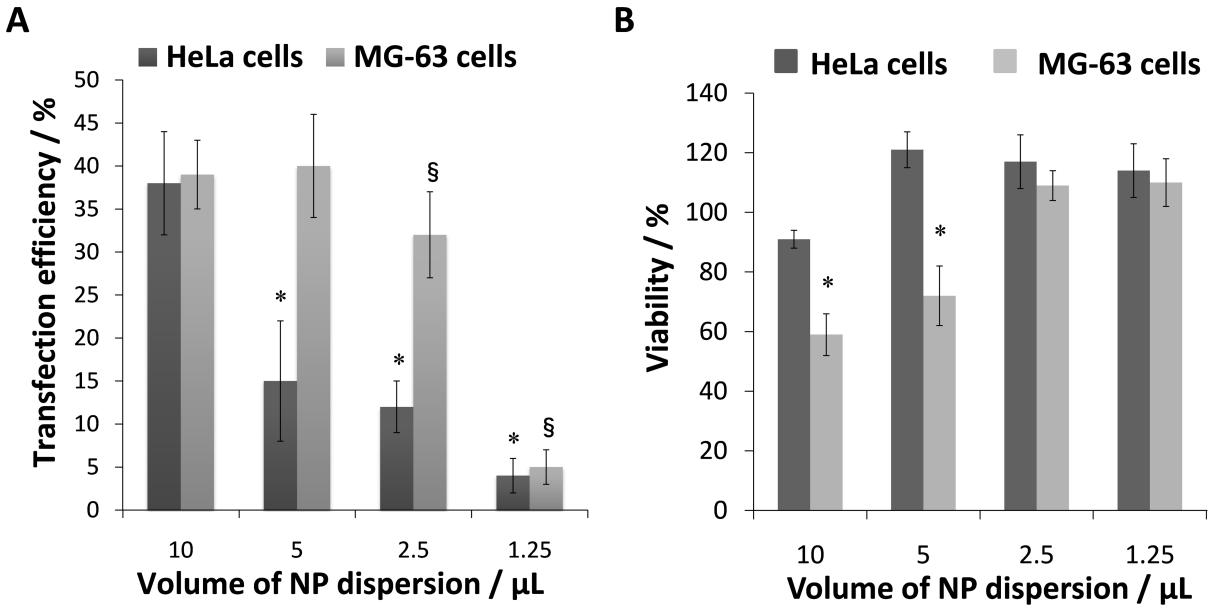

Figure 4.4 Comparison of transfection efficiency (**A**) and cell viability (**B**) of HeLa and MG-63 cells, depending on the amount of nanoparticle dispersion added per 100 µL of cell medium. **A**: * $p<0.05$ compared to the 10 µL group for HeLa cells; § $p<0.05$ compared to 10 µL group for MG-63 cells. **B**: * $p<0.05$ compared to the untreated control.

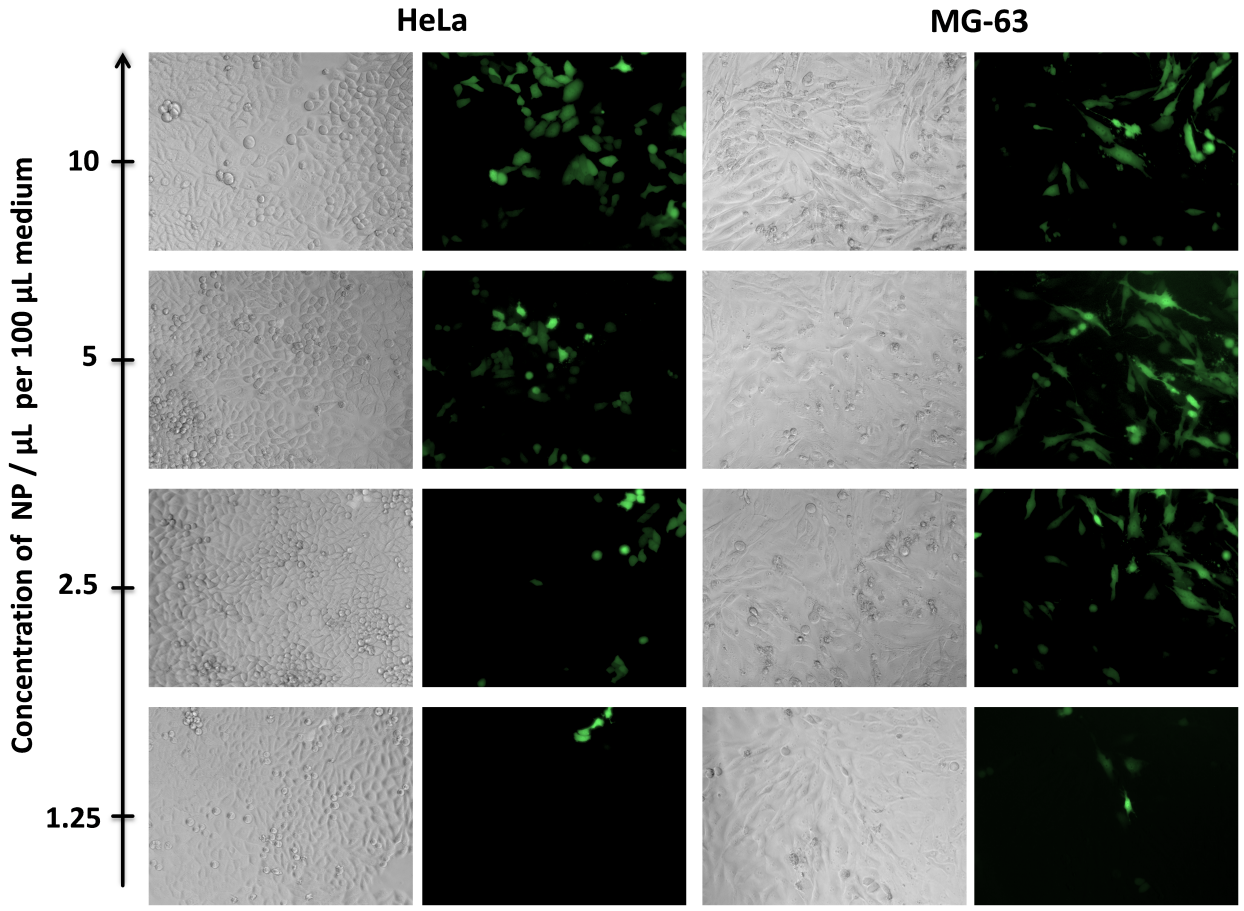

Figure 4.5 Transmission light microscopy and fluorescence microscopy of HeLa and MG-63 cells transfected with different concentrations of CaP/DNA/Protamine/CaP/PEI0.05 nanoparticles. Transfected cells appear green on fluorescence microscopy; 100x magnification.

4.1.1.3 Conclusions

We developed multi-shell calcium phosphate nanoparticles loaded with plasmid DNA, protamine and PEI. The polycationic polymer PEI provided high transfection efficiency, while protamine reduced the cytotoxicity of PEI, protecting cells from apoptosis, and at the same time improved the entry of plasmid DNA into the nucleus. Nanoparticles with the smallest concentration of PEI (CaP/DNA/Protamine/CaP/PEI0.05) were found to be most effective, showing a good transfection efficiency while preserving high viability in both cell lines.

On the whole, the following conclusions can be drawn from these results. First, the MG-63 cell line is more sensitive to the transfection procedure than the HeLa cells. Second, the interaction of the nanoparticles with cells depends on the cell type. Finally, it is important to find the optimal concentration of the transfection agent (in our case, functionalized calcium phosphate nanoparticles) for a specific cell line to receive the highest transfection efficiency, and at the same time the highest viability, which often stands in contrast to each other: the higher the transfection efficiency, the lower the viability rate.

4.1.2 Transport of various molecules across the cell membrane with calcium phosphate nanoparticles

4.1.2.1 Synthesis and characterization of functionalized calcium phosphate nanoparticles

For this experiment, we took molecules that were completely different by origin and chemical structure in order to make a proof-of-principle experiment that we can deliver any kind of molecular cargo inside the cell with calcium phosphate nanoparticles when the cargo itself is not able to penetrate the cell membrane. We chose eight fluorescent or fluorescently labeled molecules: oligonucleotide CpG (labeled with Alexa488 or Alexa555), protein BSA (labeled with fluorescein isothiocyanate (FITC) or with tetramethylrhodamine isothiocyanate (TRITC)), antibody DEC-205 (labeled with FITC), polycationic polymer PEI (labeled with rhodamine), porphyrine *p*THPP (5,10,15,20-tetrakis(4-hydroxyphenyl)-21H, 23H-porphine; has red fluorescence), and a synthetic peptide (labeled with FITC).

For this study we designed single-shell nanoparticles. For the description of the synthesis process of the nanoparticles loaded with labeled CpG, BSA, and DEC-205 molecules, refer to Subsection 3.1.1. For the synthesis of CpG-carrying nanoparticles, no addition of the stabilization agent was needed, because the strong negative charge from phosphate groups of the oligonucleotide backbone

was big enough to stabilize the nanoparticles. In the case of neutral big proteins BSA and DEC-205, a polyelectrolyte in the form of DNA from herring sperm and non-labeled CpG was added, respectively. CpG- and BSA-loaded nanoparticles were purified by centrifugation and a subsequent redispersion in pure water. For the DEC-205-carrying nanoparticles, this procedure could not be employed due to the high sensitivity of the antibody molecules to ultrasonication.

The synthesis of single-shell nanoparticles carrying PEI-rhodamine, *p*THPP porphyrin, stabilized either with PSS or PEI as well as peptide-FITC is described in Subsection 3.1.2.

The colloid-chemical characterization of all samples, performed by DLS and NTA methods, and the concentration of fluorescent molecules in the nanoparticle dispersion determined by UV-Vis spectroscopy, are summarized in Table 4.6.

Table 4.6 Colloid-chemical data of calcium phosphate nanoparticles, carrying different molecules. PDI: polydispersity index from dynamic light scattering.

	Sample	Size / nm (DLS)	PDI	Size / nm (NTA)	Zeta potential / mV	C (fluorescing molecules) / µg mL^{-1}
1	CaP/CpG-Alexa555	240	0.295	139	-24 ± 4	58
2	CaP/CpG-Alexa488	289	0.338	147	-22 ± 7	58
3	CaP/DNA/TRITC-BSA	227	0.482	209	-21 ± 6	95
4	CaP/DNA/FITC-BSA	256	0.370	189	-20 ± 6	63
5	CaP/CpG/FITC-DEC205	243	0.650	226	-19 ± 5	40
6	CaP/PEI-rhodamine	138	0.165	185	+34 ± 6	1000
7	CaP/PEI/*p*THPP	117	0.236	173	+15 ± 4	5
8	CaP/PSS/*p*THPP	122	0.198	203	-18 ± 5	7
9	CaP/PEI/FITC-Pep	109	0.169	230	+12 ± 6	49

All samples are monodisperse and have a size distribution of 100-250 nm. The zeta potential, which refers to the surface charge of the nanoparticles, completely

corresponds to the polyelectrolyte charge used for the steric stabilization of the nanoparticles. Moreover, the absorbed molecules did not reverse the surface charge of the nanoparticles, resulting in the absence of agglomeration and aggregation in DLS and NTA measurements. The concentration of the fluorescent cargo molecules can be seen in the right column of Table 4.6.

A representative scanning electron microscopy image of the functionalized nanoparticles (CaP/CpG-Alexa555) is shown in Figure 4.6. The nanoparticles are about 50 nm in diameter and have a characteristic spherical shape. It must be noted that in SEM images the nanoparticles appear to have smaller diameter than that determined by dynamic light scattering (DLS) or nanoparticle tracking analysis (NTA) because of absence of hydration and organic shell around the nanoparticles after the sample preparation for SEM, as well as some agglomeration. All dispersions were stable for several days during storage at 4 °C.

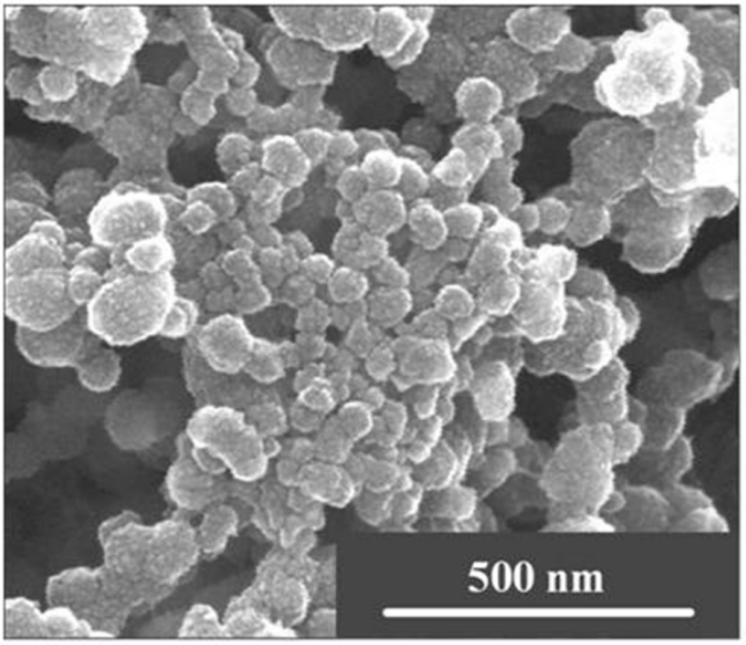

Figure 4.6 Scanning electron micrograph of CaP/CpG-Alexa555-loaded nanoparticles.

4.1.2.2 Results of uptake studies

All cell culture experiments were carried out with HeLa cell line with the samples containing fluorescent molecules adsorbed on the surface of the nanoparticles or in dissolved form at the same concentrations (control groups). The cells were incubated for 3 h with the samples and then washed 3 times with PBS. Afterwards, light and fluorescent microscopy and a viability assay (MTT test) were performed. For a more detailed protocol of cultivation, incubation, and treatment during the above mentioned procedures, refer to Subsection 3.5.1.

Figure 4.7 illustrates the results of the MTT assay of all samples, including calcium phosphate nanoparticles without any molecules (sample CaP). Untreated cells were used as control. We conclude from this figure that calcium phosphate nanoparticles alone and also loaded with different fluorescent molecules had no harmful effect on the cells, along with the dissolved molecules. Remarkably, sample 6C (dissolved labeled PEI) clearly showed a cytotoxic effect, whereas the same concentration of PEI adsorbed on the nanoparticles was not harmful for cells.

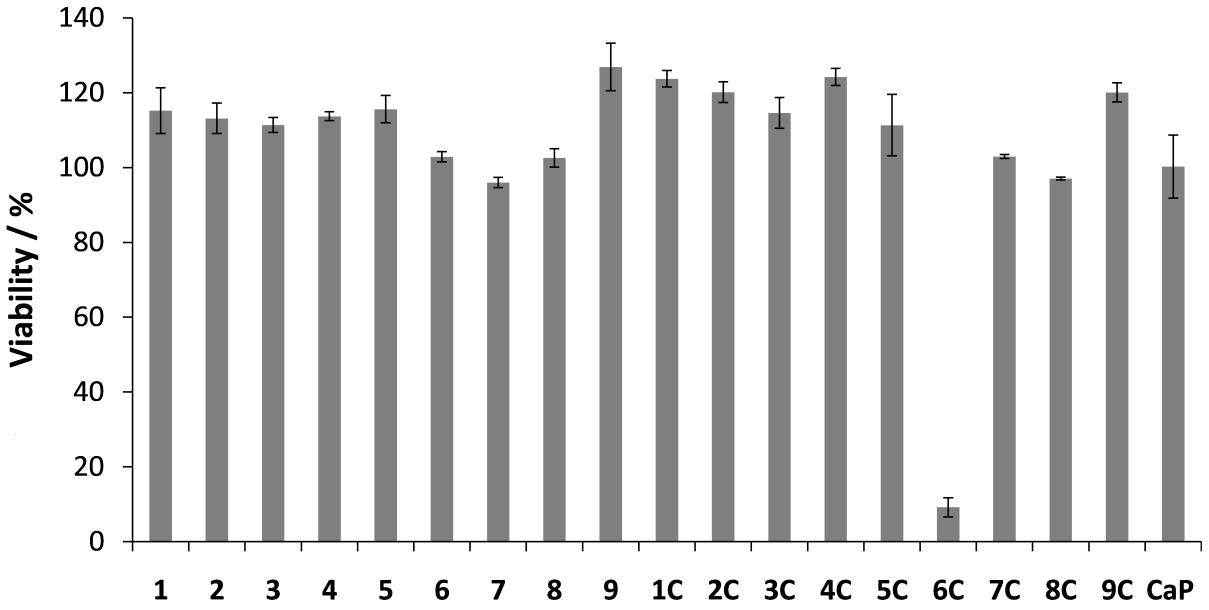

Figure 4.7 Results of the MTT test on HeLa cells. Labels 1-9 refer to the sample number from Table 4.6 and labels 1C-9C to their corresponding controls; CaP: unfunctionalized CaP nanoparticles (agglomerated).

In Figure 4.8, light and fluorescent microscopy images of HeLa cells which were treated with FITC-BSA-functionalized nanoparticles and dissolved FITC-BSA are depicted. The uptake of BSA was detected only in cells that were treated with functionalized nanoparticles; this was recognized by green fluorescence in the cell. Dissolved FITC-BSA molecules were not able to penetrate the cell membrane.

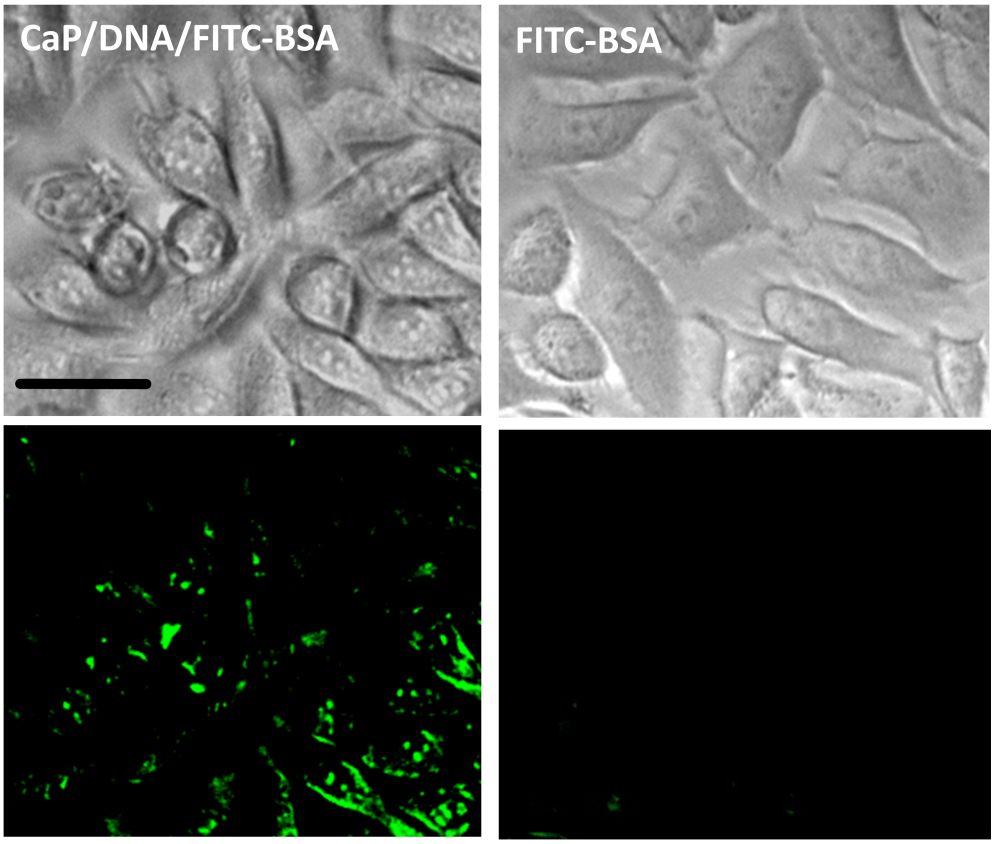

Figure 4.8 Representative light (top) and fluorescence microscopy (bottom) images of HeLa cells, incubated with CaP/DNA/FITC-BSA-loaded nanoparticles (sample 4) and with dissolved FITC-BSA (sample 4C). Scale bar 10 µm.

In order to prove that the fluorescent molecules are located inside the cells confocal laser scanning microscopy (CLSM) was performed. For this purpose, the cells were incubated with the nanoparticles and the corresponding controls, stained with DAPI and imaged by CLSM (Figure 4.9). The nanoparticles are necessary to transport the molecules over the cell membrane barrier, as can be judged by the presence of fluorescence in the image near the nucleus. Only minor amounts of CpG (samples 1 and 2) and PEI (sample 6) were internalized in a dissolved form. The charge of the nanoparticles did not influence the uptake as well as the charge of the dissolved molecules alone. It was assured in all cases by three-dimensional slicing that the fluorescent molecules were present inside the cells and not on their surface (the fluorescence from the molecules was found at

the same Z-level as the nucleus).

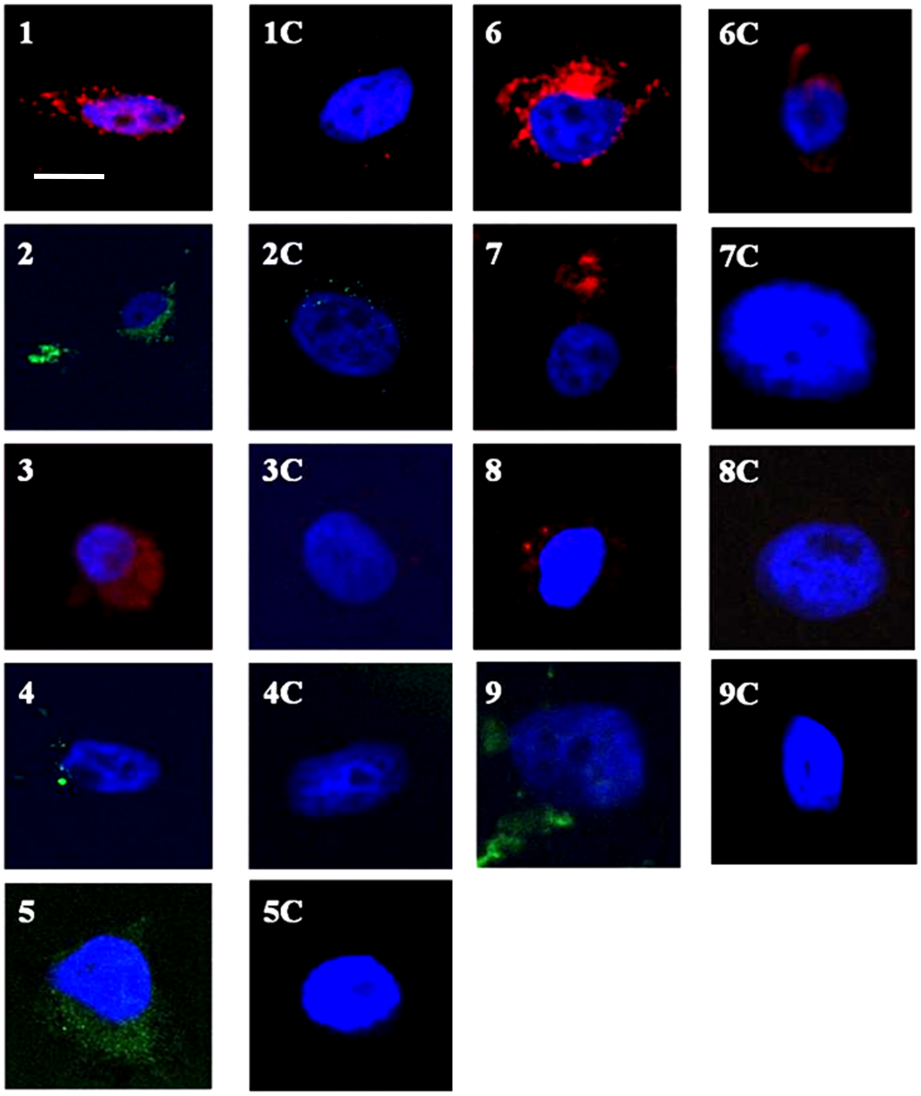

Figure 4.9 Confocal laser scanning microscopy images of cells treated with nanoparticles carrying CaP/CpG-Alexa555 (1, red), CaP/CpG-Alexa488 (2, green), CaP/DNA/TRITC-BSA (3, red), CaP/DNA/FITC-BSA (4, green), CaP/CpG/DEC205-FITC (5, green), CaP/PEI-rhodamine (6, red), CaP/PEI/*p*THPP (7, red), CaP/PSS/*p*THPP (8, red) or CaP/PEI/FITC-Pep (9, green). The corresponding controls were the dissolved fluorescent molecules at the same concentration as in the nanoparticles: CpG-Alexa555 (1C), CpG-Alexa488 (2C), TRITC-BSA (3C), FITC-BSA (4C), DEC205-FITC (5C), PEI-rhodamine (6C), *p*THPP (7C), *p*THPP (8C), and FITC-Pep (9C). Scale bar 5 μm.

Moreover, we were interested in the kinetics of the internalization process. For this purpose, we carried out a separate experiment where the cells were incubated with CaP/CpG-Alexa555 nanoparticles for different periods of time, as shown in Figure 4.10. After 15 min, the adsorbed nanoparticles were seen on the cell membrane, after 60 min the nanoparticles started to be internalized, after 180 min the nanoparticles were clearly visible inside the cell, and after 300 min the number of the nanoparticles inside the cell increased, and they could be observed all over the cytoplasm. From this, we can conclude that 3-5 h of incubation are needed for the nanoparticles to be taken up by the cells.

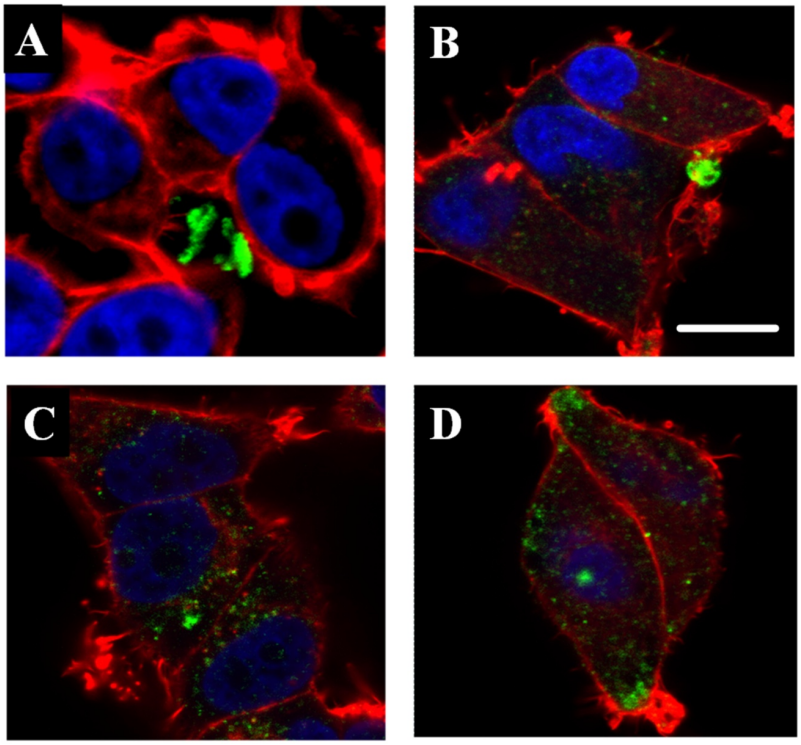

Figure 4.10 Confocal laser scanning microscopy images of HeLa cells after incubation with CpG-Alexa555-loaded nanoparticles for 15 min (**A**), 60 min (**B**), 180 min (**C**), and 300 min (**D**). Note that the color of the nanoparticles was changed from red to green by the CLSM software. The blue color represents cell nucleus (DAPI), red: actin cytoskeleton. Scale bar 10 µm.

The general uptake mechanism schematically is illustrated in Figure 4.11. After adsorption on the cell membrane, the nanoparticles are internalized by endocytosis

or pinocytosis, depending on the cell type and the nanoparticle type, degraded in the lysosome, and finally released into the cytoplasm by endosomal rupture.

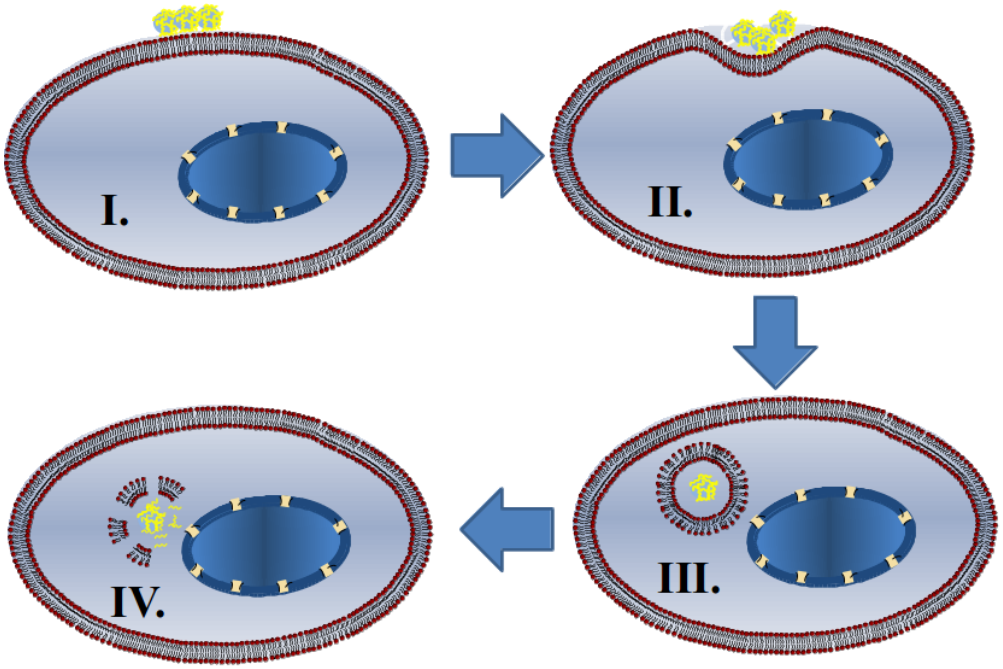

Figure 4.11 Schematic model of the nanoparticles internalization stages. The following steps can be distinguished: **I**. Adsorption of nanoparticles on the cell membrane; **II**. Cell membrane invagination; **III**. Endosome formation; **IV**. Degradation of the endosome and release of the nanoparticles and molecules into the cytoplasm.

It is noteworthy that the biomolecules that were adsorbed onto the nanoparticles surface or into a polyelectrolyte layer on the nanoparticles surface may be susceptible to enzymatic attack, e.g. by nucleases in the case of nucleic acids. This unwanted effect can be prevented by preparing multi-shell calcium phosphate nanoparticles where the biomolecules are incorporated into the nanoparticles and covered by a second shell of calcium phosphate as demonstrated in [64].

4.1.2.3 Conclusions

In this study, we demonstrated the essential role of calcium phosphate nanoparticles for the transport of various molecules of interest across the cell mem-

brane. It was clearly shown that the majority of the bio- and synthetic molecules used in these experiments could not cross the cell membrane alone. Therefore, the calcium phosphate nanoparticles can serve as an efficient carrier to deliver these cargos into cells. However, it is worth noticing that a specific synthesis method needs to be developed and optimized separately for each system and cargo molecule. In the most favorable case, nanoparticles can be functionalized directly with the cargo molecule, e.g. a nucleic acid or a polyelectrolyte, which can serve at the same time as steric and electrostatic stabilizer. In other cases, molecules that would be transported must be incorporated into a stabilizing layer covering the nanoparticles. This layer can consist of non-encoding nucleic acid or a polyelectrolyte polymer like PEI or CMC. Such stable and at the same time biodegradable nanoparticles are easily taken up by cells where they can exert their therapeutic function. Further studies are needed, however, to address in detail the mechanisms of uptake, degradation of nanoparticles and their influence on the metabolic activity of the living cell.

4.1.3 Transport of synthetic molecules across the cell membrane with calcium phosphate nanoparticles

4.1.3.1 Characterization of functionalized calcium phosphate nanoparticles

For these experiments, three different synthetic molecules were used: a polyanionic lysozyme-inhibiting copolymer (A), calixarene dimers (B), and molecular tweezers (C). For a more detailed description of the molecules, their structural formulas and properties refer to Subsection 3.3. As all these molecules are water-soluble, the synthesis of single-shell nanoparticles and their functionalization and purification were performed as described in Subsection 3.1.1 and 3.1.3.

As polyanionic copolymer and calixarene dimers are negatively and positively charged molecules, respectively, no additional polyelectrolyte was necessary for

the attachment to nanoparticles. In case of the third molecule, the polyelectrolyte polymer PEI was added first to stabilize the nanoparticles, and subsequently molecular tweezers were added to the outer shell, because the weak negative charge of the tweezers was not sufficient to stabilize the nanoparticles by themselves. This did not, however, lead to charge reversal, and the nanoparticles were still cationic (see Table 4.7). Additionally, all these molecules were visible in the ultraviolet range, due to their structure (see description in Subsection 3.3) which enabled their quantification by UV-Vis spectroscopy. For fluorescence microscopy the nanoparticles, carrying molecular tweezers were functionalized with FITC-labeled PEI, in order to visualize the nanoparticles' uptake by the cells.

The purified nanoparticles were first characterized by DLS and NTA to prove their stability and monodispersity. As it can be seen from Table 4.7 all samples had good monodispersity index ($<$0.4) and a hydrodynamic diameter in the range of 140-200 nm. Relatively high positive and negative charges, depending on the molecule used in the synthesis also proves the electrostatic stability of the nanoparticles. According to the obtained scanning electron micrographs of the samples (Figure 4.12), all functionalized single-shell nanoparticles had a typical spherical shape and an actual size about 50-60 nm.

Table 4.7 Colloid-chemical data of functionalized and purified calcium phosphate nanoparticles. PDI: Polydispersity index from dynamic light scattering.

Sample	**PDI**	**Particle size (DLS) / nm**	**Particle size (NTA) / nm**	**Zeta-potential / mV**
CaP/polymer	0.380	377	156 $\pm$ 57	-17 $\pm$ 8
CaP/calixarene dimer	0.331	169	212 $\pm$ 63	+22 $\pm$ 2
CaP/PEI/tweezers	0.315	140	150 $\pm$ 58	+44 $\pm$ 6

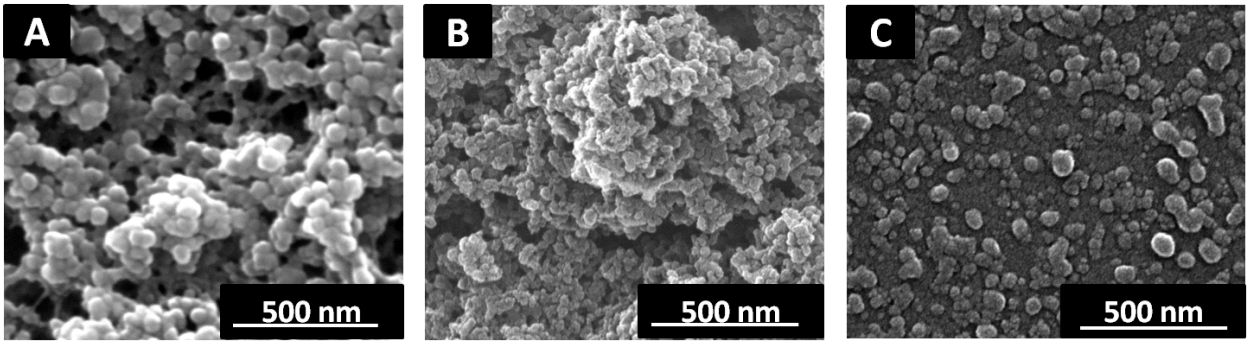

Figure 4.12 Scanning electron micrographs of calcium phosphate nanoparticles, functionalized with polymer (A), calixarene dimer (B), and molecular tweezers (C).

After the purification step, all non-adsorb synthetic molecules could be easily detected in the supernatant by UV-Vis spectroscopy, using the calibration curve for each molecule (Figure 4.13).

In Table 4.8, the amount of the adsorbed molecules on the nanoparticles is shown. It ranges between 22% and 51% of the initially present amount of synthetic molecules.

Table 4.8 The amount of synthetic molecules in the nanoparticle dispersion.

Sample	Theoretical concentration / $\mu g\ mL^{-1}$	C (molecules) after purification / $\mu g\ mL^{-1}$	Present on the nanoparticles after purification / %
CaP/polymer	167	37	22
CaP/calixarene dimer	167	86	51
CaP/PEI/tweezers	143	78	46

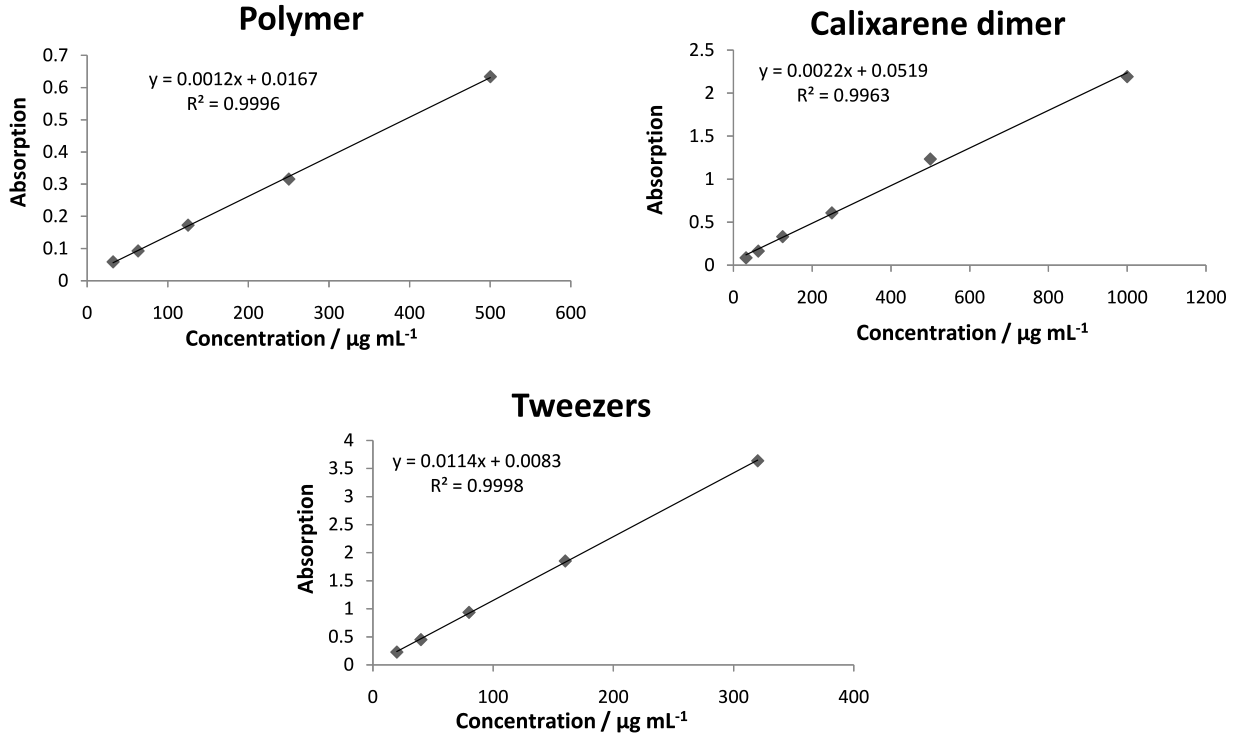

Figure 4.13 Calibration curves for the lysozyme-inhibiting polymer, the calixarene dimer and the molecular tweezers. The fluorescence of all samples was measured by UV-Vis spectroscopy. Absorption was determined at the corresponding absorption maxima: polymer at λ=320 nm; calixarene dimer at λ=495 nm; tweezers at λ=280 nm.

After the colloid-chemical characterization of the nanoparticles, the biological experiments were performed.

4.1.3.2 Results of uptake studies

In all performed *in vitro* experiments, the HeLa cell line was used. First, we checked whether these compounds are toxic for the cells. HeLa cells were incubated with functionalized nanoparticles and dissolved molecules alone (in the same concentration as in the nanoparticle dispersion) as a control group for 3 h. Afterwards, the cell viability was determined by an MTT assay (see Subsection 3.4.5). The results of this experiment are shown in Figure 4.14. No toxic effect was observed either in the nanoparticle samples or in the control samples

with dissolved molecules. The viability level was in the range between 100% and 85%. Only for the nanoparticles which carried the calixarene dimer a mild toxicity (20%) was found, which is in a good agreement with the purpose of this molecule to kill tumor cells. In this case, no therapeutic effect was needed, and we chose the low concentration of this compound only to check its uptake by the living cells.

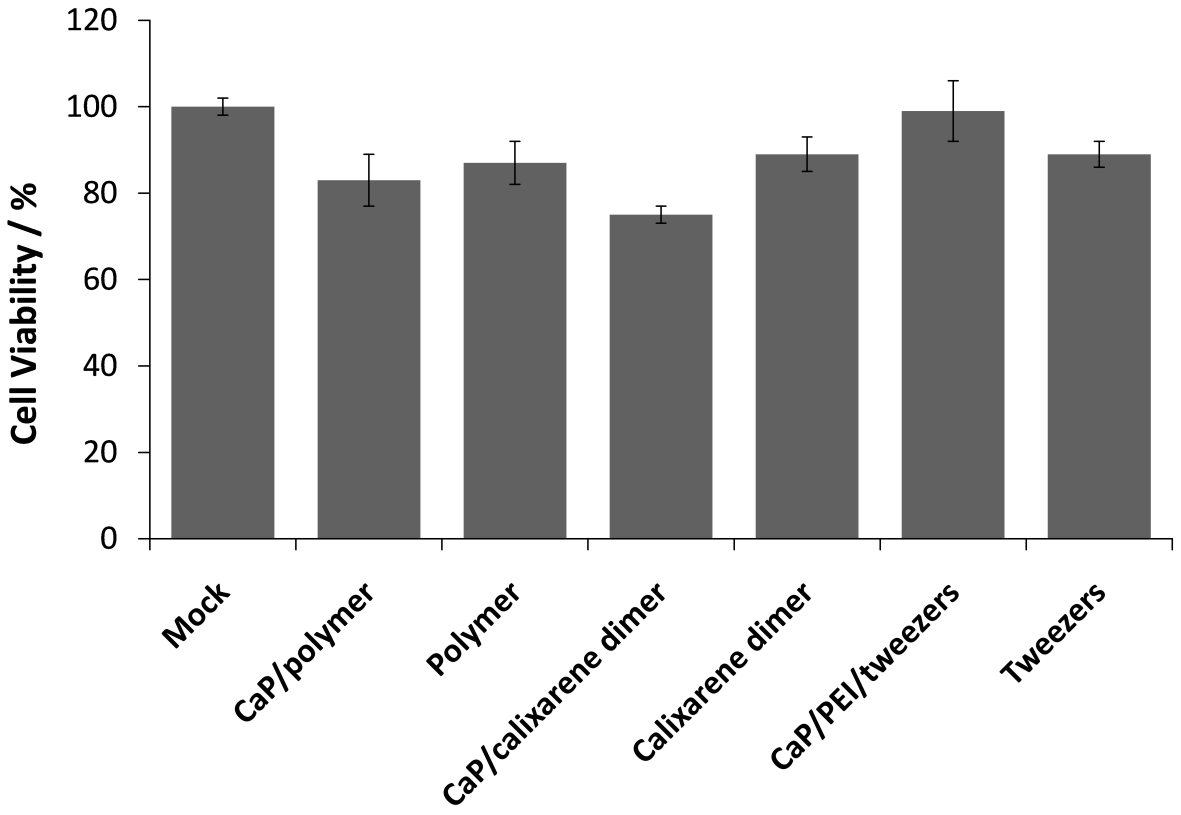

Figure 4.14 MTT assay after incubation of HeLa cells with functionalized calcium phosphate nanoparticles.

Along with the MTT assay, uptake studies of these samples were carried out. In Figure 4.15, one can see representative light and fluorescence microscopy micrographs of the samples. HeLa cells were incubated either with the molecules in dissolved form or absorbed on the calcium phosphate nanoparticles. The qualitative difference in the uptake efficiency of the fluorescent synthetic molecules between these two groups can be clearly recognized. We conclude that calcium

phosphate nanoparticles are necessary to transport these molecules across the cell membrane.

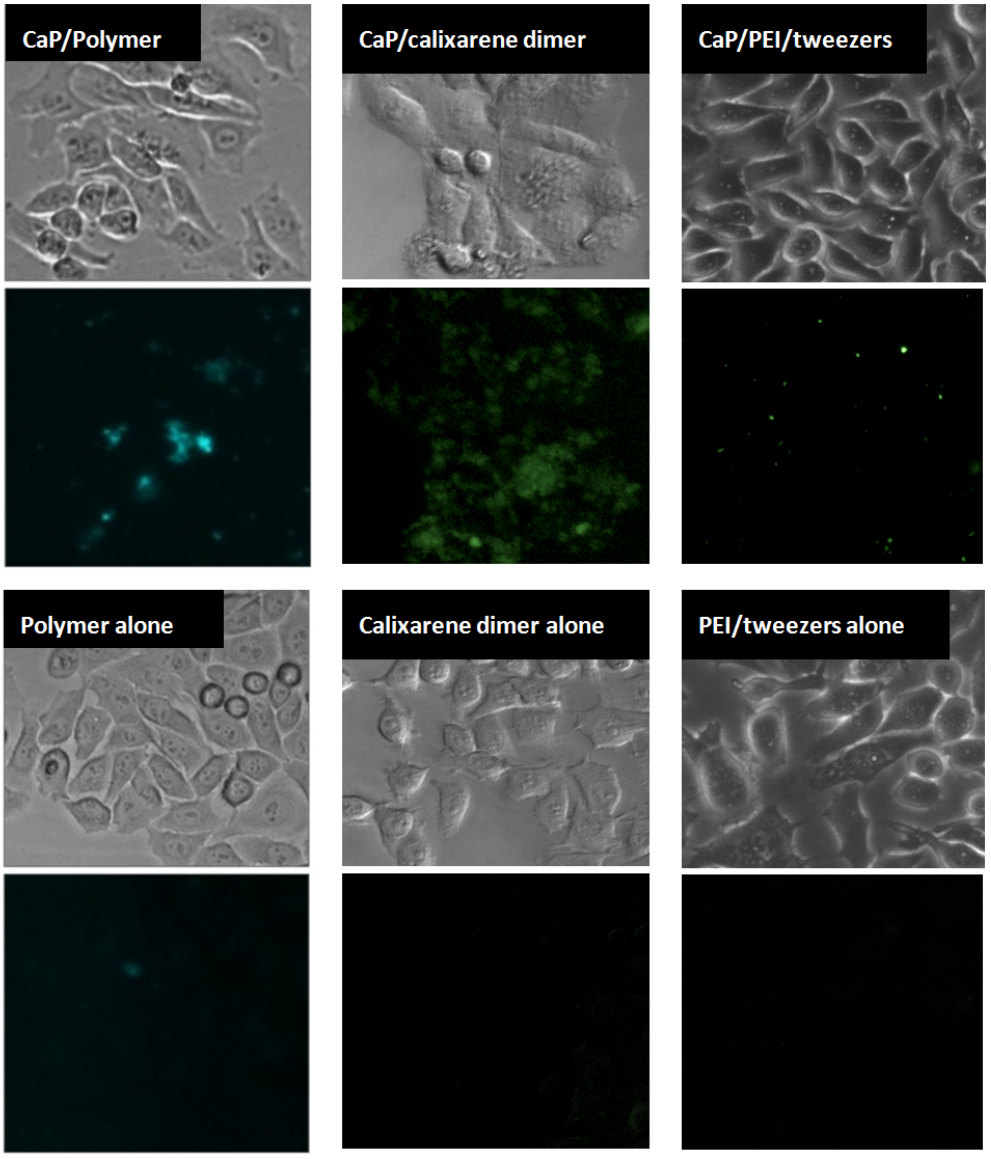

Figure 4.15 Representative light microscopy (top row) and fluorescence microscopy (bottom row) images of HeLa cells after 3 h incubation with functionalized calcium phosphate nanoparticles and with the dissolved drug molecules (equal concentrations). The fluorescence is visualized due to the polymer, the calixarene dimer, and the FITC-labeled PEI (in the case of molecular tweezers), respectively.

Using conventional fluorescence microscopy, it is often difficult to show whether

the nanoparticles are only attached to the cell membrane or already taken up inside the cytoplasm. Therefore, we have analyzed the cells by confocal laser scanning microscopy (CLSM) after staining the nucleus and the cell membrane with DAPI and Cell Mask^{TM} dyes, respectively. Figure 4.16 shows the confocal laser scanning micrographs of HeLa cells treated with functionalized CaP nanoparticles or with the corresponding controls (the same concentration of the molecules as in the nanoparticles). In all three cases, we saw the absence of fluorescence in the control group, which means that no synthetic molecules could penetrate the cell membrane in the dissolved form. In contrast, polyanionic polymer, hexacationic calixarene dimer and molecular tweezers combined with CaP nanoparticles were easily detectable within the cells. We also carried out three-dimensional slicing of the cells to prove the presence of the functionalized nanoparticles inside the cells (data not shown).

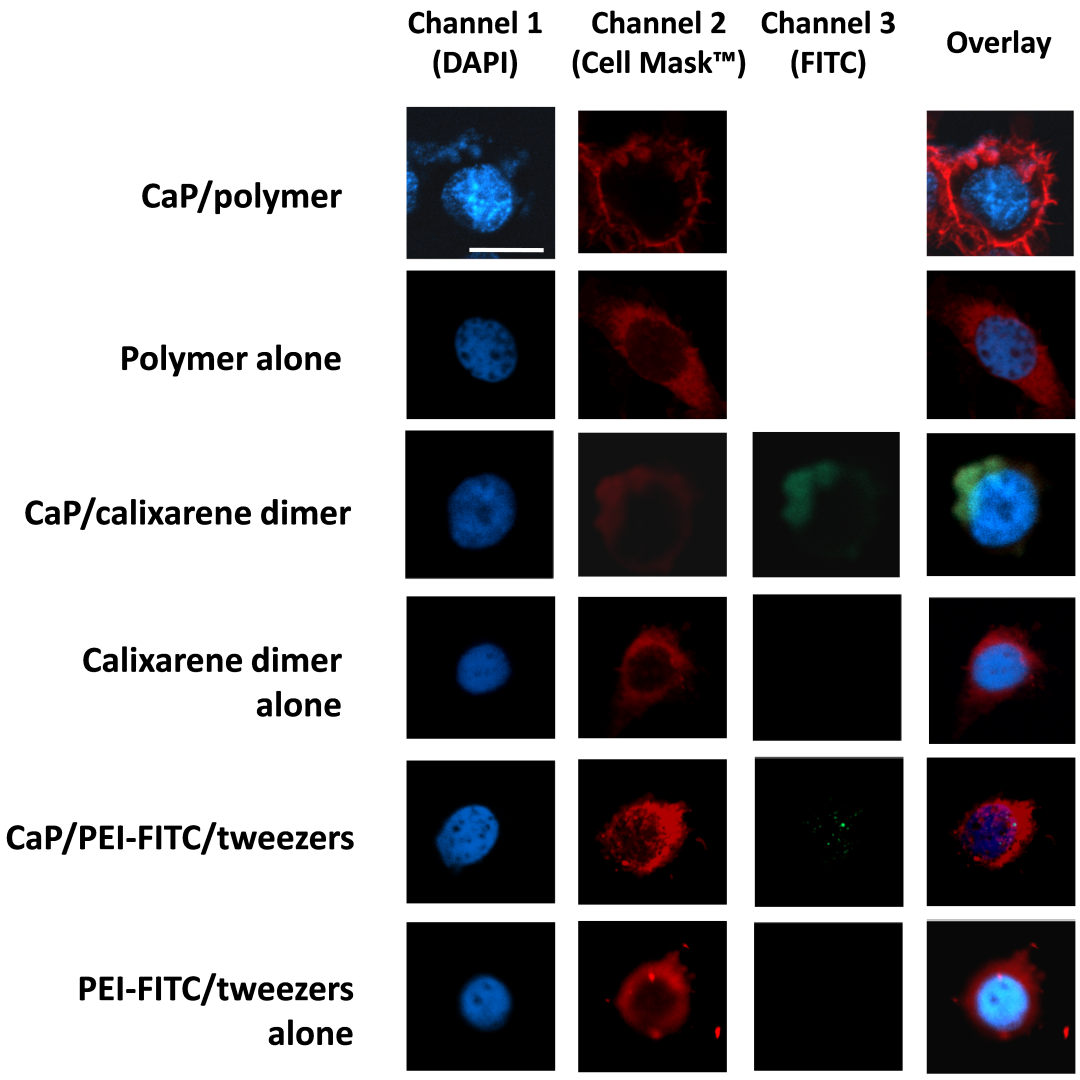

Figure 4.16 Confocal laser scanning microscopy micrographs of HeLa cells after incubation with calcium phosphate nanoparticles functionalized with polymer, calixarene dimer, PEI-FITC/tweezers, and the corresponding controls. Channel 1 (DAPI): cell nucleus; channel 2 (TRITC): cell membrane stained with the Cell Mask^{TM}; channel 3 (FITC): calixarene dimer and PEI-FITC/tweezers. The polymer appears on the picture as blue dots. Scale bar 5 µm.

4.1.3.3 Conclusions

We have prepared purified calcium phosphate nanoparticles, functionalized with a synthetic polymer, a calixarene dimer and molecular tweezers. The nanopar-

ticles were characterized and showed a stable and monodisperse character. The actual concentration of all three molecules after the purification was determined. The *in vitro* studies showed that the compounds are not harmful to the cells (only calixarene dimer can be toxic in a higher dose) and they could be transported into the cell with the help of calcium phosphate nanoparticles, whereas the dissolved molecules alone were not able to penetrate the cell membrane. Therefore, these purified functionalized calcium phosphate nanoparticles represent a well-characterized delivery system for further *in vitro* and *in vivo* application.

4.1.4 Transport of synthetic lysozyme-inhibiting polymer across the cell membrane with calcium phosphate nanoparticles

4.1.4.1 Characterization of functionalized calcium phosphate nanoparticles

The nanoparticles were synthesized as described earlier in Subsection 3.1.1, where they were functionalized first with PEI and then with the lysozyme-inhibiting polymer (in the following denoted as "polymer") or *vice versa*. Afterwards, both types of the nanoparticles were purified by centrifugation and redispersed in ultrapure water by ultrasonication. The characterization of the nanoparticles was performed by DLS, NTA and SEM methods, and the quantification of the polymer was done by UV-Vis spectroscopy.

In Figure 4.17, one can see the scanning electron microscopy micrographs of the synthesized nanoparticles. The nanoparticles had an approximate size of 50 nm and a spherical morphology. The DLS and NTA measurements summarized in Table 4.9, show that both types of the nanoparticles were stable, and no aggregation occurred during the synthesis and purification steps. The positive surface charge of the nanoparticles, loaded first with PEI and then with polymer, was slightly lower compared to the second type, which could be explained by

the negative charge of the polymer, which could partially neutralize the positive charge of PEI.

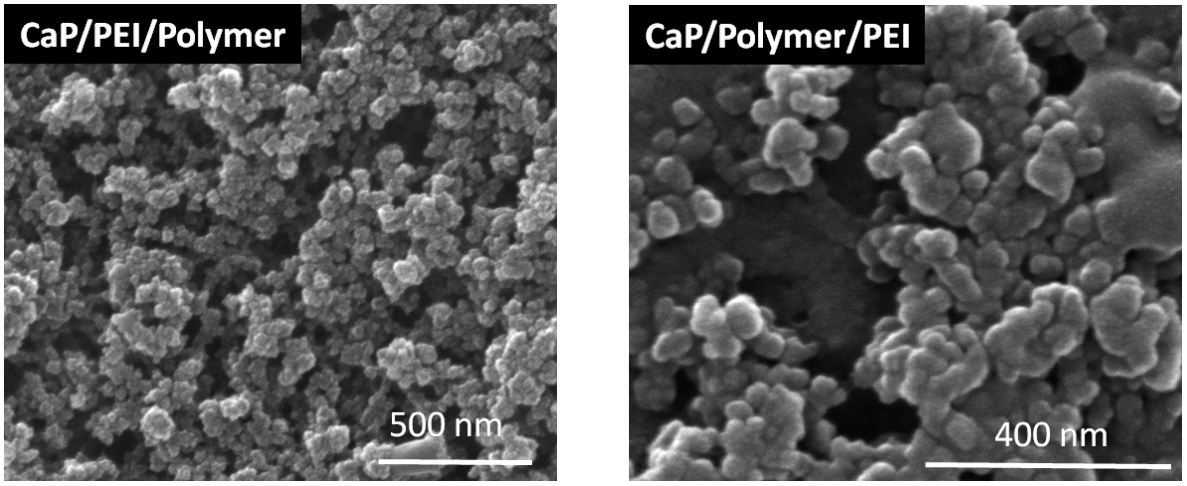

Figure 4.17 SEM images of the polymer-functionalized calcium phosphate nanoparticles.

Table 4.9 Colloid-chemical characterization of PEI- and polymer-functionalized calcium phosphate nanoparticles. PDI: polydispersity index from dynamic light scattering.

Sample	PDI	Particle size (DLS) / nm	Particle size (NTA) / nm	Zeta potential / mV
CaP/PEI/polymer	0.368	449	169 ± 63	+18
CaP/polymer/PEI	0.379	409	197 ± 77	+37

The quantification of the polymer was performed by the fluorescent labeling with a dansyl group (absorption maximum at λ=245 nm). After the centrifugation of the nanoparticle dispersions, the supernatant was taken to determine the amount of the polymer, which was then used to calculate a calibration curve (Figure 4.13). The concentration of the polymer on the nanoparticles as well as the loading efficiency for both types of the nanoparticle dispersion were calculated (Table 4.10).

Table 4.10 Results of UV-Vis spectroscopy measurements of PEI- and polymer-functionalized calcium phosphate nanoparticles.

Sample	*C* (polymer) before purification /μg mL^{-1}	Supernatant		Dispersion of nanoparticles	
		Absorption	*C* (polymer) / μg mL^{-1}	*C* (polymer) / μg mL^{-1}	Quantity/ %
CaP/PEI/polymer	500	1.936	183	317	63
CaP/polymer/PEI	250	2.337	223	27	11

As one can see, the amount of the polymer was much higher when the calcium phosphate nanoparticles were functionalized first with PEI: 63% of the polymer molecules were absorbed onto the surface of the nanoparticles.

The quantification data are shown in Table 4.11, i.e. the amount of polymer per nanoparticle and per cell.

Table 4.11 Determination of the amount of polymer and calcium phosphate nanoparticles in the dispersion and in culture medium per cell (for $5{\cdot}10^4$ cells).

Sample	Diameter (NP) from SEM / nm	*N* (NP) per m^{-3}	*N* (polymer molecules) per NP	*N* (NP) per cell	*N* (polymer molecules) per cell
CaP/PEI/polymer	49	$7.442{\cdot}10^{16}$	14	$1.353{\cdot}10^5$	$1.912{\cdot}10^6$
CaP/polymer/PEI	52	$3.493{\cdot}10^{16}$	3	$6.351{\cdot}10^4$	$1.629{\cdot}10^5$

4.1.4.2 Results of the uptake studies and viability assay

The next step was to measure the uptake of these functionalized nanoparticles and their cytotoxicity. In Figure 4.18, representative light and fluorescent micrographs of HeLa cells, incubated with the nanoparticles for 3 h, are depicted. It is clearly seen that the CaP/PEI/polymer nanoparticles were better taken up by the cells, and that the polymer which can be recognized by the cyan fluorescence could be detected. Furthermore, in Figure 4.19, at 100x magnification on THP-1

cells incubated with functionalized nanoparticles and polymer alone at the same concentration, we showed that the polymer alone did not penetrate the cell membrane. In contrast, adsorbed on the nanoparticles, the polymer was detectable inside the lysozyme-producing THP-1 cell line.

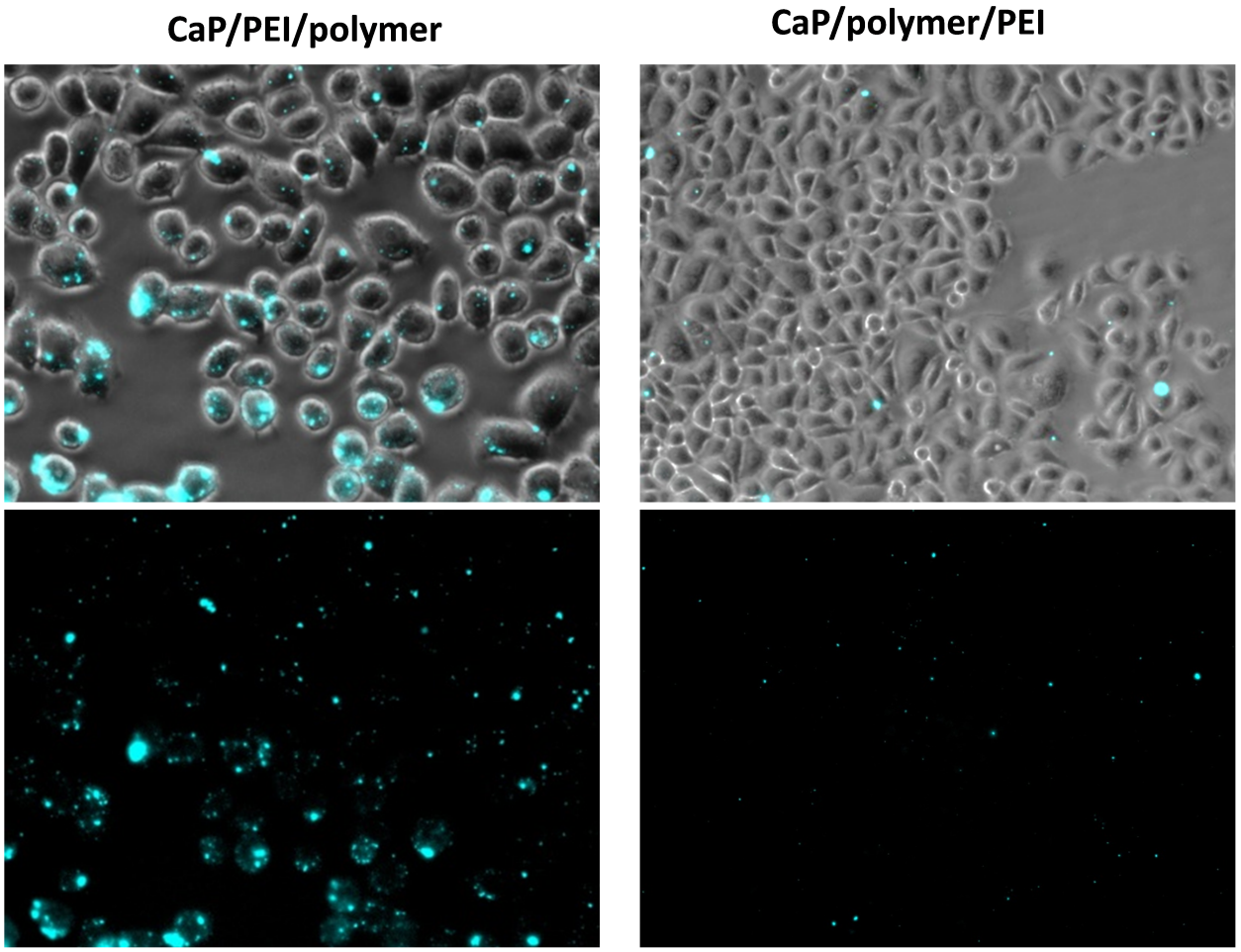

Figure 4.18 Light and fluorescence microscopy micrographs of THP-1 cells incubated with polymer-loaded CaP/PEI nanoparticles. Top row: overlay; bottom row: fluorescence images; Cyan fluorescence represents polymer; 40x magnification.

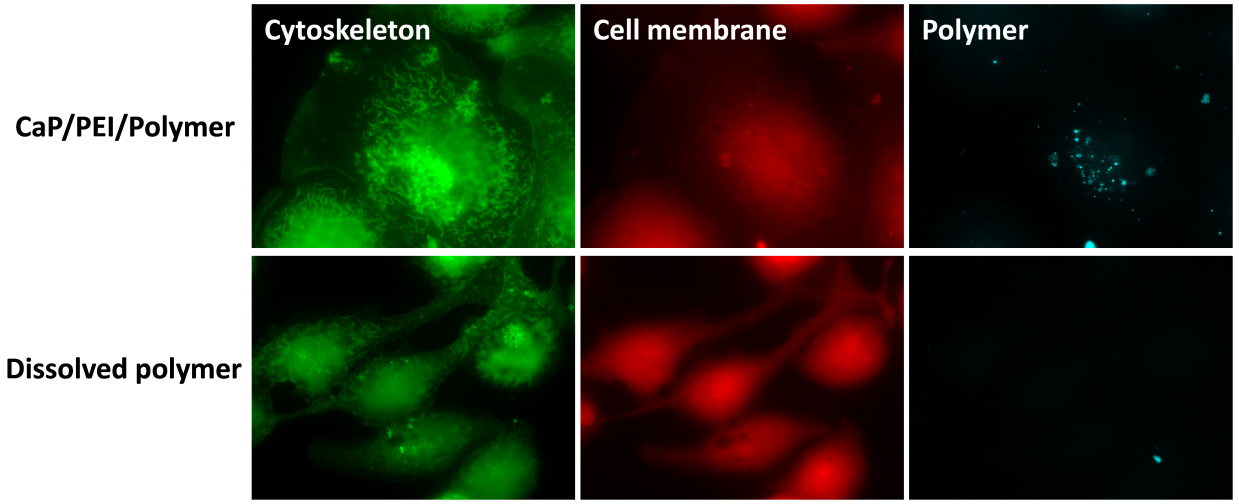

Figure 4.19 Uptake of the polymer, loaded on the CaP/PEI nanoparticles and the polymer alone on fixed THP-1 cells. Green channel: actin filaments; red channel: cell membrane; blue channel: polymer; 100x magnification.

It was also important to check the viability of the cells after the incubation with polymer-functionalized nanoparticles. As can be seen from Figure 4.20, no toxic effect was detected for both types of nanoparticles, and the viability rate of HeLa cells remained over 91%. The control group, where the cells were treated with PEI/polymer aggregates, showed a low viability level due to the toxic effect of the PEI.

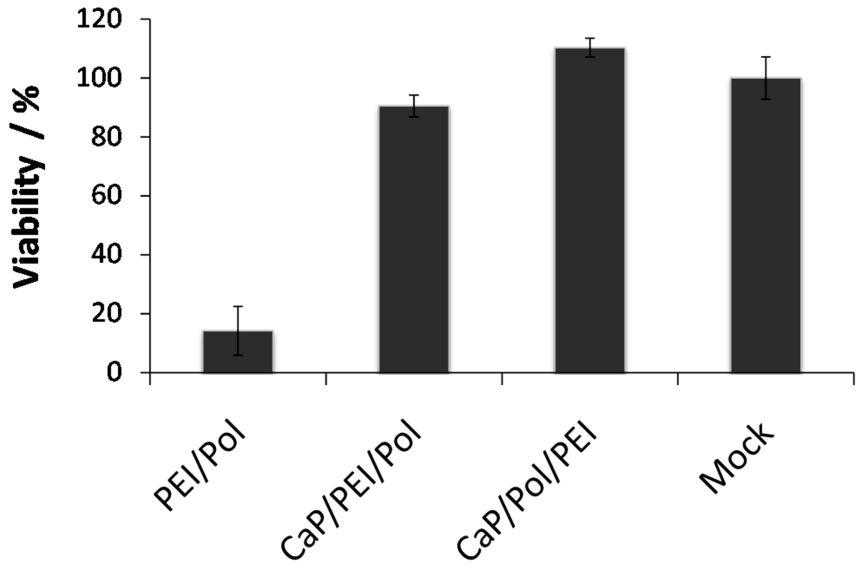

Figure 4.20 Results of viability assay on THP-1 cells, treated with functionalized calcium phosphate nanoparticles and PEI/polymer polyplexes.

4.1.4.3 Studies on lysozyme activity inhibition

Our aim was then to check the inhibitory activity of the polymer inside the cells as well as in cell medium. For these purposes, we chose the THP-1 cell line (monocytes/macrophages) which is known to produce lysozyme and is a good and well-defined model to study lysozyme activity. Before the cells were taken into the experiment, they were differentiated by the addition of PMA (phorbol-12-myristate-13-acetate) for 3 days. After this differentiation, the cells became adherent macrophages and did not divide anymore. These PMA-induced cells were used in all experiments for lysozyme-inhibiting studies. For the incubation and differentiation protocol, refer to Subsection 3.5.2.

In Figure 4.21 A, the results of lysozyme activity measurements inside the cells after the incubation with polymer-functionalized nanoparticles are presented. As control groups, the cells were treated either only with the polymer or with calcium phosphate nanoparticles functionalized with PEI (sample CaP). Mock represents

untreated cells. The CaP/PEI/polymer-treated cell samples the lysozyme activity was decreased compared to untreated cells (Mock). This is also in good agreement with UV-Vis spectroscopy measurements and the uptake studies for this type of nanoparticles. In addition, the sample CaP/polymer/PEI was not so efficient as well as the polymer itself. What also needs to be noticed here is the big standard deviation in the control group of CaP/PEI nanoparticles.

When we compared the results of the lysozyme inhibition in the cell medium, we also got a similar picture (Fig 4.21 B). The CaP/PEI/polymer had the best inhibiting action on lysozyme outside the cell, and the free polymer had no effect on the lysozyme activity in the cell medium. Nevertheless, the big standard deviations in two control groups (untreated cells and the CaP/PEI-treated cells) were disappointing. In order to improve the outcome of these experiments, some further ideas were pursued:

1. The cells were stimulated with lipopolysaccharides (LPS, 5 mg mL^{-1}) for 1 h, 3 h and 24 h before the experiment to enhance the higher production of lysozyme.
2. The incubating time with nanoparticles were increased to 24 h.
3. The nanoparticles were incubated in serum-free medium for 3-7 h.
4. The number of independent experiments for each sample was doubled.
5. The cell lysate was treated with a protease-inhibitor cocktail to prevent possible lysozyme degradation during the preparation phase.
6. The incubation time for the EnzCheck reagent was prolonged for 1 to 2 h.

All these activities, however, did not have much impact on the results and the outcome of the measured data set. Again, no statistically significant effect of the polymer on the lysozyme activity was found.

It was shown earlier that the polymer itself could inhibit the lysozyme in a dose-dependent manner in the phosphate buffer solution containing the lysozyme in the specific concentration. For this reaction the half maximal inhibitory concentration (IC_{50}=0.7 μM) was determined by the group of Prof. Thomas Schrader [292].

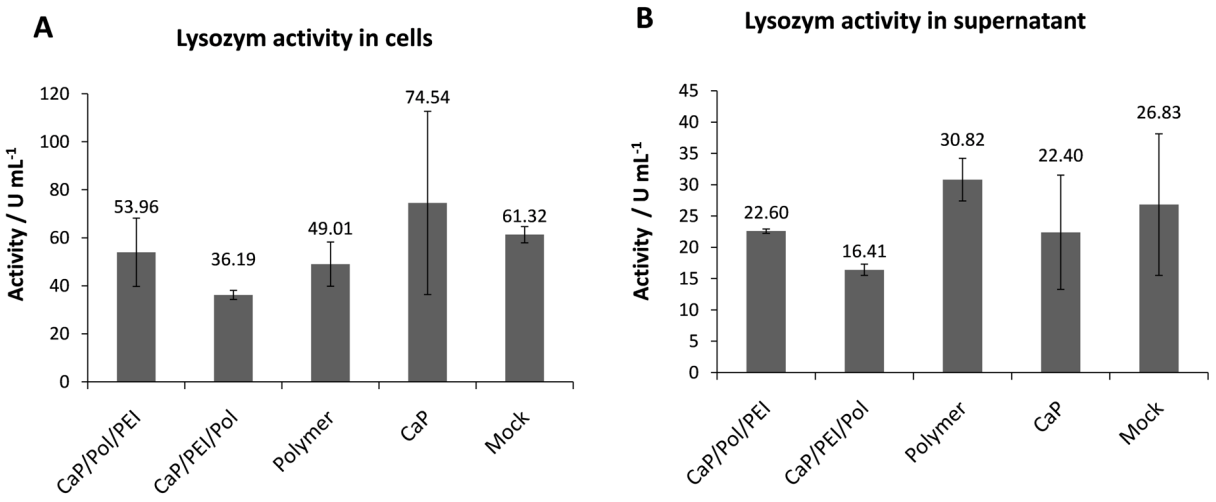

Figure 4.21 Measurements of the lysozyme activity inside THP-1 cells **(A)** and in cell medium **(B)** after incubation with polymer-functionalized calcium phosphate nanoparticles and polymer alone.

Therefore, our idea was to look if the polymer itself was still stable and active in the cell culture medium, as it was never analyzed before. For this, we took the standard lysozyme solution from the EnzCheck kit, polymer solution, and different milieus: phosphate buffer from the EnzCheck kit, serum-free cell culture medium (RPMI-1640), and cell culture medium containing 10% FCS. The same amount of lysozyme from a standard solution was added to all samples, resulting in the concentration of 0.2 mg mL^{-1}. The amount of added polymer solution (concentration 1 mg mL^{-1}) varied from 0 to 3.3 nM. Then the samples were incubated for 5 min in a 24-well plate in the cell culture incubator at 37 °C and 5% humidity to simulate the cell culture experiment conditions. Afterwards, all samples were treated simultaneously according to the EnzChek manufacture protocol (see Subsection 3.4.6).

The results of this set of experiment are shown in Figure 4.22. Graph A presents the results of the experiment carried out in phosphate buffer. A clear decrease in the lysozyme activity with increasing polymer concentration in dose-dependent manner can be seen. At the concentration of the polymer of 3.3 nM, the lysozyme activity was decreased by more than 50%, which proves the inhibiting ability of

the polymer against the lysozyme. That is also in line with former studies, carried out in the group of Prof. Thomas Schrader. Nevertheless, when we look at the Graph B, where the reaction milieu was RPMI-1640 (without FCS), the polymer was not capable to inhibit the lysozyme activity as efficiently as it was shown in the phosphate buffer. There was no further concentration-dependent drop in the lysozyme activity. It stayed at the level of 100% at the concentration of the polymer in the sample up to 2.2 nM. Only at the highest concentration of 3.3 nM of polymer, an inhibition by 40% was detected. Moreover, when we look at the results with cell culture medium containing 10% FCS, an inhibiting effect of the polymer even at the highest concentration was not detectable anymore.

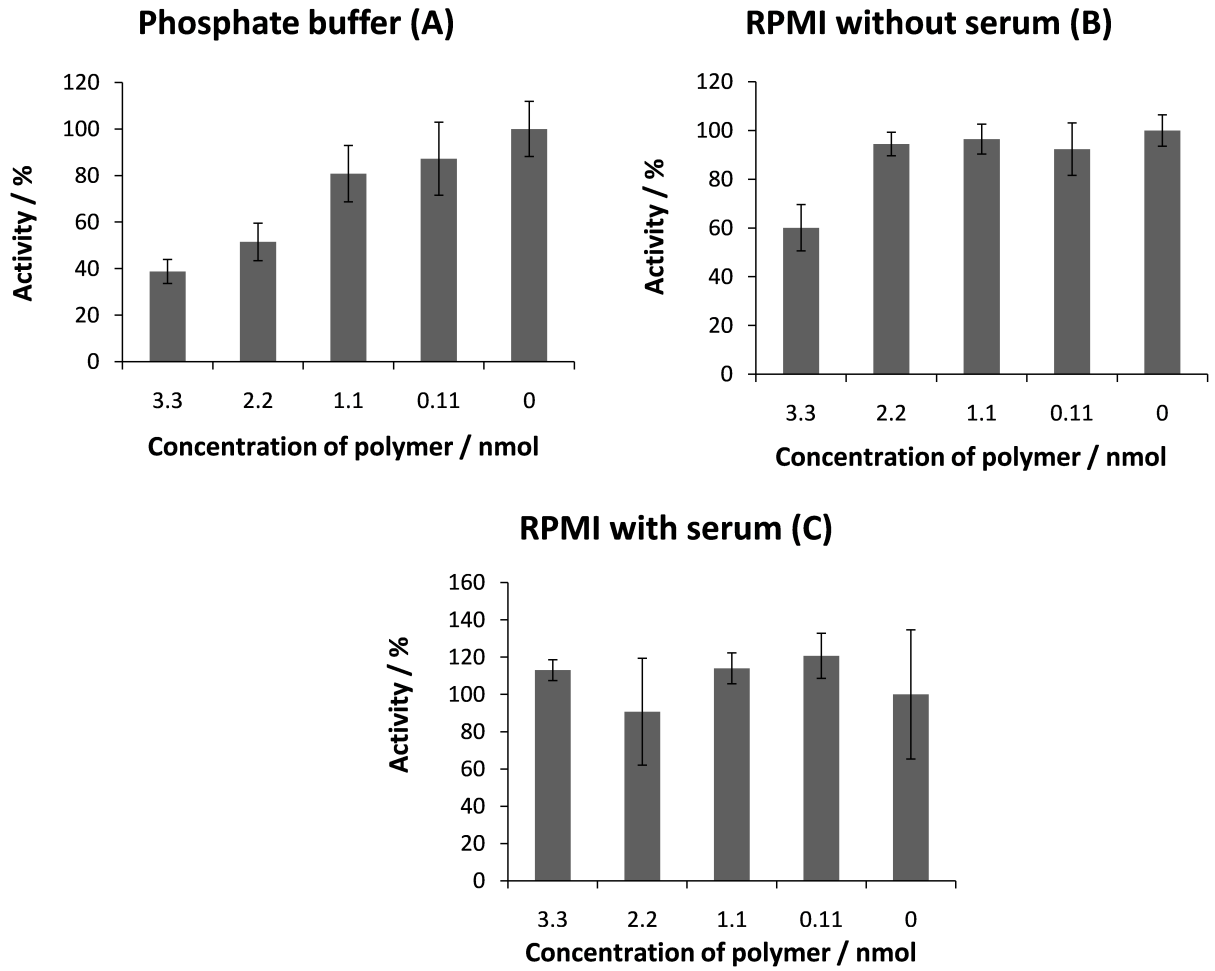

Figure 4.22 Measurements of lysozyme activity after incubation with polymer in different milieus: **(A)**: in phosphate buffer; **(B)**: in RPMI-1640 without FCS; **(C)**: in RPMI-1640 with 10% FCS.

These results can be explained only by the influence of the reaction milieu. When there are only the molecules of the target protein and only free polymer, there is very efficient inhibition. However, once the polymer appears in a complex biological medium such as cell culture medium even without FCS, its specificity drops dramatically and, in the presence of FCS, it is completely absent. This effect can be explained by the variety of the biological molecules other than lysozyme present in the cell medium such as free amino acids, vitamins, etc. (see Table 4.12), which can easily interfere with the polymer and, thus, block

its function. When we take the FCS into account, which contains a variety of different proteins, factors, and other components (Table 4.13), it becomes clear that the polymer cannot keep selectivity to just one protein among thousands of chemically similar molecules. Even if we consider that the experiment with the cells could be carried out in serum-free media, the polymer, taken up by the cell and eventually released in the cytoplasm, still would have to deal with a number of different biomolecules that are presented in the cytoplasm.

Table 4.12 RPMI-1640 medium content [309].

RPMI-1640 medium composition			
Medium Component	**g L^{-1}**	**Medium Component**	**g L^{-1}**
Calcium Nitrate · $4H_2O$	0.1	L-Proline	0.02
Magnesium Sulfate (anhydrous)	0.04884	L-Serine	0.03
Potassium Chloride	0.4	L-Threonine	0.02
L-Tryptophan	0.005	L-Valine	0.02
Sodium Chloride	6	D-Biotin	0.0002
Sodium Phosphate Dibasic (anhydrous)	0.8	Choline Chloride	0.003
L-Arginine	0.2	Folic Acid	0.001
L-Asparagine (anhydrous)	0.05	myo-Inositol	0.035
L-Aspartic Acid	0.02	Niacinamide	0.001
L-Cystine · 2HCl	0.0652	p-Aminobenzoic Acid	0.001
L-Glutamic Acid	0.02	D-Pantothenic Acid (hemicalcium)	0.00025
L-Glutamine	0.3	Pyridoxine · HCl	0.001
Glycine	0.01	Riboflavin	0.0002
L-Histidine	0.015	Thiamine · HCl	0.001
Hydroxy-L-Proline	0.02	L-Tyrosine · 2Na · $2H_2O$	0.02883
L-Isoleucine	0.05	Vitamin B12	0.000005
L-Leucine	0.05	D-Glucose	2
L-Lysine · HCl	0.04	Glutathione (reduced)	0.001
L-Methionine	0.015	L-Glutamine	0.3
L-Phenylalanine	0.015	Sodium Bicarbonate	2
		Phenol Red · Na	0.0053

Table 4.13 Composition of FCS [310].

Component	Average	Range
Endotoxins (ng mL^{-1})	0.35	0.01-10.0
Glucose (mg mL^{-1})	1.25	0.85-1.81
Protein (mg mL^{-1})	38	32-70
Albumin (mg mL^{-1})	23	20-36
Hemoglobine (µg mL^{-1})	113	24-181
Bilirubin, total (µg mL^{-1})	4	3-11
Bilirubin, direct (µg mL^{-1})	2	0-5
Urea (µg mL^{-1})	160	140-200
Urate (µg mL^{-1})	29	13-41
Creatinin (µg mL^{-1})	31	16-43
Insulin (µU mL^{-1})	10	6-14
Cortisol (ng mL^{-1})	0.5	0.1-23
Growth hormone (ng mL^{-1})	39.0	18.7-51.6
Parathormone, PTH (ng mL^{-1})	1.72	0.085-6.18
Triiodothyronine, T3 (ng mL^{-1})	1.2	0.56-2.23
Thyroxine, T4 (ng mL^{-1})	0.12	0.08-0.16
Thyroid-stimulating hormone, TSH (ng mL^{-1})	1.22	0.2-4.5
Follicle-stimulating hormone, FSH (pg mL^{-1})	95	20-338
Testosterone (pg mL^{-1})	400	210-990
Progesterone, P4 (pg mL^{-1})	80	3-360
Prolactin=Luteotropic hormone, LTH (pg mL^{-1})	176	20-500
Luteinizing hormone, LH (pg mL^{-1})	8	1.2-18
Prostaglandin E (ng mL^{-1})	5.9	0.5-30.5
Prostaglandin F (ng mL^{-1})	12.3	3.8-42.0
Vitamin A (ng mL^{-1})	90	10-350
Vitamin E (ng mL^{-1})	1.1	1-4.2
Cholesterol (µg mL^{-1})	310	120-630
Lactate-dehydrogenase, LDH (mU mL^{-1})	864	260-1,215
Alkaline Phosphatase (mU mL^{-1})	255	110-352
Aspartate-Aminotransferase, ASAT (mU mL^{-1})	130	20-200
Sodium, Na^+ (µeq mL^{-1})	137	125-143
Potassium, K^+(µeq mL^{-1})	11.2	10.0-14.0
Calcium, Ca^{2+} (µeq mL^{-1})	6.75	6.30-7.15
Chloride, Cl^- (µeq mL^{-1})	103	98-108
Phosphate, Pi (µg mL^{-1})	98	43-114
Selen (µg mL^{-1})	0.026	0.014-0.038

4.1.4.4 Conclusions

Calcium phosphate nanoparticles, functionalized with a lysozyme-inhibiting polymer, were synthesized and characterized by different methods. Their uptake by THP-1 cells was shown by CLSM. Nevertheless, the expected significant inhibitory effect of the polymer inside the living cell, as well as in the cell culture medium was not detected. Consequently, the experiments showed a dramatic influence of the experimental conditions. The inhibitory effect of the polymer was clearly shown in phosphate buffer solution in a dose-dependent way. In the presence of the cell culture medium containing various biological molecules, the inhibition of lysozyme essentially decreased and could be detected at only the highest concentration of polymer. Furthermore, when the cell culture medium was supplemented with 10% of FCS, no inhibitory effect was found. These indicates low specificity of the inhibitory polymer to target lysozyme. The polymer molecules can apparently interact with other biomolecules contained in large quantities in cell culture media.

4.1.5 Uptake of HTRA1 and HTRA2 proteins: alone and with calcium phosphate nanoparticles

4.1.5.1 Characterization of functionalized calcium phosphate nanoparticles

For these studies, single-shell and triple-shell nanoparticles, stabilized either with CMC or PEI and loaded with HTRA1 (with or without PDZ domain) and HTRA2 proteins (see Subsection 3.3.7 and 3.3.8), were used. The synthesis of the protein-functionalized calcium phosphate nanoparticles was carried out as described in Subsection 3.1.1 and purified as described in Subsection 3.1.3. The proteins were synthesized, purified, and labeled with Alexa488 in the group of Prof. Michael Ehrmann, Centre for Medical Biotechnology (ZMB) at the University

of Duisburg-Essen [311]. The concentration of both proteins was 1 mg mL^{-1}. After the synthesis, all nanoparticles were purified with the help of centrifugation and redispergation in ultrapure water. The supernatants were used to perform UV-Vis spectroscopy to determine the protein concentration in the dispersion of nanoparticles.

In Table 4.14, the characterization data of the functionalized nanoparticles are summarized. The single-shell nanoparticles showed a hydrodynamic size between 250 and 350 nm and had a good polydispersity index ($<$0.5). Apparently, the multi-shell samples contained some agglomerates that resulted in bigger size and polydispersity. The zeta potential reflects the corresponding charge of the polyelectrolyte polymer used for stabilization (CMC: negative, PEI: positive) that indicates the colloidal stability of the nanoparticles in dispersion. The concentration of each protein was determined by UV-Vis spectroscopy with a calibration curve (Figure 4.23) and labeling with Alexa488 fluorescent dye.

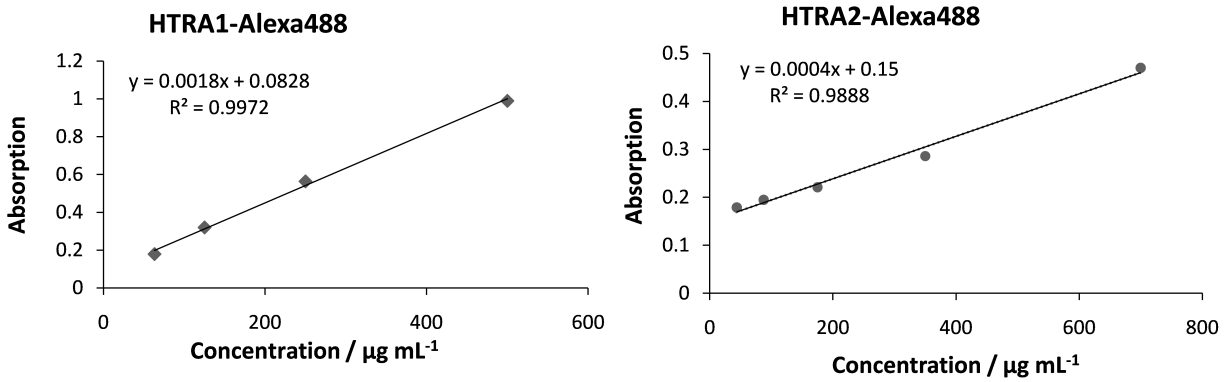

Figure 4.23 Calibration curves of Alexa488-labeled HTRA1 and HTRA2 proteins (λ_{max}=492 nm), obtained by the UV-Vis spectroscopy.

Table 4.14 Characterization of nanoparticles by dynamic light scattering (DLS) and UV-Vis spectroscopy. PDI: polydispersity index from dynamic light scattering.

Sample	Size / nm	PDI	Zeta potential / mV	*C* (protein) after purification / µg mL^{-1}
CaP/CMC/HTRA1	247	0.321	-16	168
CaP/CMC/ΔHTRA1	376	0.439	-11	168
CaP/CMC/HTRA1/PEI	958	0.837	+12	419
CaP/CMC/HTRA1/CaP/PEI	4665	1.0	+17	286
CaP/PEI/HTRA1	292	0.325	+18	410
CaP/CMC/HTRA2	696	0.565	+16	255
CaP/CMC/HTRA2/CaP/CMC	763	0.628	-10	167
CaP/PEI/HTRA2	450	0.369	+17	226
CaP/PEI/HTRA2/CaP/PEI	3514	0.323	+26	138

The quantification data for all types of functionalized nanoparticles are shown in Table 4.15.

Table 4.15 Number of fluorescently labeled HTRA1 and calcium phosphate nanoparticles in dispersion and in culture medium per cell (for $5{\cdot}10^4$ cells).

Sample	Diameter (NP) from SEM / nm	*N* (NP) per m^{-3}	*N* (protein molecules) per NP	*N* (NP) per cell	*N* (protein molecules) per cell
CaP/CMC/HTRA1	77	$4.9{\cdot}10^{16}$	56	$8.9{\cdot}10^4$	$5.0{\cdot}10^6$
CaP/CMC/ΔHTRA1	90	$2.0{\cdot}10^{16}$	197	$3.7{\cdot}10^4$	$7.3{\cdot}10^6$
CaP/CaP/PEI/HTRA1	37	$2.9{\cdot}10^{17}$	23	$5.4{\cdot}10^5$	$1.2{\cdot}10^7$
CaP/CMC/HTRA1/PEI	33	$3.3{\cdot}10^{17}$	21	$6.0{\cdot}10^5$	$1.3{\cdot}10^7$
CaP/CMC/HTRA1/CaP/PEI	149	$7.8{\cdot}10^{15}$	599	$1.4{\cdot}10^4$	$8.5{\cdot}10^6$

In Figure 4.24, representative SEM images of the protein-functionalized calcium phosphate nanoparticles are depicted. The nanoparticles had a spherical morphology, and the actual size was up to 50 nm for single-shell nanoparticles, and 150 nm for multi-shell nanoparticles.

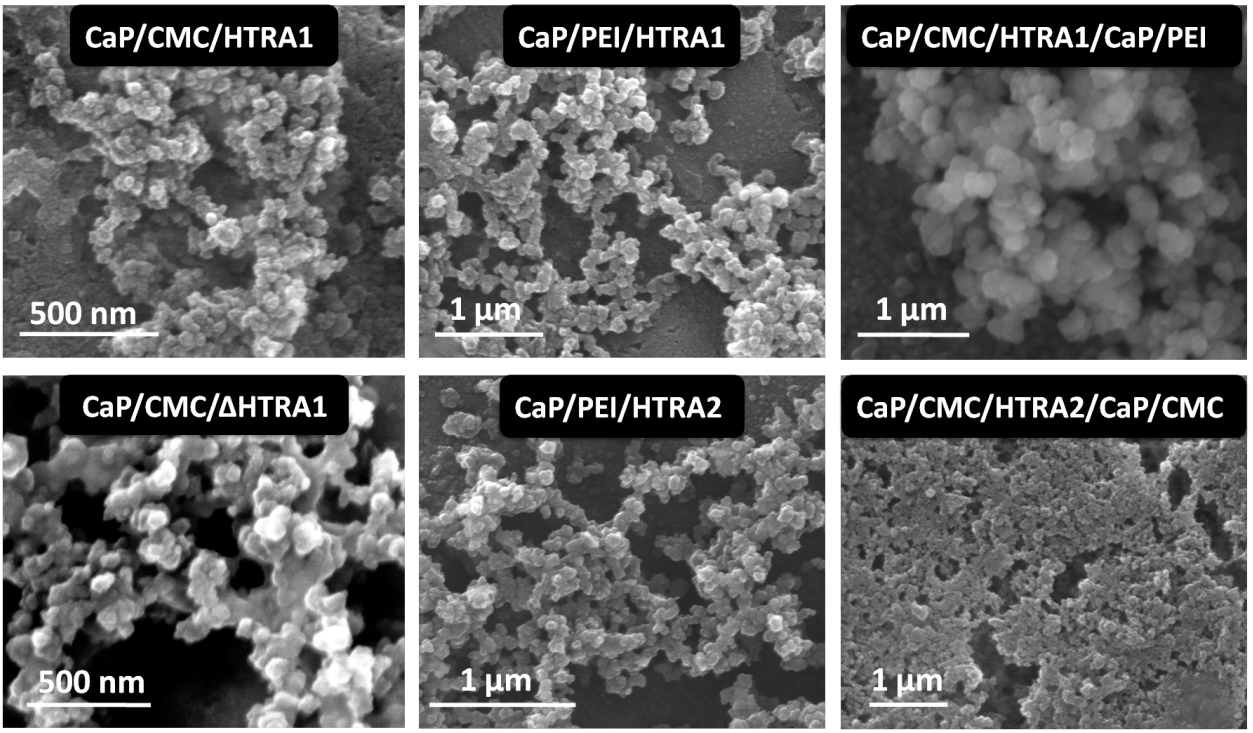

Figure 4.24 Scanning electron microscopy images of functionalized calcium phosphate nanoparticles, loaded with HTRA1 and HTRA2 proteins.

4.1.5.2 Uptake studies with different cell lines

First, we measured the uptake of the protein-loaded nanoparticles by different cell lines. HeLa, MG-63, THP-1, and hMSCs cells were incubated with calcium phosphate nanoparticles containing fluorescently labeled HTRA1 for 3 h. Afterwards, the cells were washed three times with PBS and imaged with light and florescence microscopy. The detailed process of cell imaging is described in Subsection 3.5.5. Remarkably, all tested cell lines, including hMSCs, were able to take up the nanoparticles in a very high number (Figure 4.25). The least-efficient uptake of the nanoparticles was detected by HeLa cells, which points to a different

endocytosis mechanisms of the nanoparticles uptake with this cell line.

We then went on to check whether the functional PDZ domain of HTRA1 protein plays a role in the nanoparticle uptake mechanism. We loaded HTRA1 without PDZ domain (ΔHTRA1) onto the nanoparticles and again incubated them with different cell lines. As can be seen in Figure 4.25, the absence of the PDZ domain did not influence the uptake efficiency of the nanoparticles: it neither increased the endocytosis by HeLa cells nor decreased it with the other cell lines. Therefore, we can conclude that the functional PDZ domain is not responsible for the transport of the protein across the cell membrane.

Our purpose was to deliver the HTRA1 protein into HeLa cells. It is known from the literature that positively charged nanoparticles are usually better and faster taken up by cells because of the electrostatic interaction of the negatively charged cell membrane and the positively charged surface of the nanoparticles [153, 159, 187, 188]. We prepared different nanoparticles to test which combination would be the most effective: single-shell CaP/PEI/HTRA1, where the protein was absorbed on the surface of the nanoparticles, and multi-shell CaP/CMC/HTRA1/CaP/PEI and CaP/CMC/HTRA1/PEI, where HTRA1 was encapsulated under the covering shell of CaP or covered by PEI. In all cases, PEI was present on the nanoparticles surface which gave them a positive charge. The colloid-chemical characterization data of the nanoparticles are summarized in Table 4.14. HeLa cells were incubated with the nanoparticles, carrying HTRA1 protein and with dissolved HTRA1 alone in the same concentration as on the nanoparticles. Fluorescence and light microscopic images are depicted in Figure 4.26. A very high uptake of all types of functionalized nanoparticles in contrast to the dissolved proteins is clearly observed. This indicates a key role of the surface charge of the nanoparticles in their uptake by cells *in vitro*.

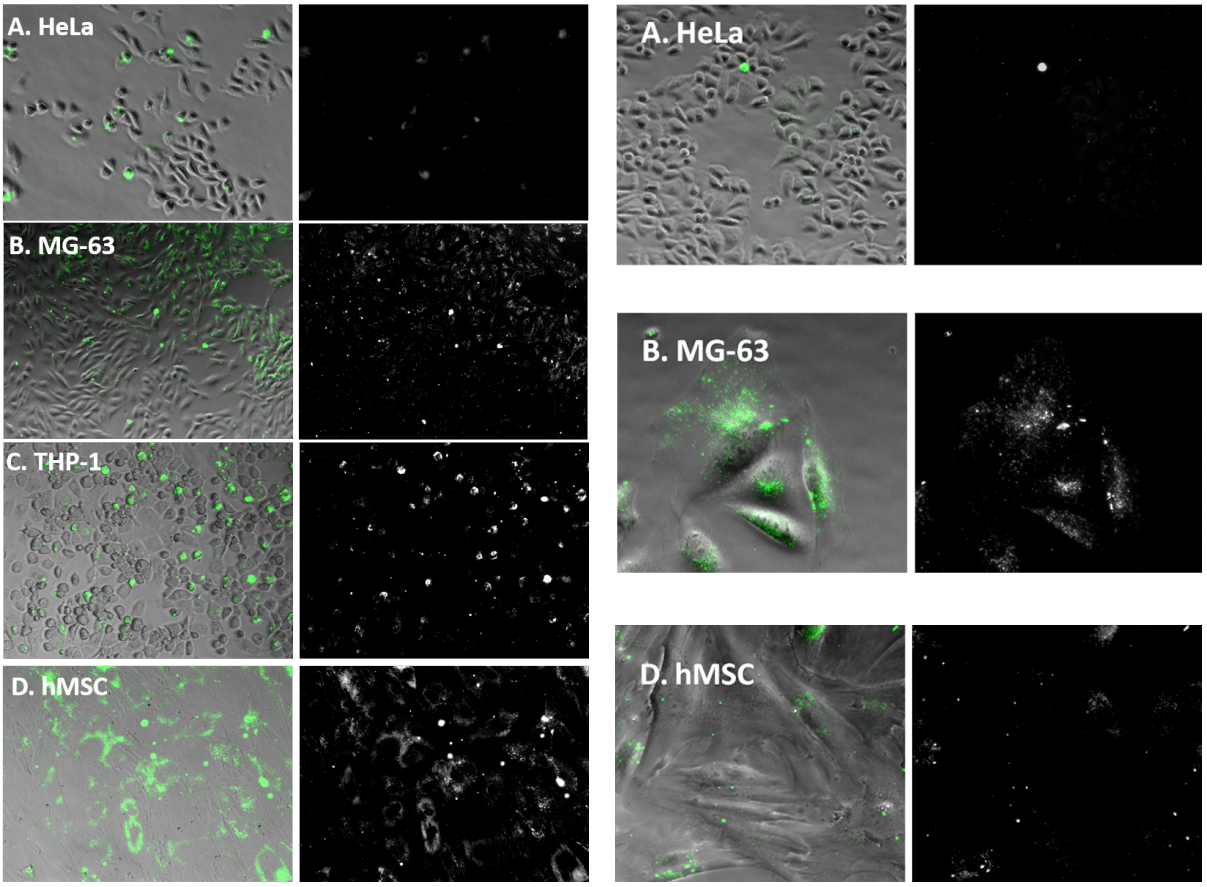

Figure 4.25 Uptake of CaP/CMC/HTRA1 (left column) and CaP/CMC/ΔHTRA1 (right column) nanoparticles by different cell lines.

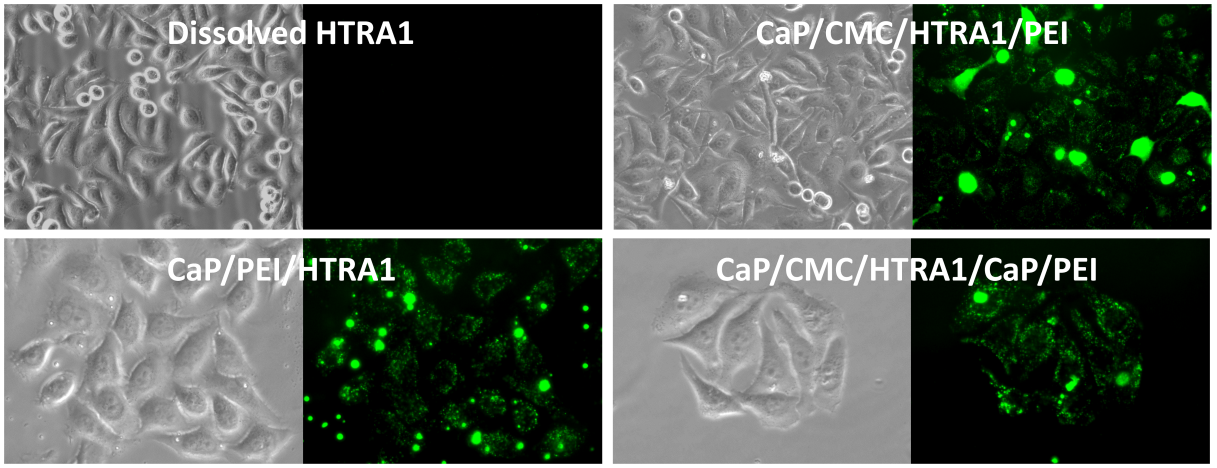

Figure 4.26 Uptake of functionalized calcium phosphate nanoparticles by HeLa cells. Left column: transmission light microscopy; right column: fluorescence microscopy micrographs.

We also performed similar experiments with HTRA2-loaded calcium phosphate nanoparticles, where we incubated HeLa cells with HTRA2-functionalized nanoparticles for 3 h. Figure 4.27 presents the light and fluorescent micrographs of the cells that were treated with single- and multi-shell nanoparticles, loaded with HTRA2-Alexa488. In all cases, the green fluorescence from the protein was detected. In contrast, no uptake of the protein was detected when cells were treated with soluble HTRA2 at the same concentrations: neither by HeLa cells, nor by MG-63 cells (Figure 4.28).

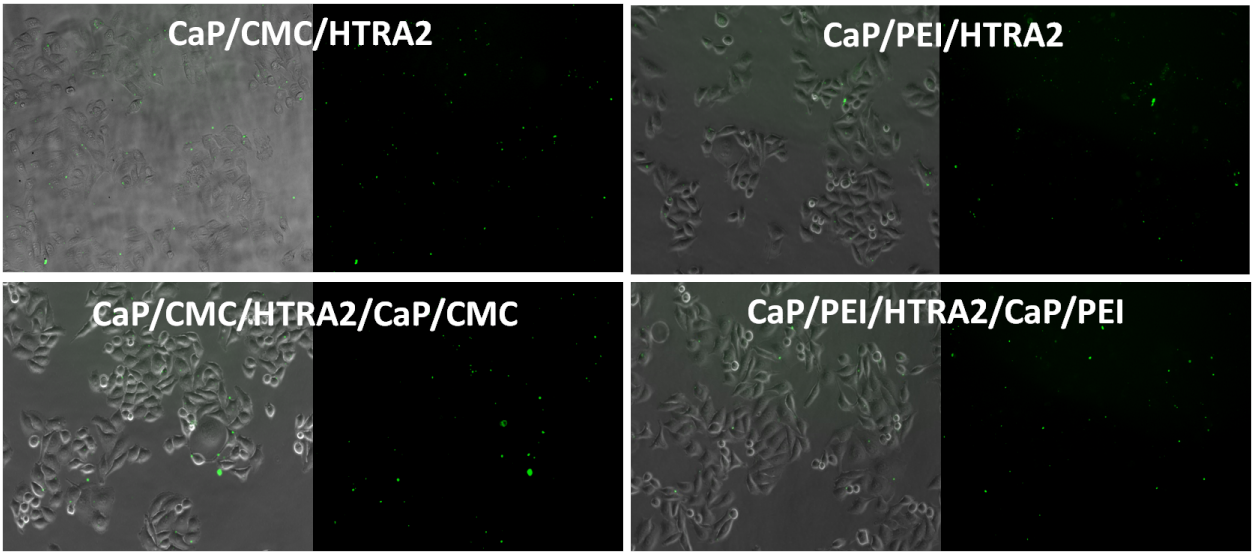

Figure 4.27 Light and fluorescent microscopy images of HeLa cells treated with HTRA2 functionalized calcium phosphate nanoparticles. Cells were incubated for 3 h. HTRA2, labeled with Alexa488, appears in the images as green dots.

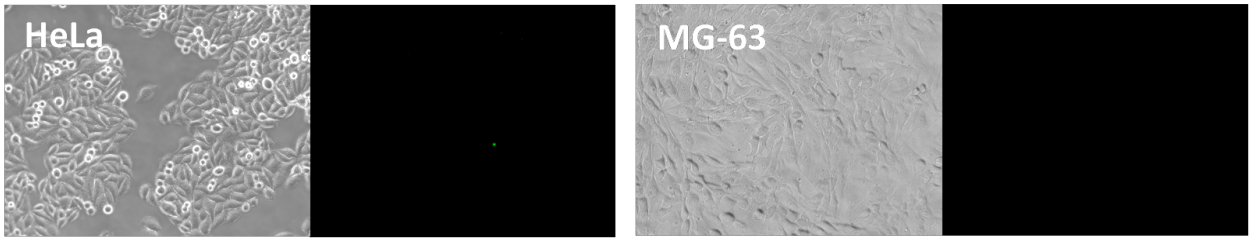

Figure 4.28 Light and fluorescent microscopy images of HeLa and MG-63 cells, treated with dissolved HTRA2-Alexa488.

For a more detailed investigation of the uptake of the HTRA2 that was loaded

onto the nanoparticles, we performed CLSM imaging on two cell lines: HeLa and MG-63 with single-shell nanoparticles. After incubation for 3 h, the cells were washed 3 times with PBS, fixated, and stained according to the protocol (see Subsection 3.5.6). In Figure 4.29, the overlay images from HeLa and MG-63 cells are depicted. In both cases, the green fluorescence of the Alexa488-labeled HTRA2 was detected.

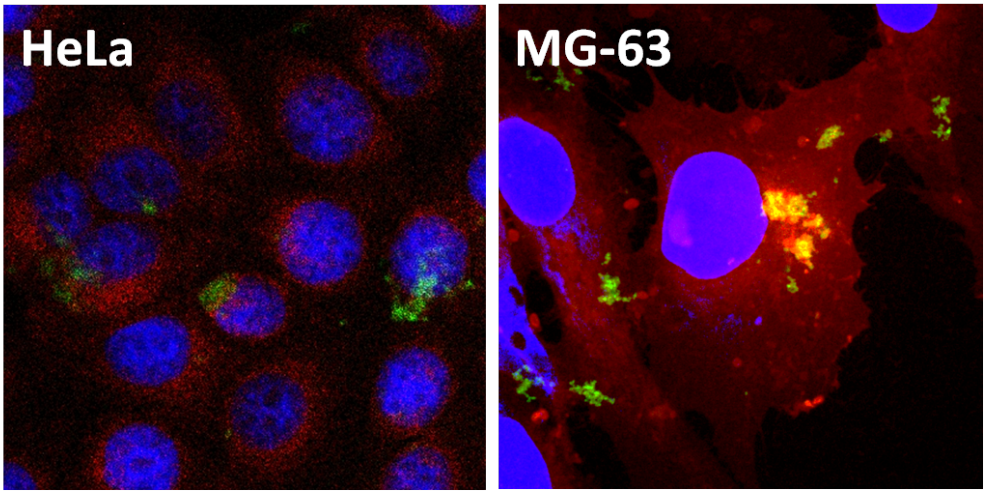

Figure 4.29 Confocal microscopy micrographs of HeLa and MG-63 cell incubated with HTRA2-loaded calcium phosphate nanoparticles. Red channel: cell membrane; blue channel: nucleus; green channel: HTRA2-Alexa488.

4.1.5.3 Studies on the uptake kinetics in MG-63 cells

To compare the uptake kinetics of the protein alone and that loaded onto the nanoparticles, we incubated MG-63 cells with either dissolved Alexa488-labeled HTRA1 or adsorbed on the nanoparticles at different time points: 3, 7, 24, and 48 h. By CLSM, the kinetics of the uptake were studied. As depicted in Figure 4.30, the amount of the internalized protein increased with time, which can be recognized by green fluorescence in both cases. This indicates that living cells (MG-63) are constantly internalizing HTRA1 for their metabolic needs. It is noteworthy that HTRA1 penetrated the cell membrane alone in high amounts, i.e. without carrier.

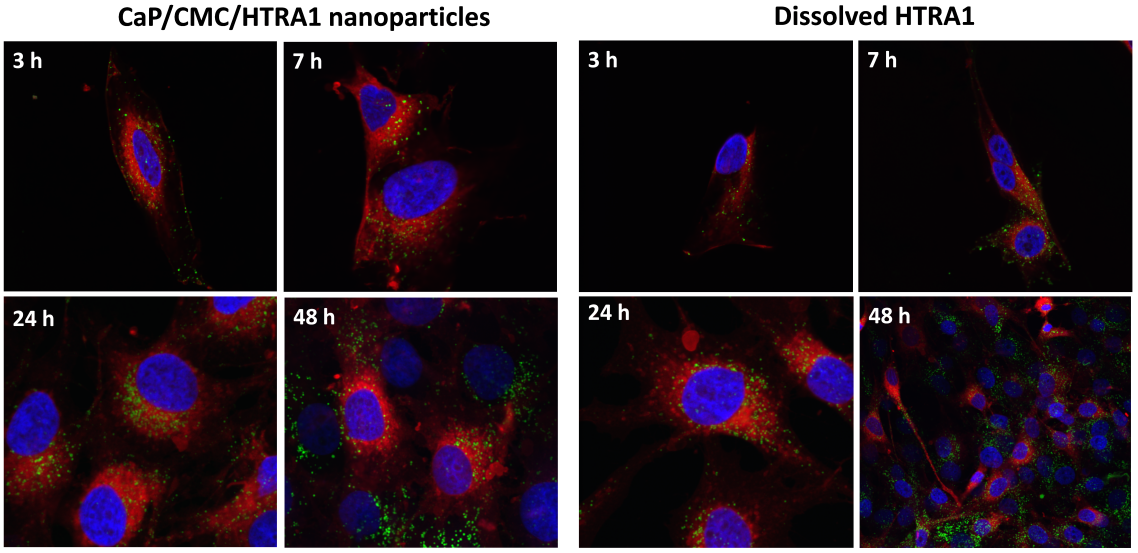

Figure 4.30 Uptake of CaP/CMC/HTRA1 nanoparticles (left) and HTRA1 alone (right) by MG-63 cells during different incubation times.

To quantify the uptake kinetics on a smaller time scale (5 min to 5 h), we performed a similar experiment with the same samples and the same cell line, and measured the uptake by FACS. A difference in the internalization rate of dissolved HTRA1 and HTRA1 adsorbed onto calcium phosphate nanoparticles was observed (Figure 4.31). One can see strong time-dependend increase in the fluorescence from HTRA1-Alexa488, which is internalized by MG-63 cells in both cases. Interestingly, protein alone is taken up faster, starting already from incubation time of 15 min, and more efficiently, compared to HTRA1-carrying nanoparticles. After 5 h of incubation with protein-loaded nanoparticles, a comparable amount of the HTRA1 was detected as by the incubation for 1 h with dissolved HTRA1. These findings suggest that HTRA1 is a highly mobile protein and, in contrast to nanoparticles, it is not take up by endocytosis, which is a time-consuming and energy-dependent process. This indicates that HTRA1 is internalized by different routes in the cells that are yet to be discovered.

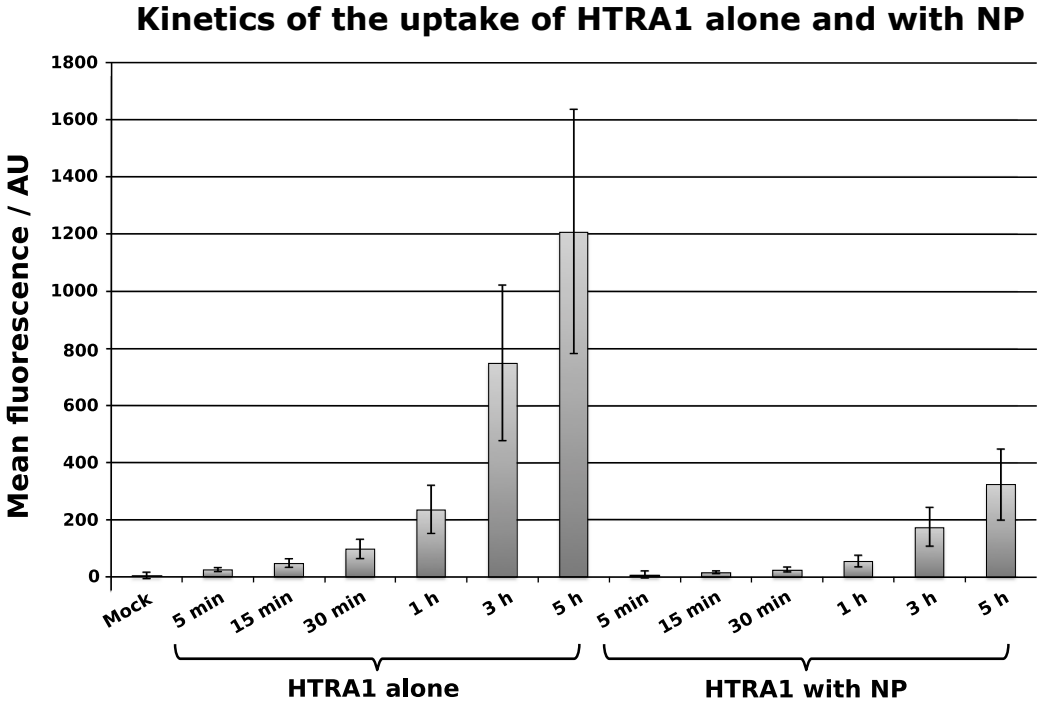

Figure 4.31 FACS measurements of the uptake of dissolved protein (HTRA1) and protein-loaded nanoparticles (NP) by MG-63 cell line during different incubation times.

4.1.5.4 Results of the endocytosis inhibition on MG-63 cell line

We carried out a series of experiments to find out the uptake pathways of the nanoparticles that carry HTRA1 and the protein alone on MG-63 cell line. For this purpose, we used inhibitors of the endocytosis that affect different pathways (Table 4.16) in order to selectively block various types of endocytosis. We incubated MG-63 cells with the inhibitors and then added either HTRA1-carrying nanoparticles or the HTRA1 protein alone and incubated for 3 more hours. The cells incubated by 4 °C before and after the addition of the samples were referred to as the negative control group and the cell with no addition of any inhibitor were referred to as the positive control group. We also used untreated cells (Mock) as control for FACS measurements. For a detailed protocol of endocytosis inhibition, see Subsection 3.5.7.

Table 4.16 List of inhibitors and endocytotic pathways they affect.

Inhibitor	**Affected pathway or cellular structure**
Wortmannin	Macropinocytosis
LY294002	Macropinocytosis
Nystatin	Caveolin-mediated endocytosis/lipid rafts
Nocodazole	Polymerization of microtubules of cytoskeleton
Chlorpromazine	Clathrin-mediated endocytosis

The nanoparticle uptake by MG-63 cell was strongly inhibited by Nystatin which inhibits caveolin-mediated endocytosis, and partially by Nocodazole, an inhibitor of microtubules cytoskeleton polymerization [312] (Figure 4.32). In contrast, other inhibitors did not affect on the internalization process. It was shown that the main internalization pathway for nanoparticles into HeLa cells is micropinocytosis [153]. Thus, it could be said that the preferable endocytosis pathway differs with different cell types.

Interestingly, the only partial inhibition effect of the HTRA1 uptake was demonstrated by Nocodazole treatment, and other agents showed no inhibition effect (Figure 4.32, left). This indicates that HTRA1 is not internalized by any of the listed endocytosis pathways and that only the inhibition of microtubules polymerization in cytoskeleton partially affects this process. It is interesting to note that the fluorescence intensity of the samples, treated only with HTRA1 protein, showed significantly higher values, compared to HTRA1-functionalized nanoparticles (Figure 4.32, right).

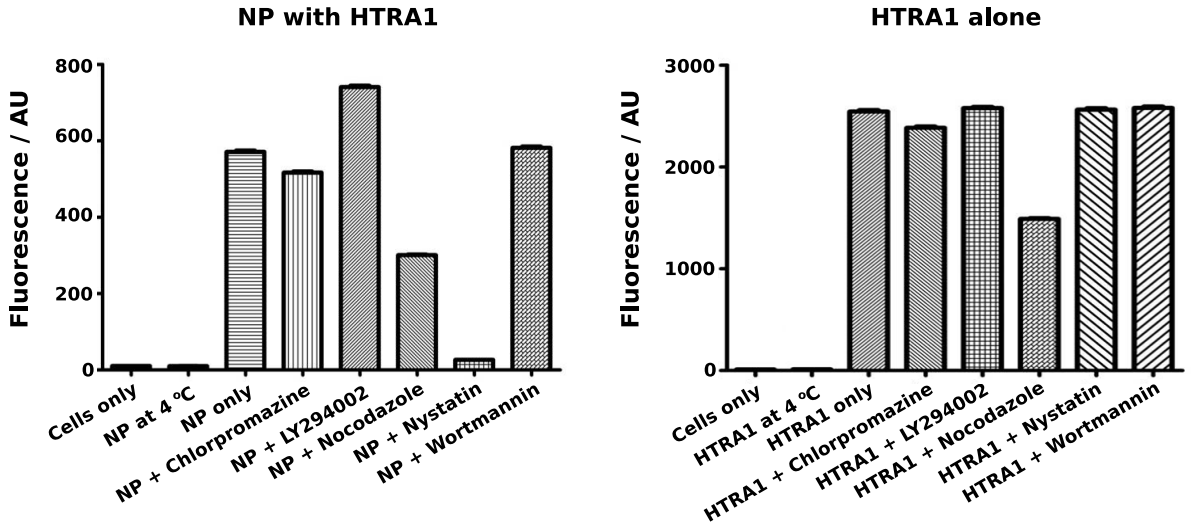

Figure 4.32 Uptake of CaP/CMC/HTRA1 nanoparticles (left) and dissolved HTRA1 protein (right) by MG-63 cells in the presence of endocytosis inhibitors.

4.1.5.5 Conclusions

In this study, we used the functional natural protein HTRA1, loaded onto calcium phosphate nanoparticles and in dissolved form for uptake experiments with different cell lines. Protein-loaded nanoparticles were taken up by HeLa, MG-63, THP-1 cell lines as well as by hMSCs. The surface charge of the nanoparticles plays an important role in the cellular uptake process, as shown in the experiments with HeLa cells. The PDZ domain of the HTRA1 protein did not play a significant role in the internalization of the protein, because its absence did not influence the uptake efficiency of the nanoparticles loaded with HTRA1 without the PDZ domain.

Kinetic studies have revealed that HTRA1 is taken up constantly by MG-63 cells and the uptake speed of dissolved protein is dramatically higher than that of HTRA1-loaded nanoparticles. This, in turn, indicates that the dissolved protein is internalized by a mechanism other than endocytosis. Moreover, the inhibition of the endocytosis on MG-63 cell showed fundamental differences in the uptake mechanisms for loaded nanoparticles and dissolved HTRA1. Taken together,

these results indicate that HTRA1 is transported to the living cells by a hitherto unknown mechanism.

4.1.6 Transport of bioactive peptides across the cell membrane with calcium phosphate nanoparticles

In the present study, we aimed to deliver the bioactive peptide LxVPc1 and its non-functional mutant LxVPc1mut into macrophages. LxVPc1 peptide is a synthetic molecule that can block the phosphorylation activity of calcineurin towards the NFAT signal molecule, thus inhibiting the activation of the proinflammatory pathway in macrophages. This is an interesting approach to fighting the inflammation-related transplantation failures.

4.1.6.1 Characterization of functionalized calcium phosphate nanoparticles

To this end, we synthesized PEI-functionalized calcium phosphate nanoparticles and loaded them with peptide FITC-labeled LxVPc1 (in the following denoted as "Pep") and its mutant form LxVPc1mut (in the following denoted as "Mut"). The nanoparticles were purified and redispersed by ultrasonication in ultrapure water and subsequently characterized with DLS, NTA, and SEM methods. The quantification of the peptides in the nanoparticles colloid after purification was performed by UV-Vis spectroscopy. For a more detailed protocol of synthesis and purification, refer to Subsection 3.1.1.

The colloid-chemical characterization data of obtained functionalized nanoparticles are summarized in Table 4.17. Both samples showed average hydrodynamic size of about 400 nm. By measuring these samples with NTA, the size was estimated in the range of 130-160 nm. This difference may occur because minor agglomeration of smaller nanoparticles could be detected in DLS as one big particle. The zeta potential measurement by DLS showed positive values for both

samples due to the presence of PEI molecules on the outer shell of the nanoparticles. The adsorbed peptides on the surface of the nanoparticles had only a slight effect on the surface charge values of the nanoparticles.

Table 4.17 The colloid-chemical characterization of purified peptide-functionalized CaP/PEI nanoparticles by DLS, NTA and UV-Vis spectroscopy. PDI: polydispersity index from dynamic light scattering.

Sample	PDI	Size (DLS) / nm	Size (NTA) / nm	Zeta potential / mV	C (peptide) in the colloid / μg mL^{-1}	C (peptide) in the colloid / %
CaP/PEI/Pep	0.384	397	158 ± 53	+12	238	52
CaP/PEI/Mut	0.438	391	128 ± 44	+10	310	65

With the help of a calibration curve (Figure 4.33), the concentration of peptides in the nanoparticles was determined and estimated with 52% for Pep and 65% for Mut peptide, corresponding to 238 and 310 μg mL^{-1}.

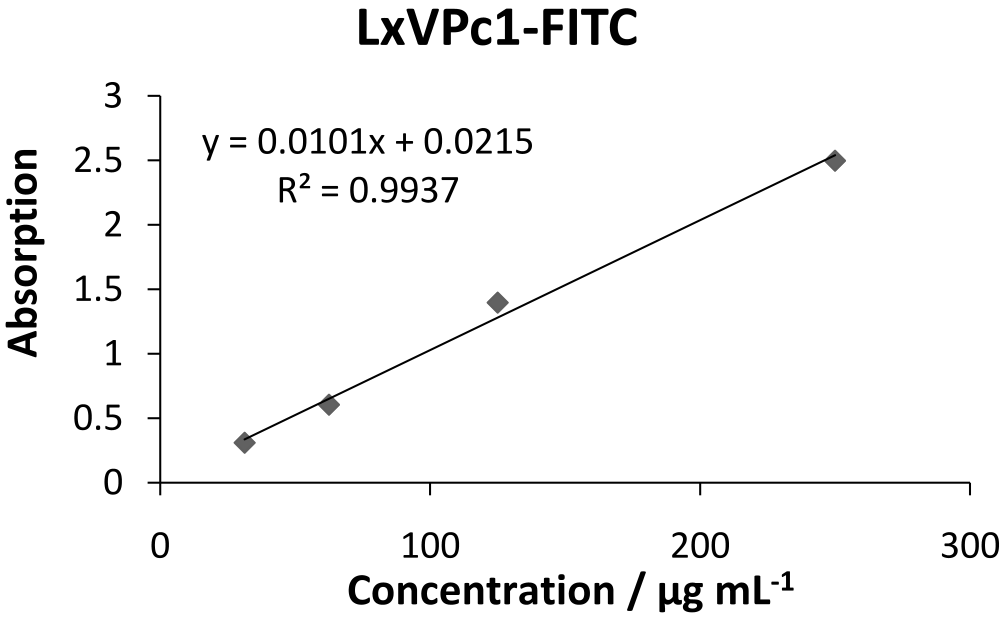

Figure 4.33 UV-Vis spectroscopy calibration curve (λ=492 nm) for determining the concentration of the peptide in the supernatant of purified peptide-functionalized nanoparticles.

With scanning electron microscopy, the actual size and morphology of the synthesized peptide-loaded calcium phosphate nanoparticles was obtained. The actual diameter of the nanoparticles ranged between 50 and 100 nm and their morphology was mostly spherical (Figure 4.34).

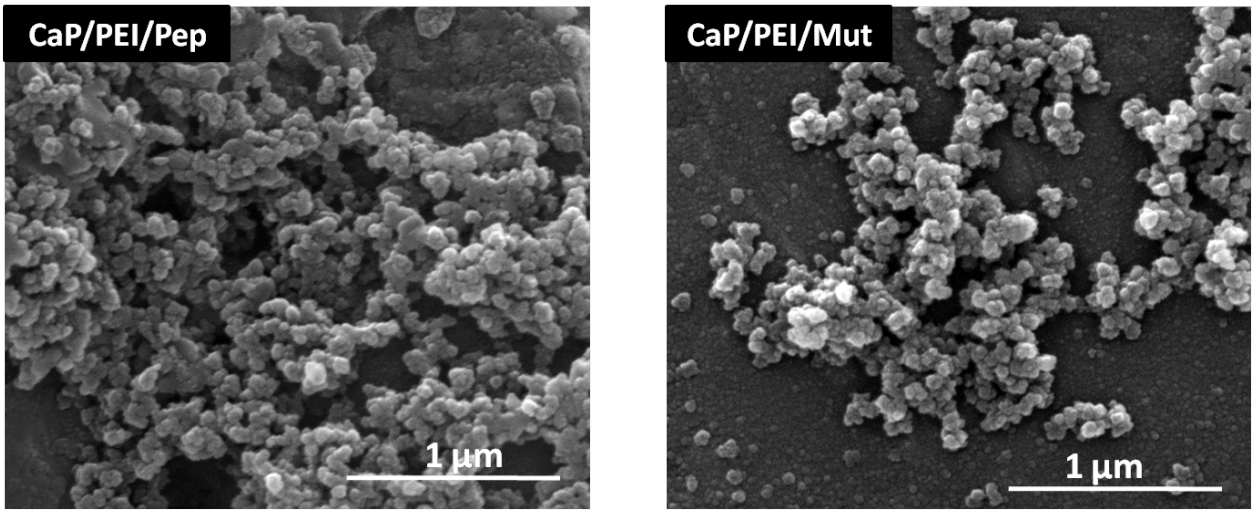

Figure 4.34 SEM images of the synthesized peptide-functionalized calcium phosphate nanoparticles.

Furthermore, we also calculated the theoretical number of the peptide molecules on the surface of the nanoparticles based on the assumption that all nanoparticles have more or less the same size and loading capacity (Table 4.18). For more detailed description of the calculation procedure, see Subsection 3.1.4.

Table 4.18 Determining the number of fluorescently-labeled peptides and calcium phosphate nanoparticles in the dispersion.

Peptide	M_w (peptide) / kg mol^{-1}	n (peptide) / mol m^{-3}	N (peptide) per m^3	N (NP) per m^3	N (peptide) per NP
Pep	1.844	0.129	$7.771 \cdot 10^{22}$	$1.717 \cdot 10^{16}$	$4.525 \cdot 10^{6}$
Mut	1.747	0.178	$1.069 \cdot 10^{23}$	$1.717 \cdot 10^{16}$	$6.225 \cdot 10^{6}$

4.1.6.2 Transport of peptides with calcium phosphate nanoparticles

All biological experiments were carried out with the THP-1 cell line as a model of differentiated macrophages. For differentiation protocol of these cells, refer to Subsection 3.5.2. First, we checked whether the nanoparticles and peptides cause any toxic damage to the living cells by an MTT assay. To do this, we incubated differentiated THP-1 cells either with peptide-functionalized calcium phosphate nanoparticles or with dissolved peptides (Ctrl) at the same concentrations as in the dispersion of nanoparticles for 3 h. This was followed by an MTT assay. The cell viability was normalized to the untreated control group (100% viability). The results of this assay showed no harmful effect on the THP-1 cells of the tested samples (Figure 4.35).

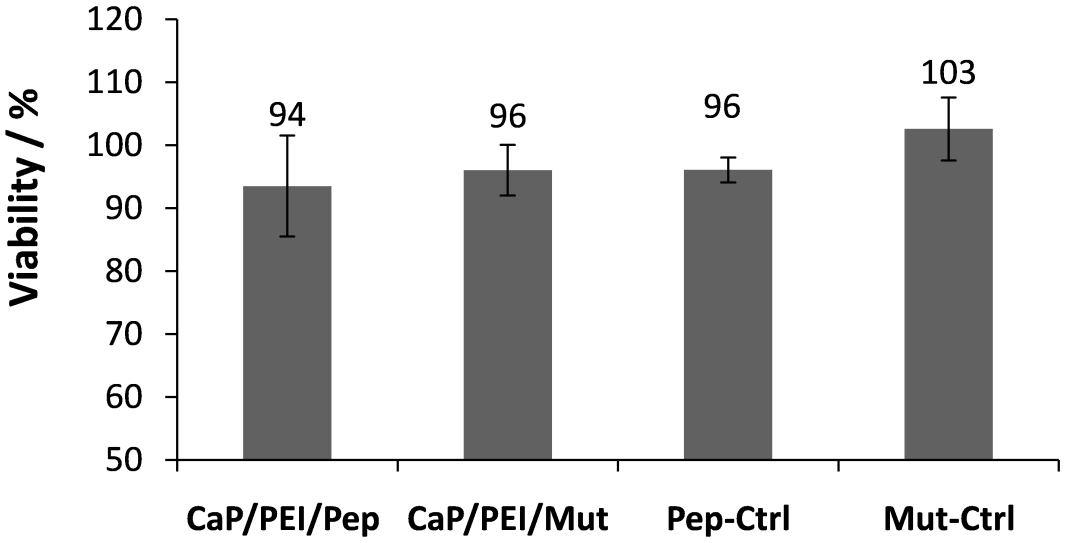

Figure 4.35 Results of MTT assay on THP-1 cells.

To determine the cellular uptake of the peptide-functionalized nanoparticles, the CLSM was performed on the fixed differentiated THP-1 cells. The cells were incubated with peptide-functionalized nanoparticles or with dissolved peptides as control. After 3 h the cells were washed 3 times with PBS and fixed for CLSM analysis (detailed fixation protocol is described in Subsection 3.5.6). Figure 4.36 shows

representative CLSM images of the nanoparticle-treated macrophages. Both peptides could be clearly recognized due to the FITC labeling. Thus, the fluorescence in green channel indicates that the peptides were taken up by the cells after 3 h of incubation. In order to prove that the peptides were located inside the cell, Z-stack slicing was performed (Figure 4.37).

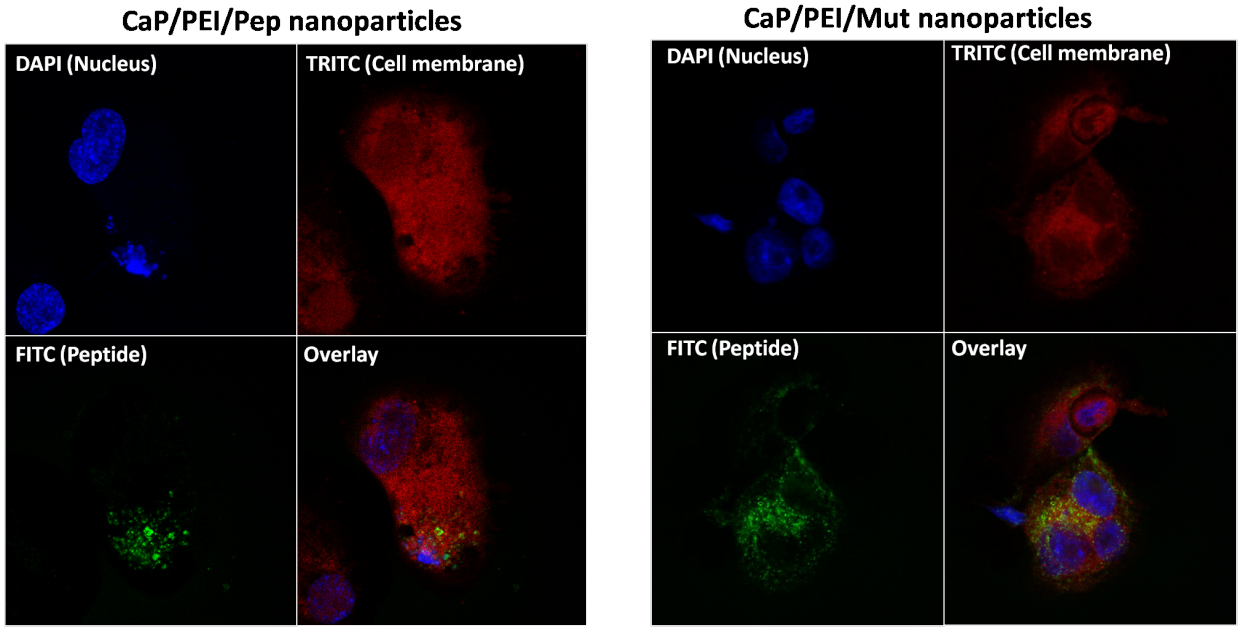

Figure 4.36 Uptake of CaP/PEI/Pep (left) and CaP/PEI/Mut (right) nanoparticles by THP-1 cells after 3 h of incubation.

It was clearly observed that the green fluorescence of both peptides was located on the same level with the DAPI-stained nucleus, thereby proving their internalization and cytosolic localization. In contrast, no fluorescence was found in the samples treated only with dissolved peptides (Figure 4.38). This suggests that peptides alone cannot be transported into the living cells and that an appropriate carrier is needed. Previously we have shown that with the help of calcium phosphate nanoparticles different cargos could be transported across the cell membrane when it was not possible for the cargo molecule alone [143].

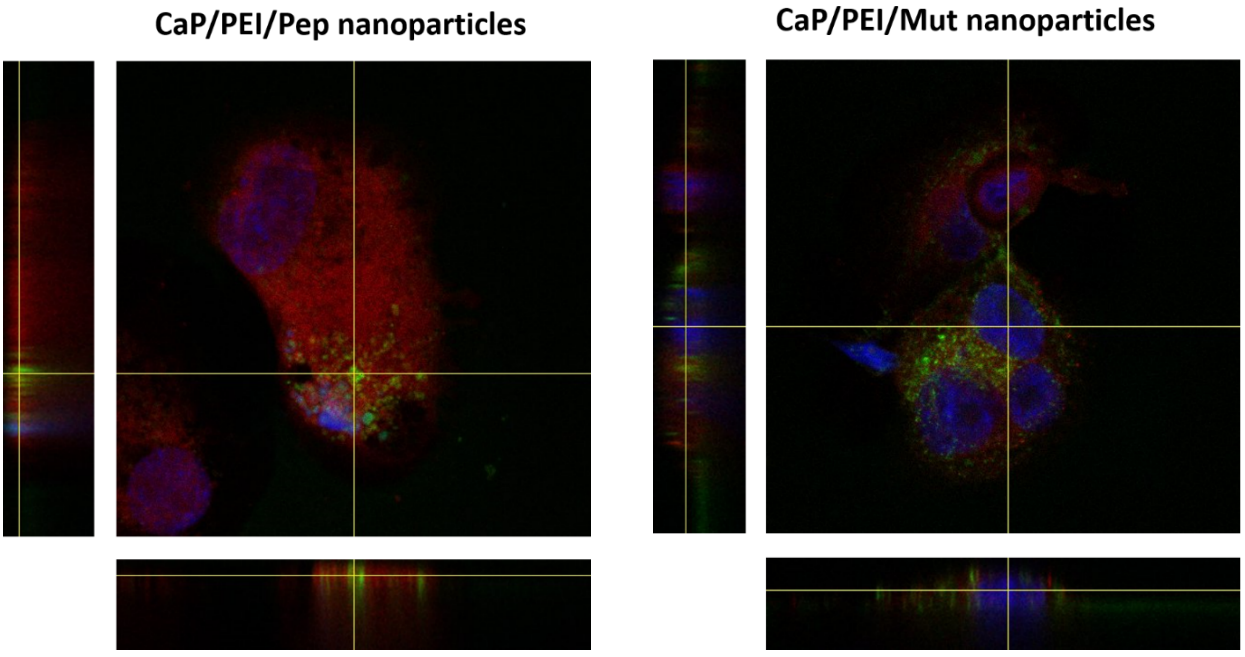

Figure 4.37 Uptake of CaP/PEI/Mut nanoparticles by THP-1 cells after 3 h of incubation. Blue channel: nucleus; red channel: cell membrane; green channel: FITC-labeled peptides.

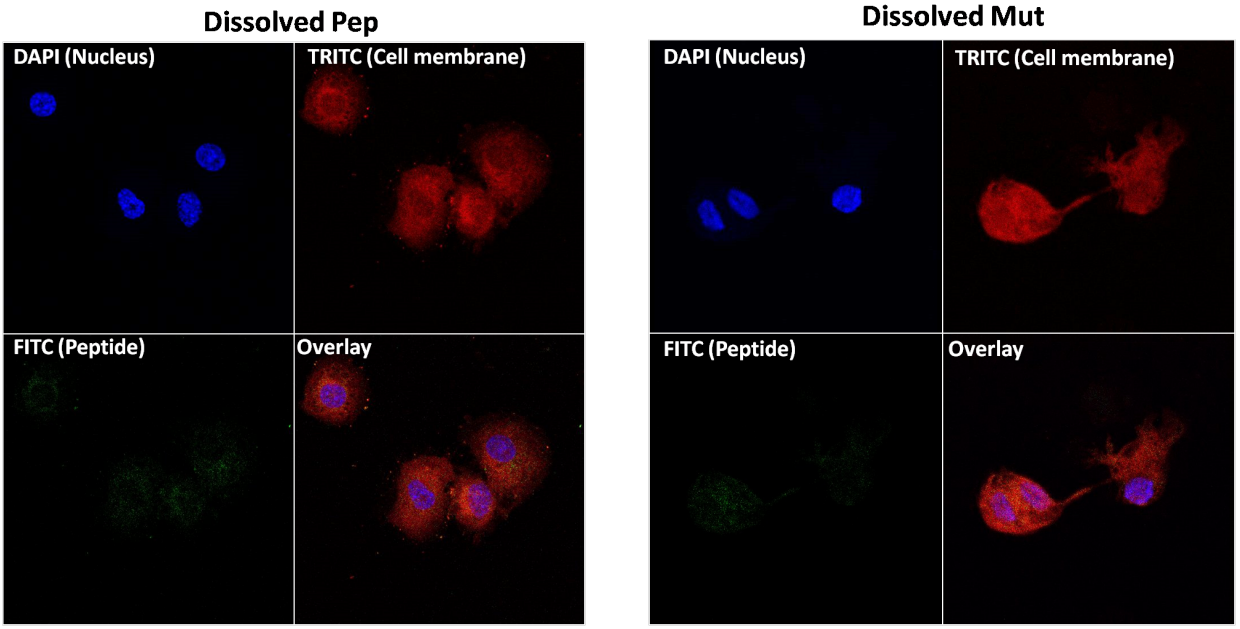

Figure 4.38 Uptake of dissolved peptides by THP-1 cells after 3 h of incubation. Blue channel: nucleus; red channel: cell membrane; green channel: FITC-labeled peptides.

4.1.6.3 Conclusions

We synthesized FITC-labeled peptide-functionalized calcium phosphate nanoparticles and characterized them by different colloid-chemical methods (DLS, NTA, SEM). With the help of UV-Vis spectroscopy, the amount of peptide in the nanoparticles colloid after purification was estimated. Furthermore, we could calculate the theoretical amount of each peptide per nanoparticle. The functionalized nanoparticles as well as the peptides themselves did not show any cytotoxic effects, and thus their practical application *in vitro* and *in vivo* is possible. CLSM revealed no uptake of the dissolved peptides by the cells (no fluorescence), whereas the peptide-functionalized nanoparticles were taken up by differentiated THP-1 cells after 3 h of incubation. Therefore, biodegradable calcium phosphate nanoparticles represent a flexible tool in bio- and nanomedicine as a carrier of peptides into macrophages.

4.1.7 Summary

The following conclusions can be drawn from the obtained results. First, the transfection of HeLa and MG-63 cell lines with PEI-functionalized calcium phosphate nanoparticles was efficient and less toxic compared to the transfection with pure DNA-PEI polyplexes. Moreover, an additional functionalization with protamine increased the efficiency of nanoparticles by facilitating the nuclear localization of plasmid DNA and by decreasing the toxic effect of PEI.

Second, functionalized calcium phosphate nanoparticles were able to transport different molecules into the cells, whereas free molecules in general were not able to penetrate the cell membrane. The studies using inhibition of endocytosis showed that the uptake route of nanoparticles differed from that of free protein molecules in the example of HTRA1.

It was also shown that the biological environment strongly influenced the function of synthetic enzyme-inhibiting molecules. In terms of the example of the

lysozyme inhibitor-polymer, this dependence was clearly demonstrated in the presence of cell culture medium with and without FCS.

4.2 Functionalized calcium phosphate nanoparticles as vaccine carriers

In this section, the application of calcium phosphate nanoparticles as a novel and flexible vaccination tool will be discussed. The results of the *in vitro* and *in vivo* experiments of immunization against influenza and Friend viruses with functionalized calcium phosphate nanoparticles are summarized. Several decades of vaccine research have failed to develop protective vaccine against persistently infecting viruses such as HCV or HIV. Protein-based vaccines or adenoviral vectors are commonly used to induce humoral and cellular T cell responses but rarely lead to a sufficient antiviral immunity [313, 314]. Therefore, the development of new strategies for prophylactic or therapeutic vaccination has attracted much attention today.

All biological experiments presented in this section were carried out at the Essen University Hospital, Institute of Medical Microbiology, Department of Infectious Immunology, in the group of Prof. Astrid M. Westendorf. The major part of the experiments was carried out by Dr Torben Knuschke.

4.2.1 Functionalized calcium phosphate nanoparticles for vaccination against the influenza virus

4.2.1.1 Synthesis and characterization of functionalized calcium phosphate nanoparticles

The synthesis protocol and optimization experiments to produce stable and immonoactive calcium phosphate nanoparticles, functionalized with a TLR9 ligand (oligonucleotide CpG) and the hemagglutinin peptide from the influenza virus (HA) (see Subsection 3.3), was recently introduced in our group by Sokolova *et al.* [151]. These CpG- and HA-loaded nanoparticles were a useful nontoxic

tool with the ability to maturate DCs and to induce Ag-specific $CD4^+$ and $CD8^+$ T cell responses *in vitro* [315, 316]. In this study, we synthesized and characterized CaP nanoparticles with regard to their potential use as a vaccination vehicle against the influenza virus. We prepared multi-shell CaP nanoparticles, using a multi-step process of subsequent precipitation and functionalization. For a more detailed description of the synthesis process, refer to Subsection 3.1.1.

The core of the nanoparticles was functionalized and stabilized with CpG. Immunogenic peptides of the influenza virus A/PR/8/34 HA: $HA_{512-520}$ (MHC Class I) or $HA_{110-120}$ (MHC Class II) were subsequently adsorbed on the surface of the CpG-functionalized nanoparticles, incrustation in the inner shell (see Figure 4.39 A). These peptides and CpG molecules were protected from degradation by the addition of a second shell consisting of calcium phosphate. Finally, the nanoparticles were colloidally stabilized by the repeated addition of CpG. The final concentrations of immunoactive molecules in the nanoparticle dispersion were as follows: CpG=65.3 $\mu g\ mL^{-1}$ (10.3 μM) and HA peptide=20.4 $\mu g\ mL^{-1}$. On average, the hydrodynamic diameter of these triple-shell nanoparticles was ~250 nm and about 150 nm in scanning electron microscopy images. One should note that in SEM micrographs the nanoparticles appear without the hydration shell and that single nanoparticles could be distinguished (see Figure 4.39 B).

For intranasal application, the nanoparticles were concentrated by means of centrifugation and redispersion in pure water in a quarter of the original volume. As we have previously quantified the number of absorbed CpG and HA molecules onto the nanoparticles after the purification [315], the concentrations in the final dispersion estimated to 130.6 $\mu g\ mL^{-1}$ (20.6 μM) of CpG molecules and 40.8 $\mu g\ mL^{-1}$ of the HA peptide.

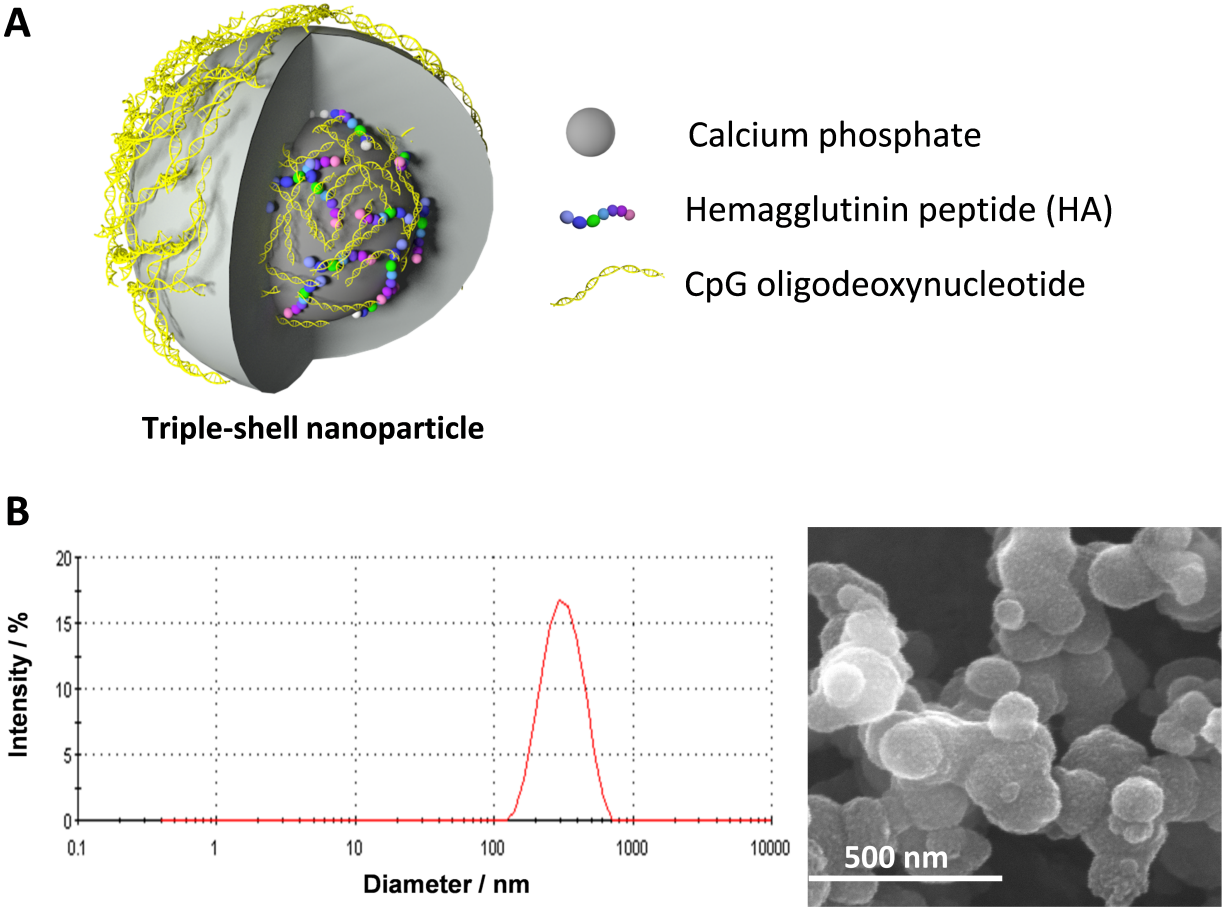

Figure 4.39 Schematic illustration of functionalized calcium phosphate nanoparticles. **A**: CaP nanoparticles are prepared in multiple steps to a final composition of three layers of CaP and TLR ligand CpG (CaP/CpG+HA/CaP/CpG). The core contains the HA peptide $HA_{110-120}$ or $HA_{512-520}$. **B**: Characterization of triple-shell CaP nanoparticles, functionalized with CpG and HA peptides by dynamic light scattering (the average particle diameter is illustrated) and scanning electron microscopy.

4.2.1.2 Uptake of calcium phosphate nanoparticles by DCs *in vitro*

We initially aimed to check the biological effect of the functionalized nanoparticles *in vitro* by treating dendritic cells (DCs) to induce their maturation. DCs are the most effective APCs and play a key role in initiating T cell mediated immune responses. DCs can activate a substantial part of the adaptive immune response by internalizing and processing Ags through the MHC Class I and II pathways and,

finally, by presenting antigenic peptides to $CD4^+$ and $CD8^+$ T cells. Therefore, targeting DCs with a maturation trigger (CpG), combined with Ag (HA) delivery, is one important goal in the development of new vaccines.

To determine the uptake efficiency of functionalized CaP nanoparticles *in vitro* by DCs, we stimulated whole splenocytes with Alexa488-labeled CpG-functionalized CaP nanoparticles. After 24 h, splenocytes were harvested, and $CD11c^+$ DCs were analyzed for the presence of fluorescence from internalized Alexa488-labeled nanoparticles. As seen in Figure 4.40 A, $CD11c^+$ DCs showed a high uptake efficiency. Nearly 37% of all DCs were positive for Alexa488. To analyze whether CaP nanoparticles alone possess an adjuvant activity for DC activation, we compared CpG-functionalized CaP nanoparticles to CaP nanoparticles, functionalized with non-immunogenic control oligonucleotides (Oligo). It was shown that only CpG-functionalized CaP nanoparticles induced the activation of $CD11c^+$ DCs with a specific upregulation of the costimulatory molecules like CD80, CD86, and CD40, and an increased secretion of IL-2, IL-12, and TNF-α (Figure 4.40 B).

Previously, we demonstrated that CaP nanoparticles loaded with an MHC Class II-restricted HA peptide of the influenza virus strongly induced a virus-specific $CD4^+$ T cell response *in vitro* [316]. For a potent antiviral vaccine candidate, it is essential to prime the induction of both virus-specific $CD4^+$ and $CD8^+$ T cell immunity. Therefore, we isolated $CD11c^+$ DCs from the spleen and determined whether these DCs can present internalized Ag on MHC Class II molecules and cross-present this Ag on MHC Class I molecules after the stimulation with CpG- and $HA_{512-520}$ or $HA_{110-120}$ peptides-functionalized CaP nanoparticles. The stimulation with dissolved CpG and HA peptides were used as control. Stimulated DCs were then co-cultured with HA-specific $CD4^+$ or $CD8^+$ T cells for 48-72 h, and afterwards the proliferation of T cells was measured. As depicted in Figure 4.40 C, functionalized CaP nanoparticles and dissolved control had a comparable effect on the presentation of HA peptides and induced strong HA-specific $CD4^+$ and $CD8^+$ T cell responses *in vitro*. These promising results suggest a great potential of functionalized CaP nanoparticles for Ag delivery *in vivo*.

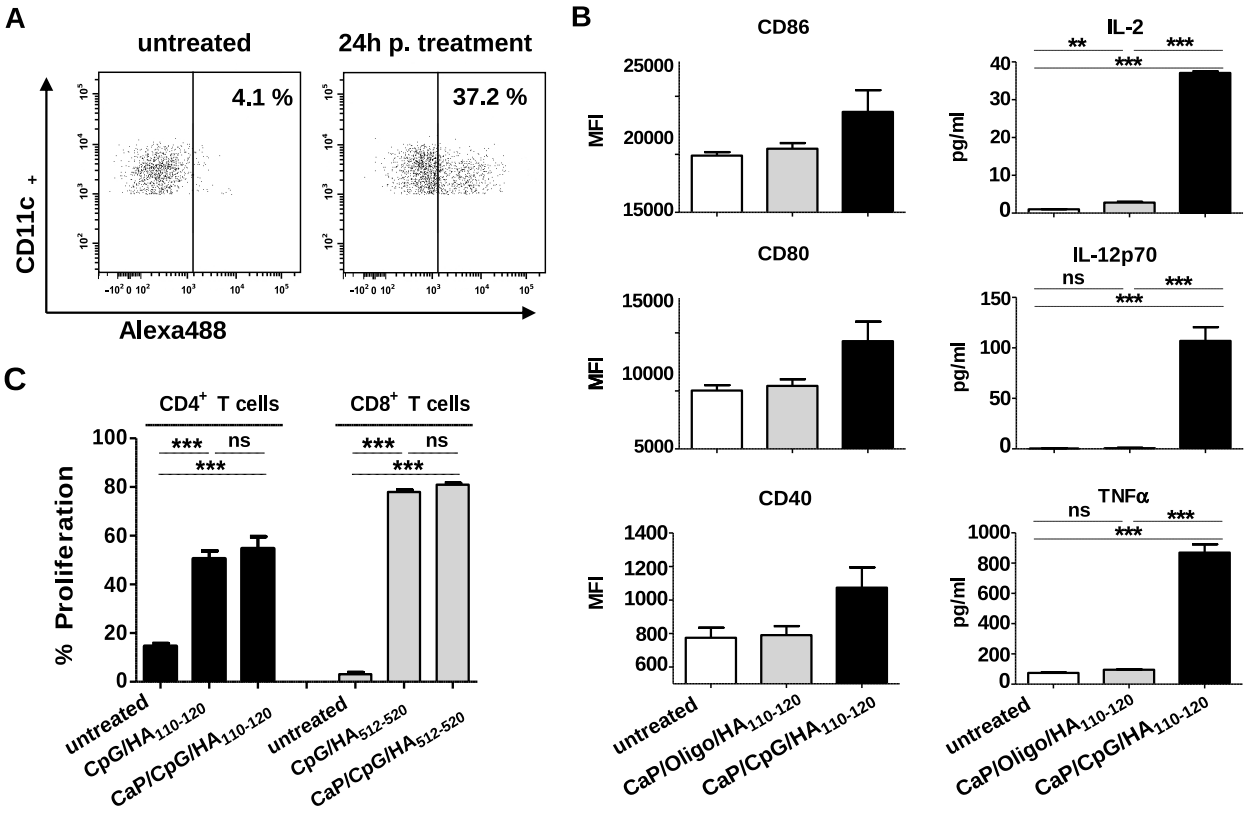

Figure 4.40 Uptake of calcium phosphate nanoparticles and presentation of virus-specific Ags *in vitro*. **A:** Spleen cells were incubated *in vitro* with Alexa488-labeled CaP nanoparticles. After 24 h, the cells were stained for CD11c and analyzed for $CD11c^{+}Alexa488^{+}$ cells. **B:** $CD11c^{+}$ splenic cells were incubated with CpG functionalized CaP nanoparticles or CaP nanoparticles functionalized with non-immunogenic oligonucleotides. Expression of CD80, CD86, and CD40 and cytokine levels of IL-2, IL-12, and TNF-α in cell culture supernatants were analyzed 24 h later. **C:** $CD11c^{+}$ splenic cells were incubated with functionalized CaP nanoparticles or with soluble CpG and $HA_{512-520}$ or $HA_{110-120}$ peptides. After 24 h, DCs were washed and co-cultured with eFluor670-labeled HA-specific $CD4^{+}$ or $CD8^{+}$ T cells for 48-72 h. Proliferation was measured by loss of eFluor670 dye and is indicated as a percentage of proliferating cells. The figure comprises the results of three independent experiments. Bars represent mean ± SEM. ** $p<0.01$, *** $p<0.001$, ns: not significant.

4.2.1.3 Induction of potent $CD4^+$ and $CD8^+$ effector T cells with functionalized calcium phosphate nanoparticles

To test the *in vivo* vaccination efficiency of CpG/$HA_{512-520}$ or CpG/$HA_{110-120}$ functionalized CaP nanoparticles, naive BALB/c mice were immunized intraperitoneally (i.p.) three times at intervals of 14 d either with PBS, soluble CpG and $HA_{512-520}$/$HA_{110-120}$ peptides or CpG/$HA_{512-520}$/$HA_{110-120}$-functionalized CaP nanoparticles (Figure 4.41 A). Two weeks after the last immunization, the percentage of HA-specific $CD8^+$ T cells and IFN-γ production was analyzed in isolated splenocytes. The number of HA-specific $CD8^+$ T cells detected in mice immunized with functionalized CaP nanoparticles was significantly higher than that detected in mice immunized with PBS and, more importantly, than that immunized with soluble CpG and HA peptides (Figure 4.41 B).

Immunized with CaP nanoparticles, mouse splenocytes were restimulated with $HA_{512-520}$ or $HA_{110-120}$ peptide. This restimulation resulted in the induction of IFN-γ-producing $CD4^+$ and $CD8^+$ T cells (Figure 4.41 C). In contrast, the restimulation of immunized with soluble CpG and HA peptides, mouse splenocytes induced a significantly lower IFN-γ response. It is to be noted that no humoral IgG Ab response against HA peptides was detected in any of the immunized mice (data not shown). These results indicate a much more efficient inducing of cellular immunity response after the i.p. immunization with functionalized CaP nanoparticles compared to soluble factors only.

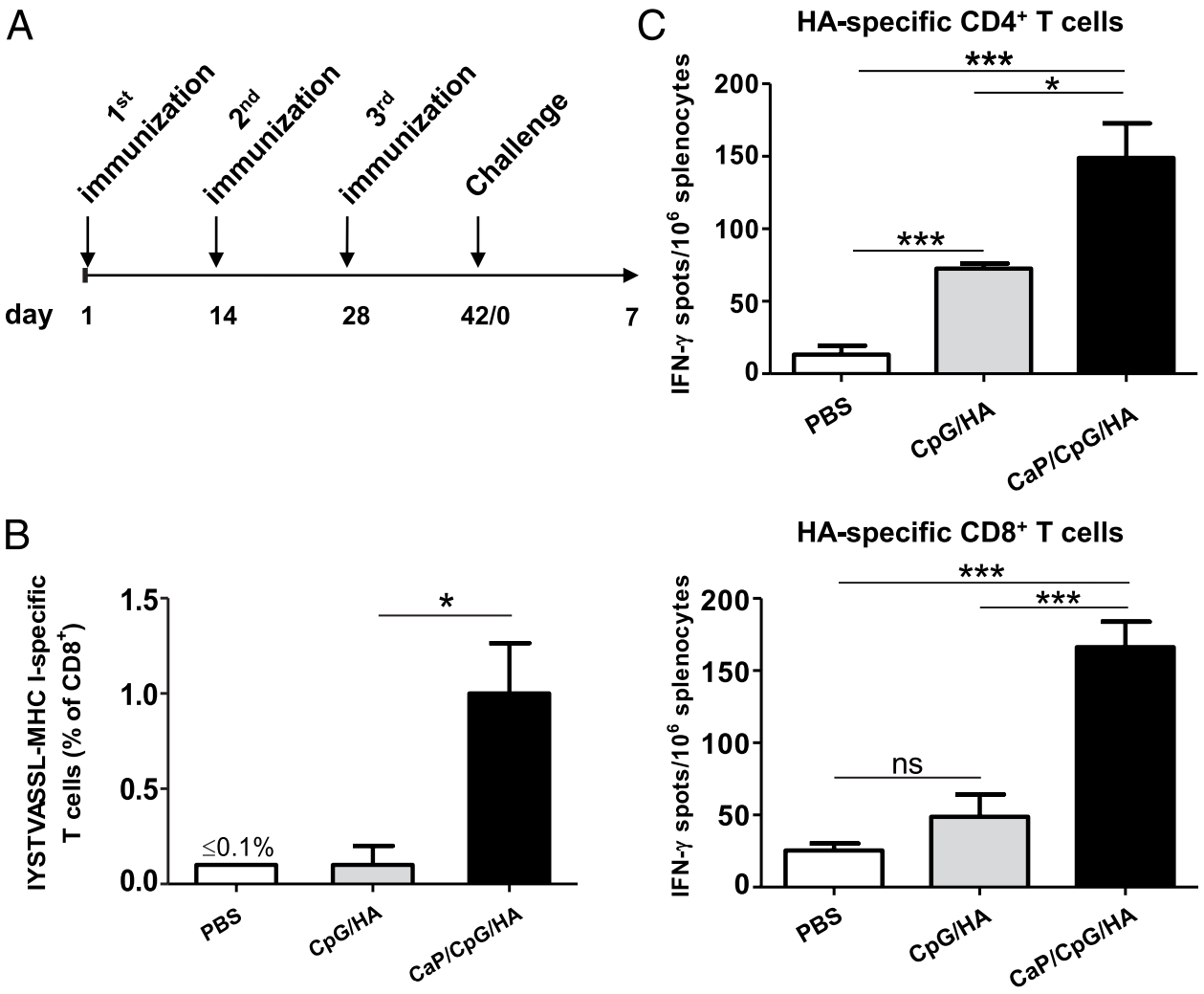

Figure 4.41 Immunization protocol and induction of influenza-specific T cell responses. **A:** BALB/c mice were immunized three times i.p. with 300 µL functionalized CaP nanoparticles containing CpG and $HA_{512-520}$ or $HA_{110-120}$ peptides, soluble CpG and HA peptides at the same concentrations. Two weeks after the final immunization, BALB/c mice were sacrificed for cellular analysis. **B:** Total spleen cells from immunized mice were stained for the presence of HA-specific $CD8^+$H-$2K^d$:IYSTVASSL$^+$ T cells (three mice per group). Bars represent mean ± SEM. **C:** Splenocytes from immunized BALB/c mice (three mice per group) were restimulated *in vitro* with 10 µg mL^{-1} $HA_{512-520}$ or $HA_{110-120}$ peptide. After 24 h, the numbers of IFN-γ-producing $CD4^+$ and $CD8^+$ T cells were determined by ELISpot in triplicate. Spots were counted and expressed as spots per splenocyte. The figure illustrates results from one of three independent experiments. Bars represent mean ± SEM. * $p<0.05$, *** $p<0.001$, ns: not significant.

4.2.1.4 Acceleration of influenza virus clearance from the lungs by means of functionalized calcium phosphate nanoparticles

The next step was to determine whether HA-specific $CD4^+$ and $CD8^+$ T cells induced by i.p. immunization with CaP nanoparticles can exhibit protective activity. To this end, we intranasally challenged the immunized mice with a high dose of influenza virus A/PR/8/34 2 weeks after the third immunization. Seven days after challenge, viral titers in lungs were determined. Importantly, all mice immunized with CaP nanoparticles had significantly lower viral titers in the lung than the PBS group (see Figure 4.42 A). Moreover, 35% of the mice in this group had completely eliminated the virus by this time. In contrast, immunization with soluble CpG and HA peptides did not help to clear the virus. It merely resulted in slightly lower viral titers compared to the PBS control group (Figure 4.42 B). More interestingly, this accelerated clearance of virus from the lungs of mice immunized with CaP nanoparticles was in vivid correlation with an increased number of HA-specific $CD8^+$ T cells in the spleens of challenged mice (Figure 4.42 B). However, total IgG concentrations in the serum showed no significant differences between groups, neither before nor 7 days post infection, indicating a minor effect of virus-specific T cells on IgG induction (Figure 4.42 C).

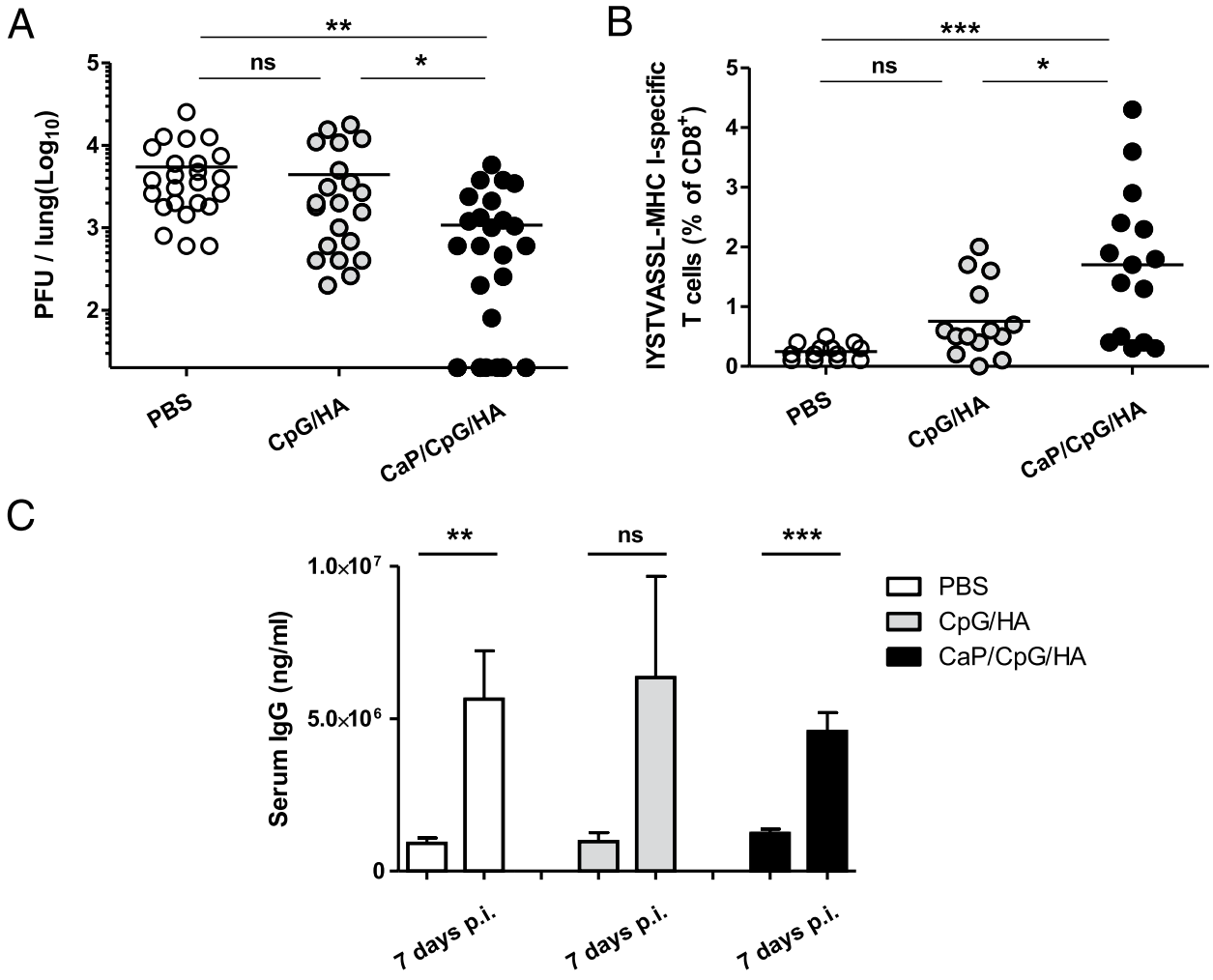

Figure 4.42 Protection of immunized mice against influenza virus replication. **A:** 14 days after the third immunization, the mice were challenged intranasally with 1,000 PFUs of influenza virus A/PR/8/34. After 7 d, the mice were sacrificed and lung virus titers were measured by plaque assay; y-axis starts at the influenza virus detection limit. The figure illustrates results from four independent experiments. Each data point represents one animal. **B:** Total spleen cells from influenza-challenged mice (7 d after challenge) were stained for the presence of HA-specific $CD8^+$ H-$2K^d$:$IYSTVASSL^+$ T cells. Each data point represents one animal. **C:** IgG concentrations in sera of immunized mice were determined by ELISA 2 weeks after the final immunization and at day 7 post infection. The figure illustrates the results of two independent experiments (four mice per group). * $p<0.05$, ** $p<0.01$, *** $p<0.001$, ns: not significant.

4.2.1.5 Results of intranasal immunization with functionalized calcium phosphate nanoparticles

The lungs are the major target for invasion of such respiratory pathogens as influenza virus. Therefore, an efficient protection against virus infection requires the induction or recruitment of virus-specific $CD4^+$ and $CD8^+$ T cells into the lung. Therefore, we examined whether the intranasal administration of functionalized CaP nanoparticles was sufficient to induce mucosal immunity and protection against influenza virus infection. First, we checked the specific uptake of nanoparticles by DCs form lung lymph nodes. For this, BALB/c mice were administered intranasally with Alexa488-labeled CaP nanoparticles. 4 h later, lung lymph node cells were stained with anti-CD11c and examined for an $Alexa488^+$ population. In Figure 4.43 one can see that approximately 30% of the $CD11c^+$ DCs were Alexa488 positive. The next step was intranasal immunization of naive BALB/c mice according to the same immunization protocol as that used for PBS, soluble CpG, and $HA_{110-120}$/ $HA_{512-520}$ peptides or CpG/$HA_{512-520}$/$HA_{110-120}$-functionalized CaP nanoparticles. Two weeks after the last immunization, mice splenocytes were isolated, restimulated with the corresponding HA peptides, and analyzed for production of IFN-γ, TNF-α, and IL-2. A higher number of $CD4^+$ and $CD8^+$ T cells producing IFN-γ, IL-2, and TNF-α were detected in the mice immunized with CaP nanoparticles compared to control groups (Figure 4.43 B and C).

Furthermore, 7 d after the influenza virus challenge, the viral replication level in the lungs of mice immunized with CaP nanoparticles was significantly lower than those treated with PBS (Figure 4.44 A). This decrease was accompanied by a higher number of HA-specific $CD8^+$ T cells in the lung lymph nodes and the spleen (Figure 4.44 B).

Although mice represent a good animal model for influenza infection, they exhibit some differences in viral manifestation compared to humans. Viral replication in mice is mainly confined to the lower respiratory tract [317,318], whereas

in humans it is mainly limited to the upper respiratory tract. Consequently, an influenza infection in mice is more severe than in humans. To simulate the infection, localized in upper respiratory tract, conscious rather than narcotized mice were challenged with the influenza virus. Generally, mice infected without anesthesia showed reduced morbidity 7 d after viral infection. More interestingly, CpG/$HA_{512-520}$/$HA_{110-120}$-functionalized CaP nanoparticles-immunized mice exhibited the highest reduction of the viral load in the lungs, compared to other control groups (Figure 4.44 C). Furthermore, increased numbers of HA-specific $CD8^+$ T cells indicate an activation of preexisting virus-specific T cells after intranasal immunization of mice with functionalized CaP nanoparticles (Figure 4.44 D).

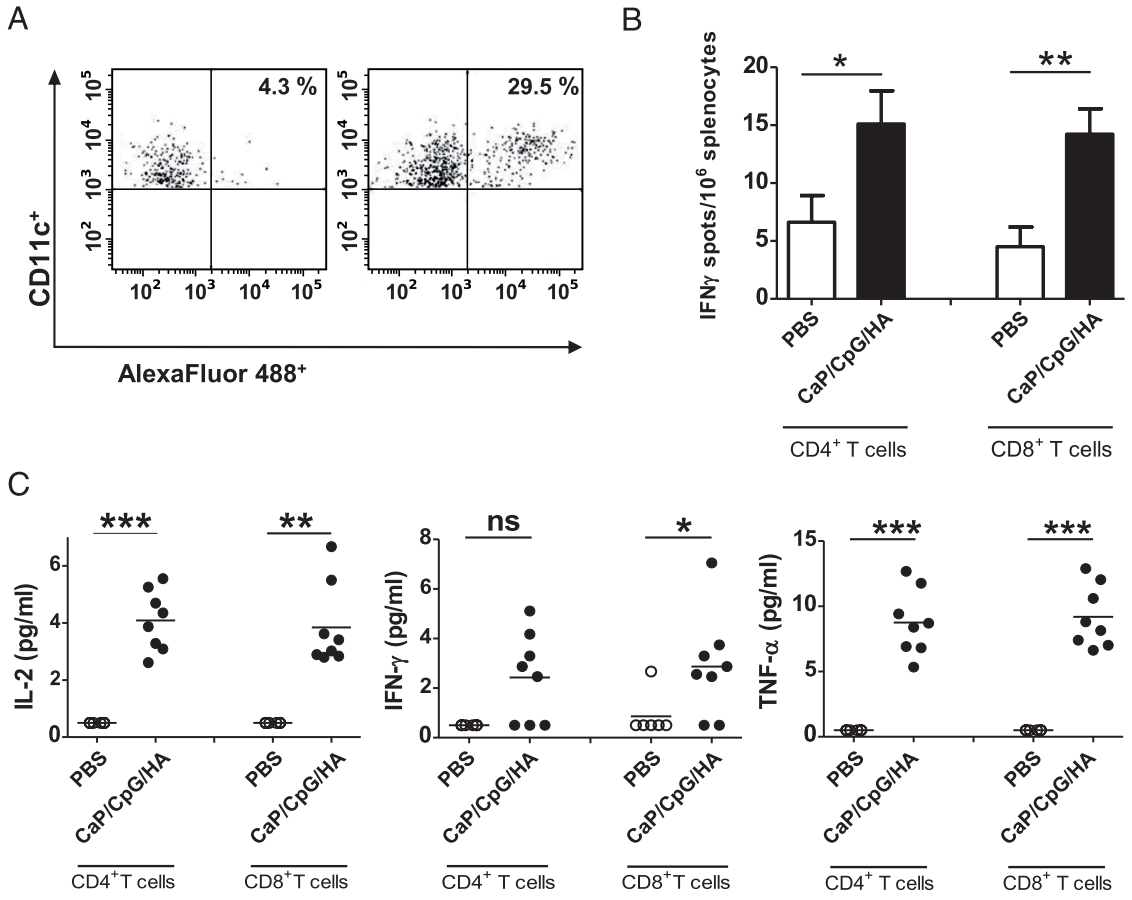

Figure 4.43 Intranasal immunization with functionalized calcium phosphate nanoparticles prevents influenza virus replication. **A:** Alexa488-labeled CaP nanoparticles were administered intranasally to BALB/c mice. After 4 h, lung lymph node cells were isolated and stained for CD11c. The percentage of Alexa488$^+$CD11c$^+$ DCs is shown. **B:** BALB/c mice were immunized intranasally with 50 µL of CpG/HA$_{512-520}$-functionalized CaP nanoparticles or soluble CpG plus HA$_{110-120;512-520}$ at the same concentrations on days 1, 14, and 28. Splenocytes from CaP nanoparticles-immunized mice were restimulated *in vitro* with 10 µg mL^{-1} of the HA$_{512-520}$ or HA$_{110-120}$ peptide. After 24 h, the numbers of IFN-γ-producing CD4$^+$ and CD8$^+$ T cells were determined by ELISpot in triplicate. Two independent experiments (five mice per group) were carried out. Bars represent mean ± SEM. **C:** Splenocytes of immunized mice were cultured in the presence of 10 µg mL^{-1} of the HA$_{512-520}$ or HA$_{110-120}$ peptide. After 48 h, supernatants were analyzed for indicated cytokines by Luminex technology. The figure illustrates the results of two independent experiments. Each data point represents one sample. * $p<0.05$, ** $p<0.01$, *** $p<0.001$, ns: not significant.

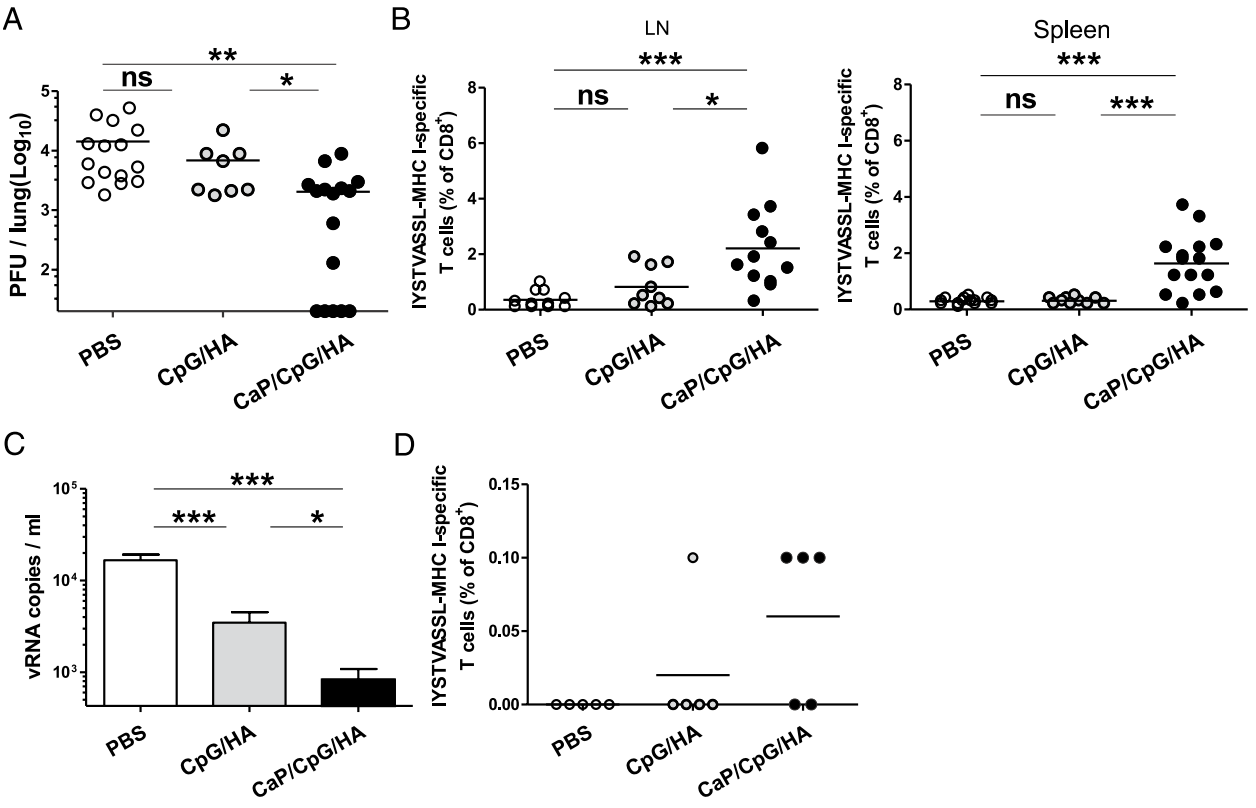

Figure 4.44 Intranasal immunization suppresses virus replication. **A:** 14 days after the third immunization, mice were challenged intranasally with 1,000 PFUs influenza virus A/PR/8/34. After 7 d, mice were sacrificed, and lung virus titers were measured by plaque assay; y-axis starts at the influenza virus detection limit. The figure illustrates the results from three independent experiments. **B:** Lung lymph node cells and total spleen cells from influenza-challenged mice (7 d after challenge) were stained for the presence of HA-specific $CD8^+$H-$2K^d$:$IYSTVASSL^+$ T cells. The figure illustrates the results from three independent experiments. **C:** 14 days after the third immunization, conscious mice were challenged intranasally with a 80,000 PFUs of influenza virus A/PR/8/34. Viral RNA was isolated on day 7 post infection from homogenized lungs. Viral copy numbers were determined by qPCR (five mice per group). The figure comprises the results of two independent experiments. Bars represent mean $\pm$ SEM. **D:** Lung lymph node cells from influenza-challenged mice (7 d after challenge) were stained for the presence of HA-specific $CD8^+$ H-$2K^d$:$IYSTVASSL^+$ T cells. Each data point represents one animal. * $p<0.05$, ** $p<0.01$, *** $p<0.001$, ns: not significant.

4.2.1.6 Results of intramuscular immunization with functionalized calcium phosphate nanoparticles

Although intranasal immunization represents an effective application route for inducing potent mucosal immune responses, it is not applicable for most of vaccination procedures on human. The predominant route for many viral vaccines including influenza is intramuscular (i.m.) injection. Thus, our final aim was to test the efficiency of functionalized CaP nanoparticles for i.m. immunization. We vaccinated mice according to the standard immunization protocol, but by i.m. injection. Two weeks after the last of the three immunizations, conscious mice were challenged with the influenza virus. In Figure 4.45, the results of this experiment are shown. Seven days after infection, only CaP/CpG/HA nanoparticles-immunized mice showed a viral RNA level in lungs below the detection limit (Figure 4.45 A). Moreover, this accelerated clearance of the virus from the lungs of mice immunized with CaP nanoparticles was accompanied by an elevated number of HA-specific $CD8^+$ T cells in the lung lymph nodes of challenged mice (Figure 4.45 B). In comparison, an i.m. immunization with soluble HA/CpG did not affect viral clearance.

Overall, these results indicate that MHC Class I and II HA peptides and TLR9 ligand CpG-functionalized CaP nanoparticles administered by various immunization routes (intraperitoneal and, more importantly, intranasal and intramuscular), are able to efficiently deliver antigen to DCs and drive sufficient maturation and signal transduction in DCs to facilitate antigen processing and presentation, thus inducing protective antiviral cellular immunity in mice.

Virus-specific $CD4^+$ and $CD8^+$ T cells in the lung are considered to provide protection against respiratory viruses like influenza. Since the lung is an entrance point for this kind of infection, particular attention should be paid to this organ as a target for mucosal immunization. It has been shown that antigens administrated by the mucosal route are poorly immunogenic because of the immunosuppressive environment, and that they often induce tolerance against viral

infections [319]. Therefore, it is preferable for mucosal vaccinations to use a delivery system that ensure both carrier and adjuvant functions. The functionalized nanoparticulate carrier, based on calcium phosphate, is easily taken up by cells and degraded in lysosomes. After release in the cytoplasm, the calcium ions are rapidly pumped out of the cell leaving the intracellular calcium concentration at a physiologically harmless level [320]. In addition, non-functionalized calcium phosphate nanoparticles showed no effect on DCs' maturation and activation, leaving this task to immunocompetent adjuvants, which can be efficiently loaded onto the nanoparticles.

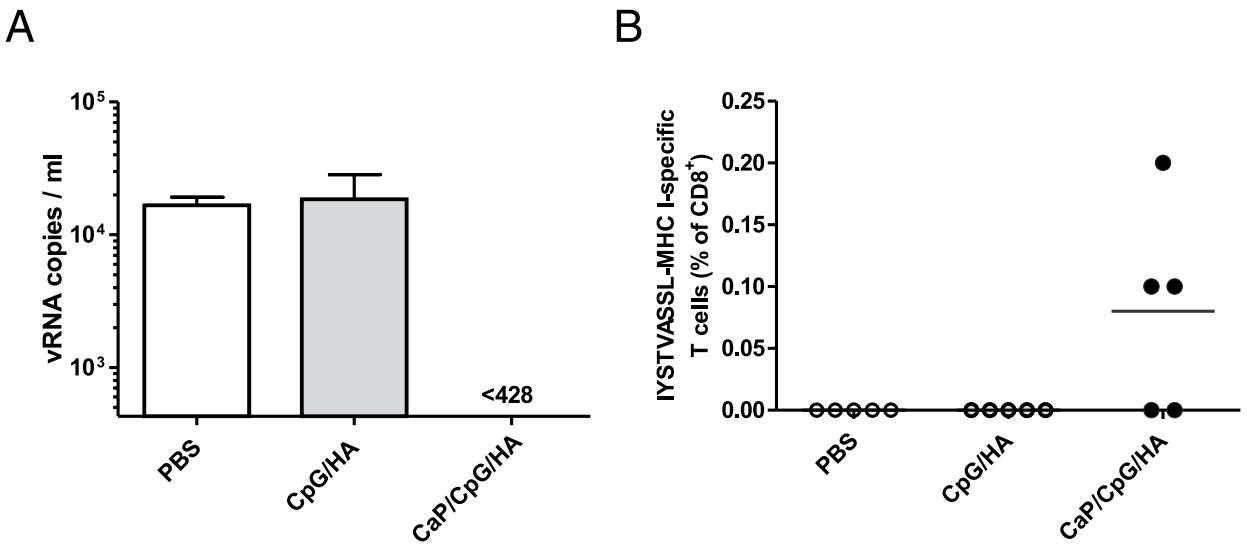

Figure 4.45 Intramuscular immunization with functionalized calcium phosphate nanoparticles prevents influenza virus replication. **A:** 14 days after the third i.m. immunization, conscious mice were challenged intranasally with 80,000 PFUs of influenza virus A/PR/8/34. Viral RNA was isolated on day 7 post infection from homogenized lungs. Viral copy numbers were determined by qPCR (five mice per group). The figure comprises the results of two independent experiments. Bars represent mean ± SEM. **B:** Lung lymph node cells from influenza-challenged mice (7 d after challenge) were stained for the presence of HA-specific $CD8^+$ H-$2K^d$:IYSTVASSL$^+$ T cells. Each data point represents one animal.

4.2.1.7 Conclusions

We have demonstrated that biodegradable calcium phosphate nanoparticles, functionalized with influenza virus antigen (HA) and TLR 9 ligand (unmethylated CpG) and introduced by various immunization routes, can provide an effective antiviral protection through driving the maturation of DCs and their subsequent activation and cross-presentation of the antigen to $CD4^+$ and $CD8^+$ T cells. Our results show that the calcium phosphate nanoparticles represent a perspective alternative and flexible vaccination tool that gives the opportunity to develop novel and effective vaccine delivery systems.

4.2.2 Functionalized calcium phosphate nanoparticles for vaccination against the Friend virus

In this study, we introduce CaP nanoparticles loaded with the Toll-like receptor 9 ligand CpG and the viral antigens GagL or gp70 derived from the Friend virus (FV) as vaccination tool for T cell-mediated immune response against retroviral infection, and more importantly for therapeutic treatment of chronic retroviral infection.

4.2.2.1 Synthesis and characterization of functionalized calcium phosphate nanoparticles

Multi-shell CaP nanoparticles were synthesized by a precipitation method and subsequent functionalized with TLR9 ligand CpG (63 μM=0.4 mg mL^{-1}) and Friend virus-specific T cell epitopes from Env-derived glycoprotein 70 (gp70, 1 mg mL^{-1}) and the leader region of Gag (GagL, 1 mg mL^{-1}) (see Subsection 3.3). Afterwards, another shell of calcium phosphate was attached to protect the biomolecules from the preliminary degradation, and finally, the nanoparticles were functionalized with CpG molecules for colloidal stabilization (Figure 4.46 A).

The final concentrations of molecules in the dispersion of nanoparticles were as follows: CpG=65.3 µg mL^{-1}, GagL and gp70=20.4 µg mL^{-1}. For a more detailed description of the synthesis process, refer to Subsection 3.1.1. Scanning electron microscopy micrographs of the functionalized nanoparticles demonstrated a spherical shape and high homogeneity of the nanoparticles (Figure 4.46 B).

The obtained nanoparticles were characterized by dynamic light scattering and nanoparticles tracking analysis to measure the hydrodynamic size. The surface charge of the functionalized particles is an important physicochemical parameter of the colloidal stability (Table 4.19). The average size of multi-shell nanoparticles in colloid dispersion was 125-130 nm. A strongly negative zeta potential (surface charge) of -21 mV, due to the negatively charged CpG molecules on the surface of the nanoparticles, ensures their stability in aqueous dispersion.

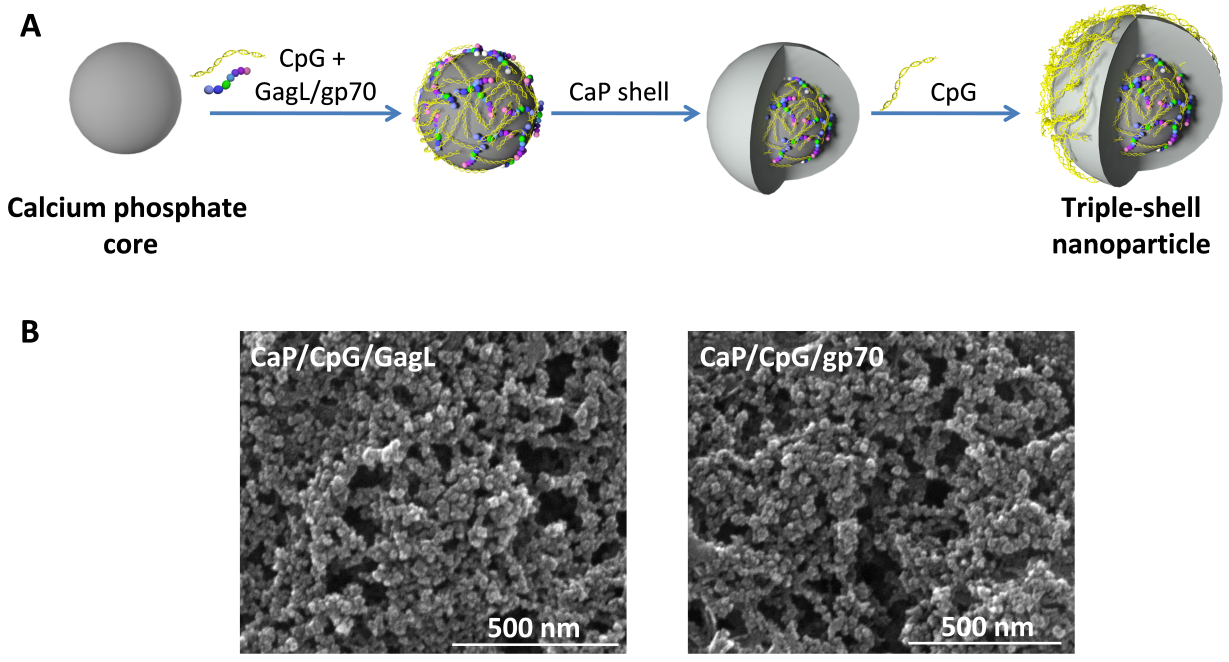

Figure 4.46 **A**: Schematic illustration of functionalized multi-shell calcium phosphate (CaP) nanoparticles. Multi-shell CaP nanoparticles consist of layers of calcium phosphate and Toll-like receptor ligand CpG (CaP/CpC+peptides/CaP/CpG). The core contains the antigenic peptides $GagL_{85-93}$ or $gp70_{123-141}$. **B**: SEM micrographs of calcium phosphate nanoparticles, functionalized with CpG and gp70 and GagL peptides.

Table 4.19 Colloid-chemical characterization of purified peptide-functionalized CaP/PEI nanoparticles by DLS and NTA and UV-Vis spectroscopy. PDI: polydispersity index from dynamic light scattering.

Sample	PDI	Size (DLS) /nm	Size (NTA) /nm	Zeta potential / mV
CaP/CpG/gp70	0.474	293	125	-20
CaP/CpG/GagL	0.253	289	129	-21

4.2.2.2 The induction of virus-specific T cell expansion *in vitro* and *in vivo* with calcium phosphate nanoparticles

The induction of FV-specific T cell proliferation by presenting encapsulated FV antigen ($CD4^+$ and $CD8^+$ epitope peptides) by targeted DCs on the major histocompatibility complex (MHC) Class I and MHC Class II was analyzed (Figure 4.47). For that, primary DCs from wild type mice were stimulated with functionalized CaP nanoparticles (CaP/CpG/gp70(GagL)). After 24 h, FV-specific $CD4^+$ or $CD8^+$ T cells were labeled with the proliferation dye eFluor670 and co-cultured with CaP nanoparticles-stimulated DCs. 72 h later, the proliferation of T cells was measured by loss of eFluor670 due to the distribution of the dye on daughter cell generations. As depicted in Figure 4.47 A and B, functionalized CaP nanoparticles-treated DCs strongly induced the proliferation of transgenic FV-specific $CD4^+$ and $CD8^+$ T cells *in vitro*.

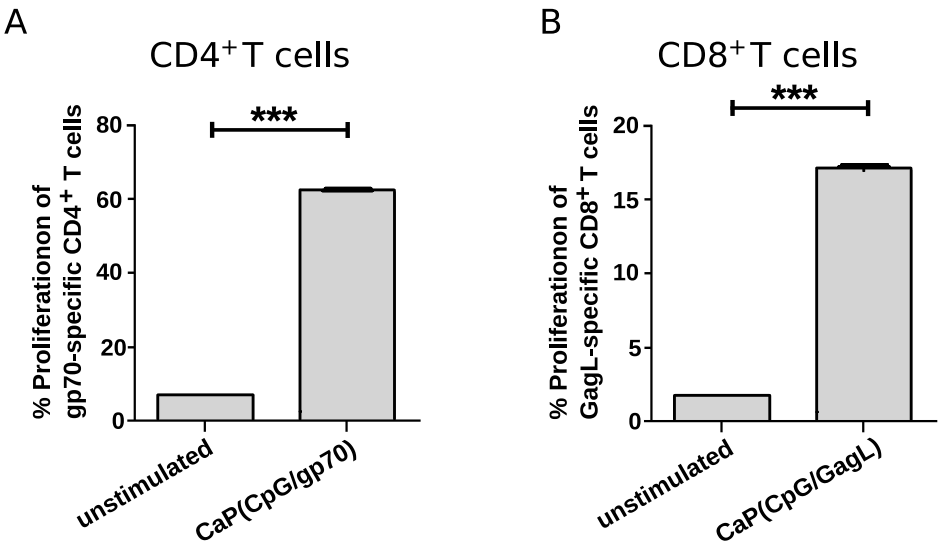

Figure 4.47 *In vitro* activation of DCs and FV-specific T cell responses. $CD11c^+$ splenic DCs were incubated with functionalized CaP nanoparticles. After 24 h, DCs were washed and co-cultured with eFluor670-labeled gp70-specific $CD4^+$(**A**) or GagL-specific $CD8^+$ T (**B**) cells for 72 h. Proliferation was measured by a loss of eFluor670 dye and was indicated as a percentage of proliferating cells. Representative histograms of proliferating $CD4^+$ or $CD8^+$ T cells are shown. The figure comprises results of 2 independent experiments. Representative histograms are shown. Bars represent mean ± SEM. *** $p<0.001$.

This is well in line with our results, as we have demonstrated that the nanoparticle-based uptake of a viral antigen, along with an adjuvant by APCs, is more sufficient to induce virus-specific $CD4^+$ and $CD8^+$ T cell responses *in vitro* and *in vivo*, compared to the uptake of soluble biomolecules. We used unmethylated Class B CpG as an adjuvant. CpG binds to TLR9 and is a well-established, safe molecule with clinical translational potential, as demonstrated by the findings of three completed clinical trials with CpG as a vaccine adjuvant [321]. CpG can evoke a range of immunostimulatory effects; it can enhance the activity of lymphocytes and APCs, trigger DC maturation, and drive the immune system toward the T_{H1} immune response against specific Ags [322]. This finding conforms to our results that immunization of mice with CaP nanoparticles functionalized with FV peptides and CpG induced IFN-γ-producing $CD4^+$ and $CD8^+$ effector T cells and significantly reduced the viral titers in acute and chronic retroviral infection.

In a recent study, we used poly(I:C) for the treatment of acute retroviral infection. In FV-infected animals, poly(I:C) treatment improved functional properties of virus-specific T cells and prevented virus-induced disease [323]. Therefore, it would be of great interest to test whether the incorporation of poly(I:C) or a combination of poly(I:C) and CpG into CaP nanoparticles would further improve the vaccination efficacy against retroviral infection. In general, we showed that poly(I:C)-functionalized CaP nanoparticles induce the maturation of DCs and T cells *in vitro* [313], but we have not yet tested these particles for vaccination.

To analyze the *in vivo* efficiency of functionalized CaP nanoparticles to induce FV-specific T cell response, naive FV-susceptible CB6F1 mice were subcutaneously immunized twice over a three-week interval either with PBS, soluble CpG/gp70/GagL, or with CpG/gp70/GagL-functionalized CaP nanoparticles in a prime-boost immunization (Figure 4.48). Two weeks after the last immunization, splenocytes of immunized mice were isolated, restimulated with GagL or gp70 peptides, and analyzed for the presence of IFN-γ-producing $CD4^+$ and $CD8^+$ T cells. As demonstrated in Figure 4.48, the number of IFN-γ-producing $CD4^+$ and $CD8^+$ T cells was the highest in mice immunized with functionalized CaP nanoparticles. These data indicate that immunization with CaP nanoparticles, functionalized with CpG, gp70, and GagL molecules, primes cellular immunity leading to the production of antiviral IFN-γ much stronger than immunization with soluble biomolecules. The applied dose of CpG was relatively low compared to other vaccine studies [324]. This impressively underlines the importance of the efficient delivery of the therapeutic agent. Here we could demonstrate that the CaP nanoparticle system was able to sufficiently induce effective immune responses even with a low concentration of adjuvants.

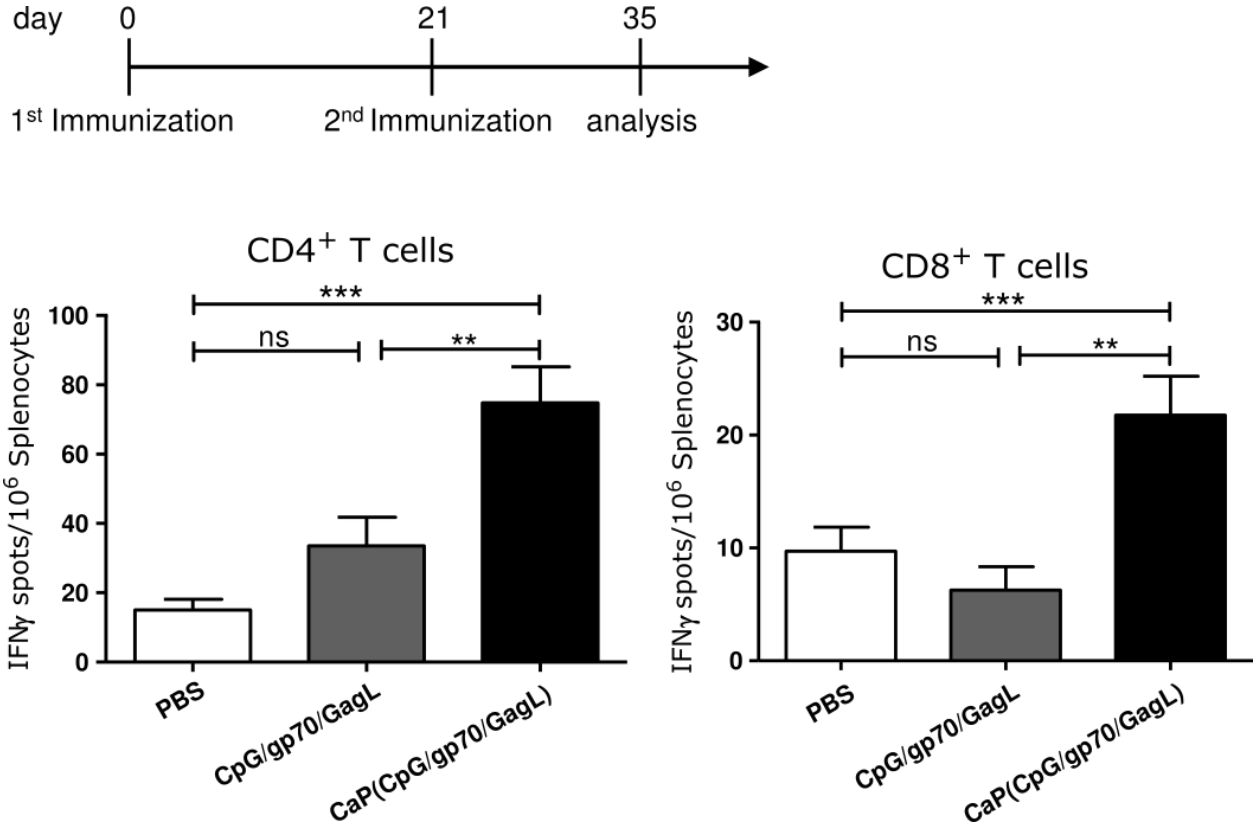

Figure 4.48 Induction of FV-specific T cell responses. FV-susceptible CB6F1 mice were immunized twice over a three-week interval with PBS, CpG/GagL/gp70 or CpG/GagL/gp70-functionalized CaP nanoparticles in a prime-boost immunization. Two weeks later, splenocytes from immunized mice were restimulated *in vitro* with $GagL_{85-93}$ or $gp70_{123-141}$ peptide. After 24 h, the numbers of IFN-γ-producing $CD4^+$ and $CD8^+$ T cells were determined by ELISpot. The figure comprises the results of 3 independent experiments. Bars represent mean ± SEM. ** $p<0.01$; *** $p<0.001$.

4.2.2.3 Results of prophylactic vaccination with calcium phosphate nanoparticles

To determine whether the nanoparticle-induced $CD4^+$ and $CD8^+$ T cells response confer protective immunity, FV-susceptible mice were challenged with a high dose (2,500 SFFU) of FV 3 weeks after the boost immunization (Figure 4.49 A). After the challenge, the disease score was monitored by the palpation of spleens, and spleen sizes were categorized as described before [322]. Remarkably, after infec-

tion only in the group of mice, immunized with CaP nanoparticles, splenomegaly was very rare and mild as demonstrated by the spleen weight on day 21 post infection (Figure 4.49 B and C).

In order to analyze vaccine-mediated control over acute FV replication, viral loads in plasma and in the spleen were determined on days 10 and 21 post infection, respectively. In all immunized mice, the mean viral loads were significantly reduced compared to unimmunized control mice. Importantly, in 80% of mice vaccinated with functionalized CaP nanoparticles, the virus was not detectable ($<10^2$ FFU), in comparison with 40% in the group of mice vaccinated with CpG/ gp70/GagL (Figure 4.50 D). The viral load in the spleen 21 days post infection was also reduced in both vaccine groups. However, the immunization with functionalized CaP nanoparticles showed the strongest reduction in the mean viral loads (Figure 4.50 E). These data clearly demonstrate the high potential of CaP nanoparticles to induce efficient antiretroviral immunity.

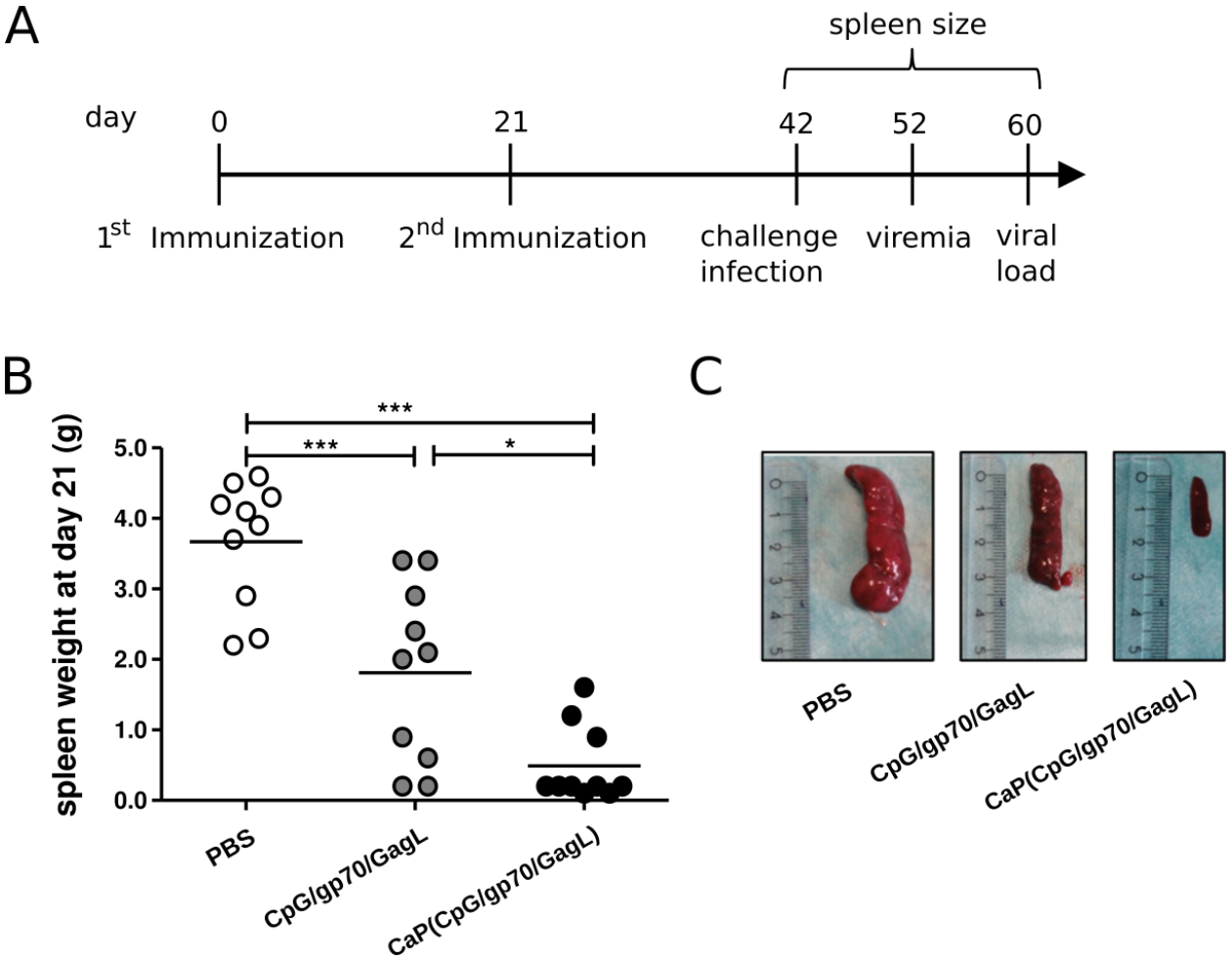

Figure 4.49 Vaccination with functionalized calcium phosphate nanoparticles confers protection from FV-induced splenomegaly and reduces viral loads **I**. **A:** FV-susceptible CB6F1 mice were immunized twice over a three-week interval with PBS, CpG/GagL/gp70 or CpG/GagL/gp70-functionalized CaP nanoparticles in a prime-boost immunization. Three weeks after boost immunization, mice were challenged with FV (2500 SFFU). **B:** Spleens were weighed 21 days post challenge infection. Spleen weight is depicted in gram (g). **C:** One representative spleen per group on day 21 is shown. Median values are indicated by horizontal lines. The figure comprises results of 2 independent experiments, each with 3-4 mice per group. * $p<0.05$; *** $p<0.001$.

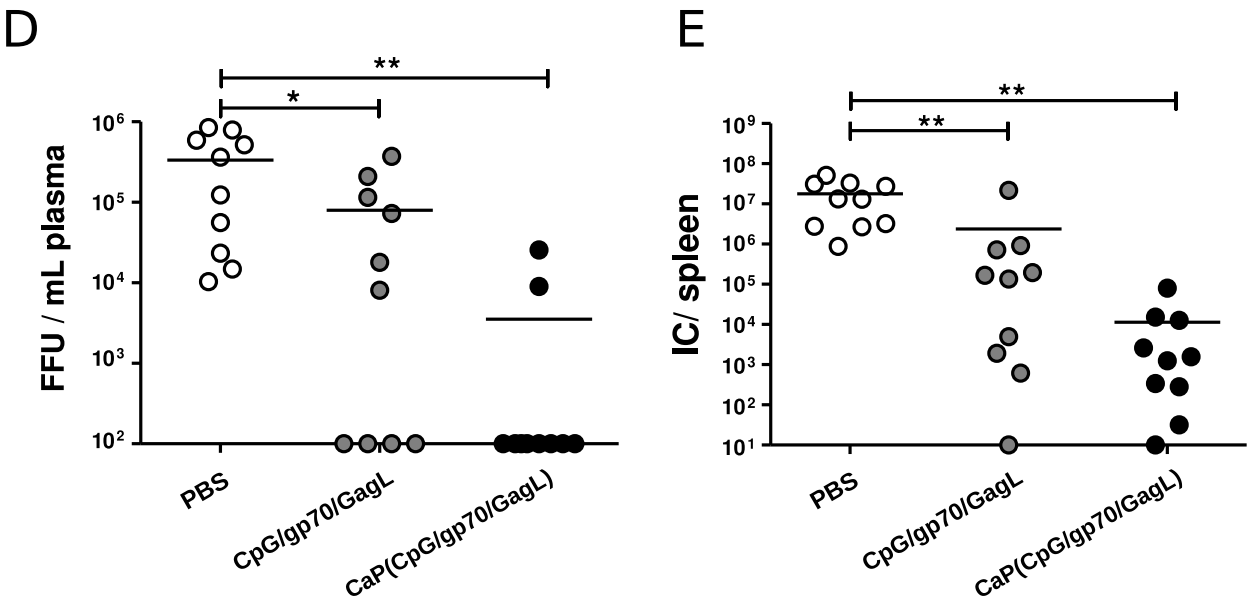

Figure 4.50 Vaccination with functionalized calcium phosphate nanoparticles confers protection from FV-induced splenomegaly and reduces viral loads **II**. **D:** Viral loads in the plasma of FV-infected mice were analyzed on day 10 after the challenge infection. Viremia levels are shown as FFU mL^{-1}. Median values are indicated by lines. **E:** On day 21 post challenge infection, viral loads in the spleen were analyzed. Viral loads are shown as IC/spleen. Median values are indicated by horizontal lines. The figure comprises results of 2 independent experiments, each with 3-4 mice per group. * $p<0.05$; ** $p<0.01$.

As previously reported, both $CD8^+$ and $CD4^+$ T cells are essential for controlling the FV infection [325, 326]. After deactivation of $CD8^+$ T cells by administration of anti-CD8 monoclonal antibodies in resistant mice, they fail to control acute virus replication and develop severe splenomegaly. $CD4^+$ T cells function during acute retrovirus infection mainly as T helper cells that activate other effector cell populations of the adaptive immune system [327, 328]. Thus, the depletion of $CD4^+$ and $CD8^+$ T cells during vaccination led to an abolishment of protection. It is relevant to use both T cell epitopes for vaccination against retroviral infection.

4.2.2.4 Results of therapeutic vaccination during chronic viral infection

The aim of therapeutic vaccination is to enhance adaptive immunity during a chronic infection and to reduce viral load. To test the efficiency of functionalized CaP nanoparticles in therapeutic vaccination against retroviral infection, resistant C57BL/6 mice were infected with a high dose of FV so that the chronic infection developed. After the establishment of chronic infection (>6 weeks after infection), mice were subcutaneously immunized once with either the solution of CpG/gp70/GagL, or CaP nanoparticles, functionalized with CpG, gp70, and GagL (Figure 4.53 A). One week after immunization, splenocytes and lymph node cells were isolated, restimulated with GagL or gp70 peptides and analyzed for the presence of IFN-γ-producing $CD4^+$ and $CD8^+$ T cells. As depicted in Figure 4.53 B and C, the highest number of IFN-γ-producing $CD4^+$ and $CD8^+$ T cells was in mice immunized with functionalized CaP nanoparticles, compared to non-vaccinated (PBS) or CpG/gp70/GagL-treated group.

In addition, a successful reactivation of cytotoxic T cells, which was demonstrated by a significant increase in the number of totally activated granzyme B (GzmB) expressing $CD4^+CD43^+GzmB^+$ and $CD8^+CD43^+GzmB^+$ T cells (Figure 4.52 D), was only found in the group of mice immunized with functionalized CaP nanoparticles. These activated cytotoxic virus-specific T cells are responsible for the reduction of the viral load in chronically retroviral infected mice. Therefore, the approach of combining virus-specific GagL and gp70 peptides and immunogenic adjuvant CpG to activation of peptide-specific T cell responses may find its application for controlling such retroviral infections as HIV [329].

It has recently been shown that regulatory T cells control virus-specific $CD8^+$ T cells during chronic FV infection [330]. Thus, we also determined the number of regulatory T cells in immunized mice and found that after immunization with functionalized CaP, their number was significantly decreased in comparison to non-immunized mice (Figure 4.52 E).

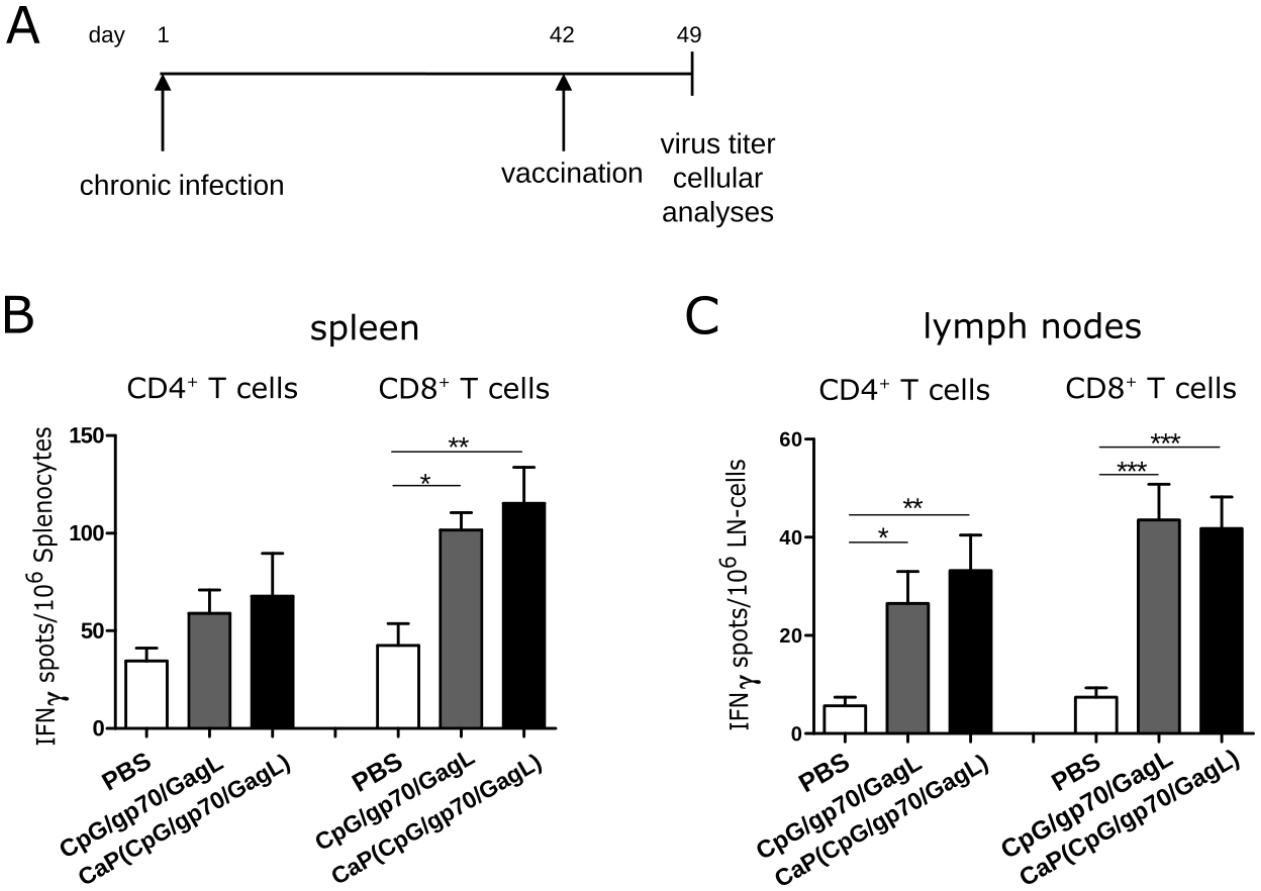

Figure 4.51 Therapeutic vaccination with functionalized calcium phosphate nanoparticles reactivates T cell immunity during chronic FV infection **I**. **A:** FV-resistant C57BL/6 mice were infected with 15,000 SFFU FV. Chronically (>6 weeks) infected mice were vaccinated once with PBS, CpG/GagL/gp70 or CpG/GagL/gp70-functionalized CaP nanoparticles. 7 days later, splenocytes **B** or lymph node cells **C** from vaccinated mice were restimulated *in vitro* with GagL or gp70 peptide. After 24 h, the numbers of IFN-γ-producing $CD4^+$ and $CD8^+$ T cells were determined by ELISpot. The figure illustrates the results of 2 independent experiments, each with 5 mice per group. Lines represent mean ± SEM. * $p<0.05$; ** $p<0.01$; *** $p<0.001$.

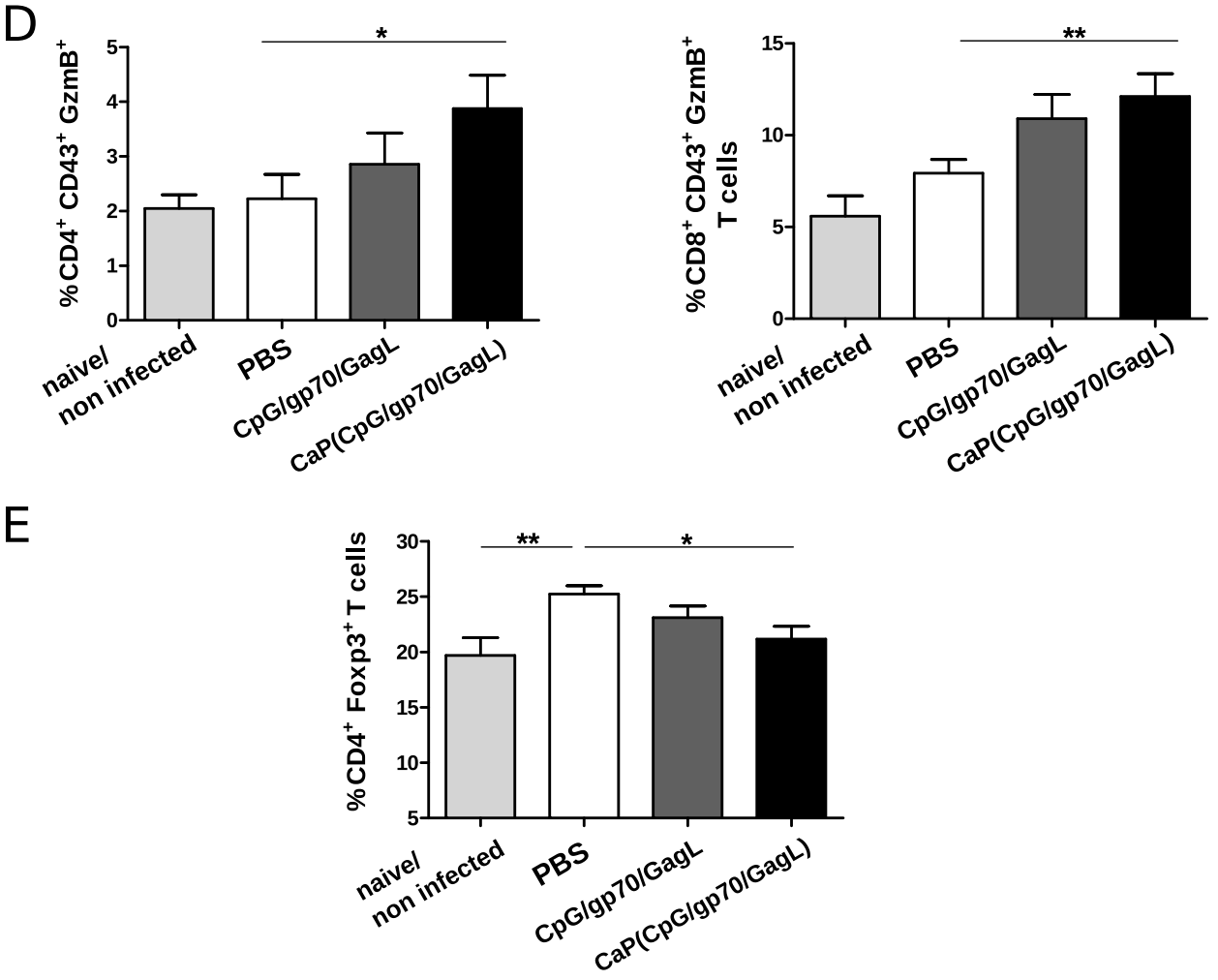

Figure 4.52 Therapeutic vaccination with functionalized calcium phosphate nanoparticles reactivates T cell immunity during chronic FV infection **II**. **D:** The number of activated cytotoxic $CD4^+$ and $CD8^+$ T cells in the spleen was analyzed by flow cytometry seven days after therapeutic vaccination. **E:** The percentage of $CD4^+Foxp3^+$ cells was analyzed by flow cytometry. The figure illustrates the results of 2 independent experiments, each with 5 mice per group. Lines represent mean $\pm$ SEM. * $p<0.05$; ** $p<0.01$.

The results of these *in vivo* experiments clearly demonstrate the high potential of the functionalized CaP nanoparticles as vaccine delivery system for therapeutic immunization against chronic retroviral infections.

Most importantly, a single-shot immunization with CpG/gp70/GagL-functionalized CaP nanoparticles during the chronic infection significantly reduced viral

loads in the spleen and lymph nodes of FV-infected mice, while the same viral antigens in soluble form did not (Figure 4.53 A). In addition, the statistical analysis demonstrates a clear correlation between the percentage of $CD8^+$ effector T cells and viral load. The higher the number of $CD8^+$ effector T cells detected in the spleen, the lower was the viral load (Figure 4.53 B). These results suggest that functionalized CaP nanoparticles are a promising tool to develop an effective therapeutic vaccines.

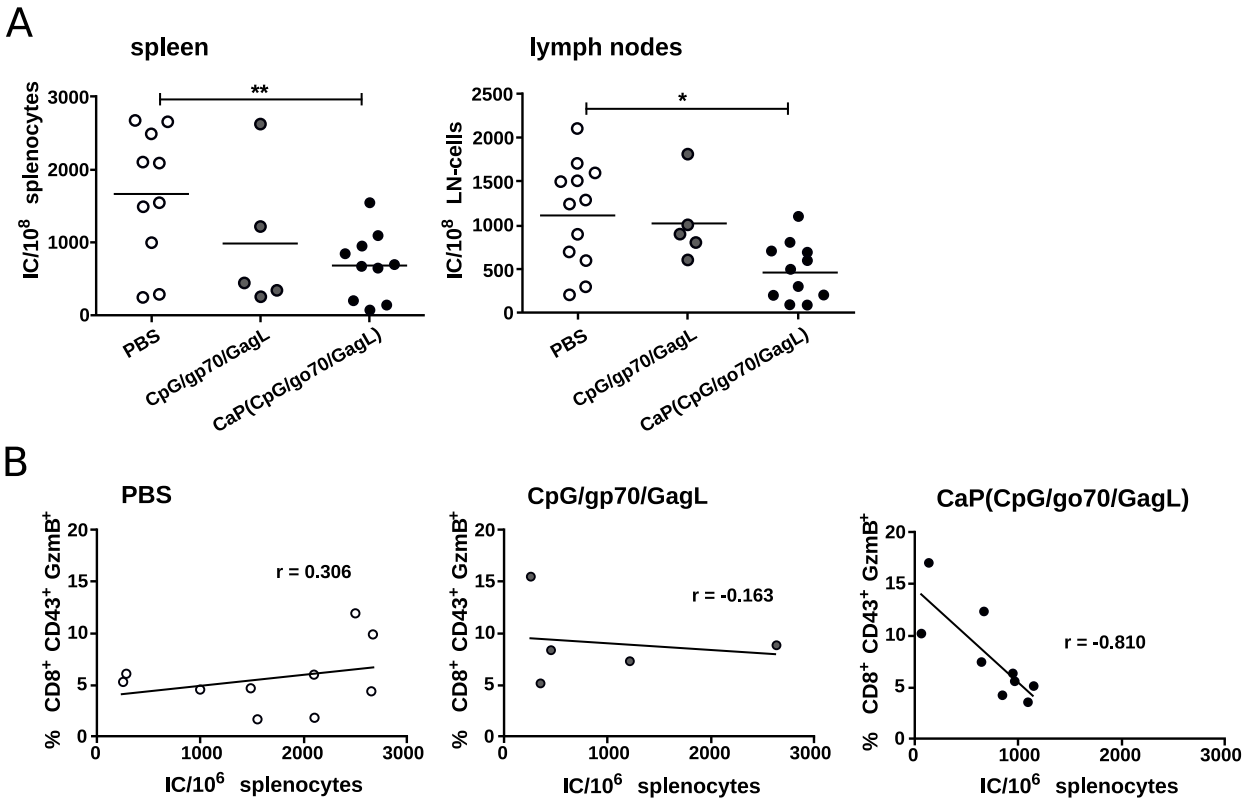

Figure 4.53 Therapeutic vaccination with functionalized calcium phosphate nanoparticles reduces viral loads. **A:** 7 days after vaccination of chronically infected mice, viral loads in the spleens and peripheral lymph nodes were analyzed. Viral loads are shown as IC/spleen. The figure illustrates results of 2 independent experiments, each with 3-5 mice per group. Lines represent mean values. **B:** The percentage of $CD8^+$ effector T cells negatively correlates with the viral load in the spleen only after immunization with CpG/gp70/GagL-functionalized CaP nanoparticles. * $p<0.05$; ** $p<0.01$.

4.2.2.5 Results of therapeutic immunization with functionalized calcium phosphate nanoparticles combined with depletion of regulatory T cells during chronic viral infection

Regulatory T cells (Tregs) are a subset of $CD4^+$ T lymphocytes with the ability to suppress the immune system for down-regulation of the immune system so that no autoimmune disorders occurs. They play a key role in the establishment and/or maintenance of chronic viral infection and constitute a barrier to efficient vaccination and immunotherapy strategies [331]. The involvement of regulatory T cells in the development of chronic viral infection was first described in mice infected with FV [332] and was then extended to other persistent viruses including HIV [333]. It is becoming increasingly clear that controlling this immunosuppressive cell subset would have widespread clinical applications to fight life-threatening viral diseases. Our results show that a sufficient reactivation of antiviral T cell immune response with an adequate vaccination vehicle such as CaP nanoparticles can overcome the suppressive barrier of Tregs and lead to a significant reactivation of T cell immunity.

It has been shown recently that transient depletion of regulatory T cells during a chronic phase of retroviral infection helps exhausted $CD8^+$ T cells to regain their antiviral function. We aimed to check whether the depletion of regulatory T cells before immunization could improve the efficacy of functionalized CaP nanoparticles. For this experiment, we used DEREG mice in which regulatory T cells were selectively eliminated by the injection of diphtheria toxin (DT) to establish chronic FV infection. 6 weeks after infection, the mice were treated with DT 4 and 2 days before as well as 2 and 4 days after the immunization with CpG/gp70/GagL-functionalized CaP nanoparticles (Figure 4.54 A). This resulted in more than 95% depletion of regulatory T cells (Figure 4.54 B). 7 days after the immunization, isolated splenocytes were restimulated with GagL or gp70 peptides and analyzed for the number of IFN-γ-producing $CD4^+$ and $CD8^+$ T cells. Interestingly, the combination of regulatory T cells depletion and immunization had further ele-

vated the number of IFN-γ producing $CD4^+$ and $CD8^+$ T cells (Figure 4.54 C). In addition, as shown in Figure 4.55 D, the strongest increase in the frequency of total activated cytotoxic $CD4^+CD43^+GzmB^+$ and $CD8^+CD43^+GzmB^+$ T cells was observed under the combination of regulatory T cell depletion and immunization with CpG/gp70/GagL-functionalized CaP nanoparticles. Although single-shot immunization with functionalized CaP nanoparticles during the chronic state of FV infection already significantly reduced viral loads in the spleen, the additional depletion of regulatory T cells during the immunization process further enhanced this effect (Figure 4.55 E).

The combination of depletion of regulatory T cells and therapeutic immunization with functionalized CaP nanoparticles of chronically infected mice resulted in the lowest viral loads in the spleen of all other subsets tested in this study. Consequently, our findings support the statement that the modulation of this immunosuppressive cell subset is an important part of a successful antiviral therapeutic vaccination.

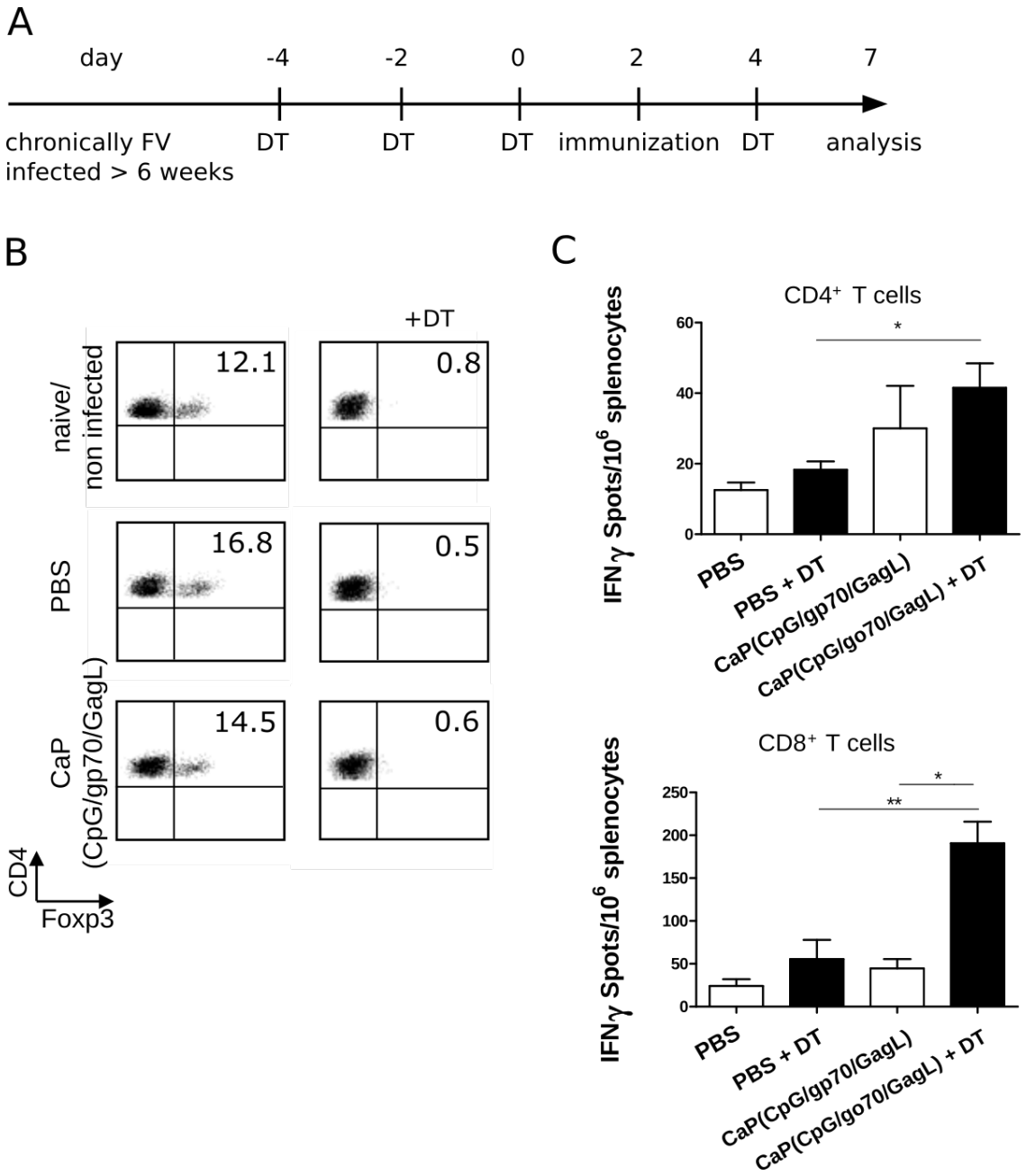

Figure 4.54 Transient depletion of regulatory T cells enhances the viral clearance after therapeutic calcium phosphate nanoparticle vaccination **I**. **A:** Transgenic DEREG mice on C57BL6 background were chronically infected with FV (>6 weeks). Regulatory T cells were depleted by peritoneal injection of diphtheria toxin (DT) on day 4 and 2 prior to and on day 2 and 4 after vaccination. **B:** The depletion of regulatory T cells is depicted by representative flow cytometry plots. **C:** 7 days later, splenocytes from vaccinated mice were restimulated *in vitro* with GagL or gp70 peptide. The numbers of IFN-γ-producing $CD4^+$ and $CD8^+$ T cells were determined by ELISpot. * $p<0.05$; ** $p<0.005$.

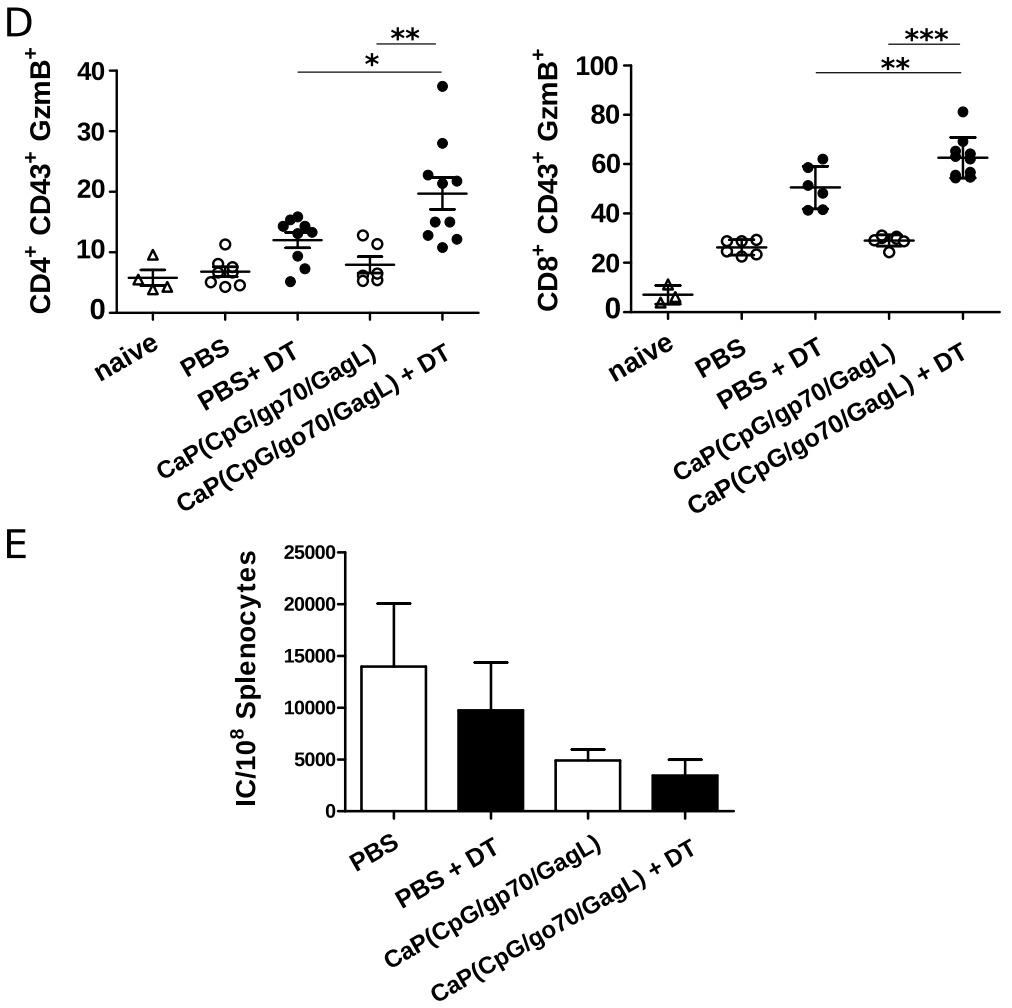

Figure 4.55 Transient depletion of regulatory T cells enhances the viral clearance after therapeutic calcium phosphate nanoparticle vaccination **II**. **D:** The number of activated cytotoxic $CD4^+$ and $CD8^+$ T cells in the spleen was analyzed by flow cytometry 7 days after the therapeutic vaccination. **E:** Viral loads in the spleens of DEREG mice were analyzed 7 days after the vaccination. Viral loads are shown as IC/spleen. The figure illustrates the results of 3 independent experiments, each with 4 mice per group. Bars represent mean ± SEM. * $p<0.05$; ** $p<0.005$; *** $p<0.0005$.

4.2.2.6 Conclusions

In summary, we demonstrated that immunization with antigen/adjuvant-functionalized CaP nanoparticles can efficiently induce the maturation of DCs and the subsequent activation and proliferation of virus-specific $CD4^+$ and $CD8^+$ T cell

response against acute as well as chronic retroviral infection on the FV infection model in mice. Furthermore, therapeutic single-shot immunization with functionalized CaP nanoparticles significantly reduced the viral loads. We have also demonstrated that the depletion of regulatory T cells during the therapeutic vaccination can significantly improve the treatment of chronic retroviral infection.

4.2.3 Summary

The data reported in this section clearly demonstrate the high potential of antigen/-adjuvant-functionalized CaP nanoparticles for the induction of protective antiviral immunity. Our results show that calcium phosphate nanoparticles represent a perspective alternative and flexible vaccination tool that allows controlled and accessible loading of various immunoactive molecules, thus giving the opportunity to develop flexible and effective vaccine delivery systems.

Owing to their comparable size and controlled composition (i.e. functionalization with different adjuvants and viral epitopes), nanoparticles can mimic the virus particles while at the same time avoiding side effects that are associated with the application of live or attenuated viruses for active immunization. They represent a powerful and novel tool for developing vaccines against various life-threatening infectious diseases.

5 Summary and Conclusions

In this work, the synthesis, characterization, and application possibilities of calcium phosphate nanoparticles functionalized with various biological and synthetic molecules in bio- and nanomedicine were investigated. Nanoparticles stabilized with different polyelectrolytes (PEI, CMC, or nucleic acids) and loaded with peptides, proteins, oligonucleotides, nucleic acids, porphyrins, polymers, and other molecules were synthesized and characterized with different physicochemical methods. The number of fluorescently labeled cargo molecules adsorbed onto the surface of the nanoparticles were determined by UV-Vis spectroscopy.

In order to study the cellular uptake of cargo-loaded calcium phosphate nanoparticles, *in vitro* experiments on HeLa, MG-63, THP-1 and hMSC cells were carried out. Light and fluorescence microscopy as well as CLSM imaging of the cells showed a high level of calcium phosphate nanoparticle internalization, regardless of the type of cargo molecule present in the nanoparticles. In contrast, dissolved molecules alone were usually not able to penetrate the cell membrane. Moreover, by using different inhibitors of endocytotic pathways on MG-63 cell line, it was observed that nanoparticles were taken up by caveolin-mediated endocytosis. Free protein molecules (HTRA1), however, used the routes other than endocytosis, which are yet to be determined.

It was also investigated how the biological milieu influenced the activity of enzyme-inhibiting polymer on the example of lysozyme. Calcium phosphate nanoparticles, functionalized with lysozyme-inhibiting polymer, were taken up by THP-1 cell line within 3 h of incubation as it was demonstrated by confocal laser scanning microscopy of the treated cells. Nevertheless, the expected significant inhibitory effect of the polymer inside the living cells, as well as in the cell culture

medium, was absent. The experiments in phosphate buffer, cell culture medium with and without FCS, with free polymer and lysozyme showed a dramatic impact of the experimental conditions on the effectiveness of the lysozyme-inhibitor polymer. The inhibitory effect of the polymer was clearly shown in phosphate buffer solution in a dose-dependent manner. In the presence of the cell culture medium containing various biological molecules, the inhibition of lysozyme decreased essentially and could be detected only at the highest concentration of polymer, and only up to 40%. Furthermore, when the cell culture medium was supplemented with 10% of FCS, no inhibitory effect was found. This may serve as evidence for the low specificity of the inhibitory polymer to target molecule. The polymer molecules interacted with other biomolecules contained in large quantities in cell culture media.

Another set of experiments was dedicated to the investigation of calcium phosphate nanoparticles as potent vaccination tool. The ability of nanoparticles, loaded with immunoactive molecules like CpG, influenza virus hemagglutinin, and Friend virus-derived proteins to stimulate the immune response, were tested *in vitro* on antigen-presenting cells (DCs) and $CD4^+$ and $CD8^+$ T cells. These functionalized nanoparticles performed significantly effectively compared to control groups, driving the maturation of DCs and subsequent promotion of the proliferation of virus-specific $CD4^+$ and $CD8^+$ T cells. Furthermore, *in vivo* studies with immunization of mice against influenza virus and Friend virus, as a retroviral mouse model, showed that the nanoparticles were able to activate the immune response and helped to clear the viral load in infected mice better than in control groups where immunoactive molecules were injected in a soluble form.

Summarizing, one can say that calcium phosphate-based nanoparticles can serve as an effective and biocompatible carrier system that can be used for many applications in bio- and nanomedicine.

5.1 Zusammenfassung

In dieser Arbeit wurden Calciumphosphat-Nanopartikel synthetisiert, mit verschiedenen biologischen und synthetischen Molekülen funktionalisiert und hinsichtlich potenzieller Anwendungsmöglichkeiten in Bio- und Nanomedizin untersucht. Die Nanopartikel wurden mit unterschiedlichen Polyelektrolyten (PEI, CMC oder DNA) stabilisiert und mit Peptiden, Proteinen, Oligonukleotiden, Nukleinsäuren, Polymeren und anderen Molekülen beladen. Danach wurden die Partikel mittels unterschiedlichen physikalisch-chemischen Methoden charakterisiert. Die Menge an fluoreszenzmarkierten Molekülen, die auf der Oberfläche der Nanopartikel adsorbiert waren, wurde mit UV-Vis-Spektroskopie bestimmt.

Um die zelluläre Aufnahme von beladenen Calciumphosphat-Nanopartikeln zu untersuchen, wurden *in vitro*-Versuche an HeLa, MG-63, THP-1 und hMSC-Zellen durchgeführt. Licht- und Fluoreszenz-Mikroskopie sowie CLSM der Zellen zeigten eine effiziente Internalisierung von Molekülen zusammen mit den Calciumphosphat-Nanopartikeln. Im Gegensatz dazu waren gelöste Moleküle allein im Allgemeinen nicht in der Lage, die Zellmembran zu durchdringen. Darüber hinaus wurde durch die Verwendung verschiedener Inhibitoren an MG-63-Zellen festgestellt, dass die Nanopartikel durch Caveolin-vermittelte Endozytose aufgenommen wurden. Freie HTRA1-Proteinmoleküle hingegen gelangten durch die anderen Aufnahmewege in die Zellen, die noch zu bestimmen sind.

Außerdem wurde am Beispiel des Lysozyms untersucht, wie das biologische Milieu die Aktivität eines enzymhemmenden Polymers beeinflusst. Calciumphosphat-Nanopartikel, wurden mit Lysozym-inhibierendem Polymer funktionalisiert. Nach 3 h Inkubation wurden sie von THP-1 Zellen aufgenommen, wie es auf CLSM-Aufnahmen von behandelten Zellen zu sehen war. Dennoch war die erwartete signifikante Hemmwirkung des Polymers sowohl innerhalb der lebenden Zelle als auch im Zellkulturmedium nicht vorhanden. Die durchgeführten Experimente in Phosphatpuffer, Zellkulturmedium mit und ohne FCS, mit freiem Poly-

mer und Lysozym, und in Abwesenheit von Zellen sowie Nanopartikeln deuteten auf einen grundlegenden Einfluss der experimentellen Bedingungen hin. Die hemmende Wirkung des Polymers konnte im Fall der Phosphatpufferlösung in dosisabhängiger Weise deutlich festgestellt werden. Im Vergleich dazu konnte die Hemmung von Lysozym im Zellmedium nur bei der höchsten Polymer-Konzentration und nur bis zu 40% festgestellt werden. Außerdem ging die hemmende Wirkung gänzlich verloren, wenn das Zellkulturmedium mit 10% FCS ergänzt wurde. Dies könnte auf eine geringe Spezifität der hemmenden Polymermoleküle hindeuten, die offenbar mit anderen Biomolekülen, die in großen Mengen in biologischen Lösungen wie dem Zellkulturmedium enthalten sind, in Wechselwirkung treten könnten.

Eine weitere Reihe von Experimenten wurde der Untersuchung der Calciumphosphat-Nanopartikel als potenziellem neuartigem Impfsystem gewidmet. Die Fähigkeit von Nanopartikeln, die mit immunoaktiven Molekülen wie CpG, Influenzavirus-Hämagglutinin oder von Friend Virus-abgeleiteten Proteinen beladen wurden, um eine Immunantwort zu stimulieren, wurden zunächst *in vitro* auf Antigenpräsentierenden dendritischen Zellen (DCs), $CD4^+$ und $CD8^+$ T-Zellen getestet. Diese funktionalisierten Nanopartikel riefen im Vergleich zu den Kontrollgruppen eine signifikant höhere Reifung der DCs hervor. Dadurch wurde die Proliferation von Virus-spezifischen $CD4^+$ und $CD8^+$ T-Zellen effektiv stimuliert. Zusätzlich zeigten die *in vivo*-Studien zur Immunisierung von Mäusen gegen Influenza-Virus und Friend-Virus (ein Retrovirus-Modell), dass die Nanopartikel eine Immunantwort aktivieren konnten und dazu beigetragen haben, die Viruslast in infizierten Mäusen deutlich zu verringern. Die signifikante Verbesserung der Immunantwort im Vergleich zur Immunisierung nur mit den löslichen immunaktiven Molekülen wurde nachgewiesen.

Zusammenfassend konnte festgestellt werden, dass dieses auf Calciumphosphat-Nanopartikeln basierende Trägersystem vielseitige Anwendungsmöglichkeiten für Bio- und Nanomedizin bieten kann.

Bibliography

[1] F. Livingston, A. Hopkins, and B. Weille, *Crosslink Magazine*, 12, **2011**.

[2] G. Nohynek, E. Dufour, and M. Roberts, *Skin Pharmacol. Physiol.*, 21, 136–149, **2008**.

[3] R. Feynman, *"Plenty of Room at the Bottom", American Physical Society*, **1959**.

[4] N. Taniguchi, *Proc. Intl. Conf. Prod. Eng. Part II*, 18–23, **1974**.

[5] E. K. Chow and D. Ho, *Sci. Transl. Med.*, 5, p. 216rv4, **2013**.

[6] S. K. Sahoo and V. Labhasetwar, *Drug Discov. Today*, 8, 1112–1120, **2003**.

[7] S. Nie, Y. Xing, G. J. Kim, and J. W. Simons, *Annu. Rev. Biomed. Eng.*, 9, 257–288, **2007**.

[8] K. K. Jain, *Clin. Chim. Acta*, 358, 37–54, **2005**.

[9] S. A. Wickline and G. M. Lanza, *Circulation*, 107, 1092–1095, **2003**.

[10] H. Liu and T. J. Webster, *Biomaterials*, 28, 354–369, **2007**.

[11] E. Engel, A. Michiardi, M. Navarro, D. Lacroix, and J. A. Planell, *Trends Biotechnol.*, 26, 39–47, **2008**.

[12] O. Rotan, V. Sokolova, P. Gilles, W. Hu, S. Dutt, T. Schrader, and M. Epple, *Materwiss Werksttech*, 44, 176–182, **2013**.

[13] J. Ruesing, O. Rotan, C. Gross-Heitfeld, C. Mayer, and M. Epple, *J. Mater. Chem. B*, 2, 4625–4630, **2014**.

[14] T. Tenkumo, O. Rotan, V. Sokolova, and M. Epple, *Nano Biomed.*, 5, 64–74, **2013**.

[15] M. L. Etheridge, S. A. Campbell, A. G. Erdman, C. L. Haynes, S. M. Wolf, and J. McCullough, *Nanomedicine*, 9, 1–14, **2013**.

[16] Terminology for nanomaterials. Publicly available specification 136, British Standards Institution (www.shop.bsigroup.com), **2007**.

[17] A. M. Smith and S. Nie, *Acc. Chem. Res.*, 43, 190–200, **2010**.

[18] M. C. Daniel and D. Astruc, *Chem. Rev.*, 104, 293–346, **2004**.

[19] Pilot study of Aurolase(TM) therapy in refractory and/or recurrent tumors of the head and neck, Nanospectra Biosciences, Inc. (www.clinicaltrials.gov), **2015**.

[20] D. C. Litzinger, A. M. Buiting, N. van Rooijen, and L. Huang, *Biochim. Biophys. Acta*, 1190, 99–107, **1994**.

[21] D. P. O'Neal, L. R. Hirsch, N. J. Halas, J. D. Payne, and J. L. West, *Cancer Lett.*, 209, 171–176, **2004**.

[22] L. Y. Chou, K. Ming, and W. C. Chan, *Chem. Soc. Rev.*, 40, 233–245, **2011**.

[23] B. D. Chithrani, A. A. Ghazani, and W. C. Chan, *Nano Lett.*, 6, 662–668, **2006**.

[24] M. J. Clift, B. Rothen-Rutishauser, D. M. Brown, R. Duffin, K. Donaldson, L. Proudfoot, K. Guy, and V. Stone, *Toxicol. Appl. Pharmacol.*, 232, 418–427, **2008**.

[25] C. L. Hardy, J. S. Lemasurier, R. Mohamud, J. Yao, S. D. Xiang, J. M. Rolland, R. E. O'Hehir, and M. Plebanski, *J. Immunol.*, 191, 5278–5290, **2013**.

[26] M. Geiser, O. Quaile, A. Wenk, C. Wigge, S. Eigeldinger-Berthou, S. Hirn, M. Schaffler, C. Schleh, W. Moller, M. A. Mall, and W. G. Kreyling, *Part. Fibre Toxicol.*, 10, p. 19, **2013**.

[27] What's so special about the Nanoscale, United States National Nanotechnology Initiative (www.nano.gov).

[28] Y. Xia, Y. Xiong, B. Lim, and S. E. Skrabalak, *Angew. Chem. Int. Ed. Engl.*, 48, 60–103, **2009**.

[29] D. Peer, J. M. Karp, S. Hong, O. C. Farokhzad, R. Margalit, and R. Langer, *Nat. Nanotechnol.*, 2, 751–760, **2007**.

[30] Z. Zhang, S. Tongchusak, Y. Mizukami, Y. J. Kang, T. Ioji, M. Touma, B. Reinhold, D. B. Keskin, E. L. Reinherz, and T. Sasada, *Biomaterials*, 32, 3666–3678, **2011**.

[31] I. H. El-Sayed, X. Huang, and M. A. El-Sayed, *Cancer Lett.*, 239, 129–135, **2006**.

[32] T. Paunesku, T. Rajh, G. Wiederrecht, J. Maser, S. Vogt, N. Stojičevič, M. Protič, B. Lai, J. Oryhon, M. Thurnauer, and G. Woloschak, *Nat. Mater.*, 2, 343–346, **2003**.

[33] J. S. Kim, E. Kuk, K. N. Yu, J. H. Kim, S. J. Park, H. J. Lee, S. H. Kim,

Y. K. Park, Y. H. Park, C. Y. Hwang, Y. K. Kim, Y. S. Lee, D. H. Jeong, and M. H. Cho, *Nanomedicine*, 3, 95–101, **2007**.

[34] M. Liong, J. Lu, M. Kovochich, T. Xia, S. G. Ruehm, A. E. Nel, F. Tamanoi, and J. I. Zink, *ACS Nano*, 2, 889–896, **2008**.

[35] H. Meng, W. X. Mai, H. Zhang, M. Xue, T. Xia, S. Lin, X. Wang, Y. Zhao, Z. Ji, J. I. Zink, and A. E. Nel, *ACS Nano*, 7, 994–1005, **2013**.

[36] H. Meng, M. Xue, T. Xia, Z. Ji, D. Tarn, J. Zink, and A. Nel, *ACS Nano*, 5, 4131–4144, **2011**.

[37] J. Kim, J. E. Lee, J. Lee, J. H. Yu, B. C. Kim, K. An, Y. Hwang, C. H. Shin, J. G. Park, J. Kim, and T. Hyeon, *J. Am. Chem. Soc.*, 128, 688–689, **2006**.

[38] K. Ajima, T. Murakami, Y. Mizoguchi, K. Tsuchida, T. Ichihashi, S. Iijima, and M. Yudasaka, *ACS Nano*, 2, 2057–2064, **2008**.

[39] K. Ajima, M. Yudasaka, T. Murakami, A. Maigne, K. Shiba, and S. Iijima, *Mol. Pharm.*, 2, 475–480, **2005**.

[40] A. Bianco, K. Kostarelos, and M. Prato, *Curr. Opin. Chem. Biol.*, 9, 674–679, **2005**.

[41] Z. Liu, K. Chen, C. Davis, S. Sherlock, Q. Cao, X. Chen, and H. Dai, *Cancer Res.*, 68, 6652–6660, **2008**.

[42] Z. Liu, S. M. Tabakman, Z. Chen, and H. Dai, *Nat. Protoc.*, 4, 1372–1382, **2009**.

[43] X. Q. Chow, E. K. Zhang, M. Chen, R. Lam, E. Robinson, H. Huang, D. Schaffer, E. Osawa, A. Goga, and D. Ho, *Sci. Transl. Med.*, 3, p. 73ra21, **2011**.

[44] H. Huang, E. Pierstorff, E. Osawa, and D. Ho, *Nano Lett.*, 7, 3305–3314, **2007**.

[45] H. Huang, E. Pierstorff, E. Osawa, and D. Ho, *ACS Nano*, 2, 203–212, **2008**.

[46] V. N. Mochalin, O. Shenderova, D. Ho, and Y. Gogotsi, *Nat. Nanotechnol.*, 7, 11–23, **2011**.

[47] K. K. Liu, W. W. Zheng, C. C. Wang, Y. C. Chiu, C. L. Cheng, Y. S. Lo, C. Chen, and J. I. Chao, *Nanotechnology*, 21, p. 315106, **2010**.

[48] V. P. Torchilin, *J. Control. Release*, 73, 137–172, **2001**.

[49] B. M. Discher, Y. Y. Won, D. S. Ege, J. C. Lee, F. S. Bates, D. E. Discher, and D. A. Hammer, *Science*, 284, 1143–1146, **1999**.

[50] A. K. Patri, I. J. Majoros, and J. R. Baker, *Curr. Opin. Chem. Biol.*, 6, 466–471, **2002**.

[51] R. Langer and N. A. Peppas, *AIChE J.*, 49, 2990–3006, **2003**.

[52] R. K. O'Reilly, C. J. Hawker, and K. L. Wooley, *Chem. Soc. Rev.*, 35, 1068–1083, **2006**.

[53] C. J. Hawker and K. L. Wooley, *Science*, 309, 1200–1205, **2005**.

[54] L. M. Ensign, B. C. Tang, Y. Y. Wang, T. A. Tse, T. Hoen, R. Cone, and J. Hanes, *Sci. Transl. Med.*, 4, p. 138ra79, **2012**.

[55] E. A. Nance, G. F. Woodworth, K. A. Sailor, T. Y. Shih, Q. Xu, G. Swaminathan, D. Xiang, C. Eberhart, and J. Hanes, *Sci. Transl. Med.*, 4, p. 149ra119, **2012**.

[56] N. Peppas, J. Hilt, A. Khademhosseini, and R. Langer, *Adv. Mater.*, 18, 1345–1360, **2006**.

[57] O. C. Farokhzad, S. Jon, A. Khademhosseini, T. N. Tran, D. A. Lavan, and R. Langer, *Cancer Res.*, 64, 7668–7672, **2004**.

[58] A. Khademhosseini and R. Langer, *Chem. Eng. Prog.*, 102, 38–42, **2006**.

[59] D. S. Katti, K. W. Robinson, F. K. Ko, and C. T. Laurencin, *J. Biomed. Mater. Res. Part B Appl. Biomater.*, 70, 286–296, **2004**.

[60] J. D. Hartgerink, E. Beniash, and S. I. Stupp, *Proc. Natl. Acad. Sci. U.S.A*, 99, 5133–5138, **2002**.

[61] M. E. Fox, F. C. Szoka, and J. M. Frechet, *Acc. Chem. Res.*, 42, 1141–1151, **2009**.

[62] C. Schwarz, W. Mehnert, J. S. Lucks, and R. H. Müller, *J. Control. Release*, 30, 83–96, **1994**.

[63] A. Mirza and F. Siddiqui, *Int. Nano Lett.*, 4, p. 94, **2014**.

[64] V. Sokolova, A. Kovtun, O. Prymak, W. Meyer-Zaika, E. A. Kubareva, E. A. Romanova, T. S. Oretskaya, R. Heumann, and M. Epple, *J. Mater. Chem.*, 17, 721–727, **2007**.

[65] E. F. Fynan, R. G. Webster, D. H. Fuller, J. C. Santoro, and H. L. Robinson, *Proc. Natl. Acad. Sci. U.S.A.*, 90, 11 478–11 482, **2004**.

[66] K. K. Sandhu, C. M. McIntosh, J. M. Simard, S. W. Smith, and V. M. Rotello, *Bioconjugate Chem.*, 13, 3–6, **2002**.

[67] M. Thomas and A. M. Klibanov, *Proc. Natl. Acad. Sci. U.S.A*, 100, 9138–9143, **2003**.

[68] C. P. Jen, Y. H. Chen, C. S. Fan, C. S. Yeh, Y. C. Lin, D. B. Shieh, C. L. Wu, D. H. Chen, and C. H. Chou, *Langmuir*, 20, 1369–1374, **2004**.

[69] S. Yang, R. Delgado, S. R. King, C. Woffendin, C. S. Barker, Z. Y. Yang, L. Xu, G. P. Nolan, and G. J. Nabel, *Hum. Gene Ther.*, 10, 123–132, **1999**.

[70] A. A. Bukovsky, J. P. Song, and L. Naldini, *J. Virol.*, 73, 7087–7092, **1999**.

[71] M. C. Garnett, *Crit. Rev. Ther. Drug Carrier Syst.*, 16, 147–207, **2004**.

[72] R. Kircheis, L. Wightman, and E. Wagner, *Adv. Drug Delivery Rev.*, 53, 341–358, **2001**.

[73] S. Kazuyoshi and S. W. Kim, *J. Control. Release*, 79, 271–281, **2002**.

[74] C. Rudolph, U. Schillinger, and C. Plank, *Biochim. Biophys. Acta Gen. Subj.*, 1573, 75–83, **2002**.

[75] D. G. Anderson, D. M. Lynn, and R. Langer, *Angew. Chem. Int. Ed.*, 42, 3153–3158, **2003**.

[76] M. Epple, K. Ganesan, R. Heumann, J. Klesing, A. Kovtun, S. Neumann, and V. Sokolova, *J. Mater. Chem.*, 20, 18–23, **2010**.

[77] H. Schreier, *Pharm. Acta Helv.*, 68, 145–159, **1994**.

[78] C. C. Mello and D. Conte, *Nature*, 431, 338–342, **2004**.

[79] B. Mitterauer, *Med. Hypotheses*, 62, 907–910, **2004**.

[80] G. Meister and T. Tuschl, *Nature*, 431, 343–349, **2004**.

[81] P. Y. Lu, F. Xie, and M. C. Woodle, *Adv. Genet.*, 54, 115–142, **2005**.

[82] R. K. Leung and P. A. Whittaker, *Pharmacol. Ther.*, 107, 222–239, **2005**.

[83] I. R. Gilmore, S. P. Fox, A. J. Hollins, and S. Akhtar, *Curr. Drug Delivery*, 3, 147–155, **2006**.

[84] M. Yokoyama, M. Miyauchi, N. Yamada, T. Okano, Y. Sakurai, K. Kataoka, and S. Inoue, *J. Control. Rel.*, 11, 269–278, **1990**.

[85] M. Yokoyama, T. Okano, Y. Sakurai, H. Ekimoto, C. Shibazaki, and K. Kataoka, *Cancer Res.*, 51, 3229–3236, **1991**.

[86] P. Couvreur, B. Kante, L. Grislain, M. Roland, and P. Speiser, *J. Pharm. Sci.*, 71, 790–792, **1982**.

[87] J. H. Thrall, *Radiology*, 230, 315–318, **2004**.

[88] S. Kashiwada, *Environ. Health Perspect.*, 114, 1697–1702, **2006**.

[89] Z. J. Deng, S. W. Morton, E. Ben-Akiva, E. C. Dreaden, K. E. Shopsowitz,

and P. T. Hammond, *ACS Nano*, 7, 9571–9584, **2013**.

[90] L. Yildirimer, N. T. Thanh, M. Loizidou, and A. M. Seifalian, *Nano Today*, 6, 585–607, **2011**.

[91] S. Bakand, A. Hayes, and F. Dechsakulthorn, *Inhal. Toxicol.*, 24, 125–135, **2012**.

[92] S. M. Hussain, K. L. Hess, J. M. Gearhart, K. T. Geiss, and J. J. Schlager, *Toxicol. In Vitro*, 19, 975–983, **2005**.

[93] S. J. Kang, B. M. Kim, Y. J. Lee, and H. W. Chung, *Environ. Mol. Mutagen.*, 49, 399–405, **2008**.

[94] Z. Liu, S. Tabakman, K. Welsher, and H. Dai, *Nano Res.*, 2, 85–120, **2009**.

[95] A. Nel, T. Xia, L. Madler, and N. Li, *Science*, 311, 622–627, **2006**.

[96] K. Donaldson, V. Stone, P. S. Gilmour, D. M. Brown, and W. MacNee, *Phil. Trans. R. Soc. A*, 358, 2741–2749, **2000**.

[97] K. Donaldson, L. Tran, L. A. Jimenez, R. Duffin, D. E. Newby, N. Mills, W. MacNee, and V. Stone, *Part. Fibre Toxicol.*, 2, p. 10, **2005**.

[98] P. J. Borm, D. Robbins, S. Haubold, T. Kuhlbusch, H. Fissan, K. Donaldson, R. Schins, V. Stone, W. Kreyling, J. Lademann, J. Krutmann, D. Warheit, and E. Oberdorster, *Part. Fibre Toxicol.*, 3, 1–35, **2006**.

[99] A. Isakovic, Z. Markovic, N. Nikolic, B. Todorovic-Markovic, S. Vranjes-Djuric, L. Harhaji, N. Raicevic, N. Romcevic, D. Vasiljevic-Radovic, M. Dramicanin, and V. Trajkovic, *Biomaterials*, 27, 5049–5058, **2006**.

[100] A. Erdely, M. Dahm, B. T. Chen, P. C. Zeidler-Erdely, J. E. Fernback, M. E. Birch, D. E. Evans, M. L. Kashon, J. A. Deddens, T. Hulderman, S. A. Bilgesu, L. Battelli, D. Schwegler-Berry, H. D. Leonard, W. McKinney, D. G. Frazer, J. M. Antonini, D. W. Porter, V. Castranova, and M. K. Schubauer-Berigan, *Part. Fibre Toxicol.*, 10, p. 53, **2013**.

[101] Nanotechnology, Joint Research Centre, The European Commission's in-house science service (Ec.europa.eu).

[102] Nanomaterials, archived on 02.02.2015, European Commission, Enterprise and Industry (www.ec.europa.eu).

[103] S. Bose and S. Tarafder, *Acta Biomater.*, 8, 1401–1421, **2012**.

[104] J. Temenoff and A. Mikos, *Biomaterials: the Intersection of Biology and Materials Science*. Upper Saddle River, NJ: Prentice Hall, **2008**.

[105] J. Park and R. Lakes, *Biomaterials: An Introduction*. Berlin: Springer,

2007.

[106] L. Hench, *Science, Faith and Ethics*. London: Imperial College Press, **2001**.

[107] V. Uskokovič and D. P. Uskokovič, *J. Biomed. Mater. Res. Part B Appl. Biomater.*, 96, 152–191, **2011**.

[108] M. Epple, *Biomineralien und Biomineralisation*. Wiesbaden: Teubner Verlag / GWV Fachverlage GmbH, **2003**.

[109] S. Brown, I. Clarke, and P. Williams, *Key Eng. Mater.*, 218, 35–38, **2002**.

[110] N. Ignjatovič, E. Suljovrujič, Z. Stojanovič, and D. Uskokovič, *Sci. Sintering*, 34, 79–93, **2002**.

[111] Y. Fang, D. Agrawal, and D. Roy, Thermal Stability of Synthetic Hydroxyapatite, In: *Brown PW, Constantz B, editors. Title: Hydroxyapatite and Related Materials*, 269–282. Boca Raton, FL: CRC Press, **1994**.

[112] N. Ignjatovič, E. Suljovrujič, J. Budinski, I. Krakovsky, and D. Uskokovič, *J. Biomed. Mater. Res. Part B: Appl. Biomater. B*, 71, 284–294, **2004**.

[113] T. Welzel, W. Meyer-Zaika, and M. Epple, *Chem. Commun.*, 218, 1204–1205, **2004**.

[114] M. Pretto, A. Costa, E. Landi, A. Tampieri, and C. Galassi, *J. Am. Ceram. Soc.*, 86, 1534–1539, **2003**.

[115] J. Gomez-Morales, J. Torrent-Burgues, T. Boix, J. Fraile, and R. Rodriguez-Clemente, *Crystal Res. Technol.*, 36, 15–26, **2001**.

[116] A. Tas, F. Korkusuz, M. Timucin, and N. Akkas, *J. Mater. Sci: Mater. Med.*, 8, 91–96, **1997**.

[117] M. Ashok, S. Kalkura, N. Sundaram, and D. Arivuoli, *J. Mater. Sci: Mater. Med.*, 18, 895–898, **2007**.

[118] D. Janackovič, I. Jankovič, R. Petrovič, L. Kostič-Gvozdenovič, S. Milonjič, and D. Uskokovič, *Key Eng. Mater.*, 240, 437–440, **2003**.

[119] E. Thian, Z. Ahmad, J. Huang, M. Edirisinghe, S. Jayasinghe, D. Ireland, R. Brooks, N. Rushton, W. Bonfield, and S. Best, *Biomaterials*, 29, 1833–1843, **2008**.

[120] Y. Wu, L. Hench, J. Du, K.-L. Choy, and J. Guo, *J. Am. Ceram. Soc.*, 87, 1988–1991, **2005**.

[121] Y. Fang, D. Agrawal, D. Roy, R. Roy, and P. Brown, *J. Mater. Res.*, 7, 2294–2298, **1992**.

[122] S. Xu, J. Long, L. Sim, C. Diong, and K. Ostrikov, *Plasma Process Polym.*, 2, 373–390, **2005**.

[123] V. Sokolova, O. Prymak, W. Meyer-Zaika, H. Cölfen, H. Rehage, A. Shukla, and M. Epple, *Materialwiss. Werkst.*, 37, 441–445, **2006**.

[124] N. Puvvada, K. P. Panigrahi, and A. Pathak, *Nanocscale*, 2, 2631–2638, **2010**.

[125] R. Kumar, K. H. Prakash, P. Cheang, and K. A. Khor, *Langmuir*, 20, 5196–5200, **2004**.

[126] J. Zhan, Y.-H. Tseng, J. Chan, and C.-Y. Mou, *Adv. Funct. Mater.*, 15, 2005–2010, **2005**.

[127] F. Huang, Y. Shen, A. Xie, J. Zhu, C. Zhang, S. Li, and J. Zhu, *J. Mater. Sci.*, 42, 8599–8605, **2007**.

[128] F. Zhang, Z.-H. Zhou, S.-P. Yang, L.-H. Mao, H.-M. Chen, and X.-B. Yu, *Mater. Lett.*, 59, 1422–1425, **2005**.

[129] L. Yan, Y. Li, Z.-X. Deng, J. Zhuang, and X. Sun, *Int. J. Inorganic Mater.*, 3, 633–637, **2001**.

[130] A. Wang, D. Liu, H. Yin, H. Wu, Y. Wada, M. Ren, T. Jiang, X. Cheng, and Y. Xu, *Mater. Sci. Eng. C.*, 27, 865–869, **2007**.

[131] D. Walsh, J. Kingston, B. Heywood, and S. Mann, *J. Crystal Growth*, 133, 1–12, **1993**.

[132] D. Kopeliovich, Substances and Technologies. Knowledge source on Materials Engineering, available from: Substech.com.

[133] T. Tadros, *Colloid Stability: The Role of Surface Forces - Part I, Volume 1.* Wiley-VCH Verlag, **2011**.

[134] E. Schroder, T. Jonsson, and L. Poole, *Anal. Biochem.*, 313, 176–178, **2003**.

[135] R. Giovannini and R. Freitag, *Bioseparation*, 9, 359–368, **2000**.

[136] C. Phandugath, *J. Sci. Technol.*, 27, 201–212, **2005**.

[137] L. Sas, C. Tang, and Z. Rengel, *Plant Soil*, 235, 159–166, **2001**.

[138] M. Okazaki, Y. Yoshida, S. Yamaguchi, M. Kaneno, and J. Elliott, *Biomaterials*, 22, 2459–2464, **2001**.

[139] G. Lim, J. Wang, S. Ng, and L. Gan, *Mater. Lett.*, 28, 431–436, **1996**.

[140] V. Ball, J.-M. Planeix, O. Flix, J. Hemmerl, P. Schaaf, M. Hosseini, and J. Voegel, *Cryst. Growth Des.*, 2, 489–492, **2002**.

[141] M. Jevtič, M. Mitrič, S. Skapin, B. Jančar, N. Ignjatovič, and D. Uskokovcč, *Cryst. Growth Des.*, 8, 2217–2222, **2008**.

[142] C. Fowler, M. Li, S. Mann, and H. Margolis, *J. Mater. Chem.*, 15, 3317–3325, **2005**.

[143] V. Sokolova, O. Rotan, J. Klesing, P. Nalbant, J. Buer, T. Knuschke, A. Westendorf, and M. Epple, *J. Nanopart. Res.*, 14, p. 910, **2012**.

[144] S. Neumann, A. Kovtun, I. D. Dietzel, M. Epple, and R. Heumann, *Biomaterials*, 30, 6794–6802, **2009**.

[145] W. Gamble, *J. Theor. Biol.*, 239, 16–21, **2005**.

[146] A. E. Ewence, M. Bootman, H. L. Roderick, J. N. Skepper, G. McCarthy, M. Epple, M. Neumann, C. M. Shanahan, and D. Proudfoot, *Circ. Res.*, 103, 28–34, **2008**.

[147] T. Miyai, A. Ito, G. Tamazawa, T. Matsuno, Y. Sogo, C. Nakamura, A. Yamazaki, and T. Satoh, *Biomaterials*, 29, 350–358, **2008**.

[148] V. Martins, G. Goissis, A. Ribeiro, E. Marcantonio, and M. Bet, *Artif. Organs*, 22, 215–221, **1998**.

[149] M. Rauchmann, T. Wichelhaus, V. Stirnal, E. Dingeldein, L. Zichner, R. Schnettler, and V. Alt, *Biomaterials*, 26, 2677–2684, **2005**.

[150] T. N. T. Do, W.-H. Lee, C.-Y. Loo, A. V. Zavgorodniy, and R. Rohanizadeh, *Ther. Deliv.*, 3, 623–632, **2012**.

[151] V. Sokolova, S. Neumann, A. Kovtun, S. Chernousova, R. Heumann, and M. Epple, *J. Mater. Sci.*, 45, 4952–4957, **2010**.

[152] T. Knuschke, V. Sokolova, O. Rotan, M. Wadwa, M. Tenbusch, W. Hansen, P. Staeheli, M. Epple, J. Buer, and A. M. Westendorf, *J. Immunol.*, 190, 6221–6229, **2013**.

[153] V. Sokolova, D. Kozlova, T. Knuschke, J. Buer, A. M. Westendorf, and M. Epple, *Acta Biomater.*, 9, 7527–7535, **2013**.

[154] V. Sokolova, A. M. Westendorf, J. Buer, K. Uberla, and M. Epple, *J. Mater. Chem. B*, 3, 4767–4779, **2015**.

[155] B. Alberts, A. Johnson, J. Lewis, D. Morgan, M. Raff, K. Roberts, and P. Walter, *Molecular Biology of the Cell*, 6th ed. Garland Publishing, **2014**.

[156] B. Van de Berg, M. Nieuwdorp, E. S. Stroes, and H. Vink, *Pharmacol. Rep.*, 57, 75–80, **2006**.

[157] M. McKinley and V. O'Loughlin, *Human Anatomy*, 3rd ed. McGraw-Hill,

2012.

[158] S. Conner and S. Schmid, *Nature*, 422, 37–44, **2003**.

[159] G. J. Doherty and H. T. McMahon, *Annu. Rev. Biochem.*, 78, 857–902, **2009**.

[160] V. A. Fadok and G. Chimini, *Semin. Immunol.*, 13, 365–372, **2001**.

[161] A. Hall and C. D. Nobes, *Philos. Trans. R. Soc. Lond., B, Biol. Sci.*, 355, 965–970, **2000**.

[162] A. J. Ridley, *Traffic*, 2, 303–310, **2001**.

[163] I. Mellman and R. M. Steinman, *Cell*, 106, 255–258, **2001**.

[164] O. Steele-Mortimer, L. A. Knodler, and B. B. Finlay, *Traffic*, 1, 107–118, **2000**.

[165] R. G. Anderson, *Annu. Rev. Biochem.*, 67, 199–225, **1998**.

[166] B. Razani, S. E. Woodman, and M. P. Lisanti, *Pharmacol. Rev.*, 54, 431–467, **2002**.

[167] S. L. Schmid, *Annu. Rev. Biochem.*, 66, 511–548, **1997**.

[168] F. M. Brodsky, C.-Y. Chen, C. Kneuhl, M. C. Towler, and D. E. Wakeham, *Annu. Rev. Cell Dev. Biol.*, 17, 517–568, **2001**.

[169] P. P. Di Fiore and P. De Camilli, *Cell*, 106, 1–4, **2001**.

[170] E. S. Seto, H. J. Bellen, and T. E. Lloyd, *Genes Dev.*, 16, 1314–1336, **2002**.

[171] E. C. Beattie, R. C. Carroll, X. Yu, W. Morishita, H. Yasuda, M. von Zastrow, and R. C. Malenka, *Nature Neurosci.*, 3, 1291–1300, **2000**.

[172] P. De Camilli and K. Takei, *Neuron*, 16, 481–486, **1996**.

[173] C. Lamaze, A. Dujeancourt, T. Baba, C. G. Lo, A. Benmerah, and A. Dautry-Varsat, *Mol. Cell*, 7, 661–671, **2001**.

[174] H. Damke, T. Baba, A. M. van der Bliek, and S. L. Schmid, *J. Cell Biol.*, 131, 69–80, **1995**.

[175] G. Sahay, D. Y. Alakhova, and A. V. Kabanov, *J. Control. Release*, 145, 182–195, **2010**.

[176] T. Jamieson, R. Bakhshi, D. Petrova, R. Pocock, M. Imani, and A. Seifalian, *Biomaterials*, 28, 4717–4732, **2007**.

[177] X. Michalet, F. Pinaud, L. Bentolila, J. Tsay, S. Doose, J. Li, G. Sundaresan, A. Wu, S. Gambhir, and S. Weiss, *Science*, 307, 538–544, **2005**.

[178] J. Vasir and V. Labhasetwar, *Adv. Drug Deliv. Rev.*, 59, 718–728, **2007**.

[179] S. Agasti, S. Rana, M. Park, C. Kim, C. You, and V. Rotello, *Adv. Drug Deliv. Rev.*, 62, 316–328, **2010**.

[180] T. Skotland, T. Iversen, and K. Sandvig, *Nanomedicine*, 6, 730–737, **2010**.

[181] N. Zaki and N. Tirelli, *Expert Opin. Drug Deliv.*, 7, 895–913, **2010**.

[182] T. Iversen, T. Skotland, and K. Sandvig, *Nano Today*, 6, 176–185, **2011**.

[183] M. Nazarenus, Q. Zhang, M. G. Soliman, P. del Pino, B. Pelaz, S. Carregal-Romero, J. Rejman, B. Rothen-Rutishauser, M. J. D. Clift, R. Zellner, G. U. Nienhaus, J. B. Delehanty, I. Medintz, and W. J. Parak, *J. Nanotechnol.*, 5, 1477–1490, **2014**.

[184] B. Chithrani and W. Chan, *Nano Lett.*, 7, 1542–1550, **2007**.

[185] W. Jiang, B. Kim, J. Rutka, and W. Chan, *Nat. Nanotechnol.*, 7, 145–150, **2008**.

[186] H. Jin, D. Heller, R. Sharma, and M. Strano, *ACS Nano*, 3, 149–158, **2009**.

[187] A. M. Fra, M. Masserini, P. Palestini, S. Sonnino, and K. Simons, *FEBS Lett.*, 375, 11–14, **1995**.

[188] T. Richter, M. Floetenmeyer, C. Ferguson, J. Galea, J. Goh, M. R. Lindsay, G. P. Morgan, B. J. Marsh, and R. G. Parton, *Traffic*, 9, 893–909, **2008**.

[189] G. Orr, D. Panther, K. Cassens, J. L. Phillips, B. Tarasevich, and J. Pounds, *Toxicol. Appl. Pharmacol.*, 236, 210–220, **2009**.

[190] O. Harush-Frenkel, N. Debotton, S. Benita, and Y. Altschuler, *Biochem. Biophys. Res. Commun.*, 353, 26–32, **2007**.

[191] L. Zhang and N. Monteiro-Riviere, *Toxicol. Sci.*, 110, 138–155, **2009**.

[192] J. Champion, Y. Katare, and S. Mitragotri, *Proc. Natl. Acad. Sci. U.S.A.*, 104, 11 901–11 904, **2007**.

[193] J. Champion and S. Mitragotri, *Proc. Natl. Acad. Sci. U.S.A.*, 103, 4930–4934, **2006**.

[194] O. Harush-Frenkel, N. Debotton, S. Benita, and Y. Altschuler, *Biochem. Biophys. Res. Commun.*, 353, 26–32, **2007**.

[195] O. Harush-Frenkel, E. Rozentur, S. Benita, and Y. Altschuler, *Biomacromolecules*, 9, 435–443, **2008**.

[196] U. Lahtinen, M. Honsho, R. Parton, K. Simons, and P. Verkade, *FEBS Lett.*, 538, 85–88, **2003**.

[197] U. Vogel, K. Sandvig, and B. van Deurs, *J. Cell. Sci.*, 111, 825–832, **1998**.

[198] C. Tekle, B. Deurs, K. Sandvig, and T.-G. Iversen, *Nano Letters*, 8, 1858–1865, **2008**.

[199] S. E. Gratton, S. S. Williams, M. E. Napier, P. D. Pohlhaus, Z. Zhou, K. B. Wiles, B. W. Maynor, C. Shen, T. Olafsen, E. T. Samulski, and J. M. Desimone, *Acc. Chem. Res.*, 41, 1685–1695, **2008**.

[200] S. Gratton, P. Ropp, P. Pohlhaus, J. Luft, V. Madden, M. Napier, and J. DeSimone, *Proc. Natl. Acad. Sci. U.S.A.*, 105, 11 613–11 618, **2008**.

[201] S. K. Lai, K. Hida, C. Chen, and J. Hanes, *J. Control. Release*, 125, 107–111, **2008**.

[202] K. M. Kitchens, A. B. Foraker, R. B. Kolhatkar, P. W. Swaan, and H. Ghandehari, *Pharm. Res.*, 24, 2138–2145, **2007**.

[203] F. P. Seib, A. T. Jones, and R. Duncan, *J. Control. Release*, 117, 291–300, **2007**.

[204] K. von Gersdorff, N. N. Sanders, R. Vandenbroucke, S. C. De Smedt, E. Wagner, and M. Ogris, *Mol. Ther.*, 14, 745–753, **2006**.

[205] A. Akinc, M. Thomas, A. M. Klibanov, and R. Langer, *J. Gene Med.*, 7, 657–663, **2005**.

[206] K. Sapsford, W. Algar, L. Berti, K. Gemmill, B. Casey, E. Oh, M. Stewart, and I. Medintz, *Chem. Rev.*, 113, 1904–2074, **2013**.

[207] K. Sandvig and B. van Deurs, *Gene Ther.*, 12, 865–872, **2005**.

[208] V. Sokolova, A. Kovtun, R. Heumann, and M. Epple, *J. Biol. Inorg. Chem.*, 12, 174–179, **2007**.

[209] C. C. Scott and J. Gruenberg, *Bioessays*, 33, 103–110, **2011**.

[210] D. Fischer and A. Fahr, *Pharm. Unserer Zeit*, 40, 212–219, **2011**.

[211] Y. Wang, J. Su, F. Wu, P. Lu, L. Yuan, W. Yuan, J. Sheng, and T. Jin, *Int. J. Nanomed.*, 7, 693–704, **2012**.

[212] L. Zhang, F. Gu, J. Chan, A. Wang, R. Langer, and O. Farokhzad, *Clin. Pharmacol. Ther.*, 83, 761–769, **2008**.

[213] G. Zhang, T. Liu, Y. Chen, Y. Chen, M. Xu, J. Peng, S. Yu, J. Yuan, and X. Zhang, *Clin. Cancer Res.*, 15, 201–7, **2009**.

[214] T. Roth and K. Porter, *J. Cell Biol.*, 20, 313–332, **1964**.

[215] S. Laporte, R. Oakley, J. Holt, L. Barak, and M. Caron, *J. Biol. Chem.*, 275, 23 120–23 126, **2000**.

[216] M. Maurer and J. Cooper, *J. Cell Sci.*, 119, 4235–4246, **2006**.

[217] M. Koivusalo, C. Welch, H. Hayashi, C. Scott, M. Kim, T. Alexander, N. Touret, K. Hahn, and S. Grinstein, *J. Cell Biol.*, 188, 547–563, **2010**.

[218] M. Kerr and R. Teasdale, *Traffic*, 10, 364–371, **2009**.

[219] L. Wang, K. Rothberg, and R. Anderson, *J. Cell Biol.*, 123, 1107–1117, **1993**.

[220] L. Fujimoto, R. Roth, J. Heuser, and S. Schmid, *Traffic*, 1, 161–171, **2000**.

[221] S. Rodal, G. Skretting, O. Garred, F. Vilhardt, B. van Deurs, and K. Sandvig, *Mol. Biol. Cell*, 10, 961–974, **1999**.

[222] P. van Kerkhof, M. Sachse, J. Klumperman, and G. Strous, *J. Biol. Chem.*, 276, 3778–3784, **2001**.

[223] K. Sandvig, M. Torgersen, H. Raa, and B. van Deurs, *Histochem. Cell Biol.*, 129, 267–276, **2008**.

[224] S. Grimmer, B. van Deurs, and K. Sandvig, *J. Cell Sci.*, 115, 2953–2962, **2002**.

[225] L. Pelkmans, D. Puntener, and A. Helenius, *Science*, 296, 535–539, **2002**.

[226] D. Vercauteren, R. Vandenbroucke, A. Jones, J. Rejman, J. Demeester, S. De Smedt, N. Sanders, and K. Braeckmans, *Mol. Ther.*, 18, 561–569, **2010**.

[227] P. H. Raven and G. B. Johnson, *Biology, 6th edition*. Mcgraw-Hill College, **2001**.

[228] J. Parkin and B. Cohen, *Lancet*, 357, 1777–1789, **2001**.

[229] T. W. Mak and M. E. Saunders, *Primer to the immune response*. Academic Press, **2008**.

[230] I. Todd, *Encyclopedia of life science*, 1–7, **2001**.

[231] V. Witko-Sarsat, P. Rieu, B. Descamps-Latscha, P. Lesavre, and L. Halbwachs-Mecarelli, *Lab. Invest.*, 80, 617–53, **2000**.

[232] G. Pier, J. Lyczak, and L. Wetzler, *Immunology, Infection, and Immunity*. ASM Press, **2004**.

[233] R. Geisberger, M. Lamers, and G. Achatz, *Immunology*, 118, 889–898, **2006**.

[234] K. Chen, W. Xu, M. Wilson, B. He, N. Miller, E. Bengten, E. Edholm, P. Santini, P. Rath, A. Chiu, M. Cattalini, J. B. Litzman, J. Bussel, B. Huang, A. Meini, K. Riesbeck, C. Cunningham-Rundles, A. Plebani,

and A. Cerutti, *Nat. Immunol.*, 10, 889–898, **2009**.

[235] B. Underdown and J. Schiff, *Annu. Rev. Immunol.*, 1, 389–417, **1986**.

[236] L. Klavinskis, L. Gao, C. Barnfield, T. Lehner, and S. Parker, *Vaccine*, 818–20, **1997**.

[237] A. Sheik, M. Al-Shamisi, and W. Morrow, *Curr. Opin. Molec. Therapeut.*, 2, 37–54, **2000**.

[238] M. E. Marohn and E. M. Barry, *Vaccine*, 13, 3485–3491, **2013**.

[239] P. Verdijk, N. Y. Rots, M. G. van Oijen, M. S. Oberste, C. J. Boog, H. Okayasu, R. W. Sutter, and W. A. Bakker, *Vaccine*, 31, 5531–5536, **2013**.

[240] P. Riese, K. Schulze, T. Ebensen, B. Prochnow, and C. A. Guzman, *Curr. Top. Med. Chem.*, 13, 2562–2580, **2013**.

[241] R. Mazid, X. M. Tan, and K. M. Danquah, *Curr. Pharm. Biotechnol.*, 14, 615–622, **2013**.

[242] D. M. Smith, J. K. Simon, and J. R. Baker Jr, *Nat. Rev. Immunol.*, 13, 592–605, **2013**.

[243] L. M. Kaminskas, V. M. McLeod, C. J. Porter, and B. J. Boyd, *Mol. Pharm.*, 9, 355–373, **2012**.

[244] S. Kannan, H. Dai, R. S. Navath, B. Balakrishnan, A. Jyoti, J. Janisse, R. Romero, and R. M. Kannan, *Sci. Transl. Med.*, 4, p. 130ra46, **2012**.

[245] M. Higaki, T. Ishihara, N. Izumo, M. Takatsu, and Y. Mizushima, *Ann. Rheum. Dis.*, 64, 1132–1136, **2005**.

[246] B. Buyuktimkin, Q. Wang, P. Kiptoo, J. M. Stewart, C. Berkland, and T. J. Siahaan, *Mol. Pharm.*, 9, 979–985, **2012**.

[247] L. Buonaguro, M. Tagliamonte, M. L. Tornesello, and F. M. Buonaguro, *Expert Rev. Vaccinesy*, 10, 1569–1583, **2011**.

[248] S. M. Goldinger, R. Dummer, P. Baumgaertner, D. Mihic-Probst, K. Schwarz, A. Hammann-Haenni, J. Willers, C. Geldhof, J. O. Prior, T. M. Kundig, O. Michielin, M. F. Bachmann, and D. E. Speiser, *Eur. J. Immunol.*, 42, 3049–3061, **2012**.

[249] H. de Wolf, N. Johansson, A. Thong, C. Snel, E. Mastrobattista, W. Hennink, and G. Storm, *Pharm. Res.*, 25, 1654–62, **2008**.

[250] E. A. Levenson and K. L. Kiick, *Acta Biomater.*, 10, 1134–1145, **2014**.

[251] J. F. Manna, P. F. McKaya, S. Arokiasamya, R. K. Patelb, K. Kleina, and

R. J. Shattocka, *J. Control. Release*, 170, 452–459, **2013**.

[252] D. Christensen, K. S. Korsholm, P. Andersen, and E. M. Agger, *Expert Rev. Vaccines*, 10, 513–521, **2011**.

[253] S. Hamdy, O. Molavi, Z. Ma, A. Haddadi, A. Alshamsan, Z. Gobti, S. Elhasi, J. Samuel, and A. Lavasanifar, *Vaccine*, 26, 5046–5057, **2008**.

[254] A. Uenaka, H. Wada, M. Isobe, T. Saika, K. Tsuji, E. Sato, S. Sato, Y. Noguchi, R. Kawabata, T. Yasuda, Y. Doki, H. Kumon, K. Iwatsuki, H. Shiku, M. Monden, A. A. Jungbluth, G. Ritter, R. Murphy, E. Hoffman, L. J. Old, and E. Nakayama, *Cancer Immun.*, 7, p. 9, **2007**.

[255] S. Kitano, S. Kageyama, Y. Nagata, Y. Miyahara, A. Hiasa, H. Naota, S. Okumura, H. Imai, T. Shiraishi, M. Masuya, M. Nishikawa, J. Sunamoto, K. Akiyoshi, T. Kanematsu, A. M. Scott, R. Murphy, E. W. Hoffman, L. J. Old, and H. Shiku, *Clin. Cancer Res.*, 12, 7397–7405, **2006**.

[256] A. E. Gregory, R. Titball, and D. Williamson, *Front. Cell. Infect. Microbiol.*, 25, 1–13, **2013**.

[257] M. Wei, N. Chen, J. Li, M. Yin, L. Liang, Y. He, H. Song, C. Fan, and Q. Huang, *Angew. Chem. Int. Ed. Engl.*, 51, 1202–1206, **2012**.

[258] D. Zhao, D. Alizadeh, L. Zhang, W. Liu, O. Farrukh, E. Manuel, D. J. Diamond, and B. Badie, *Clin. Cancer Res.*, 17, 771–782, **2011**.

[259] N. Matsuoka, M. Nishikawa, K. Mohri, S. Rattanakia, and Y. Takakura, *J. Control. Release*, 148, 311–316, **2010**.

[260] S. Swapp, Scanning Electron Microscopy (SEM), available from: www.serc.carleton.edu.

[261] J. W. Snowman, *Downstream Processes: Equipment and Techniques*. Alan R. Liss, Inc., **1988**.

[262] N. Green, H. Alexander, A. Olson, S. Alexander, T. M. Shinnick, J. G. Sutcliffe, and R. A. Lerner, *Cell*, 28, 477–487, **1982**.

[263] C. Schneider and M. H. Van Regenmortel, *Arch. Virol.*, 125, 103–119, **1992**.

[264] R. Zadmard and T. Schrader, *Angew. Chem.*, 45, 2703–2706, **2006**.

[265] L. O'Neill and E. Brint, *Toll-like Receptors in Inflammation*. Birkhäser-Verlag, **2005**.

[266] G. J. Weiner, H. M. Liu, J. E. Wooldridge, C. E. Dahle, and A. M. Krieg, *Proc. Natl. Acad. Sci. U.S.A.*, 94, 10 833–10 837, **1997**.

[267] S. Bauer and H. Wagner, *Curr. Top. Microbiol. Immunol.*, 270, 145–154,

2002.

[268] S. Rothenfusser, E. Tuma, S. Endres, and G. Hartmann, *Hum. Immunol.*, 63, 1111–1119, **2002**.

[269] Z. G. Ramirez-Ortiz, C. A. Specht, J. P. Wang, C. K. Lee, D. C. Bartholomeu, R. T. Gazzinelli, and S. M. Levitz, *Infect. Immun.*, 76, 2123–2129, **2008**.

[270] T. Sparwasser, T. Miethke, G. Lipford, A. Erdmann, H. Hacker, K. Heeg, and H. Wagner, *Eur. J. Immunol.*, 27, 1671–1679, **1997**.

[271] K. J. Stacey, M. J. Sweet, and D. A. Hume, *J. Immunol.*, 157, 2116–2122, **1996**.

[272] T. Sparwasser, E. S. Koch, R. M. Vabulas, K. Heeg, G. B. Lipford, J. W. Ellwart, and H. Wagner, *Eur. J. Immunol.*, 28, 2045–2054, **1998**.

[273] A. M. Krieg, A. K. Yi, S. Matson, T. J. Waldschmidt, G. A. Bishop, R. Teasdale, G. A. Koretzky, and D. M. Klinman, *Nature*, 374, 546–549, **1995**.

[274] S. Bendigs, U. Salzer, G. B. Lipford, H. Wagner, and K. Heeg, *Eur. J. Immunol.*, 29, 1209–1218, **1999**.

[275] G. B. Lipford and T. Sparwasser, *Curr. Top. Microbiol. Immunol.*, 247, 119–129, **2000**.

[276] G. B. Lipford, M. Bauer, C. Blank, R. Reiter, H. Wagner, and K. Heeg, *Eur. J. Immunol.*, 27, 2340–2344, **1997**.

[277] R. S. Chu, O. S. Targoni, A. M. Krieg, P. V. Lehmann, and C. V. Harding, *J. Exp. Med.*, 186, 1623–1631, **1997**.

[278] R. M. Vabulas, H. Pircher, G. B. Lipford, H. Hacker, and H. Wagner, *J. Immunol.*, 164, 2372–2378, **2000**.

[279] S. Zimmermann, O. Egeter, S. Hausmann, G. B. Lipford, M. Rocken, H. Wagner, and K. Heeg, *J. Immunol.*, 160, 3627–3630, **1998**.

[280] G. J. Weiner, *Curr. Top. Microbiol. Immunol.*, 247, 157–170, **2000**.

[281] S. Poepsel, A. Sprengel, B. Sacca, F. Kaschani, M. Kaiser, C. Gatsogiannis, S. Raunser, T. Clausen, and M. Ehrmann, *Nat. Chem. Biol.*, 11, 862–869, **2015**.

[282] A. Baldi, A. De Luca, M. Morini, T. Battista, A. Felsani, F. Baldi, C. Catricalà, A. Amantea, D. M. Noonan, A. Albini, P. G. Natali, D. Lombardi, and M. G. Paggi, *Oncogene*, 21, 6684–6688, **2002**.

[283] J. M. Milner, A. Patel, and A. D. Rowan, *Arthritis Rheum.*, 58, 3644–3656,

2008.

[284] K. F. Winklhofer and C. Haass, *Biochim. Biophys. Acta*, 1802, 29–44, **2010**.

[285] B. Fadeel and E. Grzybowska, *Biochim. Biophys. Acta*, 1790, 1139–1148, **2009**.

[286] L. Vande Walle, M. Lamkanfi, and P. Vandenabeele, *Cell Death Differ.*, 15, 453–460, **2008**.

[287] C. W. Gray, R. V. Ward, E. Karran, S. Turconi, A. Rowles, D. Viglienghi, C. Southan, A. Barton, K. G. Fantom, A. West, J. Savopoulos, N. J. Hassan, H. Clinkenbeard, C. Hanning, B. Amegadzie, J. B. Davis, C. Dingwall, G. P. Livi, and C. L. Creasy, *Eur. J. Biochem.*, 267, 5699–5710, **2000**.

[288] H. J. Huttunen, S. Y. Guenette, C. Peach, C. Greco, W. Xia, D. Y. Kim, C. Barren, R. E. Tanzi, and D. M. Kovacs, *J. Biol. Chem.*, 282, 28 285–28 295, **2007**.

[289] H. Yin and A. Hamilton, *Angew. Chem. Int. Edit.*, 44, 4130–4163, **2005**.

[290] S. Koch, C. Renner, X. Xie, and T. Schrader, *Angew. Chem. Int. Ed.*, 45, 6352–6355, **2006**.

[291] K. Renner, J. Piehler, and T. Schrader, *J. Am. Chem. Soc.*, 128, 620–628, **2006**.

[292] K. Wenck, S. Koch, C. Renner, W. Sun, and T. Schrader, *J. Am. Chem. Soc.*, 127, 16 015–16 029, **2007**.

[293] P. Talbiersky, F. Bastkowski, F. Klaerner, and T. Schrader, *J. Am. Chem. Soc.*, 130, 9824–9828, **2008**.

[294] R. L. Davidson and M. Sittig, *Water-soluble resins*. Reinhold Book Corp. New York, **1962**.

[295] A. Hunter, *Adv. Drug Deliv. Rev.*, 58, 1523–1531, **2006**.

[296] S. Moghimi, P. Symonds, J. Murray, A. Hunter, G. Debska, and A. Szewczyk, *Mol. Ther.*, 11, 990–995, **2005**.

[297] R. Balhorn, L. Brewer, and M. Corzett, *Mol. Reprod. Dev.*, 56, 230–234, **2000**.

[298] D. Lochmann, J. Weyermann, C. Georgens, R. Prassl, and A. Zimmer, *Eur. J. Pharm. Biopharm.*, 59, 419–429, **2005**.

[299] T. Masuda, H. Akita, and H. Harashima, *FEBS Lett.*, 579, 2143–2148, **2005**.

[300] F. Reynolds, R. Weissleder, and L. Josephson, *Bioconjugate Chem.*, 16, 1240–1245, **2005**.

[301] M. Kerkmann, D. Lochmann, J. Weyermann, A. Marschner, H. Poeck, M. Wagner, J. Battiany, A. Zimmer, S. Endres, and G. Hartmann, *Oligonucleotides*, 16, 313–322, **2006**.

[302] S. Futaki, T. Suzuki, W. Ohashi, T. Yagami, S. Tanaka, and Y. Ueda, K. Sugiura, *Biol. Chem.*, 276, 5836–5840, **2001**.

[303] M. Meistrich, B. Mohapatra, C. Shirley, and M. Zhao, *Chromosoma*, 111, 483–488, **2003**.

[304] J. Chen, Z. Yu, H. Chen, and W. Gao, J.and Liang, *Biomaterials*, 32, 1412–1418, **2011**.

[305] F. Sorgi, S. Bhattacharya, and L. Huang, *Gene Ther.*, 4, 961–968, **1997**.

[306] A. Noguchi, N. Hirashima, and M. Nakanishi, *Pharm. Res.*, 19, 933–938, **2002**.

[307] K. Spring and M. Davidson, Introduction to Fluorescence Microscopy, Available from: Microscopyu.com.

[308] V. Prasad and D. Semwogerere, *ER Weeks, J. Phys.: Cond. Mat.*, 19, 1131–1202, **2007**.

[309] Sigma-Aldrich, RPMI-1640 Media Formulation, available from: sigmaaldrich.com.

[310] T. Lindl, *Zell- und Gewebekultur*, 5th ed. Heidelberg: Spektrum Akademischer Verlag, **2002**.

[311] A. Tennstaedt, S. Pöpsel, L. Truebestein, P. Hauske, A. Brockmann, N. Schmidt, I. Irle, B. Sacca, C. Niemeyer, R. Brandt, H. Ksiezak-Reding, A. Tirniceriu, R. Egensperger, A. Baldi, L. Dehmelt, M. Kaiser, R. Huber, T. Clausen, and M. Ehrmann, *J. Biol. Chem.*, 282, 20 931–20 941, **2012**.

[312] R. J. Vasquez, B. Howell, A. M. Yvon, P. Wadsworth, and L. Cassimeris, *Mol. Biol. Cell*, 8, 973–985, **1997**.

[313] J. Cohen, *Science*, 299, 1290–1291, **2003**.

[314] P. Pitisuttithum, P. Gilbert, M. Gurwith, W. Heyward, M. Martin, and F. van Griensven, *J. Infect. Dis.*, 194, 1661–1671, **2006**.

[315] V. Sokolova, T. Knuschke, J. Buer, A. M. Westendorf, and M. Epple, *Acta Biomater.*, 7, 4029–4036, **2011**.

[316] V. Sokolova, T. Knuschke, A. Kovtun, J. Buer, M. Epple, and A. M. Westendorf, *Biomaterials*, 31, 5627–5633, **2010**.

[317] J. A. Belser, X. Lu, T. Maines, C. Smith, Y. Li, R. O. Donis, J. M. Katz, and T. M. Tumpey, *J. Virol.*, 81, 11 139–11 147, **2007**.

[318] J. A. Belser, D. A. Wadford, C. Pappas, K. M. Gustin, T. R. Maines, M. B. Pearce, H. Zeng, D. E. Swayne, M. Pantin-Jackwood, J. M. Katz, and T. M. Tumpey, *J. Virol.*, 84, 4194–4203, **2010**.

[319] B. N. Lambrecht and H. Hammad, *Immunity*, 31, 412–424, **2009**.

[320] S. Neumann, A. Kovtun, I. D. Dietzel, M. Epple, and R. Heumann, *Biomaterials*, 30, 6794–6802, **2009**.

[321] D. Hart, *Blood*, 90, 3245–3287, **1997**.

[322] K. Hasenkrug, D. Brooks, and U. Dittmer, *J. Virol.*, 72, 6559–6564, **1998**.

[323] K. Dietze, G. Zelinskyy, K. Gibbert, S. Schimmer, S. Francois, L. Myers, T. Sparwasser, K. Hasenkrug, and U. Dittmer, *Proc. Natl. Acad. Sci. U.S.A.*, 103, 2420–2425, **2011**.

[324] A. de Titta, Z. Ballester, M.and Julier, C. Nembrini, L. Jeanbart, and A. van der Vlies, *Proc. Natl. Acad. Sci. U.S.A.*, 110, 19 902–19 907, **2013**.

[325] U. Dittmer, D. Brooks, and K. Hasenkrug, *J. Virol.*, 73, 3753–3757, **1999**.

[326] M. Robertson, G. Spangrude, K. Hasenkrug, L. Perry, J. Nishio, and K. Wehrly, *J. Virol.*, 66, 3271–3277, **1992**.

[327] S. Nair, W. Bayer, M. Ploquin, G. Kassiotis, K. Hasenkrug, and U. Dittmer, *Retrovirology*, 8, p. 76, **2011**.

[328] W. Bayer, R. Lietz, T. Ontikatze, L. Johrden, M. Tenbusch, G. Nabi, S. Schimmer, P. Groitl, H. Wolf, C. M. Berry, K. Uberla, U. Dittmer, and O. Wildner, *Retrovirology*, 8, p. 75, **2011**.

[329] M. Altfeld and T. Allen, *Trends Immunol.*, 27, 504–510, **2006**.

[330] K. Dietze, G. Zelinskyy, K. Gibbert, S. Schimmer, S. Francois, and L. Myers, *Proc. Natl. Acad. Sci. U.S.A.*, 108, 2420–2425, **2011**.

[331] W. Zou, *Nat. Rev. Immunol.*, 6, 295–307, **2006**.

[332] G. Zelinskyy, A. Kraft, S. Schimmer, T. Arndt, and U. Dittmer, *Eur. J. Immunol.*, 36, 2658–2670, **2006**.

[333] J. Nilsson, A. Boasso, P. Velilla, R. Zhang, M. Vaccari, and G. Franchini, *Blood*, 108, 3808–3817, **2006**.

Appendix

Der Lebenslauf ist in der Online-Version aus Gründen des Datenschutzes nicht enthalten.

For the reasons of data protection, the Curriculum Vitae is not included in the online version.

List of scientific publications

1. T. Knuschke, O. Rotan, W. Bayer, V. Sokolova, W. Hansen, T. Sparwasser, U. Dittmer, M. Epple, J. Buer, A.M. Westendorf, "Combination of nanoparticle-based therapeutic vaccination and transient ablation of regulatory T cells strongly enhances anti-viral immunity during chronic retroviral infection", **Retrovirology** (accepted, DOI: 10.1186/s12977-016-0258-9).
2. B. Neuhaus, B. Tosun, O. Rotan, A. Frede, A.M. Westendorf, M. Epple, "Nanoparticles as transfection agents: a comprehensive study with ten different cell lines", **RSC Adv**ances **6** (2016) 18102–18112.
3. S. Range, D. Hagmeyer, O. Rotan, V. Sokolova, J. Verheyen, B. Siebers, M. Epple, "A continuous method to prepare a poorly crystalline silver-doped calcium phosphate ceramics with antibacterial properties", **RSC Adv**ances **5** (2015) 43172–43177.
4. T. Knuschke, W. Bayer, O. Rotan, V. Sokolova, M. Wadwa, W. Hansen, T. Sparwasser, U. Dittmer, M. Epple, J. Buer, A. M. Westendorf, "Prophylactic and therapeutic vaccination with a nanoparticle-based peptide vaccine induces efficient protective immunity during acute and chronic retroviral infection", **Nanomedicine**: Nanotechnology, Biology, and Medicine **10** (2014) 1787–1798.
5. J. Ruesing, O. Rotan, C. Gross-Heitfeld, C. Mayer, M. Epple, "Nanocapsules of a cationic polyelectrolyte and nucleic acid for efficient cellular uptake and gene transfer", **J**ournal of **Mater**ials **Chem**istry **B 2** (2014) 4625-4630.
6. T. Tenkumo, O. Rotan, V. Sokolova, M. Epple, "Protamine increases transfection efficiency and cell viability after transfection with calcium phosphate nanoparticles", **Nanobiomedicine 5** (2013) 64-74.
7. T. Knuschke, V. Sokolova, O. Rotan, M. Wadwa, M. Tenbusch, W. Hansen, P. Staeheli, M. Epple, J. Buer, A. M. Westendorf, "Immunization with biodegradable nanoparticles efficiently induces cellular immunity and protects against influenza virus infection", The **J**ournal of **Immunol**ogy **190** (2013) 6221–6229.

8. O. Rotan, V. Sokolova, P. Gilles, W. Hu, S. Dutt, T. Schrader, M. Epple, "Transport of supramolecular drugs across the cell membrane by calcium phosphate nanoparticles", **Materialwiss**enschaft und **Werkst**off**tech**nik **44** (2013) 176-182.
9. V. Sokolova, O. Rotan, J. Klesing, P. Nalbant, J. Buer, T. Knuschke, A. M. Westendorf, M. Epple, "Calcium phosphate nanoparticles as versatile carrier for small and large molecules across cell membranes", **J**ournal of **Nanopart**icle **Res**earch **14** (2012) 910.
10. V. Sokolova, A. K. Ludwig, S. Hornung, O. Rotan, P. A. Horn, M. Epple, B. Giebel, "Characterisation of exosomes derived from human cells by nanoparticle tracking analysis and scanning electron microscopy", **Colloids** and **Surf**aces **B**: Biointerfaces **87** (2011) 146 - 150.

List of citable conference abstracts

1. B. Neuhaus, O. Rotan, B. Tosun M. Epple, "Die Transfizierbarkeit unterschiedlicher Zelltypen mit Nanopartikeln", **BioNanoMaterials 16** (2015) 189.
2. M. Nitschke, O. Rotan, K. Severin, S. Pöpsel, M. Ehrmann, M. Epple, "Calcium phosphate nanoparticles as delivery system for proteins across the cell membrane of living cells", **BioNanoMaterials 16** (2015) 90.
3. O. Rotan, V. Sokolova, T. Knuschke, A. Westendorf, J. Buer, M. Epple, „Prophylaktische Vakzinierung gegen Tumoren mit funktionalisierten Calciumphosphat-Nanopartikeln in einem murinen Tumortransplantations-Modell“, **BioNanoMaterials 15 (S1)** (2014) S5.
4. O. Rotan, V. Sokolova, P. Gilles, T. Schrader, M. Epple, "Funktionalisierung von Calciumphosphat-Nanopartikeln mit einem synthetischem Enzyminhibitor", **BioNanoMaterials 14** (2013) 21.
5. O. Rotan, V. Sokolova, T. Knuschke, W. Bayer, J. Buer, U. Dittmer, A.M. Westendorf, M. Epple, "Calciumphosphat-Nanopartikel zur Immunisierung gegen retrovirale Infektionen", **BioNanoMaterials 13** (2012) 26.
6. O. Rotan, V. Sokolova, T. Knuschke, J. Buer, A.M. Westendorf, M. Epple, "Calciumphosphat-Nanopartikel zur Stimulation des Immunsystems", **BioNanoMaterials 12** (2011) 150.
7. J. Ruesing, V. Sokolova, A.K. Ludwig, S. Hornung, O. Rotan, P.A. Horn, B. Giebel, M. Epple, "Charakterisierung von Exosomen mittels Rasterelektronenmikroskopie und Nanoparticle Tracking Analysis", **BioNanoMaterials 12** (2011) 146.
8. J. Klesing, V. Sokolova, O. Rotan, A. Kovtun, P. Nalbant, J. Buer, T. Knuschke, A.M. Westendorf, M. Epple, "Calciumphosphat-Nanopartikel als effiziente Träger für Biomoleküle durch die Zellmembran", **BioNanoMaterials 12** (2011) 147.

List of scientific presentations

- 5th German-Ukrainian Symposium: Physics and Chemistry of Nanostructures and Nanobiotechnology, Kyiv, Ukraine (20.09 – 23.09.2015), *"Calcium phosphate nanoparticles as carriers for synthetic lysozyme-inhibitor polymer"*, Olga Rotan, Viktoriya Sokolova, Patrick Gilles, Thomas Schrader, Matthias Epple. (**Oral presentation**)
- Annual Meeting of the German Society for Biomaterials (DGBM), Freiburg, Germany, (12.11– 14.11.2015), *"Calcium phosphate nanoparticles as delivery system for proteins across the cell membrane of living cells"*, Mathis Nitschke, Olga Rotan, Katharina Severin, Simon Pöpsel, Michael Ehrmann, Matthias Epple. (**Poster**)
- Annual Meeting of the German Society for Biomaterials (DGBM), Freiburg, Germany, (12.11– 14.11.2015), *„Die Transfizierbarkeit unterschiedlicher Zelltypen mit Nanopartikeln"*, Bernhard Neuhaus, Olga Rotan, Benjamin Tosun, Matthias Epple. (**Poster**)
- Center for Nanointergration Duisburg-Essen (CENIDE) NanoBio Workshop 2015, Essen, Germany (12.03.2015), *"The potential of biodegradable calcium phosphate nanoparticles as molecular carriers in nanomedicine"*, Olga Rotan, Viktoriya Sokolova, Jan Klesing, Torben Knuschke, Perihan Nalbant, Jan Buer, Astrid M. Westendorf, Matthias Epple. (**Oral presentation**)
- 9th winter seminar of medical faculty of university clinic Essen, Pichl, Austria (02.03 – 04.03.2015), *„Prophylaktische und therapeutische Impfung gegen akute und chronische Retrovirusinfektionen"*, Olga Rotan, Torben Knuschke, Wibke Bayer, Viktoriya Sokolova, Munisch Wadwa, Carsten J. Kirschning, Wiebke Hansen, Ulf Dittmer, Matthias Epple, Jan Buer, Astrid M. Westendorf. (**Oral presentation**)
- Annual Meeting of the German Society for Biomaterials (DGBM), Dresden, Germany(6.11– 8.11.2014), *„Prophylaktische Vakzinierung gegen Tumoren mit funktionalisierten Calciumphosphat-Nanopartikeln in einem murinen Tumortransplantations-Modell"*, Olga Rotan, Viktoriya Sokolova, Torben Knuschke, Astrid M. Westendorf, Jan Buer, Matthias Epple. (**Oral presentation**)
- TRR60 4th Annual Workshop, Bochum, Germany (24-28.09.2014), *"Flagellin-functionalized calcium phosphate nanoparticles effectively activate in-*

nate immune response in vitro and in vivo", Olga Rotan, Diana Kozlova, Viktoriya Sokolova, Maohua Zhong, Ejuan Zhang, Jingyi Yang, Wei Li, Yi Yang, Jan Buer, Astrid M. Westendorf, Matthias Epple, Huimin Yan. (**Oral presentation**)

- Conference on Biomaterials in Medicine and Veterinary, Rytro, Poland (09.09 – 12.09.2014), *„Calcium phosphate nanoparticles for delivering synthetic drug candidates across the cell membrane"*, Olga Rotan, Viktoriya Sokolova, Thomas Schrader, Matthias Epple. (**Oral presentation**)
- Annual Meeting of the German Society for Biomaterials (DGBM), Erlangen, Germany (26.09 – 28.09.2013), *"Funktionalisierung von Calciumphosphat-Nanopartikeln mit einem synthetischen Enzyminhibitor"*, Olga Rotan, Viktoriya Sokolova, Patrick Gilles, Thomas Schrader, Matthias Epple. (**Repid fire presentation** + **Poster**)
- II Freiburger Bioceramic Symposium, Freiburg, Germany (6.07.2013), *„Calciumphosphat-Nanopartikel als Träger für natürliche und synthetische Moleküle"*, Olga Rotan, Matthias Epple. (**Oral presentation**)
- Materials Research Society (MRS) Spring Meeting, San Francisco, USA (01.04 – 05.04.2013), *„Transport of supramolecular drugs across the cell membrane by calcium phosphate nanoparticles"*, Olga Rotan, Viktoriya Sokolova, Patrick Gilles, Wenbin Hu, Som Dutt, Thomas Schrader, Matthias Epple. (**Poster**)
- Annual Meeting of the German Society for Biomaterials (DGBM), Hamburg, Germany (01.11 – 03.11.2012), *„Calciumphosphat-Nanopartikel zur Immunisierung gegen retrovirale Infektionen"*, Olga Rotan, Viktoriya Sokolova, Torben Knuschke, Wibke Bayer, Jan Buer, Ulf Dittmer, Astrid M. Westendorf, Matthias Epple. (**Rapid fire presentation** + **Poster**)
- 4th German-Ukrainian Symposium: Physics and Chemistry of Nanostructures and Nanobiotechnology, Ilmenau, Germany (18.09 – 20.09.2012), *"The use of calcium phosphate nanoparticles for in vitro and in vivo immunization against the influenza virus"*, Olga Rotan, Viktoriya Sokolova, Torben Knuschke, Wiebke Hansen, Peter Staeheli, Jan Buer, Astrid M. Westendorf, Matthias Epple. (**Oral presentation**)
- 4th German-Ukrainian Symposium: Physics and Chemistry of Nanostructures and Nanobiotechnology, Ilmenau, Germany (18.09 – 20.09.2012), *"Calcium phosphate nanoparticles as versatile carrier for small and large molecules across cell membranes"*, Viktoriya Sokolova, Olga Rotan, Jan

Klesing, Perihan Nalbant, Jan Buer, Torben Knuschke, Astrid M. Westendorf, Matthias Epple. (**Oral presentation**)

- 4th German-Ukrainian Symposium: Physics and Chemistry of Nanostructures and Nanobiotechnology, Ilmenau, Germany (18.09 – 20.09.2012), *"Transport of synthetic molecules over cell membranes by calcium phosphate nanoparticles"*, Viktoriya Sokolova, Olga Rotan, Thomas Schrader, Matthias Epple. (**Oral presentation**)
- Annual Meeting of the German Society for Biomaterials (DGBM), Gießen, Germany (09.11 – 12.11.2011), *"Calciumphosphat-Nanopartikel zur Stimulation des Immunsystems"*, Olga Rotan, Viktoriya Sokolova, Torben Knuschke, Jan Buer, Astrid M. Westendorf, Matthias Epple. (**Poster**)
- Annual Meeting of the German Society for Biomaterials (DGBM), Gießen, Germany (09.11 – 12.11.2011), *"Calciumphosphat-Nanopartikel als effiziente Träger für Biomoleküle durch die Zellmembran"*, Jan Klesing, Viktoriya Sokolova, Olga Rotan, Anna Kovtun, Perihan Nalbant, Jan Buer, Torben Knuschke, Astrid M. Westendorf, Matthias Epple. (**Poster**)
- Annual Meeting of the German Society for Biomaterials (DGBM), Gießen, Germany (09.11 – 12.11.2011), *"Charakterisierung von Exosomen mittels Rasterelektronenmikroskopie und Nanoparticle Tracking Analysis"*, Johannes Rüsing, Viktoriya Sokolova, Anna-Kristin Ludwig, Olga Rotan, Bernd Giebel, Matthias Epple. (**Poster**)
- IV International Conference of young scientists, Odessa, Ukraine (16.09 – 19.09.2009) , *"Specific properties of osmotic, detergentic and peroxide hemolysis after the effect of ferric chloride on erythrocytes in vitro"*, Olga Rotan, Anna Gurieva, Iryna Chuprina, Tetyana Barannik. (**Poster**)

Acknowledgments

I am grateful to my supervisor Prof. Dr Matthias Epple for welcoming me into his group and for providing excellent working facilities that resulted in this thesis; and furthermore, for the possibility of constant professional and personal development.

I thank Prof. Dr Astrid M. Westendorf for assessment of this work and also together with Dr Torben Knuschke for great cooperative and productive work, as well as helpful discussions.

I would like to thank Prof. Dr Thomas Schrader and his group (Dr Patrick Gilles, Dr Marco Hellmert and Mr Daniel Smolin) for interesting and fruitful cooperation and friendly communication.

I would like to thank Prof. Dr Michael Ehrmann and his group (Dr Simon Pöpsel, Dr Melisa Verdanovic and Ms Katharina Severin) for interesting ideas and productive cooperation as well as nice and friendly working atmosphere.

I want to thank my former and present lab/office colleagues Dr Dirk Mahl, Dr Jan Klesing, Dr Alexander Peetsch, Dr Johannes Rüsing, Dr Joachim Enax, Dr Svitlana Chernousova, Mr Benjamin Schütze, Mr Sascha Büscher, Mr Jens Nelsen and Mr Mathis Nitschke and also Dr Anna Kovtun, Dr Gregor Dördelmann, Mr Bernhard Neuhaus, Ms Kateryna Loza, Ms Sabine Kiefer, Mrs Sabine Bollmann and Mrs Carola Fischer for their personal and professional help, great common work experience and just friendly talks.

I am also thankful to all my colleagues and coworkers from our department for useful advice, readiness to help and shared memories from business trips, celebrated holidays and events.

I am very grateful to Dr Oleg Prymak and Dr Viktoriya Sokolova for the opportunities they showed me and for help in their achievement; for broadening my knowledge in different fields on science and life.

I want to very much thank my family, especially my parents and my brother, my friends and relatives for their continuous support and belief in me.

And last but not least, I am endlessly grateful to my beloved husband Sergey for his unconditional regard and love, as well as his great help while preparing this thesis.